Karlsruher Institut für Technologie

Photophysical and Magnetic Properties of Multifunctional Lanthanide-based Polynuclear Clusters

Zur Erlangung des akademischen Grades eines

DOKTORS DER NATURWISSENSCHAFTEN

(Dr. rer. nat.)

von der KIT-Fakultät für Chemie und Biowissenschaften des

Karlsruher Instituts für Technologie (KIT)

genehmigte

DISSERTATION

von

M.Sc. Sai Prasanna Kumar Panguluri

aus

Chintapalli, Karempudi, India

1. Referent: Prof. Dr. Mario Ruben

2. Korreferentin: Prof. Dr. Annie. K. Powell

Tag der mündlichen Prüfung: 23.04.2024

Committee

Referent: Prof. Dr. Mario Ruben

Korreferent: Prof. Dr. Annie K. Powell

1. Prüfer: Prof. Dr. Horst Geckeis

2. Prüfer: Priv.-Doz. Dr. Detlef Schooß

Prüfungsvorsitz: Prof. Dr. Manfred Kappes

Tag der mündlichen Prüfung: 23.04.2024

Declaration

I, Sai Prasanna Kumar Panguluri, declare that this thesis entitled "**Exploring Photophysical and Magnetic Properties of Multifunctional Lanthanide-based Nonanuclear Clusters**" and the work presented in it are my own and the work was undertaken under the supervision of Prof. Mario Ruben at the **Institute for Quantum Materials and Technologies (IQMT)**, at the Karlsruhe Institute of Technology (KIT). I confirm that:

- This work was done wholly while in candidature for a research degree at the KIT.
- The whole thesis was written by me, and no other sources other than the specified were used.
- The rules for ensuring the good scientific practice of the Karlsruhe Institute of Technology (KIT) have been used, and the submission and archiving of the primary data, in accordance with section A(6) of the rules for ensuring the good scientific practice of KIT, has been ensured.
- The electronic version of the work is consistent with the written version.
- Where I have consulted the published work of others, this is always clearly attributed.
- I have acknowledged all main sources of help.
- Where the thesis is based on work done by myself jointly with others, I have made clear exactly what was done by others and what I have contributed myself.
- Furthermore, I declare that I did not undertake any previous doctoral studies, and I am currently not enrolled in any other ongoing doctoral procedure.

Signature: ....

Date: ....

Erklärung

Ich, Sai Prasanna Kumar Panguluri, erkläre, dass diese Arbeit mit dem Titel "**Exploring Photophysical and Magnetic Properties of Multifunctional Lanthanide-based Nonanuclear Clusters**" und die darin vorgestellten Ergebnisse meine eigenen sind. Die Arbeit wurde unter der Leitung von Prof. Dr. Mario Ruben am **Institut für QuantenMaterialien und Technologien (IQMT)**, am Karlsruher Institut für Technologie (KIT) angefertigt. Ich bestätige:

- Diese Arbeit wurde vollständig während der Kandidatur für ein Forschungsstudium am KIT durchgeführt.
- Die gesamte Arbeit wurde von mir verfasst und es wurden keine anderen Quellen als die angegebenen verwendet.
- Es wurden Maßnahmen zur Sicherstellung einer guten wissenschaftlichen Praxis des Karlsruher Instituts für Technologie (KIT) angewendet und die Übermittlung und Archivierung der Primärdaten gemäß Abschnitt A(6) der Regeln zur Sicherstellung einer guten wissenschaftlichen Praxis des KIT sichergestellt.
- Die elektronische Fassung des Werkes entspricht der schriftlichen Fassung.
- Im Fall, dass ich die veröffentlichten Arbeiten anderer konsultiert habe, wird dies immer eindeutig zugeordnet.
- Ich habe alle wichtigen Hilfsquellen zur Kenntnis genommen.
- Wenn die Arbeit auf Arbeiten basiert, die ich gemeinsam mit anderen geleistet habe, habe ich kenntlich gemacht, was von anderen geleistet wurde und was ich selbst beigesteuert habe.
- Des Weiteren erkläre ich, dass ich kein vorheriges Promotionsstudium absolviert habe und mich derzeit nicht in einem anderen laufenden Promotionsverfahren befinde.

Unterschrift:……………………………………………………

Datum:……………………………………………………

నా ప్రియమైన తల్లిదండ్రులకు,

తమ్ముడికి,

అమ్మమ్మకి,

మరియు, ఆత్మీయులకు ....

Acknowledgements

First and foremost, I would like to express my profound gratitude for having been accorded the privilege of undertaking my doctoral studies within his esteemed research group and for having been furnished with such a superlative topic. I am deeply appreciative of the myriad of scientific deliberations we shared and of the exceptional tutelage and patronage that was extended to me by my doctoral supervisor, the distinguished **Prof. Dr. Mario Ruben**, throughout the course of my research expedition. My sincere thanks to **Prof. Dr. Annie K. Powell** for agreeing to be my co-referent.

I express my utmost gratitude to my esteemed mentor, **Dr. Svetlana Klyatskaya**, whose unwavering presence and steadfast guidance have been a constant source of fortitude since the commencement of my journey. Her astute counsel and discerning advice have been of immense worth, and an unerring compass in my academic sojourn. Furthermore, I extend my profound thanks to the erudite **Dr. Eufemio Moreno Pineda**, whose generosity of spirit and magnanimity have been of inestimable assistance in my academic pursuits. His perspicacity and judgment have been a source of inspiration, and I am deeply grateful for his benevolent support and counsel. I also thank **Dr. Senthil Kumar Kuppusamy** for his supervision and guidance over the years.

Dr. Loïc J Charbonnière, Dr. Aline. M. Nonat I cannot express my gratitude enough for the opportunity you gave me to have my secondment at IPHC, UNISTRA, Strasbourg. Those four months were truly valuable and I will always cherish them. I want to thank you both for being such gracious hosts and for your relentless support and guidance even after my secondment ended. Your mentorship has helped me grow both personally and professionally and I am sincerely thankful to you for that. I thank **Prof. Dr.Jürgen Schnack** and **Prof. Dr. Marco Affronte** for their diligence in studying the Magnetocaloric effect.

I want to take a moment to express my gratitude to my amazing lab mates and colleagues at INT and IQMT. I'm forever thankful for each and every one of you and for all the memories we've shared over the past four years. A special shout out to **Dr. Nithin Suryadevara**, **Dr.**

Asato Mizuno, **Dr. Nico Balzer**, **Dr. Liang Xu**, **Dr. Jordan Appleton**, **Yaorong Chen**, **Zhaoyang Jing**, **Jo Komeda**, **Dr. Camila Gouveia Barbosa**, **Patrick Lawes**, **Dr. Shagor Chowdhury**, **Dr. Pinar Apacay**, **Dr. Barbora Brachnakova**, **Rihab Sayid**, **Dr. Najoua Sbei**, **Onur Uslu**, **Nikoleta Malinova**, **Moritz Rodert**, **Hagen Sparrenberger, Dr. Bastian Weinhart** and **Dr. Michal Valášek**, **Dr. Olaf Fuhr**, **late Dr. Andreas Eichhöfer**, **Prof. Dieter Fenske** and **Dr. Christopher E. Anson**. Oh, and a huge shout out to the **SYNPA team** in Strasbourg! Thank you all for everything, you guys are the best!

Dr. Shirin Shakouri (Serena van der Woodson), **Dr. Sören Schlittenhardt** (dingus), and **Dr. Ting-Ting Ruan** (sista), I need to express my deepest gratitude for everything you have done for me in the past four years. Your unwavering support, unconditional love, and acceptance of who I am have made all the difference in my life. You have stood by me through thick and thin, tolerating my madness and helping me navigate the challenges of this journey. I cannot express how grateful I am to have had you three in my life. Your friendship has been a beacon of light, and your presence has made me feel at home. I know that I would not have made it this far without your guidance and encouragement. As I move forward from this chapter of my life, I will never forget the memories we have made together. You have touched my heart and soul in ways that I will always cherish. Thank you for being the incredible human beings that you are and here’s to many more years of our friendship.

My friends back home **Vinaya Siby**, **Sai Rohini Narayanan Kolusu**, **Teja Gowtham Nakka**, **Mohammad Danish Hannan and Sai Sindhuja Vadlavalli** for always believing in me and for being the biggest cheer leaders and critics. I thank you all and know that I love you all. A special mention to my Masters supervisor **Prof. Dr. Rajadurai Chandrasekar** for his trust in me.

A heartfelt thank you to **Sören** for thoroughly reviewing my thesis and providing valuable suggestions and corrections that significantly improved its overall quality. Philippe Priester (**Pepe)**, thank you for stepping in and helping me with the Zusammenfassung.

I am grateful to my beloved parents, **Anjaiah Chowdary** and **Lakshmi**, my loving brother, **Gowtham Kishore**, and my amazing grandparents, **Late Hanumanthurao** and **Venkamma**.

They instilled in me the right beliefs and morals that shaped me into the individual I am today. Without all of you, there would be no me. I love you all, and you mean the world to me. **Loïc**, thank you for keeping me grounded, holding it all together for the two of us, believing in me, and being the center to which I could always return. To my **peddamama**, **peddaatta**, my **cousins**, and my **nieces**, thank you all.

I would like to express my utmost appreciation towards a certain cat by the name of **Minouch**, whose invaluable presence has aided me in maintaining a state of tranquility and in alleviating my emotional distress.

It goes without saying that it would have been a Herculean task to navigate the enchanting yet arduous journey of acquiring a Ph.D. without the invaluable support and contributions of each and every one of you and every other who helped me and believed in me during this journey.

Abstract

Consider the hypothetical scenario of a narrative being crafted regarding the elements situated in the periodic table. In such a case, the tale of lanthanides surmounting obstacles to achieve supremacy in cutting-edge technological advancements would undoubtedly be the top contender. These elements are routinely utilized in a variety of applications, for instance, YAG:**Ce**- light-emitting diodes (LEDs), **Gd**OS:**Pr**- medical X-ray instruments, **Eu^{3+}** pigments as anti-counterfeiting agents in Euro banknotes, and **Nd**FeB- strong permanent magnets employed in an extensive range of fields such as MRI scanners, generators, speakers, and transportation, including magnetic levitation trains. Due to their unparalleled optical properties, intricate energy diagrams, and extended lifetimes, there has been a surge in emphasis on luminescent tags and probes for bioanalysis and microscopy. The magnetic and optical properties of the lanthanide complexes facilitate the establishment of quantum superposition, which is the foundation of any quantum algorithm. As a matter of fact, the first successful experiments of quantum algorithms utilizing molecular Ln(III) compounds have already been conducted.

Metal clusters containing lanthanides have been found to exhibit an exceptional combination of molecular and material chemistry properties. Our study in Chapter 4 presents an efficacious cooperative sensitization up-conversion (UC) phenomenon in a nonanuclear cluster of lanthanides containing Eu^{3+} and Yb^{3+} in CD_3OD. We provide a comprehensive account of the synthesis and characterization of the heteronuclear cluster in both solid state and solution and the accompanying UC phenomenon that triggers Eu^{3+} luminescence in the visible region at concentrations as low as 100 nM when Yb^{3+} is excited by 980 nm NIR. This unique cluster not only displays the UC phenomenon with a quantum yield value of 4.88 x 10^{-8} under 1.13 W/cm^2 excitation at 980 nm but also exhibits Yb^{3+} downshifted light emission in the NIR region upon 578 nm visible excitation of Eu^{3+}. This can be fully attributed to sensitization pathways for Yb through the $^5D_0$ energy levels of Eu^{3+}. Furthermore, cooperative luminescence of Yb^{3+} is observed at approximately 500 nm upon 980 nm excitation. The $[Eu_8Yb(BA)_{16}(OH)_{10}]Cl$ cluster (BA = benzoylacetonate) is a single molecular magnet (SMM) under 4K with a modest

$U_{\mathrm{eff}}/k_B = 8.48$ K, thereby emerging as a promising prototype system for next-generation devices that combine luminescence with single molecular magnetism in a molecular cluster.

Chapter 5 entails around the compound $[Gd_9(BA)_{16}(OH)_{10}]Cl$, where we performed a rigorous analysis through single crystal X-ray diffraction, Mass spectrometry, EDX, Photoluminescence measurements, and continuous shape measures (CShMs), thereby revealing the presence of high symmetric metal coordination sites, specifically the peripheral and central sites that possess approximately C_{3v} and D_{4d} point symmetry, respectively. The inquiry into the possible application of isotropic analogues in magnetic cooling was conducted, and it was discovered that achieving up to 72% of the theoretical magnetic entropy change was possible. The magnetic data was meticulously simulated, enabling the deduction of the fact that there was an antiferromagnetic coupling between the spin centers, which ultimately accounted for the observed magnetic entropy value.

For the past three decades, the fascinating potential of storing and processing quantized information at the molecular level has been a subject of great interest, leading to the extensive study of Single-Molecule Magnets (SMMs). While recent breakthroughs have been achieved in the realm of SMMs containing a solitary lanthanide ion, we posit that SMMs can reveal a much deeper narrative beyond the constraints of single-ion anisotropy. In Chapter 6, we undertook a meticulous exploration of polynuclear lanthanide SMMs, manipulated via ligand alterations across a selected range of lanthanide ions. We present an exhaustive analysis of their magnetic characterization and the intricacies of their slow relaxation magnetic behavior, elucidating the role of lanthanide ion anisotropy and ligand field.

Zusammenfassung

Im Gegensatz zu vergangenen Annahmen sind Lanthanide heute zu einem der Fokuspunkte modernster, technologischer Entwicklungen geworden. Diese Elemente werden routinemäßig in einer Vielzahl von Anwendungen, z.B. YAG:**Ce**- Leuchtdioden (LEDs), **Gd**OS:**Pr**-medizinische Röntgengeräte, **Eu**$^{3+}$-Pigmente als Fälschungsschutzmittel in Euro-Banknoten und **Nd**FeB- starke Dauermagnete, welche in einer Vielzahl von Bereichen wie MRT-Scannern, Generatoren, Lautsprechern und im Verkehrswesen vorhanden sind, einschließlich Magnetschwebebahnen verwendet. Aufgrund ihrer unvergleichlichen optischen Eigenschaften, ihrer haben lumineszierende Markierungen und Sonden für die Bioanalyse und Mikroskopie stark an Bedeutung gewonnen. Die magnetischen und optischen Eigenschaften der Lanthanidenkomplexe erleichtern den Aufbau von koheränten Zuständen, die die Grundlage für jeden Quantenalgorithmus bilden. In unserer Anbeitsgruppe wurden inzwischen die ersten erfolgreichen Experimente mit Quantenalgorithmen unter Verwendung von molekularen Ln(III)-Verbindungen durchgeführt.

Metallcluster, die Lanthanide enthalten, weisen eine außergewöhnliche Kombination von molekularen und materialchemischen Eigenschaften auf. In unserer Studie wird in Kapitel 4 ein wirksames Phänomen der kooperativen Sensibilisierung und Aufwärtskonversion (UC) in einem nonanuklearen Lanthanoid-Cluster mit Eu^{3+} und Yb^{3+} in CD_3OD vorgestellt. Wir untersuchen umfassend die Synthese und Charakterisierung des heteronuklearen Clusters sowohl im festen Zustand als auch in Lösung. So betrachteten wir einhergehende UC-Phänomen, welches Eu^{3+}-Lumineszenz im sichtbaren Bereich bei Konzentrationen von nur 100 nM auslöst, wenn Yb^{3+} mit 980 nm NIR angeregt wird. Diese einzigartigen Cluster zeigten nicht nur das UC-Phänomen mit einer Quantenausbeute von 4,88 x 10^{-8} bei einer Anregung von 1,13 W/cm^2 bei 980 nm, sondern auch eine zu niedrigeren Wellenlängen verschobene Lichtemission von Yb^{3+} im NIR-Bereich bei einer sichtbaren Anregung von Eu^{3+} bei 578 nm. Dies kann vollständig auf Sensibilisierungspfade von Yb durch die $^5D_0$-Energieniveaus von Eu^{3+} zurückgeführt werden. Darüber hinaus wird bei einer Anregung bei 980 nm eine kooperative Lumineszenz von Yb^{3+} bei etwa 500 nm beobachtet. Der $[Eu_8Yb(BA)_{16}(OH)_{10}]Cl$-Cluster (BA = Benzoylacetonat) ist ein Einzelmolekülmagnet (SMM), der unter 4K mit einer bescheidenen magnetischen Anisotropiebarriere U_{eff}/k_B = 8,48 K und ist damit ein vielversprechendes Prototypsystem für Anwendungen der nächsten Generation. Die Lumineszenz mit einem Einzelmolekülmagnetismus in einem molekularen Cluster Kombination von ist beachtenswert.

Das eingehend befasst sich mit der Verbindung $[Gd_9(BA)_{16}(OH)_{10}]Cl$, bei der wir eine Analyse mittels Röntgeneinkristallbeugung, Massenspektrometrie, Energiedispersive Röntgenspektroskopie, Photolumineszenzmessungen und kontinuierlichen Formmessungen (CShMs) durchgeführt haben. Dabei wurde das Vorhandensein hochsymmetrischer Metallkoordinationsstellen, insbesondere der peripheren und zentralen Stellen, die eine C_{3v}- bzw. D_{4d}-Punktsymmetrie besitzen, aufgedeckt. Die Untersuchung der möglichen Anwendung isotroper Analoga bei der magnetischen Kühlung wurde durchgeführt, und es wurde gezeigt, dass bis zu 72 % der theoretischen magnetischen Entropieänderung erreicht werden können. Die magnetischen Daten wurden simuliert, so dass auf eine antiferromagnetische Kopplung zwischen den Spinzentren geschlossen werden konnte, die den beobachteten Wert der magnetischen Entropie erklärt.

In den letzten drei Jahrzehnten hat die Speicherung und Verarbeitung quantisierter Informationen auf molekularer Ebene großes Interesse geweckt, was zu umfangreichen Studien über Einzelmolekülmagnete (SMMs) geführt hat. Während jüngste Durchbrüche im Bereich der SMMs, welche ein einzelnes Lanthanid-Ion enthalten, erzielt wurden, gehen wir davon aus, dass SMMs interessante Eigenschaften jenseits der Beschränkungen der Einzelionenanisotropie enthüllen können. In Kapitel 6 haben wir eine sorgfältige Untersuchung mehrkerniger Lanthanid-SMMs vorgenommen. Die durch Ligandenveränderungen kann in einem ausgewählten Bereich der Gesamtmagnetismus der Lanthanidionen manipuliert wurden. Wir präsentieren eine umfassende Analyse ihrer magnetischen Charakterisierung und ihrer magnetischen Eigenschaften bei langsamer Relaxation von magnetischem insbesondere der Rolle der Anisotropie der Lanthanidionen und des Ligandenfeldes.

Table of Contents

Chapter 1: Insight

Motivation

In the present era of digitalization, our way of life is intricately intertwined with the internet, computers, mobile phones, and other analogous devices, which necessitate the storage and transmission of vast quantities of data. The sphere of information technology is concerned with the multidisciplinary application of principles derived from the fields of physics, chemistry, mathematics, and logic to the development of techniques for the management of data. Formerly, we relied on floppy disks and CD-ROMs to store information, but the modern-day commercially available hard drives boast of storage densities up to 1Tbit/in^2.[1] In recent years, due to the proliferation of high-speed computers and the miniaturization of devices, the data density of hard drives has been increasing at an exponential rate, doubling every 12 months, which is a pace faster than the prognostications of Moore's law.[2] Nonetheless, the extensive use of social networks, the internet, and high-end computing devices has led to a tremendous volume of data being generated every second, hence raising concerns about the storage and maintenance of this data. To increase the capacity of data storage, scientists are endeavoring to minimize the size of silicon chips, albeit this is an exorbitant method.

In 2022, OpenAI launched ChatGPT - an AI chatbot that became the fastest-growing app in history, with over a million users within a week and 100 million monthly active users in two months.[3, 4] Its success is linked to its versatility, providing users everything from specific answers to creative outputs like poetry. To evaluate trends in large datasets, machine learning algorithms are gaining popularity, which requires immense computational power accessible only through modern supercomputers. However, the current size of classical transistors is limited by quantum mechanics, necessitating quantum computation. Quantum algorithms offer exponential speedups compared to classical algorithms, such as Shor's algorithm for prime factorization[5] and Grover's search algorithm.[6] Quantum chemical calculations are expected to be the first beneficiaries of applicable quantum computers, while quantum machine learning is a longer-term application. The construction of qubits, the quantum equivalent of classical bits, has been proposed in various ways, including superconducting transmon qubits and molecular systems. IBM's Osprey is the largest quantum computer to date, with 433 individual qubits, while Google's Sycamore has 53 qubits.[6, 7]

The development of machines that operate according to the principles of quantum mechanics is a highly ambitious goal. One approach to constructing quantum bits (or qubits) is through the use of molecular systems, which offer several advantages. Complex molecules made of lanthanide ions are particularly promising candidates due to their physical properties. These ions can be utilized to create two-level systems that can function as qubits, with their optical and magnetic properties being exploited to this end. Additionally, depending on which particular lanthanide ion is employed, multi-state systems can be established that function as qu*d*its, allowing for even higher computational complexity.

There are, however, several challenges that must be addressed on the path to realizing this breakthrough technology. One such challenge concerns the scalability of the available Hilbert space. Recently, proof-of-principle experiments have been conducted, in which quantum algorithms (such as Grover's search algorithm) were implemented in a single-molecule nuclear spin qu*d*it (with $d = 4$) called $^{159}TbPc_2$.[8] This involved using the nuclear spins of the lanthanide ions as a quantum register to execute simple quantum algorithms.

The goal of linear and exponential up-scalability of the available Hilbert space expressed by the qu*d*it dimension "*d*" is addressed by synthesizing lanthanide metal complexes as quantum computing hardware. The synthesis of multinuclear large-Hilbert space complexes must be carried out under strict control of the nuclear spin degree of freedom leading to isotopologues. This enables electronic coupling between several nuclear spin units, which exponentially extends the Hilbert space available for quantum information processing. As a result, improved multilevel spin qu*d*its can be achieved, exhibiting an exponentially scalable Hilbert space, thereby enabling high-performance quantum computing and information storage.[9]

Compounds containing lanthanide elements, particularly in their prevalent +3 oxidation state, engender a plethora of states that furnish a diverse array of 4f-4f transitions spanning from the near infrared to the ultraviolet and visible regions, [10] despite these transitions being formally prohibited. However, such transitions can be accessed by energy transfer processes that lead to the emergence of the sensitized metal luminescence phenomenon.[11] These compounds have been widely employed for diverse applications such as optical and magnetic resonance imaging agents or as components of light-emitting diodes.[11] The shielding of electrons in lanthanides serves to constrain the states of these elements significantly perturbed by crystal fields, which splinter them into the so-called Stark levels. Consequently, these levels respond differentially to an external magnetic field, instigating an energy barrier that impedes the inversion of the magnetization of each individual ion.[12] Such properties have provoked researchers to contemplate the use of lanthanide complexes for single-molecule magnetic information storage and spin-based quantum information processing.[12] The incorporation of two lanthanides within molecules under the requisite conditions could satiate all these requirements.[12] Moreover, molecules that accommodate multiple lanthanides could facilitate the execution of multi-qubit quantum gates or simplify the implementation of other intricate operations such as quantum error corrections that would otherwise necessitate the artificial connection of several qubits.[13]

Objectives of the thesis

Due to their exceptional utility, the investigation of polynuclear lanthanide complexes has garnered significant interest. The primary objective of this study is to scrutinize, assay and interpret, various facets of magnetism and luminescence in the aforementioned fields by utilizing clusters designed using potent *ß*-diketonate ligands based on lanthanide polynuclear compounds.

Objective 1: To study the upconversion luminescence of the *ß*-diketonate ligands-based lanthanide polynuclear compounds especially in the context of upconversion of light from the NIR to the Visible region. The growing interest in UC materials for biological applications has led to a focus on scaling down UC to the molecular level.

Objective 2: In order to scrutinize a *ß*-diketonate ligand-based nonanuclear cluster based on Gadolinium within the domain of solid-state magnetic coolants, we shall endeavor to analyze the feasibility of harnessing compounds that comprise Lanthanide(III) ions, particularly Gadolinium(III), as magnetocaloric substances that exhibit exceptional proficiency in the low-temperature millikelvin spectrum, thereby challenging the efficacy of dilution refrigeration techniques based on $^{3}He/^{4}He$.

Objective 3: The overarching objective pertains to the synthesis and characterization of a class of polynuclear SMM complexes comprising lanthanides, which are predicated on the coordination of *ß*-acetylacetonate and 9-hydroxyphenalen-1-one ligands. Furthermore, the magnetic properties of these aforementioned complexes are to be studied and comprehended. To this end, the same measurements will be employed to elucidate the effect that different ligands have on the SMM properties of the complexes.

Chapter 2: Fundamentals and Theoretical Framework

2.1. Lanthanides

2.1.1. Introduction

Scandinavia was the birthplace of lanthanide chemistry, which started in 1794 when Johann Gadolin succeeded in obtaining an ‘earth’ (oxide) from a black mineral called gadolinite. He named the earth yttria. Shortly after, ceria, another earth, was obtained from cerite by M.H. Klaproth, J.J. Berzelius, and W. Hisinger. However, only in 1839–1843 did C.G. Mosander, a Swede, first separated these earths into their component oxides. Mosander resolved ceria into the oxides of cerium and lanthanum and a mixed oxide called ‘didymia,’ which is a mixture of the oxides of the metals from Pr through Gd. Similarly, the original yttria was separated into substances named erbia, terbia, and yttria, although the first two names were reversed some 40 years later. The new means of spectroscopic analysis created confusion and permitted misidentifications, resulting in the erroneous claim of around 70 'new' elements in the course of the century. Mendeleev's Periodic Table was not helpful either. When he first published his Periodic Table in 1869, he included only lanthanum, cerium, didymium (now known to have been a mixture of Pr and Nd), another mixture in the form of erbia, and yttrium. The unreliable information about atomic mass made it difficult to correctly position these elements in the table; some had not yet been isolated as elements. It was impossible to predict how many of these elements existed until Henry Moseley (1887–1915) analyzed the X-ray spectra of elements and gave meaning to the concept of atomic number. He determined the 15 elements from lanthanum to lutetium (only identified in 1907) (**Figure 1**). The discovery of radioactive promethium was made after World War II. The classification and eventual separation of the lanthanides into individual elements was extremely difficult because of their pronounced similarity to each other, especially regarding their general adoption of the +3-oxidation state in aqueous solution. It was only after the work of Bohr and Moseley that precisely how many of these elements existed was known. Most current versions of the Periodic Table place lanthanum under scandium and yttrium.

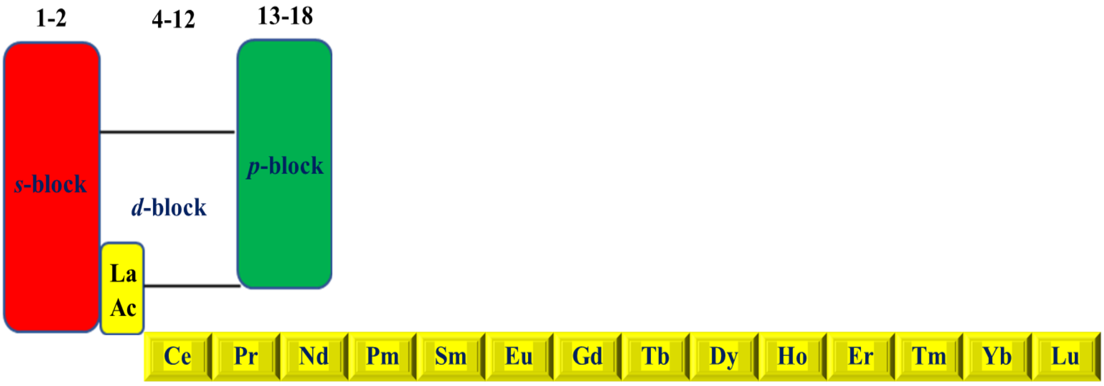

Figure 1. Schematic demonstration of Lanthanides and their positioning in the periodic table.

The chemistry of lanthanides has distinct features that differentiate them from d-block metals. These elements show greater reactivity than transition metals, similar to Group II metals. They exhibit a wide range of coordination numbers, usually 6-12, and sometimes 2, 3, or 4. The geometry of coordination is determined by ligand steric factors rather than crystal field effects.

Lanthanides form often labile 'ionic' complexes that undergo easy exchange of ligands. The 4f orbitals in the Ln^{3+} ion do not play a direct role in bonding since they are well shielded by the $5s^2$ and $5p^6$ orbitals. This makes their spectroscopic and magnetic properties largely uninfluenced by the ligand. Compared to d-block metals, they have small crystal-field splitting and very sharp electronic spectra. Lanthanides prefer anionic ligands with donor atoms of relatively high electronegativity, such as O and F. Since the small Ln^{3+} ion has high hydration energy, they form hydrated complexes, which can cause uncertainty in assigning coordination numbers. Insoluble hydroxides precipitate at neutral pH unless complexing agents are present. Lanthanides have a chemistry that mostly involves one (3+) oxidation state, especially in aqueous solution and occasional 2+ and 4+ oxidation states. They do not form Ln=O or Ln≡N multiple bonds like many transition metals and some actinides. Unlike transition metals, they do not form stable carbonyls and have hardly any chemistry in the 0-oxidation state.

2.1.2. Abundance of the Lanthanides

Table 1. Abundance of the Lanthanides.

Abundance	**La**	**Ce**	**Pr**	**Nb**	**Pm**	**Sm**	**Eu**	**Gd**	**Tb**	**Dy**	**Ho**	**Er**	**Tm**	**Yb**	**Lu**	**Y**
Crust (ppm)	**35**	**66**	**9.1**	**40**	**0.0**	**7**	**2.1**	**6.1**	**1.2**	**4.5**	**1.3**	**3.5**	**0.5**	**3.1**	**0.8**	**31**
Solar System	**4.5**	**1.2**	**1.7**	**8.5**	**0.0**	**2.5**	**1.0**	**3.3**	**0.6**	**3.9**	**0.9**	**2.5**	**0.4**	**2.4**	**0.4**	**40.0**

*** with respect to 10^7 atoms Si**

The abundance of lighter lanthanides is higher than that of the heavier ones (**Table 1**).[14] Elements having even atomic numbers are more abundant than those having odd atomic numbers. Cerium, the most abundant lanthanide on earth, has a comparable crustal concentration as that of lighter metals like Ni and Cu. Even the rarest lanthanides, like Tm and Lu, are more common than Bi, Ag, or platinum metals. The abundance of elements is determined by how they were synthesized by atomic fusion in the cores of stars. Heavy elements are only made in supernovae, and synthesizing heavier nuclei requires higher temperature and pressure, which becomes increasingly difficult as the atomic number increases. The Oddo-Harkins rule, also known as odd/even alternation, is a general phenomenon that reflects the fact that elements with odd mass numbers have larger nuclear capture cross sections and are more likely to take up another neutron, resulting in less common odd atomic number elements as compared to even mass number elements. Nuclei with an even atomic number are more stable when formed.

2.1.3 Oxidation States and Electronic Configurations

The lanthanides and actinides belong to a group of elements in which the 4f and 5f orbitals are gradually filled. Starting from lanthanum, which has the electron configuration [Xe] $6s^25d^1$ (as listed in **Table 2**),[15] the 5d subshell is lower in energy than 4f. As more protons are added to the nucleus, the 4f orbitals contract rapidly and become more stable than the 5d subshell, as the 4f orbitals penetrate the 'xenon core' more deeply. This leads to cerium having the electron configuration [Xe] $6s^25d^14f^1$, and the trend continues with the metals praseodymium and neodymium having arrangements of [Xe] $6s^24f^3$ and [Xe] $6s^24f^4$, respectively. The pattern of filling the 4f orbitals continues with the metals from neodymium to europium, all of which have configurations of [Xe] $6s^24f^n$ (n = 4-7). However, at europium, the stability of the half-filled f subshell becomes such that the next electron is added to the 5d orbital instead, leading to gadolinium having the electron configuration [Xe] $6s^25d^14f^7$. The earlier pattern of filling the 4f orbitals resumes at terbium, which has the configuration [Xe] $6s^24f^9$. The succeeding elements from terbium to ytterbium have configurations of [Xe] $6s^24f^n$ (n = 10-14). Finally, the last lanthanide, lutetium, has the 4f subshell filled, resulting in the electron configuration [Xe] $6s^25d^14f^{14}$. The most studied trivalent ions have [Xe] $4f^n$, which is shown in the **Table 2**.

Table 2. Lanthanides elctronic configurations and Oxidation states.

Element name	**Symbol**	**Z**	**Ground state electronic configuration**				**Radius/pm**	
			Ln	**Ln^{2+}**	**Ln^{3+}**	**Ln^{4+}**	**Ln**	**Ln^{3+}**
Lanthanum	La	57	$[Xe]6s^{2}5d^{1}$	$[Xe]5d^{1}$	$[Xe]\ 4f^{0}$		188	116
Cerium	Ce	58	$[Xe]4f^{1}6s^{2}5d^{1}$	$[Xe]4f^{2}$	$[Xe]\ 4f^{1}$	$[Xe]\ 4f^{0}$	183	114
Praseodymium	Pr	59	$[Xe]4f^{3}6s^{2}$	$[Xe]4f^{3}$	$[Xe]\ 4f^{2}$	$[Xe]\ 4f^{1}$	182	113
Neodymium	Nd	60	$[Xe]4f^{4}6s^{2}$	$[Xe]4f^{4}$	$[Xe]\ 4f^{3}$		181	111
Promethium	Pm	61	$[Xe]4f^{5}6s^{2}$	$[Xe]4f^{5}$	$[Xe]\ 4f^{4}$		181	109
Samarium	Sm	62	$[Xe]4f^{6}6s^{2}$	$[Xe]4f^{6}$	$[Xe]\ 4f^{5}$		180	108
Europium	Eu	63	$[Xe]4f^{7}6s^{2}$	$[Xe]4f^{7}$	$[Xe]\ 4f^{6}$		199	107
Gadolinium	Gd	64	$[Xe]4f^{7}6s^{2}5d^{1}$	$[Xe]4f^{7}5d^{1}$	$[Xe]\ 4f^{7}$		180	105
Terbium	Tb	65	$[Xe]4f^{9}6s^{2}$	$[Xe]4f^{9}$	$[Xe]\ 4f^{8}$	$[Xe]\ 4f^{7}$	178	104
Dysprosium	Dy	66	$[Xe]4f^{10}6s^{2}$	$[Xe]4f^{10}$	$[Xe]\ 4f^{9}$	$[Xe]\ 4f^{8}$	177	103
Holmium	Ho	67	$[Xe]4f^{11}6s^{2}$	$[Xe]4f^{11}$	$[Xe]\ 4f^{10}$		176	102
Erbium	Er	68	$[Xe]4f^{12}6s^{2}$	$[Xe]4f^{12}$	$[Xe]\ 4f^{11}$		175	100
Thulium	Tm	69	$[Xe]4f^{13}6s^{2}$	$[Xe]4f^{13}$	$[Xe]\ 4f^{12}$		174	99
Ytterbium	Yb	70	$[Xe]4f^{14}6s^{2}$	$[Xe]4f^{14}$	$[Xe]\ 4f^{13}$		194	99
Lutetium	Lu	71	$[Xe]4f^{14}6s^{2}5d^{1}$	$[Xe]4f^{14}5d^{1}$	$[Xe]\ 4f^{14}$		173	98

2.1.4. Electronic and Magnetic Properties of Lanthanides

The Russell-Saunders coupling scheme can explain the behavior of electrons in certain electronic configurations. It separates the coupling of electron spins from the coupling of electron orbital angular momenta. This scheme allows for unquenched orbital moment. Despite ligands being bound to a lanthanide ion, the ground state of the ion remains unaffected, and crystal field splittings are weak. This is due to the 4f electrons being shielded by the already filled 5s and 5p orbitals. The electron spins are coupled together and added vectorially to obtain the spin quantum number (S) of the ion. Similarly, the electron orbital angular momenta (l) are also coupled together. For an f electron, the magnetic quantum number (m_l) can have one of seven integral values between +3 and -3. The total orbital angular momentum quantum number (L) (**Table 3**) is obtained by vectorially adding the m_l-values for the f electrons for the multi-electron ion. There exists a weaker coupling between S and L, known as spin-orbit coupling.

Table 3. State symbols for different values of L.

L	0	1	2	3	4	5	6	7
State symbol	S	P	D	F	G	H	I	K

The sum of two vectors, L and S, results in a quantum number called J. J can take on values ranging from (L + S) to (L - S), with possible values including (L + S) - 1, ..., and (L - S). To illustrate, if L is equal to 6 and S is equal to 2, J can be 8, 7, 6, 5, or 4.

Every ion has a number of possible electronic states, and determining the ground state is important in understanding its properties. This can be done using Hund's Rules, which involve several conditions. Firstly, the spin multiplicity (2S + 1) must be as high as possible. Secondly, if there are multiple terms with the same spin multiplicity, the ground state is the one with the highest L-value. Finally, for a shell less than half-filled, the J value for the ground state must be the lowest possible, while for a shell more than half-filled, the J value must be the highest possible.

As an example, let's consider Eu^{3+}. We must first calculate the spin multiplicity to determine the term symbol for its ground state. In this case, $S = \sum m_s = 6/2 = 3$, so $2S + 1 = 2(3) + 1 = 7$. Next, we calculate the magnetic quantum numbers (m_l) sum to find the L-value. For Eu^{3+}, $L = \sum m_l = +3 + 2 + 1 + 0 - 1 - 2 = +3$, which makes it an F state.

Lastly, we can determine the possible values of J using the equation J = (L + S); (L + S) − 1; (L + S) − 2; ....; (L − S). In this case, J can have the values of 6; 5; 4; 3; 2; 1; 0. Since the shell is less than half-filled, the state with the lowest J-value is the ground state, which in this case is $J = 0$. Therefore, the term symbol for the ground state of Eu^{3+} is $^7F_0$.

Now let's consider another case with the 4f shell more than half-filled for e.g. Yb^{3+}. The (2S + 1) and the L term are calculated similar to Eu^{3+}. Therefore $S = \sum m_s = 1/2 = 3$, so $2S + 1 = 2(1/2) + 1 = 2$ and $L = \sum m_l = 3$, which makes it an F state. Now the *J* value for more than half-filled ions is calculated differently to Eu^{3+} (less than half-filled) with the ground state being the highest *J* value (L + S). Therefore, the term symbol for the ground state of Yb^{3+} is $^2F_{7/2}$.

Except for La^{3+} and Lu^{3+}, as well as Y^{3+}, all Ln^{3+} ions possess unpaired electrons, making them paramagnetic. Their magnetic properties are solely determined by their ground state, with two exceptions we will come across. This is because their excited states are too far apart from the ground state, making them thermally inaccessible, thanks to spin-orbit coupling (**Figure 2**)[16] The proximity of the 4f orbitals towards the nucleus causes several interesting effects like hyperfine coupling and spin-orbit coupling, which are, in turn, majorly responsible for the physical and chemical properties of lanthanides. Spin-orbit coupling (SOC) is a general phenomenon observed in open-shell systems with $L > 0$ (where L is the orbital angular momentum quantum number). In heavy atoms, the electrons that are close to the nucleus show an increased mass due to relativistic effects based on their high velocities. In closed-shell systems, this does not affect SOC (because $L = 0$); however, in lanthanides, relativistic effects are not negligible and, as the 4f shell is only partially occupied, cause very strong SOC. As a reference, **Figure 2**[16] shows a schematic energy diagram of a lanthanide ion emphasizing the different contributions. In Ln's the SOC is playing a major role, stronger than the effect of the ligand field exerted by the chemical environment. In comparison, for transition metals, SOC is typically only viewed as a perturbation much weaker than the splitting caused by the ligand field. Unlike transition metals, where one can differentiate between coordination geometries, the magnetic moment of Ln^{3+} ions is almost independent of their environment. For example,

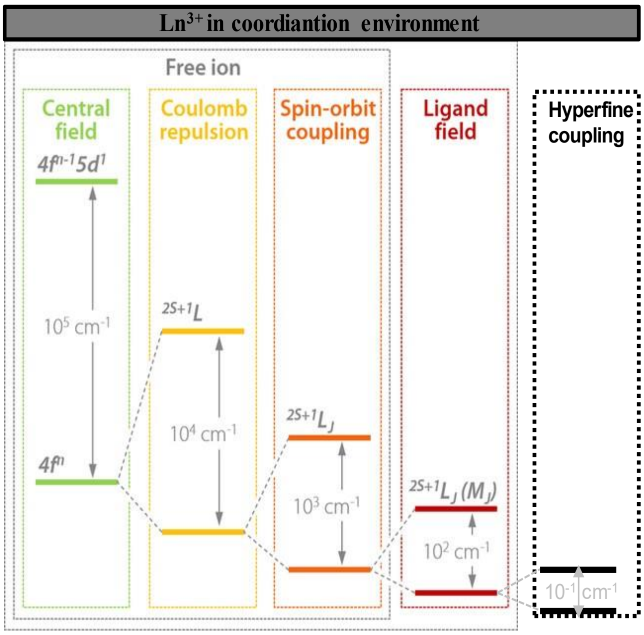

Figure 2. Contributions of different factors on the energy levels of a triply oxidized lanthanide ion (Ln^{3+}) in a certain coordination environment. (Reproduced from the Reference 16)

this is possible in the case of octahedral and tetrahedral Co^{2+} complexes. The magnetic moments can be calculated using the equation:

$$\mu_{eff} = g_J\sqrt{J(J+1)}$$

where the Landè g-factor is defined by:

$$g_J = 3/2 + \frac{\lfloor S(S+1) - L(L+1) \rfloor}{2J(J+1)}$$

The ground state is typically separated from excited states due to spin-orbit coupling strength, except for Sm^{3+} and Eu^{3+} (the energy gap is too big for the excited states to be relevant at T up to RT). In these exceptional cases, the magnetic moment is influenced by contributions from low-lying paramagnetic excited states, as demonstrated in **Figure 3**.[17] Although the $^7F_0$ ground state would make Eu^{3+} compounds diamagnetic, contributions from thermally accessible levels, such as $^7F_1$ and $^7F_2$ (factoring in a Boltzmann factor of $\exp(-\Delta E/kT)$), lead to observed magnetic moments at room temperature that range around $3.5\mu_B$. Likewise, in the case of Sm^{3+}, the population of the $^6H_{7/2}$ state due to thermal activity results in magnetic moments around 1.6 μ_B. If only the $^6H_{5/2}$ ground state were responsible, the magnetic moment would be expected to be 0.845 μ_B.

Energy level diagrams for all the Ln^{3+} ions are shown in **Figure 3**.[17] These are based on theoretical predictions, coupled with experimental results. Accurate values have been determined in many experimental situations, such as halide lattices like LnF_3, which closely resemble those of the gaseous ions. In the lanthanide ions, the filled 'outer' 5s and 5p orbitals efficiently shield the 4f electrons from surrounding ligands, with the result that crystal field splittings are of the order of 100 cm^{-1}. The weak crystal field (CF) splitting can thus be treated as a perturbation upon the free-ion levels; in contrast, of course, in the 3d metals, CF splitting is large, and L–S coupling is weak. A consequence of the lack of CF effects in the lanthanides is that the thermal motion of the ligands has very little effect upon them (as is not the case in the 3d situation), so the f–f absorption bands in the spectra are very narrow, almost as narrow as for free (gaseous) ions.

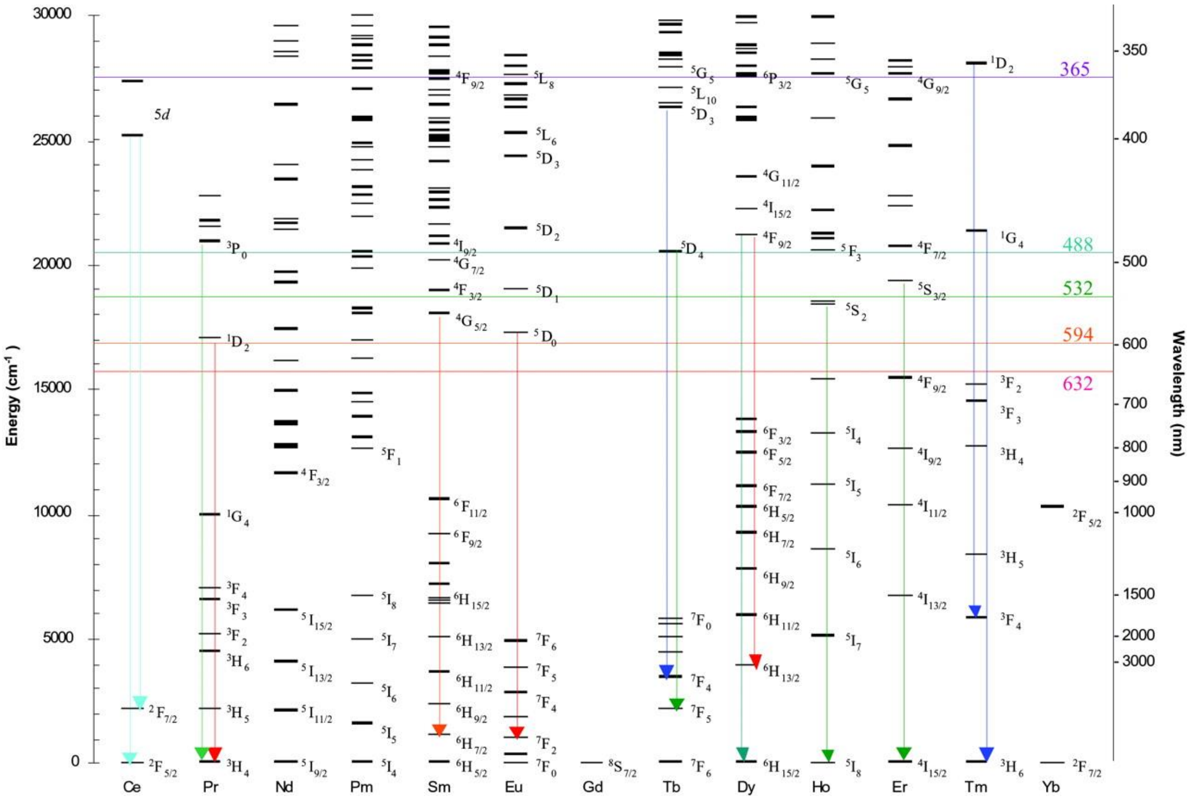

Figure 3. Energy level diagram of trivalent Ln ions with dominant visible emission transitions observed in silicate glasses designated by arrows representing the approximate color of the fluorescence. Horizontal lines extending across the diagram designate the location of common organic label excitation sources labeled by wavelength in nm. (Taken from the Reference 17).

2.1.5. Electronic Spectra of Lanthanides

Lanthanide ions can absorb electromagnetic radiation, particularly in the visible region of the spectrum, which excites the ion from its ground state to a higher electronic state due to the partially filled 4f subshell. The f-f transitions can be excited by both magnetic dipole and electric dipole radiation. Magnetic dipole transitions are usually not observable, but in the case of lanthanides, magnetic dipole transitions can often be seen, especially in fluorescence spectra, as electric dipole transitions are much weaker than those of transition metal complexes. Electric dipole transitions are parity-forbidden (also called Laporte-forbidden) in the same way as d-d transitions in transition metal ions, while magnetic dipole transitions are parity-allowed. The f-f transitions gain more intensity through mixing in higher electronic states of opposite parity, including d states, which is caused by the permanent effects of a low-symmetry ligand field or through asymmetric molecular vibrations that momentarily destroy any center of symmetry. This effect is referred to as vibronic coupling, but it is still weaker than in transition metal complexes.

Not all lanthanide ions give rise to f-f transitions, such as f^0 and f^{14} species, La^{3+} and Lu^{3+}. Similarly, there are no f-f transitions for f^1 (Ce^{3+}) and f^{13} (Yb^{3+}) ions since there is only a single L-value and no upper 4f state. In the case of Ce^{3+}, transitions between $^2F_{5/2}$ and $^2F_{7/2}$ are observed as a broad band in the infrared region around 2000 cm^{-1}. However, Ce^{3+} and Yb^{3+} give rise to broad $4f^{n} \rightarrow 4f^{n-1}5d^1$ transitions, as do many lanthanides. Even Eu^{3+} ions, which have several absorptions in the visible region of the spectrum, have only weak absorptions, making many of its compounds appear colorless.

Only three tripositive ions have colored compounds, namely Pr^{3+}, Nd^{3+}, and Er^{3+}. **Table 4**[15] lists the colors of Ln^{3+} ions in aqueous solution, In contrast to transition metal chemistry, the electronic spectra of lanthanide compounds are similar to those of free ions. The crystal-field splittings can be treated as a perturbation on the unsplit $^{2S+1}L_J$ levels. In this way, complexes have much the same color as the corresponding aqua ions, and one cannot distinguish between coordination geometries, such as octahedrally and tetrahedrally coordinated Co^{2+}, for example (let alone note profound color differences). The sharpness of the f-f transitions is another consequence of the weak CF splittings.

Table 4. Colors of aqueous solutions of Ln^{3+} ions.

Lanthanide ions ($^{3+}$)	**f^n ($0\leq n \geq 14$)**	**Colour**
La, Ce, Eu, Gd, Yb, Lu	f^0, f^1, f^6, f^7, f^{13}, f^{14}	Colourless
Pr	f^2	Green
Nd	f^3	Violet
Pm	f^4	Pink
Sm, Dy	f^5, f^9	Pale Yellow
Tb	f^8	Very pale pink
Ho	f^{10}	Yellow
Er	f^{11}	Rose
Tm	f^{12}	Pale Green

The 4f-4f transitions in the electronic spectra of lanthanide complexes don't typically have a diagnostic purpose, unlike the situation with the 3d transition metals. However, the electronic spectra of the octahedral $[LnX^6]^{3-}$ ions (X = Cl, Br) have very small extinction coefficients compared to the corresponding aqua ions, due to the high symmetry of the environment. Some transitions are "hypersensitive" to changes in the symmetry and strength of the ligand field, which leads to shifts in the absorption bands, usually towards longer wavelengths, as well as variations in band splitting and intensity. Most notably, this is observed for Ho^{3+}, Er^{3+} and particularly for the $^4I_{9/2} \rightarrow ^2H_{9/2}$, $^4F_{5/2}$ and $^4I_{9/2} \rightarrow ^4G_{5/2}$, $^4G_{7/2}$ transitions in the case of the Nd^{3+} ion.

2.1.6. Luminescence Spectra of Lanthanides

Luminescence can be observed in numerous lanthanide ions, which emit radiation from an excited electronic state. The light produced by these ions has distinct lines characteristic of f-f transitions of a Ln^{3+} ion. By attaching an appropriate organic ligand, such as a β-diketonate, phenanthroline, or crown ether, to the lanthanide, the luminescence can be significantly enhanced. A summary of the process is shown in **Figure 4**.

The mechanism of luminescence in lanthanide complexes involves the promotion of an electron to an excited singlet state in a ligand upon the absorption of a quantum of energy (from ultraviolet light, for example). The photon relaxes back to the lowest state of the excited singlet before returning to the ground state either directly (ligand fluorescence) or through a non-radiative path to a triplet state of the ligand. From there, it may return to the ground state through phosphorescence or non-radiative emission, or it may undergo non-radiative intersystem crossing to reach an excited state of a nearby Ln^{3+} ion.

Certain Ln^{3+} ions, particularly Eu^{3+} and Tb^{3+}, have excited states that are slightly lower in energy than the triplet states of typical ligands, resulting in strong metal-ion fluorescence. Other Ln^{3+} ions, such as La^{3+} and Lu^{3+}, have no f^n excited state, while Gd^{3+} has all of its excited states above the ligand triplet states. Tb^{3+} and Eu^{3+} are the most employed ions for these studies and produce green and red luminescence, respectively.

In Eu^{3+} complexes, careful study of the $^7F_0 \rightarrow ^5D_0$ separation has shown it to depend on the donor atoms involved, with the actual values varying between 17232 cm^{-1} in $[Eu(dpa)_3]^{3-}$ and

17280 cm^{-1} in $[Eu(H_2O)_9]^{3+}$. The ligand field in a complex ion partially or completely removes the degeneracy of a given $^{2S+1}L_J$ term, resulting in the splitting of the emission line depending on the symmetry of the ligand field. In many cases, individual transitions in the luminescence spectra consist of more than one line.

The intensity and splitting pattern of certain transitions in the fluorescence spectra of Eu^{3+} and Tb^{3+} compounds can provide valuable information about the environment of the lanthanide ion. The magnetic dipole transitions are of comparable intensity to the electric dipole transitions because of the weakness of the latter. The luminescence technique is particularly applicable to lanthanide complexes, and because interpretation is simplest in the case of Eu^{3+}, discussion will focus on that ion, particularly since it is most involved in applications.

For the europium(III) ion, the $^7F_0$ ground state is unsplit, so transitions to it provide straightforward information about the excited state. If more than one component is seen for the $^5D_0$ state, it indicates the presence of more than one europium site. In the luminescence spectrum of the crown-ether complex $[Eu(NO_3)_3(15\text{-crown-}5)]$, which contains a pentadentate

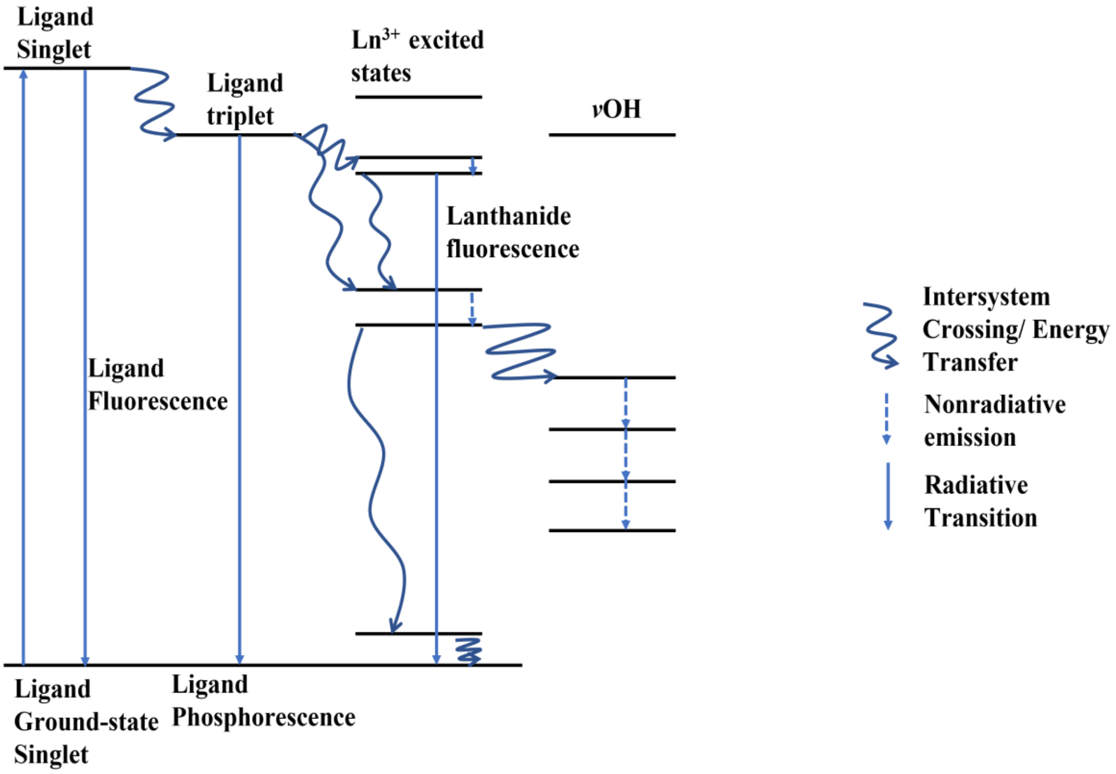

Figure 4. Luminescence and quenching in lanthanide complexes.

macrocycle and three bidentate nitrates, indicating 11-coordinate europium, a single, very sharp line is seen for the $^5D_0 \rightarrow ^7F_0$ transition, indicating only one europium site. The $^5D_0 \rightarrow ^7F_1$ transition appears as a doublet and singlet, consistent with the pentagonal pseudosymmetry observed in its crystal structure. The $^5D_0 \rightarrow ^7F_2$ transition is an electric dipole in origin and absent if the ion is on an inversion center. Its intensity is very sensitive to the environment, making it a good 'probe,' so its strength indicates a relatively low site symmetry.

It is possible for luminescence in an aqueous solution to be deactivated by transferring the energy of the lanthanide to water molecules in the form of vibrational energy transfer (**νOH**). In **Figure 4**, this process is shown, along with the processes involved in Eu^{3+} luminescence (only a selection of radiative transitions of vibration levels of water are displayed). The use of multidentate ligands that prevent water from entering the metal coordination sphere and ligands that encapsulate the lanthanide ion can minimize this "quenching" of luminescence, apart from working in the solid state or using non-aqueous solvents. The inherent weakness of luminescence from lanthanides can be attributed to Laporte-forbidden transitions. We discussed how vibrational transfer deactivation can be reduced, but another way to enhance luminescence considerably is to use a chromophore as a ligand. The chromophore absorbs a specific wavelength of radiation strongly, acting as an "antenna" that can transfer it to the lanthanide and excite it to the emissive state. Excitation in the 330-430 nm region (**Figure 5**) is required for this process. The most probable acceptor levels for Eu^{3+} and Tb^{3+} are 17200 and 20400 cm^{-1}, respectively, whereas competing thermally activated back-energy-transfer occurs if the

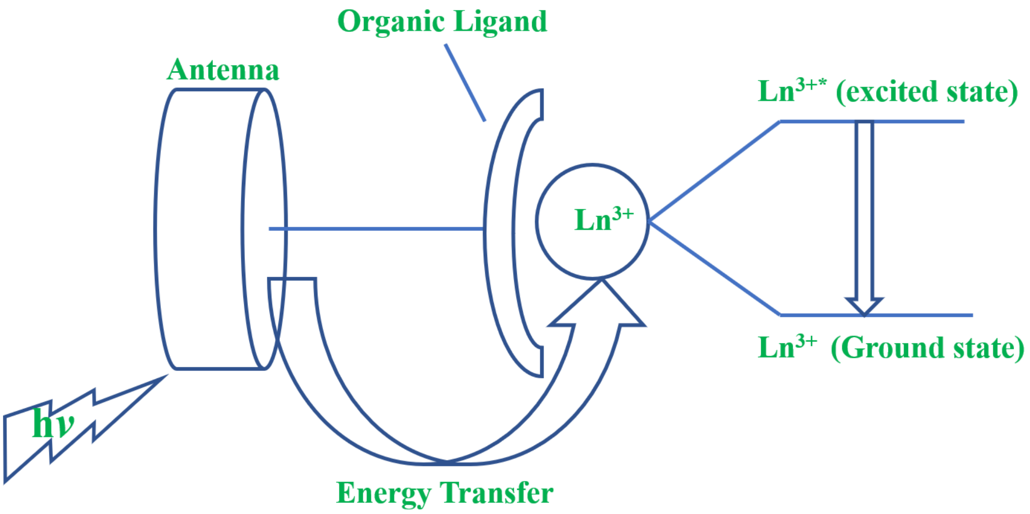

Figure 5. Antenna effect in Ln^{3+} coordination complexes.

triplet level in the acceptor ligand is below 22000 cm^{-1}. Some of the most suitable ligands utilized in the past 20 years include Lehn's tris(bipyridyl) cryptand,[18] calixarenes,[19] and substituted macrocycles containing phenanthridines.[20] The acceptor chromophore does not need to be directly connected to the lanthanide but should be close for optimal results. Some lanthanides, particularly Yb^{3+}, Nd^{3+}, and Er^{3+}, emit in the near-IR, and they can be directly excited with an optical parametric oscillator.

2.1.7 Polynuclear Lanthanide Complexes

Polyhedral structures that self-assemble are frequently observed in biology. For example, the coats of many viruses have an icosahedral symmetry-based structure. Although creating synthetic polyhedral molecular assemblies is a challenging task, recent advances in supramolecular chemistry have made this possible. The creation of macromolecular and supramolecular entities with predetermined geometric shapes and well-defined internal environments could have significant implications for inclusion phenomena, molecular recognition, and catalysis. The self-assembly of nanoscale high-nuclearity metal clusters using coordination chemistry methods has gained considerable attention in recent years. Due to their size-dependent physical properties, these supermolecules exhibit unique structural characteristics and are essential in biology and materials chemistry, particularly in potential precursors utilized in magnetic, optical, electronic, and catalytic processes. To obtain these high-nuclearity clusters, a common strategy is to control the hydrolysis of metal ions in the presence of appropriate chelating ligands.[21] A variety of ligands can be used, including *ß*-diketonates (**Figure 6**),[22] polyketonates, polyamines, polyols, carboxylates, pyridonate, and alkoxides.[23] Hydrophilic groups, such as oxo and hydroxo, bridge the metal ions to form a cluster core, while hydrophobic groups take up positions in the periphery, preventing the core from further aggregation, thus forming a finite-sized polynuclear complex. Polynuclear lanthanide complexes are receiving much attention due to their distinguished applications. Great efforts have been focused on constructing luminescent nanodevices[24,25] using europium(III) nanoclusters. Similarly, gadolinium(III) nanoclusters with tunable electron relaxation behavior have piqued interest in magnetic resonance imaging applications.[26,27]

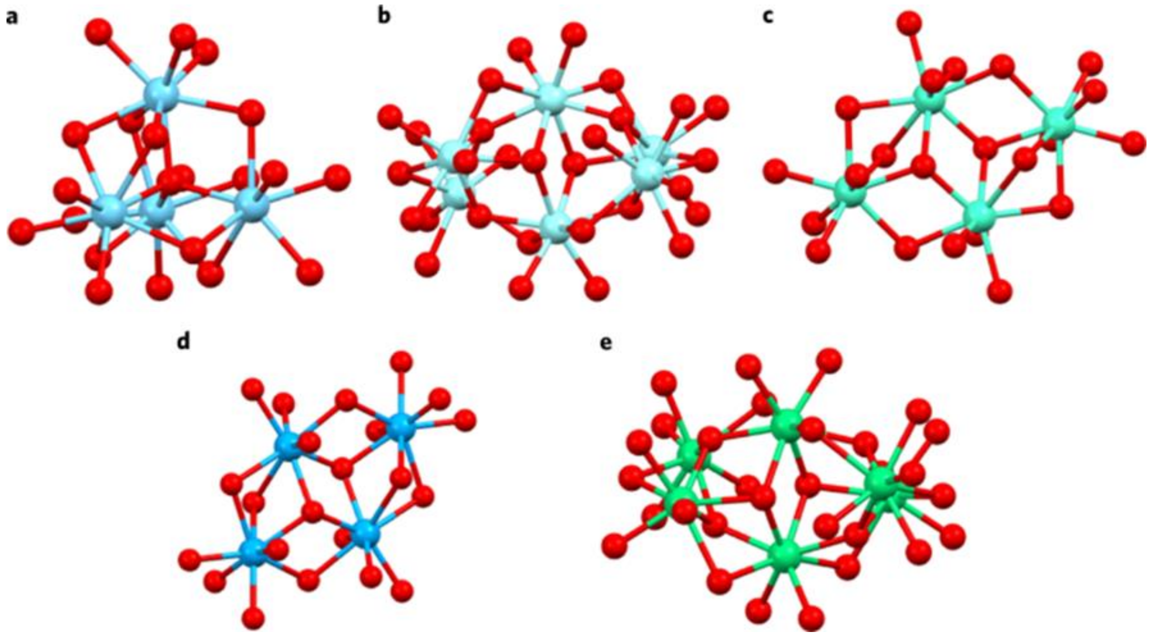

Figure 6 Polynuclear lanthanide–diketonato clusters_. **a**, Lanthanum, La. **b**, Yttrium, Y. **c**, Gadolinium, Gd. **d**, Europium, Eu. **e**, Erbium, Er. All hydrogen and carbon atoms have been omitted for clarity. (Reproduced from the Reference 22)

2.2. Molecular Upconversion

Cooperative Sensitization Upconversion

2.2.1 Introduction

When light interacts with matter, it transfers energy to the matter in the form of photons. This causes the electrons to redistribute, resulting in the formation of an excited state. Some of the excess energy is transferred to the material as heat, while the remaining energy can be emitted as photons. This causes photoluminescence, which occurs at a lower energy than the incident light. George Stokes studied this phenomenon extensively,[28] particularly in luminescent solutions like quinine sulfate. He observed that the energy loss resulted in an increase in emission wavelength compared to the absorption one, which he named the "Stokes shift."(**Figure 7a**)

Sometimes, when a compound is in an excited state (L*), it can absorb the energy of a second photon and reach an even higher excited state (L**). This is shown as L** in (**Figure 7b**). If this energy is then released in the form of a photon, the luminescence will happen at a lower wavelength than the original incident one. This process is called upconversion (UC), and it is an anti-Stokes process.[29](**Figure 7 a**)

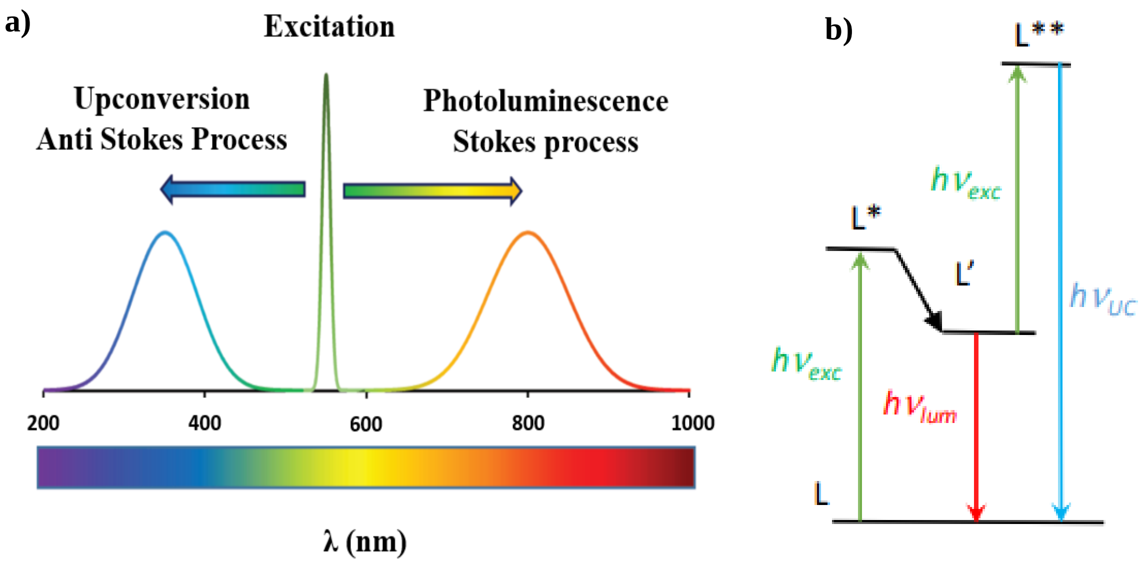

Figure 7. a) Wavelength dependence of the luminescence phenomena. b) Schematic representation of the phenomenon of photoluminescence and upconversion.

The UC mechanisms can be categorized into two broad divisions.[29] The first one entails phenomena related to non-linear processes such as two-photon absorption excitation, second harmonic generation, and cooperative luminescence. As early as 1931, Maria Göppert-Meyer developed the concept of two-photon absorption while studying these phenomena.[30] The concept was experimentally demonstrated thirty years later with the observations of second harmonic generation[31] and two-photon fluorescence,[32] thanks to the income of high energy excitation sources, the MASERs (Microwave Amplification by Stimulated Emission of Radiations).[33] However, these mechanisms are based on virtual excited states and are generally weakly efficient.

The second category of upconversion (UC) processes involves the successive absorption of photons by the material. This process is known as a first-order process, and it results in improved efficiency. In 1959, Nicolaas Bloembergen proposed the concept of quantum counters,[34] which involves the absorption of an infrared photon to reach a first excited state, followed by optical pumping to a higher-energy excited state. There are three main mechanisms involved in this process: excited state absorption (ESA), energy transfer upconversion (ETU), and cooperative sensitization (CS). **Figure 8** summarizes these mechanisms.

In the excited state absorption (ESA) mechanism, a photon is absorbed, leading to an intermediate excited state. Then, a second photon is absorbed, which takes the molecule to the emitting UC luminescent level.[35] Energy transfer UC (ETU), on the other hand, involves the absorption of a second photon by another ion in the molecule. Then, an energy transfer occurs between the two ions, which ultimately feeds the emitting upper excited state.[36, 37]

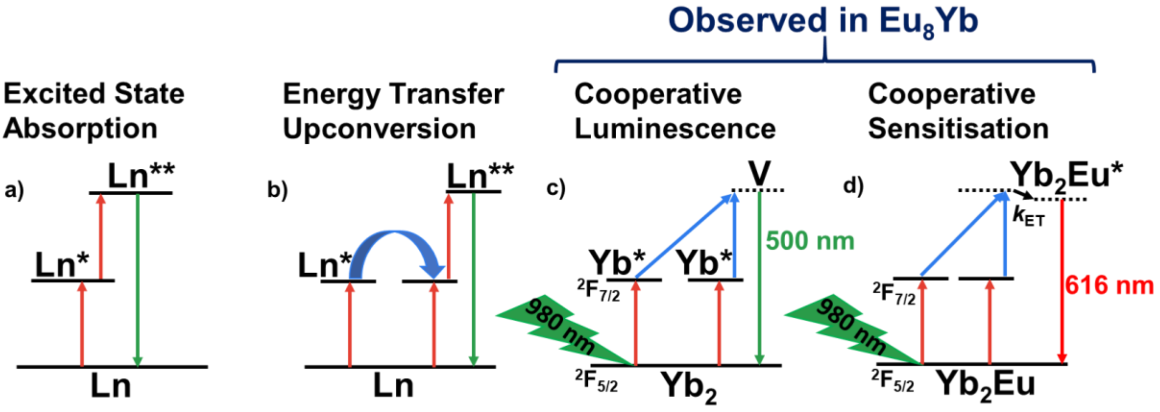

Figure 8. Upconversion mechanisms. a) Excited state absorption. b) Energy transfer upconversion. c) Cooperative luminescence from Yb_2. d) Cooperative sensitization of Eu in Yb_2Eu.

Cooperative sensitization (CS) is an interplay between three atoms, where two donor atoms transfer their energy to the third atom, which emits light.[38, 39] It is the most frequent mechanism in molecular upconverters based on the Tb^{III}/Yb^{III} pair.[40-42] Finally, cooperative luminescence (CL) is achieved when pairs of lower-energy excited states interact cooperatively to produce the emission of photons at a higher excited state. This phenomenon has been reported on solid-state materials[43, 44] and more recently using homonuclear Yb^{3+} clusters or dimers in solution.[45-48] These cooperative processes are treated by two operator transitions between pair levels, and they are generally less efficient than ESA or ETU.[49]

To observe UC, two basic prerequisites are necessary. The first prerequisite is that the elements used for UC emission should possess a ladder-like energy level diagram to climb up to the higher excited state. However, there is an exception to this requirement in the case of cooperative sensitization (CS). In CS, the two donors should have a single excited state level situated at half the energy of the emitting element. For example, the CS of Tb can be observed by Yb, where the excited state of Tb is situated at around 20600 cm^{-1} and Yb has a single excited state at around 10200 cm^{-1}.[50] The second prerequisite is that the intermediate excited states must have long lifetimes, so that the excited state can undergo the process leading to the upper state before it decays back to the ground state. This explains why lanthanide (Ln) cations are so frequently used in UC materials. The radiative lifetimes of Ln ions, τ_r, vary from a few tens of μs to tens of ms.[51] Ln ions are particularly long-lived and hence adapted to UC processes, provided they are well shielded from non-radiative processes. Additionally, the $[Xe]4f^n$ ($n = 0$ to 14) electronic configuration of Ln ions leads to the presence of numerous electronic levels. Their energy diagrams generally display a plethora of intermediate steps in the visible and near-infrared (NIR) regions, building a rich ladder-like energy level structure.[11] However, the major drawback of Ln ions is that the f-f electronic transitions are forbidden by selection rules, and the corresponding absorption coefficients are very low. This results in the need for powerful excitation sources to obtain enough population of the excited states. In summary, the prerequisites of UC are the elements' ladder-like energy level diagram and long-lived intermediate excited states. Ln cations are suitable for UC due to their long-lived excited states and rich energy level structure, while powerful excitation sources are required to obtain enough population of the excited states due to the low absorption coefficients of f-f electronic transitions. It has been observed that the vibrations of molecules in solutions offer more de-excitation pathways for excited states than phonons in solid materials. This is why the first observations of upconversion (UC) materials were made with solids, and more recently, in the last two decades, with nanoparticles,[52, 53] which have numerous bioanalytical applications.[54] However, due to the challenging batch-to-batch reproducibility and potential toxicity of doped nanoparticles,[55] there is a growing interest in downsizing UC materials to the molecular scale to achieve stable and perfectly controlled molecular assemblies.

2.2.2. Solid vs Solution: Investigating the Lifetime of the Intermediate Excited State

The observation of UC at the molecular level largely depends on the issue of a long-lived excited state of the intermediate level, which is a crucial question.[56, 57] If there are too many non-radiative processes, the population of the excited state decays rapidly, making it harder to achieve the second energy jump. Therefore, it is essential to minimize non-radiative deactivation processes. As mentioned earlier, these non-radiative processes arise from the interaction between the excited state and the surroundings, and the ability of the excited state to transfer some of its energy to the lattice (for solids) or to the ligand and solvent molecules (for complexes in a solution). In the solid state, phonons refer to quasi-particles that possess a quantum of energy corresponding to vibration of the solid matrix. The interaction of the excited states with phonons leads to energy loss at a rate that depends on the energy of the phonons (or vibrations) with the relation [58]:

$$\boldsymbol{k_{n_r} = A * exp^{\frac{-B\Delta E_{em}}{\Delta E_p}}} \qquad (1),$$

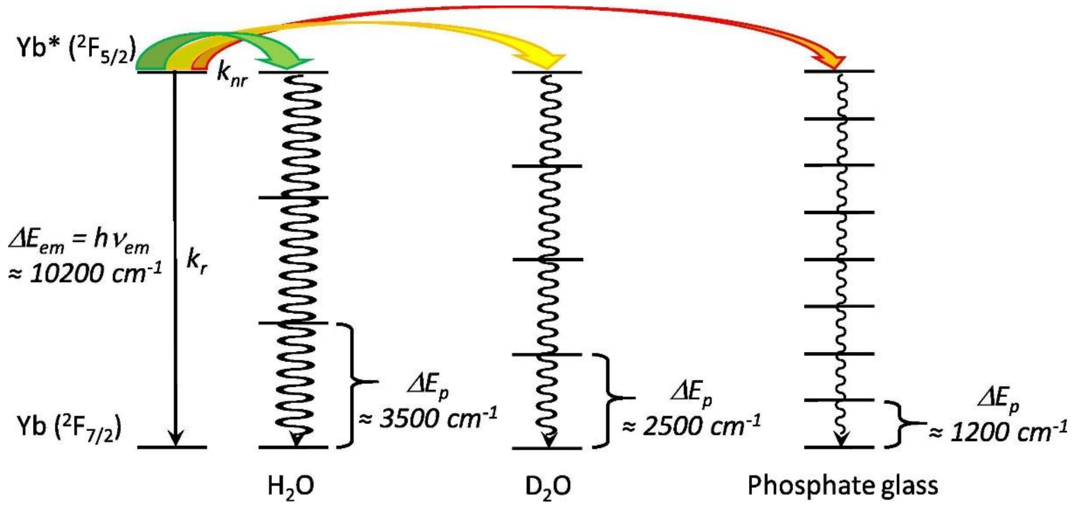

Figure 9. Schematic representation of the non-radiative transition probabilities of the Yb excited state in water, deuterated water and phosphate glasses. Reused with permission, Copyright (2020) Elsevier.[59]

where k_{n_r} is the non-radiative rate constant, A and B are system specific constants, ΔE_{em} is the energy difference between the ground and excited state of the molecule, and ΔE_p is the energy of the implicated phonon. Equation (1) shows a strong exponential dependence of the probability of non-radiative decay with the phonon energy. The probability of non-radiative decay decreases with decreasing phonon energy. **Figure 9**[59] depicts this principle in the case of the $^2F_{5/2} \rightarrow {}^2F_{7/2}$ transition of Yb at ~ 10200 cm^{-1}, which would occur in a matrix of water, deuterated water, or a phosphate glass.[59] To illustrate this point, when Yb is doped at one percent in a phosphate glass, the luminescence lifetime was determined to be superior to 1 ms[60], whereas for complexes in water solution, this value rarely exceeds few microseconds for the best of them,[61] and can be notably improved in D_2O.[62] Considering that the Yb centered luminescence quantum yield Φ_{Yb} is related to the luminescence lifetime, τ_{lum}, and to the radiative lifetime τ_r by the relation. The estimated radiative lifetime of Yb is 1.449 ms for the phosphate glass and range from 0.5 to 1.3 ms for complexes in solutions.[51] One can see that the luminescence efficiency dropped from 76% in the glass to only few percent for the best complexes in solution.

$$\boldsymbol{\Phi_{Yb} = \tau_{lum}/\tau_r} \qquad (2)$$

In order to enhance the luminescence quantum yield of NIR emitting Ln complexes, a number of steps should be taken. Firstly, it is important to design polydentate ligands that can fully occupy the first coordination sphere of the Ln cations.[63] This helps stabilize the compound and reduce the likelihood of non-radiative decay. Secondly, wherever possible, CH, NH and OH bonds should be replaced by CD, ND and OD ones,[64] or even CF bonds.[65, 66] This is because these heavier isotopes reduce the vibrational energy of the surrounding molecules, thus minimizing quenching of the luminescence. Another important consideration is the introduction of large aromatic parts to repel solvent and water molecules away from the Ln cation.[67] This helps to reduce non-radiative decay by promoting a more stable environment around the molecule. Additionally, the use of low phonon liquids or deuterated solvents can help to reduce the vibrational energy of the surrounding molecules, further minimizing quenching of the luminescence. Finally, the coordination sphere of Yb can be manipulated to decrease the radiative lifetime,[68, 69] which in turn increases the quantum yield. This can be achieved by introducing appropriate ligands that promote a favourable electronic environment around the molecule, or by adjusting the temperature or pressure conditions under which the compound is synthesized.

2.2.3. The Overview of Molecular Upconversion with Lanthanide Complexes.

Upconversion (UC) materials have been extensively researched, with most studies based on solid state lanthanide materials[35-38] or nanoparticles.[52, 53, 67, 70] Recent interest has been focused on scaling down UC to the molecular level for biological applications. This approach aims to enhance solubility, reduce toxicity, improve stability, and create environmentally friendly and reproducible molecular assemblies. Coordination chemistry has played a central role in the study of molecular-scale UC in solution over the past decade.[56, 57]

To observe UC, three prerequisites must be met. Firstly, the elements used for UC emission must have a ladder-like energy level diagram to climb to the higher excited state. This can be achieved by using a single element (e.g., ESA with Er^{3+})[71-73] or by using a combination of elements - donors and acceptors such as Yb^{III}/Er^{III},[74, 75] Yb^{III}/Tb^{III}, [40-43] Cr^{III}/Er^{III},[76, 77] or Ru^{III}/Yb^{III}.[46] The only exception is cooperative luminescence, which can be observed from the single $^2F_{5/2}$ excited state of Yb^{3+}.[42, 43]

In all cases, the intermediate excited states must possess long lifetimes to ensure an uninterrupted process leading to the population of the upper state before its return to the ground state through decay. The spatial proximity of energy donors and acceptors[78] is another key to exhibiting energy transfer, and thus, UC. In the last decade, molecular upconversion in solution has been achieved by reducing the de-excitation pathways of Ln(III) complexes, selecting appropriate donor-acceptor pairs, and arranging them spatially. This accomplishment has been made possible by designing discrete heteropolynuclear coordination complexes[40, 41, 72, 76, 79] and molecular clusters.[42, 46, 47]

Overall, the study of molecular-scale UC in solution has opened up new possibilities for developing efficient and effective UC materials for biological applications. These materials can be used for imaging, sensing, and therapeutic purposes, making them an exciting and promising area of research.

2.3. Single Molecular Magnetism

2.3.1. Fundamentals of Magnetism

The phenomenon of magnetism is exhibited by all substances in varying degrees. This magnetic behavior is primarily influenced by the movement of electrons in their respective orbitals and electronic spins, as well as their interactions with one another. Depending on how a material responds to magnetic fields at different temperatures, it can be classified into one of the five fundamental types of substances: diamagnetic, paramagnetic, ferromagnetic, ferrimagnetic, and antiferromagnetic (**Figure 10**). Each of these types has unique properties that set them apart from one another.

Diamagnetism: Diamagnetism is a fundamental property of all matter, including materials that are composed of molecules that have no net magnetic moment. These materials possess filled orbital shells with no unpaired electrons. However, when such materials are exposed to a magnetic field, they generate a negative magnetization. Consequently, the magnetic susceptibility of diamagnetic materials is negative. Even though ferromagnetic and paramagnetic materials (see below) have unpaired electrons, they also exhibit some diamagnetic behavior due to the presence of paired electrons. This behavior occurs in all materials to some extent.

Paramagnetism: Paramagnetic materials are substances that have magnetic properties due to the presence of unpaired electrons in their molecular orbitals. When placed in a magnetic field, the magnetic moments of these materials align with the direction of the field, resulting in a positive magnetization (M) and positive susceptibility. However, they lose their magnetization when the magnetic field is removed.

Ferromagnetism: Ferromagnetic materials are substances in which the magnetic moments of individual atoms or molecules are aligned parallel to each other to form domains, under the influence of a magnetic field these domains align. This leads to a collective magnetic behavior and the substance becomes magnetized. Unlike paramagnetic materials, which also get magnetized in the presence of a magnetic field, ferromagnetic materials retain their magnetization even after the field is removed. However, when the temperature of the material exceeds a certain value, known as the Curie's temperature, the ferromagnetic behavior disappears and the substance starts behaving like a paramagnetic material with no net magnetic moment.

Antiferromagnetism: In antiferromagnetic materials, the magnetic moments of the neighboring atoms or molecules are arranged in such a way that they are aligned in opposite directions, thus making the material have zero net magnetic moments. However, when the temperature of the material is raised to a certain point, known as Neel's temperature, the materials lose their magnetic ordering due to thermal agitation and begin to behave like paramagnetic materials. This transition from antiferromagnetic to paramagnetic behavior is an important phenomenon in materials science and has many practical applications.

Ferrimagnetism: Ferrimagnetism is a phenomenon that occurs when the spins of atoms or ions in a lattice align in an anti-parallel orientation, similar to antiferromagnetism. However, unlike antiferromagnetism, the net magnetic moment in ferrimagnetism is non-zero. This is due to the

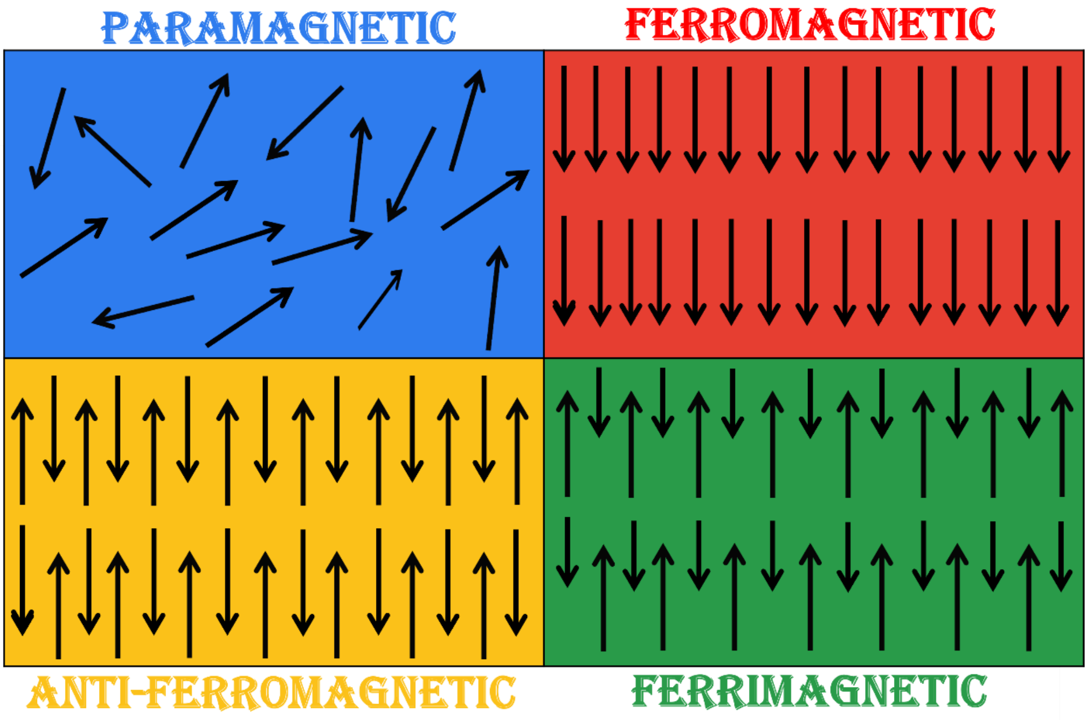

Figure 10. Magnetic ordering in Top left - paramagnetic $\chi > 0$ (very small), Top right - ferromagnetic $\chi > 0$ (large), Bottom left - antiferromagnetic $\chi > 0$ (rather small), and Bottom right - ferrimagnetic materials $\chi > 0$ (very small) (where χ is the magnetic susceptibility).

presence of different materials or ions in the lattice, each with a different magnetic moment. The resulting magnetic moment of the lattice is determined by the difference in magnetic moments between the two types of ions or materials.

When a substance is subjected to a magnetic field **H**, the total magnetic field inside the substance is a combination of the magnetic field applied and the magnetic field produced by the substance itself. This combined magnetic field is termed as magnetic induction and is represented by the symbol **B**.

$$\boldsymbol{B = H + 4\pi M}$$

$$\boldsymbol{\frac{B}{H} = 1 + 4\pi\left(\frac{M}{H}\right)}$$

$$\boldsymbol{\frac{B}{H} = 1 + 4\pi\chi_v}$$

In the field of magnetism, the magnetization of a material is denoted by **M**, while the volume magnetic susceptibility is denoted by χ_v. The property of magnetic susceptibility is defined as the degree of magnetization exhibited by a sample when subjected to an external magnetic field. The term volume susceptibility is used to describe this property since the variables **B**, **H**, and **M** are all defined per unit volume. Magnetic susceptibility is independent of the magnetic field, making it a convenient parameter to work with. In most research studies, the molar magnetic susceptibility $\boldsymbol{\chi_M}$ is used, which is measured in units of cm^3 mol^{-1}. In this thesis, all magnetic measurements are presented in terms of $\chi_M T$, which is measured in units of cm^3 K mol^{-1}. The molar magnetic susceptibility of paramagnetic materials is given by Curie's law.

$$\boldsymbol{\chi_M = \frac{C}{T}}$$

The constant **C**, known as Curie's constant, is dependent on the eigenvalue of the S^2 operator., while the temperature T does not play a significant role in its value. The formula for Curie's constant is expressed as follows:

$$\boldsymbol{C = \frac{\mathrm{N}_A\mu_B^2 g^2 S(S+1)}{3k_B}}$$

The inverse relationship between T and χ is commonly observed in paramagnetic compounds, where N_A represents Avogadro's number, k_B is the Boltzmann constant, S stands for the spin quantum number, μ_B is Bohr magneton, and g denotes the Landé factor. However, a deviation from this relationship can also be observed upon extrapolation to zero Kelvin, which is referred to as the Curie-Weiss law:

$$\chi_M = \frac{C}{T - \theta}$$

Where θ is the Weiss constant, a positive θ indicates ferromagnetic interaction, whereas a negative θ indicates antiferromagnetic interaction.

2.3.2. Molecular Magnetism in Lanthanides

In the early 1990s, researchers discovered a fascinating phenomenon in a compound called $[Mn_{12}O_{12}(OAc)_{16}(H_2O)_4]_4(H_2O)_2AcOH$.[80] This complex features a $\{Mn_{12}\}$ cage with four Mn(IV) and eight Mn(III) ions that interact magnetically to create a well-isolated $S = 10$ ground state at low temperatures. The large spin ground state is characterized by a negative zero field splitting (ZFS) term, D, which arises due to the nearly collinear alignment of the Jahn-Teller axes of the Mn(III) ions. This magnetic anisotropy creates an energy barrier that opposes the reversal of the magnetization, leading to slow magnetic relaxation. At temperatures below the blocking temperature (T_B) of the magnetic moment, an open hysteresis can be observed, which is purely molecular in origin. Such compounds are called single-molecule magnets (SMMs),[81] and they exhibit a range of interesting magnetic and quantum phenomena, including quantum tunneling of the magnetization and Berry phase quantum interference.[82] These properties make SMMs promising candidates for various applications, such as molecular magnetic memories, quantum information processors, and spintronic devices. [83-86]

The field of molecular magnetism initially focused on transition metal ions, which can produce large spin ground states (S) and high relaxation barriers (U_{eff}) through exchange coupling between neighboring metal ions. However, it is challenging to synthesize exchange-coupled SMMs with large U_{eff} barriers due to the difficulty of achieving strong magnetic exchange within polymetallic cages of several metal centers and a collinear arrangement of the local Ising axes. [87, 88]

In 2003, Ishikawa and coworkers introduced a novel approach to slow magnetic relaxation by discovering the occurrence of monometallic lanthanide phthalocyaninato double-decker complexes.[89] These systems, termed single-ion magnets (SIMs), exhibit slow magnetic relaxation due to the unquenched spin-orbit coupling of the 4f ion and the ligand field surrounding that metal (Tb, Dy) performing few orders better than the transition metal polynuclear- SMM.[90] Nowadays, nanomagnets based on lanthanides and actinides are intensively researched.

Many f-block SIMs have been reported, some of which are lanthanide-based SIMs that exhibit extremely high energy barriers and enhanced blocking temperatures in comparison to d-block SIMs or SMMs.[91, 92] Moreover, certain design principles that were initially developed for f-SIMs have been employed to transition metals, resulting in d-SIMs with energy barriers much greater than those of exchange-coupled polymetallic SMMs.[93] The slow magnetization dynamics of polymetallic cages based on lanthanides are frequently a consequence of single-ion behaviors being combined.[94] Both lanthanide-SIMs and lanthanide-SMMs have piqued the interest of the magnetism community and are being proposed for a variety of applications, including quantum information technologies.[95]

Slow Magnetic Relaxation in Lanthanide-based Nanomagnets

Certain systems exhibit a characteristic of remaining magnetized along a quantization axis or easy axis for an extended period even after the magnetic field is removed; this is known as slow relaxation of magnetization. In the case of f-block elements, this property of slow relaxation is highly sensitive to changes in the ligand-field environment and its symmetry, and it is associated with the local ion magnetic anisotropy. The reason behind the increased single-ion anisotropy of 4f-elements can be attributed to their significant unquenched orbital angular momentum. However, with the exception of gadolinium and lutetium, the electronic and magnetic characteristics of 4f ions are best defined by the spin-orbit coupled quantum number (J). The barrier to relaxation is determined by the spacing between energetic microstates of m_J. It is important to note that even though the magnetic anisotropy is related to spin-orbit coupling (SOC), the nature of the ground m_J multiplet and the energetic distribution of low-lying m_J microstates are significantly dependent on crystal field effects. For example, an energy gap of around 400 cm^{-1} between the ground state $m_J = \pm 6$ and the first excited state $m_J = \pm 5$ has been

Table 5. Ground and first excited state terms of 4*f* ions, g_J-values, and energy gaps to the first excited states.(Reproduced from Novel Magnetic Nanostructures[114])

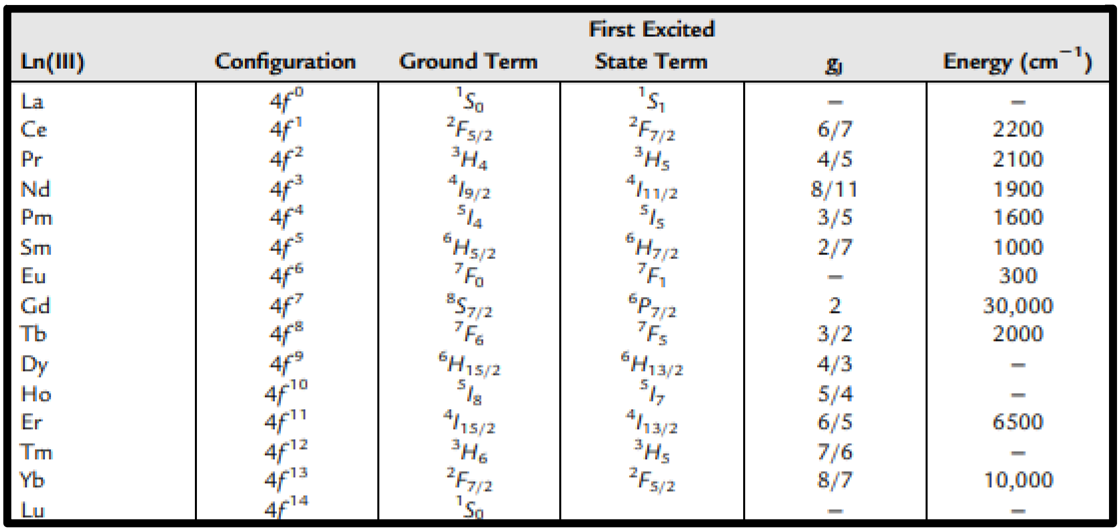

Ln(III)	Configuration	Ground Term	First Excited State Term	g_J	Energy (cm^{-1})
La	$4f^0$	$^1S_0$	$^1S_1$	–	–
Ce	$4f^1$	$^2F_{5/2}$	$^2F_{7/2}$	6/7	2200
Pr	$4f^2$	$^3H_4$	$^3H_5$	4/5	2100
Nd	$4f^3$	$^4I_{9/2}$	$^4I_{11/2}$	8/11	1900
Pm	$4f^4$	$^5I_4$	$^5I_5$	3/5	1600
Sm	$4f^5$	$^6H_{5/2}$	$^6H_{7/2}$	2/7	1000
Eu	$4f^6$	$^7F_0$	$^7F_1$	–	300
Gd	$4f^7$	$^8S_{7/2}$	$^6P_{7/2}$	2	30,000
Tb	$4f^8$	$^7F_6$	$^7F_5$	3/2	2000
Dy	$4f^9$	$^6H_{15/2}$	$^6H_{13/2}$	4/3	–
Ho	$4f^{10}$	$^5I_8$	$^5I_7$	5/4	–
Er	$4f^{11}$	$^4I_{15/2}$	$^4I_{13/2}$	6/5	6500
Tm	$4f^{12}$	$^3H_6$	$^3H_5$	7/6	–
Yb	$4f^{13}$	$^2F_{7/2}$	$^2F_{5/2}$	8/7	10,000
Lu	$4f^{14}$	$^1S_0$		–	–

observed, resulting in slow magnetic relaxation at 40–50 K in $(Bu_4N)[TbPc_2]$.[89] Conversely, a much weaker relaxation was observed for the isostructural Dy(III) derivative, $(Bu_4N)[DyPc_2]$, consistent with a smaller energy gap to the lowest lying excited m_J microstate (**Table 5**)[90, 96]

As an example and the best performing Ln in the context of SMMs, Dysprosium(III) is an element that has a unique electronic configuration of $4f^9$. In this configuration, the $^6H_{15/2}$ ground multiplet is stabilized by SOC (spin-orbit coupling), which is characterized by S = 5 /2, L = 5 and $J = \pm 15/2$. The crystal field interactions can break the 16-fold degeneracy of the ground multiplet into eight Kramers doublets, which are $m_J = \pm 15/2, \pm 13/2, \pm 11/2, \pm 9/2, \pm 7/2, \pm 5/2, \pm 3/2, \pm 1/2$ (**Figure 11**).[97] The energies of these doublets depend on both the symmetry and strength of the ligand field. Strongly axial ligand fields are known to stabilize the $m_J = \pm 15/2$ microstate, which places the other states at high separations above the ground state. The stronger the axiality, the bigger the Ising anisotropy, and thus, the larger the energy separation between microstates is. This situation leads to slow magnetic relaxation, which is often characterized by a hysteresis in the field dependence of the magnetization because the magnetic moment is prevented from relaxing in time to its equilibrium value. In general, the loop width increases with an increase in the field-sweeping rate, and upon lowering the temperature. Sometimes, relaxation of the magnetization via the lowest-lying excited states is blocked, and superior excited states engage in spin relaxation, which leads to even longer magnetization relaxation times.

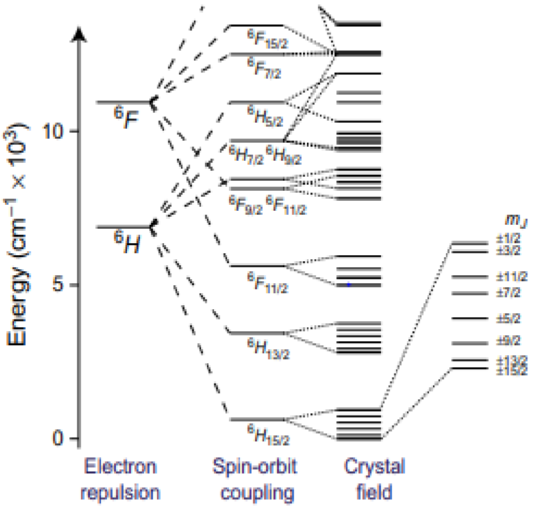

Figure 11. Scheme outlining the energy levels displays the varying degrees of interelectronic repulsion, spin-orbit coupling, and ligand-field effects. The electronic structure of the Dy(III) ion at low energy is perturbed sequentially by electron-electron repulsions, spin-orbit coupling, and the crystal field (Reproduced from the reference 97).

Effect of Crystal field

The strong SOC inherent to f-ions causes their large anisotropy. It is interesting to note that while the ligand field is much smaller than that of the spin-orbit coupling, it still plays a crucial role in determining the SMM behavior by splitting the ($2J + 1$) degenrate manifold. The key to creating high-performance SMMs is to engineer a ligand field that provides a significant splitting between $\pm m_J$ states. Rinehart and Long have introduced a simple electrostatic model for predicting which ligand environment is likely to encourage SMM behaviors in f-element complexes.[98]

Lanthanide ions have electron densities (**Figure 12**) that determine their shape - either spherical (Gd^{III}), equatorially expanded or "oblate" (Ce^{III}, Pr^{III}, Nd^{III}, Tb^{III}, Dy^{III}, and Ho^{III}), or axially elongated or "prolate" (Pm^{III}, Sm^{III}, Er^{III}, Tm^{III}, and Yb^{III}). Gd^{III} is unsuitable for Single Molecule Magnet (SMM) purposes because of its isotropic nature, but the series of late lanthanides with their high multiplicity of states are ideal for investigating slow magnetization dynamics in single molecules. By examining the lanthanide electron density and the ligand-field environment, we can determine the ligand field maximizing highly anisotropic ground states. The surrounding ligand field induces two energetically different orientations of the magnetic anisotropy, easy axis or easy plane, depending on the metal ion used.

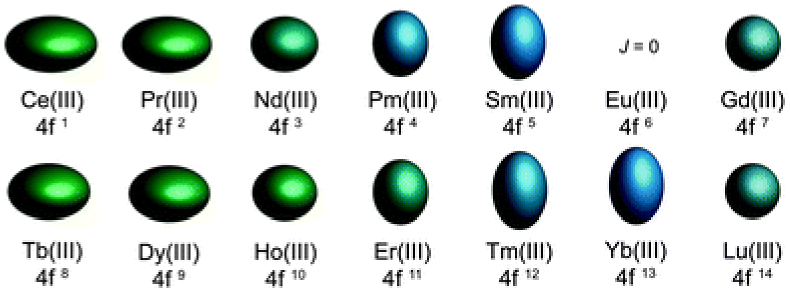

Figure 12. Quadrupole approximations of the 4f-shell electron distribution for the Ln(III) ions. (Reproduced from the Ref. 63).

To achieve maximum anisotropy for an oblate ion, it is recommended to place it in a crystal field where the ligand electron density is concentrated above and below the xy plane. This can be achieved with a sandwich-type ligand geometry. In such a crystal field, the ground state will have bistable orientations of m_J parallel and antiparallel to the molecular axis. This is because these configurations minimize repulsive contacts between the ligand and f-electron charge clouds. On the other hand, low magnitude m_J orientations will force the f-electron charge cloud into direct contact with the ligands, resulting in a high-energy state.

For a prolate ion, an equatorially-coordinating geometry is preferred to minimize charge contact with the axially-located f-element electron density. This simple model (**Figure 13**) provides valuable insights for designing single-molecule magnets for the f-elements. It explains why most of the systems studied so far have involved axially-coordinated ligand environments, as the most used ion, Dy(III), has an oblate electron density. In fact, Dy(III) ion may represent the ideal ion for single-molecule magnetism due to its Kramers ion property, which ensures a doubly degenerate m_J ground state. It combines a large-moment $^6H_{15/2}$ ground state with significant anisotropy of the 4f shell. The Tb(III) ion offers similar properties with even greater electronic anisotropy. However, a bistable ground state can only be achieved if rigorous axial symmetry is maintained or if magnetic coupling is employed to create an exchange bias since bistability is not guaranteed for a non-Kramers ion. This model also suggests a less explored method of generating strong single-ion anisotropy for single-molecule magnet synthesis involving strongly prolate ions like Tm(III) and Yb(III). Here, an equatorial ligand coordination environment can be paired with an ion of prolate electron density to generate the anisotropy barrier.

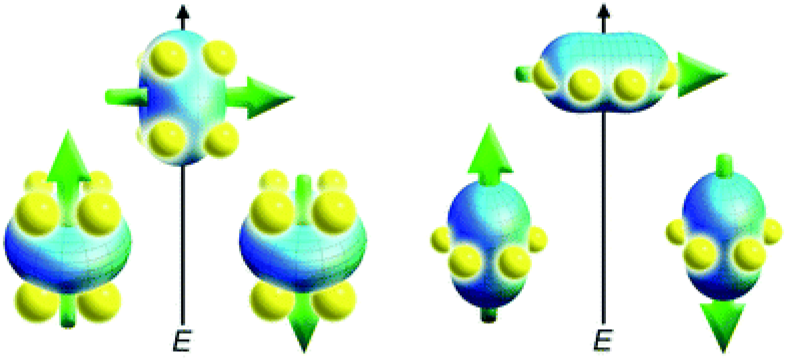

Figure 13. Schematic representation of low- and high-energy configurations of f-orbital electron density of oblate (left) and prolate (right) electron density. The thick arrow represents the spin angular momentum coupled to the orbital moment. As observed, an axial-type crystals field minimizes the energy of m_J states with highest multiplicity, while prolate ions, an equatorial configuration, minimizes the m_J with highest multiplicity. Reproduced with permission from J.D. Rinehart, J.R. Long, Exploiting single-ion anisotropy in the design of f-element single-molecule magnets, Chem. Sci. 2 (2011) 2078–2085. Royal Society of Chemistry.

Symmetry of the Ligand Field around the Ln ion

The symmetry of the ligand field surrounding the lanthanide ion plays a crucial role in the design of efficient SMMs, as it eliminates the degeneracy of the $2J + 1$ microstates. The Stevens formalism[99] can be employed to mathematically represent the ligand field. The Hamiltonian takes the form:

$$H = \sum_{k=2,4,6} ß_k \sum_{q=-k}^{k} B_k^q \, \hat{O}_k^q$$

The parameters B_k^q and $\hat{O}_k^q$, as well as the Stevens constant $ß_k$, which depends on the 4f configuration, account for the electrostatic potential. For f-elements, k ranges from 0 to 7, while q is determined by the local symmetry of the lanthanide ion (equation above), which represents the ligand-field potential, can be split into two parts: (i) the even part (k = even), which is responsible for the ligand-field splitting; and (ii) the odd part (k = odd), which is responsible for the intensity of the induced electric dipole transitions. The B_k^q terms are associated with the local symmetry of the lanthanide ion. In the absence of symmetry conditions, a total of 27 nonzero coefficients must be considered, making the experimental determination of ligand-field parameters nearly impossible. **Table 6**[97] displays the ligand-field parameter based on symmetry dependence.

The magnetic properties of 4f-SMMs are significantly influenced by the symmetry of the ligand field. In particular, for a square antiprismatic geometry (SAP) with a D_{4d} point group, which is prevalent in well-performing SMMs such as the $TbPc_2$ family and LnPOMs, four symmetry parameters, namely, the distance between the squares (d_{pp}), the shorter L-L distance within the square (d_{in}), the skew angle (Φ), and the angle between the C_4 axis and the Ln-L direction (α) are crucial in defining their magnetic behavior.[100] For an ideal SAP geometry, d_{pp} is equal to din, Φ equals 45°, and α equals 54.74°. When a lanthanide ion is embedded in such a ligand-field environment, it experiences the effect of three terms (B_2^0+B_4^0+B_6^0) that prevent mixing of ground and excited states. If other terms are mixed into the ground state, a temperature-independent relaxation pathway called quantum tunneling of the magnetization (QTM) is activated. This effect is observed at discrete field positions and is dependent on transverse, hyperfine fields, and symmetry. For instance, for a Dy(III)- or Tb(III) SMM with SAP geometry (**Figure 14**), the highly symmetric environment dramatically reduces the QTM effect.[101] However, Gatteschi et al. demonstrated that by altering Φ, that is, if the symmetry of the same material is reduced from D_{4d} to C_4, the B_4^4 + B_6^4 summation needs to be included. These terms are essential since they allow the mixing of states, i.e., $|J_z>$and $|J_z -4>$, and enhance QTM at low fields and low temperatures.[102] Additionally, it is worth noting that although QTM is not ideal for data storage applications, it is a crucial property for quantum computation applications,

Table 6. Symmetry and ligand-field parameters dependence

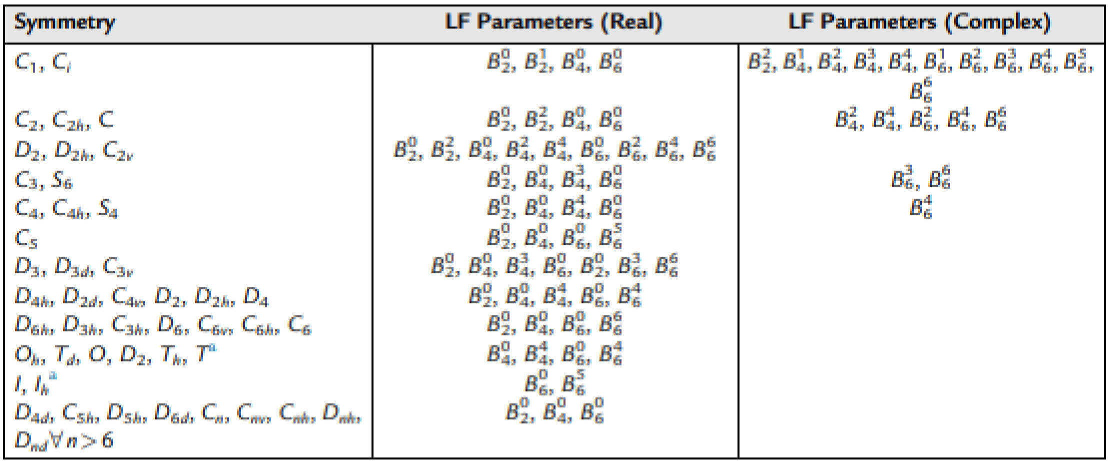

Symmetry	LF Parameters (Real)	LF Parameters (Complex)
C_1, C_i	B_2^0, B_2^1, B_4^0, B_6^0	B_2^2, B_4^1, B_4^2, B_4^3, B_4^4, B_6^1, B_6^2, B_6^3, B_6^4, B_6^5, B_6^6
C_2, C_{2h}, C	B_2^0, B_2^2, B_4^0, B_6^0	B_4^2, B_4^4, B_6^2, B_6^4, B_6^6
D_2, D_{2h}, C_{2v}	B_2^0, B_2^2, B_4^0, B_4^2, B_4^4, B_6^0, B_6^2, B_6^4, B_6^6	
C_3, S_6	B_2^0, B_4^0, B_4^3, B_6^0	B_6^3, B_6^6
C_4, C_{4h}, S_4	B_2^0, B_4^0, B_4^4, B_6^0	B_6^4
C_5	B_2^0, B_4^0, B_6^0, B_6^5	
D_3, D_{3d}, C_{3v}	B_2^0, B_4^0, B_4^3, B_6^0, B_2^0, B_6^3, B_6^6	
D_{4h}, D_{2d}, C_{4v}, D_2, D_{2h}, D_4	B_2^0, B_4^0, B_4^4, B_6^0, B_6^4	
D_{6h}, D_{3h}, C_{3h}, D_6, C_{6v}, C_{6h}, C_6	B_2^0, B_4^0, B_6^0, B_6^6	
O_h, T_d, O, D_2, T_h, T^a	B_4^0, B_4^4, B_6^0, B_6^4	
I, I_h^a	B_6^0, B_6^5	
D_{4d}, C_{5h}, D_{5h}, D_{6d}, C_n, C_{nv}, C_{nh}, D_{nh}, $D_{nd} \forall n > 6$	B_2^0, B_4^0, B_6^0	

[a] For cubic and icosahedral groups, not all parameters are independent.

where QTM at the avoided level crossings may be used to manipulate electronic states.[101] Furthermore, besides the effect of Φ on the B_4^4 and B_6^4 terms, compression or elongation along the C_4 axis, that is, modification of α, has been demonstrated to alter the sign of the term. Thus, an elongation of the SAP geometry is more favorable for a Dy(III) ion, where stabilization of the highest m_J ground doublet is preferred. In contrast, compression favors the highest m_J ground doublet for Er(III) ions.

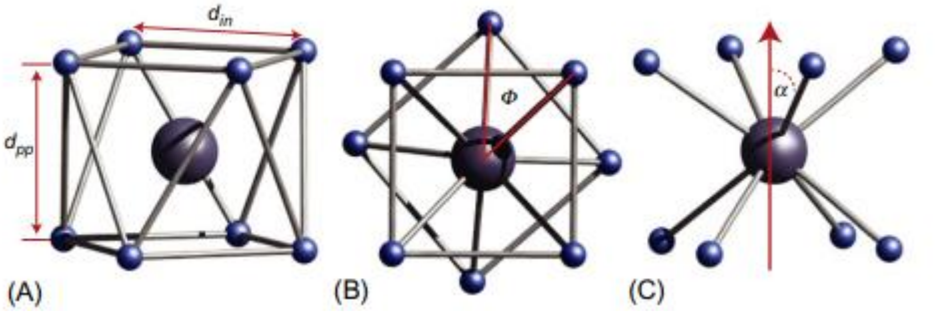

Figure 14. Structural parameters in square antiprismatic geometry (SAP). (A) Schematic structures of SAP geometry. (B) Skew angle (Φ) and (C) angle between the C_4 axis and lanthanide-ligand direction in SAP geometry. (Reproduced from Novel Magnetic Nanostructures)

Magnetic Relaxation Mechanisms

In the world of f-element single molecule magnets (SMMs), the magnetic anisotropy is primarily driven by a highly anisotropic ground doublet. This results in the preferential alignment of the magnetic axis along a particular direction. The anisotropic character of f-elements is heavily influenced by several factors such as the ligand field in which the ions are embedded, the symmetry, coordination number, and neighboring centers. The magnetic axis becomes frozen below a certain temperature known as the blocking temperature (T_B). However, above T_B, spin reversal can occur through thermally activated processes. The experimentally measured relaxation time (τ) is temperature-dependent and usually follows the Arrhenius law, $\tau = \tau_0 \exp(\Delta E/k_B T)$ (or $\tau = \tau_0 \exp(U_{eff}/k_B T)$). Here, τ_0 represents the relaxation rate, U_{eff} is the effective energy barrier, and the other symbols have their usual meaning. The relaxation times are typically obtained from fitting the alternating current magnetic susceptibility data, while the energy barrier is calculated from the linear portion of the Arrhenius plot of $\ln\tau$ versus $1/T$, which describes the thermally activated process.

Interestingly, the relaxation of the magnetization in f-SMMs involves different mechanisms. The spin-lattice relaxation processes occur through absorption and emission of one or two phonons. The efficacy of these processes depends on the nature of the metal ion involved, i.e., the low-temperature processes depend on the Kramers or non-Kramers spin parity character of the ions involved. For a Kramers ion, a minimum degeneracy of two is always attained due to time reversal considerations. However, in the non-Kramers case, the ground state can be totally nondegenerated. Three processes are primarily involved in the relaxation dynamics of f-SMMs: (i) direct, (ii) Raman, and (iii) Orbach process and iv) QTM.[101] The direct process involves direct interaction between the ground and excited states, while the Raman process involves a virtual excitation of the molecule to a higher energy level. The Orbach process involves a relatively complex mechanism, where the relaxation occurs through the lowest excited state of the molecule, which is coupled to the ground state through a higher energy state.

Direct relaxation mechanism: The direct relaxation process involves the modulation of a transition between one m_J state to a different m_J state by the emission or absorption of a phonon to or from the surrounding bath. This phonon has the same quanta of energy as the transitions. In this process, the frequency of the emitted or absorbed phonon is very short and is limited by the phonon density of states. However, this mechanism is efficient only at very low temperatures and is ion dependent. The frequency required for the transition is determined by the energy difference between the two distinct levels, which follows the equation $h\upsilon = \Delta$.
The relaxation process for Kramers ions follows the form $\tau^{-1} = R_d(\hbar\omega)^5 \coth(\hbar\omega/2kT)$, while for non-Kramers ions, it follows the form $\tau^{-1} = R_d(\hbar\omega)^3 \coth(\hbar\omega/2kT)$. Here, τ^{-1} represents the rate of relaxation, R_d represents the relaxation rate constant, and ω represents the frequency of the transition. The coth function represents the hyperbolic cotangent, while k is the Boltzmann constant and T is the temperature. Therefore, the rate of relaxation depends on the ion type and the temperature, with Kramers ions relaxing faster than non-Kramers ions.

Raman and Orbach relaxation mechanisms: The scattering of phonons is involved in the Raman relaxation process, which results in either the increase or decrease of the energies of the phonons, thereby causing the system to absorb or release the difference in energy. There are two ways in which relaxation can occur, depending on whether the scattered energy causes a direct transition or spin relaxation via virtual states. The relaxation process that occurs as a result of direct transition is known as first-order Raman, while the one associated with spin relaxation via virtual states is called second-order Raman mechanism (**Figure 15**). It is important to note that both first and second-order Raman processes require the presence of phonons and become significant at finite temperatures. The Raman relaxation mechanisms are influenced by the lanthanide ion involved, much like the direct relaxation process. For Kramers ions, the relaxation time is given by $\tau^{-1} = T^9 + R'_R(\hbar\omega)^5T^9$, whereas for non-Kramers ions, it is $\tau^{-1} = R_RT^7$.

The Orbach process is a relaxation mechanism that occurs when the doubly degenerated ground state relaxes through a low-lying excited state. This mechanism involves the absorption of a phonon by the spin system, causing it to be excited to a low-lying excited state. This excitation is accompanied by the emission of a phonon whose energy corresponds to the difference between the ground and the low-lying excited state. Through this process, the spin system can effectively relax between the low-lying states. It is important to note that the Orbach process exhibits an exponential temperature dependence, which means that the relaxation rate increases exponentially with temperature.

$$\tau^{-1} = R_{Or}\Delta^3\left[exp\left(\frac{\Delta}{kT}\right) - 1\right]^{-1}$$

Quantum tunneling of the magnetization (QTM): is an important relaxation mechanism for spin, in addition to the spin-lattice relaxation processes. It allows the spin to tunnel through the energy barrier when the $\pm m_J$ substates have equal energy. QTM is influenced by distortion of the ligand fields, hyperfine interaction, and transverse fields. For Kramers ions, QTM is not prompted by lowering of the ligand-field symmetry. However, both Kramers and non-Kramers ions are highly sensitive to small transverse fields. These fields create a symmetric and antisymmetric superposition of states, resulting in an energy difference between the two states, which is commonly referred to as tunnel splitting (Δ_T).The tunnel splitting is a measure of the rate of tunneling between the two states involved and has the form $\tau_{tunnel}^{-1} = \frac{2\omega_T^2}{1 + \frac{\tau_{mm'}^2\left(E_m - E_{m'}\right)^2}{\hbar^2}}$.The tunneling rate can be simplified as $\tau_{tunnel}^{-1} = \frac{B_1}{1+B_2\,H^2}$, where B_1 and B_2 are fitting parameters. [103] Once all of the processes have been collected into a single form, the outcome is an expression of the Kramers and non-Kramers rates that leads to relaxation.

$$\tau^{-1} = R_d(\hbar\omega)^5 \coth\left(\frac{\hbar\omega}{2kT}\right) + R_{Or}\Delta^3\left[exp\left(\frac{\Delta}{kT}\right) - 1\right]^{-1} + R_R T^9 + R_R^{'}(\hbar\omega)^5 T^9 + \frac{B_1}{1+B_2H^2}$$ and

$$\tau^{-1} = R_d(\hbar\omega)^3 \coth\left(\frac{\hbar\omega}{2kT}\right) + R_{Or}\Delta^3\left[exp\left(\frac{\Delta}{kT}\right) - 1\right]^{-1} + R_R T^7 + \frac{B_1}{1+B_2H^2},$$

respectively.

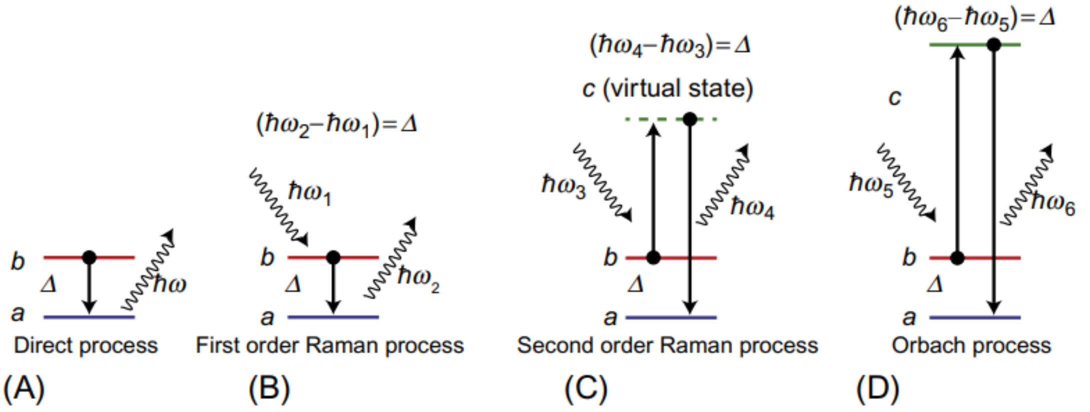

Figure 15. Schematic representation of common spin-lattice relaxation processes in f-SMMs. (A) Direct relaxation process, where a phonon corresponding to the difference between states a and b is absorbed (emitted) causing a transition between states b and a. (B) First-order Raman process, where the difference in energy of the scattered phonon cause a de-excitation from state b to a. (C) Relaxation through a second-order Raman process. Similar to the first-order Raman process, the difference in energy of the scattered phonon is absorbed by the spin system. In contrast, however, the spin system is excited to a virtually excited state and followed by de-excitation to the ground state. (D) In the Orbach process, absorption of a phonon excites the spin system to a low-lying excited state, followed by de-excitation to state a and emission of a photon of energy corresponds to the difference in energy of the low-lying excited state and the ground state. (Reproduced from Moreno-Pineda, Eufemio & Nodaraki, Lydia & Tuna, Floriana. (2018). Molecular Nanomagnets Based on f-Elements. 10.1016/B978-0-12-813594-5.00001-1).

2.3.3. Magnetic Susceptibility Measurements

Magnetic susceptibility measurements are a crucial technique for examining the magnetic properties of Single Molecule Magnets (SMMs). Such measurements involve measuring the magnetic susceptibility of a material at various temperatures, which allows for the extraction of the spin state of the material at a specific temperature. Faraday-balance and Gouy-balance are two of the oldest examples of magnetic susceptibility measurement techniques. However, they have become less crucial over time, as they are limited to room temperature operation. In contrast, SQUID magnetometers (Superconducting QUantum Interference Device) are a modern and powerful tool for determining the magnetic susceptibility of a given complex. These devices can measure magnetic fields with high sensitivity and can operate at temperatures as low as 1.5 Kelvin. Overall, these techniques are essential for understanding the magnetic properties of SMMs.

A SQUID is a highly sensitive magnetometer that can detect even the tiniest magnetic fields. This is made possible by utilizing the unique properties of electron pair wave coherence and Josephson junctions. Josephson junctions are specialized junctions where two superconductors are separated by an insulating material, allowing electrons to tunnel from one conductor to the other without the need for an external voltage. The magnetic flux of a sample passing through this junction modulates the current flowing through it, which is then precisely measured by the system. This enables SQUIDs to detect extremely small magnetic fields with remarkable accuracy and precision.

A commercial SQUID magnetometer (**Figure 16**) comprises of four key components - a superconducting magnet, one or more superconducting detection coils inductively coupled to the sample, a SQUID connected to the detection coil, and a superconducting magnetic shield. The sample produces changes in magnetic flux in the pickup coils as it moves up and down.

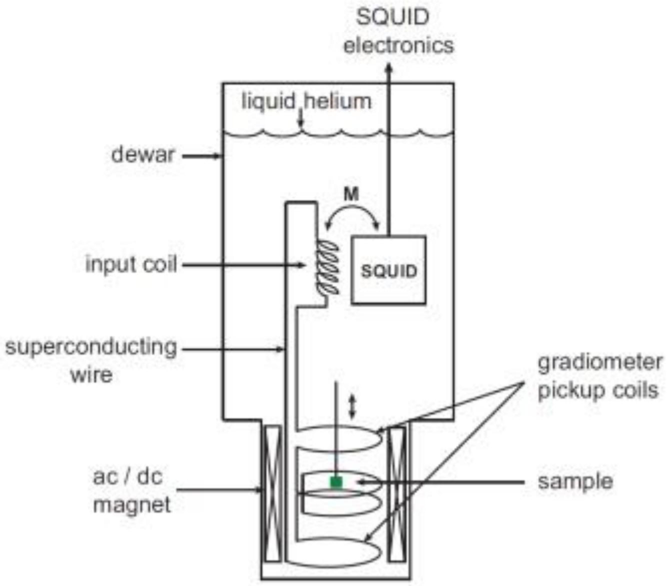

Figure 16. Schematic diagram of the SQUID magnetometer (reproduced from Quantum Design MPMS3-SQUID manual).

The change in magnetic flux alters the current in the detection system, resulting in variations in the SQUID output voltage, which is proportional to the magnetic moment of the sample. The input coils and SQUID are typically maintained in liquid helium to keep them in a superconducting state.

Molecular nanomagnets based on f-elements are evaluated through a set of parameters that determine their performance. The two main parameters are the effective energy barrier, the blocking temperature, and there is also the hysteresis of the system. The effective energy barrier is the energy required to overcome the magnetic anisotropy of the molecule and define its high-temperature dynamics. The Arrhenius law $\tau = \tau_0 exp\left(\frac{U_{eff}}{k_B T}\right)$ is used to calculate the relaxation time at a specific field, where τ represents the relaxation time, τ_0 is the relaxation rate, and k_B is Boltzmann's constant. A plot of the natural logarithm of relaxation time versus inverse temperature results in a linear trend, where the slope is the effective energy barrier divided by Boltzmann's constant. However, at low temperatures, alternative relaxation processes dominate, leading to deviation from the linear behavior.

The blocking temperature is the maximum temperature at which open hysteresis loops are observed. It determines the stability of the magnetic state, and its value is obtained through magnetization versus field studies at different temperatures. A higher blocking temperature suggests better stability of the magnetic state. Several magnetic techniques are employed for the characterization of the magnetic properties of SMMs. These techniques are discussed in detail in the following section.

DC Magnetometry

Extensive research has been conducted on the static magnetic properties of SMMs using SQUIDs. The working principle of SQUID magnetometers is based on inductive detection of the magnetic moment of the sample. When a paramagnetic substance is exposed to an external magnetic field (H), the spin of the material tends to align with the H, reducing the energy of the system. The susceptibility of the substance, $\chi = dM/dH$, is defined by the rate of change in magnetization upon the application of a magnetic field. At low fields, this relationship becomes independent of H.

The plots of $\chi_M T$ (where χ_M refers to the molar magnetic susceptibility) versus temperature (T) provide insight into interactions and/or crystal field effects in the studied material. In 4f materials, the value of $\chi_M T$ at room temperature is typically close to the free ion $\chi_M T$ value, which is $\chi_M T = \frac{N g_J^2 ß^2}{3k} J(J+1) \approx \frac{g_J^2}{8} J(J+1)$, due to the shielding effects that limit the interaction of 4f-electrons with the surroundings. However, at low temperatures, changes in $\chi_M T$ can indicate the type of interactions or crystal field effects.

When the quotient of *kT/H* is small, the magnetic moment of a material tends to align completely with the magnetic field applied externally. This leads to the magnetization reaching saturation (M_{sat}). These measurements can provide insight into the populated ground m_J state at the lowest temperature. Additionally, in SMMs with strong anisotropy and a significant gap between the ground and first excited states, *M*(*H*) can be utilized to investigate the residual magnetization via hysteresis curves in field-dependent magnetization measurements at varying temperatures. Typically, hysteresis loops increase in size with lower temperatures and faster sweeping rates.

DC magnetic susceptibility studies can be used to determine relaxation times for slow-relaxing systems. These experiments involve investigating the time-dependent magnetization at different isotherms, where the decay is fitted to an exponential law of the form

$$M_{(t)} = M_0 + M \exp\left(-\frac{t-t_0}{\tau}\right).$$

The expected $\chi_M T$ values for any given lanthanide, as shown in **Table 7.**

Table 7. $\chi_M T$ values of Ln(III) ions at 300 K.[104]

Element	g_J	$\chi_M T$ [cm^3 K mol^{-1}]
La	-	0.00
Ce	6/7	0.80
Pr	4/5	1.60
Nd	8/11	1.64
Pm	3/5	0.90
Sm	2/7	0.09
Eu	5	0.00

Gd	2	7.88
Tb	3/2	11.82
Dy	4/3	14.17
Ho	5/4	14.07
Er	6/5	11.48
Tm	7/6	7.15
Yb	8/7	2.57
Lu	-	0.00

The behavior of La(III) and Lu(III) ions can be explained by the fact that they are closed-shell systems. Therefore, they are expected to be diamagnetic. Similarly, Eu(III) is also expected to exhibit diamagnetic behavior despite being an open-shell system. This is due to the spin-orbit coupled ground state that shows $J = 0$. However, in the case of Eu(III) and Sm(II), the energy gap towards the first excited state with $J = 1$ is small enough, allowing for weak paramagnetic behavior to be observed at room temperature. The values of magnetic susceptibility ($\chi_M T$) observed at room temperature are typically around 1.5 cm^3 K mol^{-1}.

According to the given assumption, a plot of $\chi_M T$ vs T should result in a temperature-independent and horizontal line. However, in practice, this is usually observed only at high temperatures. When molecular materials are cooled down, the depopulation of the Stark sublevels leads to a decrease in magnetic susceptibility and a deviation from Curie's law. The Stark splitting of the magnetic ground state is caused by the influence of the ligand field on the central magnetic ion. The T-dependent behavior is also influenced by magnetic interactions. When two or more magnetic moments are placed in close proximity to each other, they feel the field created by the neighboring moment. These magnetic interactions can be through-space interactions, also known as dipolar interactions, or ligand-promoted exchange interactions. Exchange interactions are generally stronger, but they depend on the structure of the complex molecule.

In molecular systems, dipolar interaction is a significant phenomenon that occurs between magnetic centers. The strength of this interaction decreases rapidly with an increase in distance between the two magnetic centers.[105] This decrease is inversely proportional to the distance cubed. Dipolar interactions become negligible when the distance is greater than 10 Å. The magnetic interactions can occur both intra- and intermolecularly. However, intramolecular interactions are stronger as the distance between the two magnetic ions is generally smaller than intermolecular distances. The coupling constant J determines the sign of the interaction and can take both positive and negative values. In the $-2J$-formalism, (**Figure 17**) a positive sign represents ferromagnetic coupling, where the two magnetic moments align with each other. Meanwhile, a negative sign represents antiferromagnetic interaction, where the moments align antiparallel to one another. Similar to the magnetic alignment induced by an external field, the alignment via magnetic interactions is counteracted by the thermal movement of the particles. Magnetic interactions in molecular systems are typically of the order of 10^{-2} to 10^{0} cm^{1} and are only observable at low temperatures.

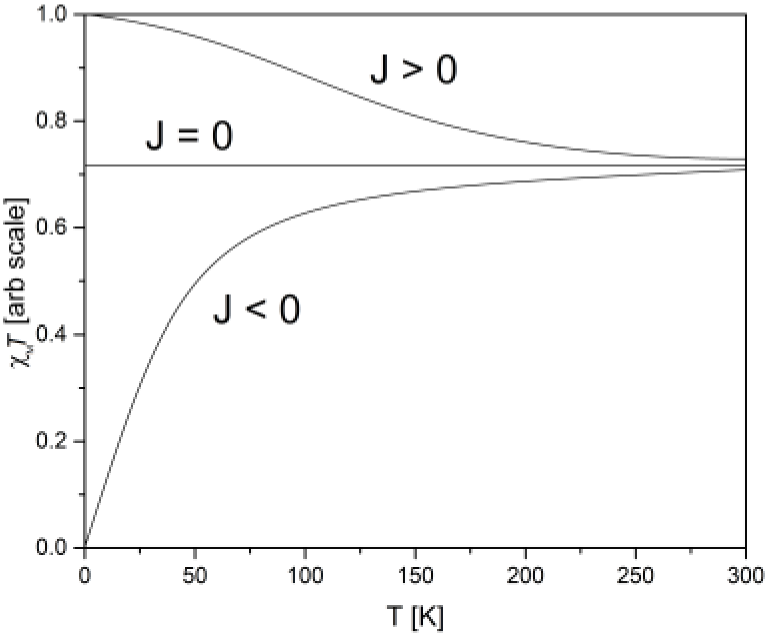

Figure 17. Schematic plot of the temperature product of the molar magnetic susceptibility with and without the influence of (anti-)ferromagnetic interactions. (Reproduced from Sören Schlittenhardt, M. Sc. 2023, Magnetic and photoluminescent properties of rare earth complexes of pyrazole-substituted 1,10-phenanthroline, KIT).

Experimental deduction of the J parameters can be achieved by fitting the $\chi_M T$ vs T data. The depopulation of the Stark levels in molecular materials produces a similar decrease in antiferromagnetic interactions. This makes it difficult to distinguish between the two effects based solely on visual appearance of the T-dependent behavior without mathematical analysis.

The behavior described so far applies only to the interaction with a non-changing DC magnetic field and is applicable to any paramagnetic system.

AC Magnetometry

The slow-relaxation property of single-molecule magnets (SMMs) is commonly analyzed through alternating current (*ac*) magnetic susceptibility measurements. These measurements involve placing the sample between two coils and passing current at different frequencies. The dynamic magnetic properties of SMMs are obtained by detecting the response of the sample after applying a small oscillating magnetic field that induces a small magnetization in the sample, detected by secondary coils.

During the measurements, the frequency (v) of the small oscillating magnetic field is varied, typically ranging from 0.1 to 10,000 Hz in commercial SQUIDs. This variation results in two different signals: in-phase (χ') and out-of-phase (χ'') *ac* magnetic susceptibility signals. The out-of-phase *ac* susceptibility signal is observed when the operating frequency of the *ac* field is close to the flipping rate of the magnetic moment of the molecule.

When an SMM is kept at a certain temperature and the frequency of the ac field is varied, a maximum is observed once the rate of the ac relaxation equals the rate at which the molecule

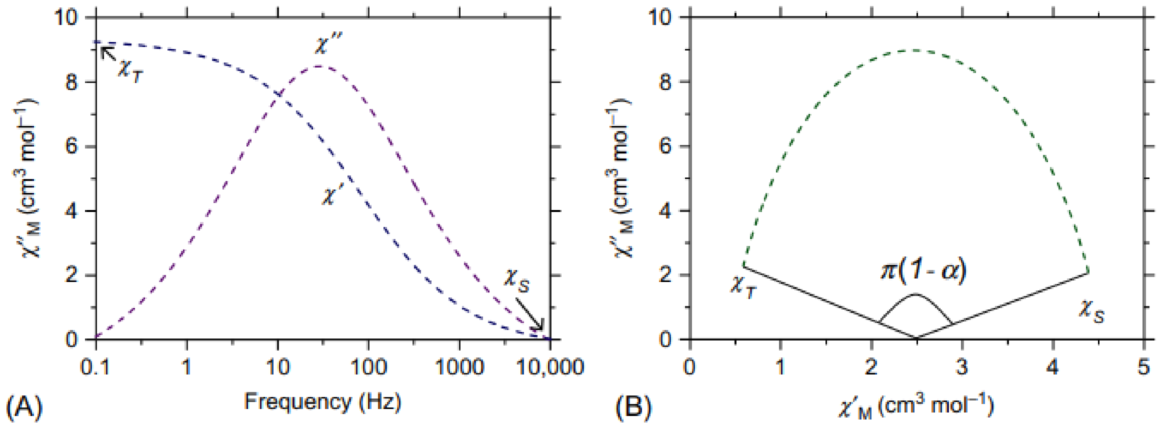

Figure 18. Frequency dependence of the real and imaginary component of the magnetic susceptibility. χT and χS are the isothermal and adiabatic susceptibility, respectively and (B) Argand plot (or Cole-Cole): χ00 vs χ0 at a given temperature. (Reproduced from Moreno-Pineda, Eufemio & Nodaraki, Lydia & Tuna, Floriana. (2018). Molecular Nanomagnets Based on f-Elements. 10.1016/B978-0-12-813594-5.00001-1.)

interconverts between the halves of the potential-energy double well. This characterization is performed over a temperature range at zero field or under the application of small DC fields. Such detailed analysis helps researchers understand the complex magnetic properties of SMMs. The energy barrier of magnetization relaxation, U_{eff}, can be determined by fitting in-phase (χ') and out-of-phase (χ'') susceptibility data (**Fig. 18 (A)**). For a single relaxation process, χ' and χ'' are expressed by $\chi'(\omega) = \chi_S + \left(\frac{\chi_T-\chi_S}{1+\omega^2\tau^2}\right)$ and $\chi''(\omega) = \left(\frac{\chi_T-\chi_S}{1+\omega^2\tau^2}\right)\omega\tau$, respectively. Here, χ_S and χ_T are adiabatic and isothermal susceptibilities, respectively, $\omega = 2\tau\upsilon$ is the angular frequency, and τ is the relaxation time. However, in practice, single relaxation processes are rare due to slight variations across the SMM molecules present in the crystal lattice. Therefore, the in- and out-of-phase components are fitted to a range of processes. These are given by:

$$\chi'(\omega) = \chi_S + \frac{(\chi_T-\chi_S)[1+(\omega\tau)^{1-\alpha}\sin(^{\alpha\pi}/_2)]}{1+2(\omega\tau)^{1-\alpha}\sin(^{\alpha\pi}/_2)+(\omega\tau)^{(2-2\alpha)}} \text{ and } \chi''(\omega) = \frac{(\chi_T-\chi_S)[1+(\omega\tau)^{1-\alpha}\cos(^{\alpha\pi}/_2)]}{1+2(\omega\tau)^{1-\alpha}\sin(^{\alpha\pi}/_2)+(\omega\tau)^{(2-2\alpha)}}$$

Alpha (α) is a parameter that quantifies the extent of relaxation process distribution, taking values between 0 and 1. A small α value corresponds to a narrow distribution of relaxation processes.

When studying the behavior of electron spin in magnetic materials, researchers often apply direct current (dc) fields to reduce quantum tunneling of the magnetization (QTM), which is a

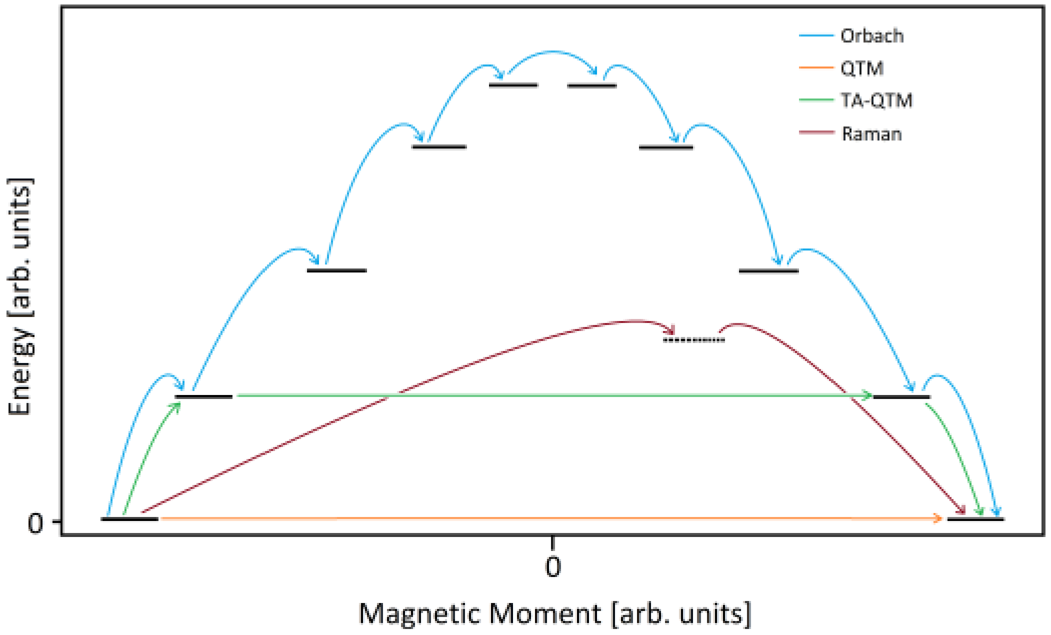

Figure 19. Energy diagram with different mechanisms of magnetic relaxation. (Reproduced from Sören Schlittenhardt, M.Sc. 2023, Magnetic and photoluminescent properties of rare earth complexes of pyrazole-substituted 1,10-phenanthroline, KIT).

source of electron spin relaxation. For these studies, it is important to use applied fields that result in the slowest relaxation process. To determine the energy barrier to the relaxation of the magnetization (U_{eff}), researchers typically use $\chi_M''(\nu)$ curves. These curves involve plotting the relaxation times (τ) as a function of temperature, and using the Arrhenius equation $\tau = \tau_0 \exp(U_{\mathrm{eff}}/k_BT)$. By analyzing the graph of $\ln(\tau)$ vs T^{-1}, where the slope of the graph represents the U_{eff}, researchers can gain insight into the type of relaxation pathways to the magnetization, such as direct, Orbach, Raman, or quantum tunneling processes (**Figure 19**). This information can be useful for understanding the behavior of electron spin in magnetic materials, and for developing new technologies that rely on magnetic properties.

Single molecule magnets (SMMs) are molecular systems that show slow relaxation. The energy barrier required for magnetic reversal is due to magnetic anisotropy. A magnetically isotropic system, on the other hand, acts as a paramagnet and not as an SMM. At low temperatures, hysteresis can be observed in SMMs, provided other relaxation processes are negligible. Hysteresis refers to the behavior where the system shows remanent magnetization at zero applied field after exposure to an external field. To completely demagnetize a sample displaying remanence, a magnetic field in the opposite direction must be applied. The strength of this negative field is called the coercivity. With increasing temperature, the remanence and coercivity decrease, leading to the closure of hysteresis loops. The highest temperature that exhibits open hysteresis is typically referred to as the blocking temperature (T_B), which is an important quality measure of SMMs. T_B can be defined more quantitatively as the temperature where $\tau = 100$ s. The extremely long magnetization relaxation times of SMM complexes (even in years), combined with their molecular-scale, make them attractive towards high-density information storage.[8, 9] Furthermore, their quantum phenomena, which include quantum tunneling effects and quantum interference, make them applicable for quantum computing and molecular spintronics. So far, the SMMs reported have shown magnetic bistable ground state only at very low temperatures. To make them applicable for devices, researchers are exploring new complexes to find bistable ground state around room temperature.

2.4. Magnetocaloric Effect

2.4.1. Introduction

The field of molecular magnets has numerous potential applications, with two of the most studied applications being their use in molecular magnetism and in spintronic components. While these fields are relatively new and may not see real-world usage for several years, magnetocaloric materials have been established since the 1930s[106] and have been employed in various ways around the world as an alternative refrigeration technique. In this chapter, we will examine how cages and polymers containing Ln(III) ions, specifically Gd(III), can be utilized as magnetocaloric materials with high performance in the low-temperature millikelvin regime, competing with ^{3}He/^{4}He methods like dilution refrigeration.

A vast number of molecular magnetocaloric materials have been investigated and reported over the last few decades, with polymeric structures and Metal-Organic Frameworks (MOFs) being the best-performing candidates. These materials are further divided into homometallic 3d or 4f compounds and heterometallic 3d-4f compounds.

To better understand the ideal magnetocaloric material for low-temperature applications, we will need to identify the importance of several factors through different reported materials and study how they contribute to a larger magnetocaloric effect.

2.4.2. Magnetocaloric Effect

Langevin first proposed the idea of this phenomenon in 1905 as a theoretical concept.[107] He suggested that a paramagnetic substance's temperature should vary depending on the strength of the magnetic field. This effect, later known as magnetocaloric effect, was initially observed by Weiss and Picard in 1917 when they noticed a temperature shift in Ni upon the application of a magnetic field. The magnetocaloric effect (MCE) is a phenomenon where certain materials heat up when exposed to a magnetic field. These materials are known as magnetocaloric materials (MCM). By utilizing this effect, it is possible to create a magnetic cooling cycle that can be operated at or near room temperature.

The MCE is the change in the thermodynamic state of a magnetic material when subjected to an external changing magnetic field H. The magnitude of the magnetocaloric effect is commonly characterized by either the isothermal entropy change ΔS_t or the adiabatic temperature change ΔT_AD, depending on whether the magnetic field H is applied under isothermal or adiabatic conditions. These numerical parameters are used to quantify the extent of the magnetocaloric effect.

When a magnetic material is exposed to an increasing magnetic field H, the magnetic moments or spins of the material align with H in a parallel direction. This alignment causes a decrease in magnetic entropy, S_M. The total energy of the system remains constant due to adiabatic conditions within it. As a result, the material experiences a temperature increase, ΔT_AD, and the lattice entropy, S_{lat}, increases. The net temperature of the material becomes $T_\mathrm{start} + \Delta T_\mathrm{AD}$. Compounds that exhibit the magnetocaloric effect (MCE) are known as magnetocaloric materials. Examples of such materials include pure elements like Gadolinium or alloys such as Lanthanum-iron-silicon (LaFeSi) or Iron-phosphorus ($\mathrm{Fe_2P}$).

Why Lanthanides-based Materials?

The rising cost and limited supply of helium as a cooling agent has led researchers to explore alternative cooling methods. Lanthanide-based materials have emerged as promising substitutes for helium, especially in low-temperature applications. Lanthanide-based coolants can act as effective refrigerants due to their paramagnetic properties. In this context, we try to explore the theoretical aspects of refrigeration using paramagnetic materials, the unique features that make Ln(III) ions suitable for this application, and the current technologies available in this field. It is worth noting that while helium is abundant in the universe, including in its most useful form to us ^{3}He, its limited supply on Earth has made it necessary to develop alternative cooling methods. Gd on the other hand has a high spin of ($s = 7/2$) and is isotropic in nature making it a suitor for MCE studies.

State-of-the-art Technologies

The process of transferring helium into a cryostat is a common technique in many physics or chemistry laboratories. This method is used to obtain temperatures below 5 K for routine magnetic measurements using a SQUID magnetometer or for experiments involving EPR and NMR. Cooling below 1.8 K is more complex and typically involves dilution refrigeration, which uses both ^{3}He and ^{4}He to potentially reach 2 mK.[108] This technique creates a 'two-phase' system where the spontaneous separation of isotopes absorbs energy from the surroundings. Dilution refrigeration is used in labs on Earth and in space, such as the Planck Observatory [109]. Magnetic cooling is a viable alternative to dilution refrigeration, more often in space where the limitations of an open system make it difficult to separate mixed ^{3}He-^{4}He practically.

Paramagnets as Refrigerants

The magnetocaloric effect refers to the change in temperature of a paramagnetic material when exposed to a magnetic field. If this field is applied adiabatically, meaning it is done under constant entropy, the material will heat up. Once the field is removed, the paramagnet returns to its original temperature. The most useful parameter for characterizing a paramagnet in terms of its magnetocaloric effect is the adiabatic temperature change, or ΔT_{AD} (K), which is a direct measure of the material's cooling ability. Different paramagnets have distinct responses in terms of both magnitude and the temperature range that they work best in. For instance, gadolinium metal is most effective for cooling at room temperature,[110] while the dimetallic gadolinium acetate molecule $[\mathrm{Gd^{III}}_2(\mathrm{H_3CCO_2})_6(\mathrm{H_2O})_4]\cdot4\mathrm{H_2O}$ works better at 2 K[111]. Physicists and chemists can understand why this discrepancy occurs and can use this knowledge to design and synthesize new materials for specific applications.

The reason for the heating is caused by the way entropy is distributed within the paramagnet when a field is applied. Equation 2.4.1 allows us to express the sum of all entropies, where the total entropy is denoted as S_{total}. The magnetic entropy is represented by S_{M}, the lattice entropy by S_{lattice}, and the electronic entropy of the system by $S_{\mathrm{electronic}}$.

$$S_{\mathrm{total}} = S_M + S_{\mathrm{lattice}} + S_{\mathrm{electronic}} \qquad \text{eq (2.41)}$$

When a magnetic field is applied to a paramagnet, the spin angular momenta (s) of its constituent atoms align with the field, resulting in a decrease in magnetic entropy (S_M). This process can be visualized using **Figure 20**, where spins are represented as arrows that align with the magnetic field (H). Under adiabatic conditions, the total entropy remains constant, and

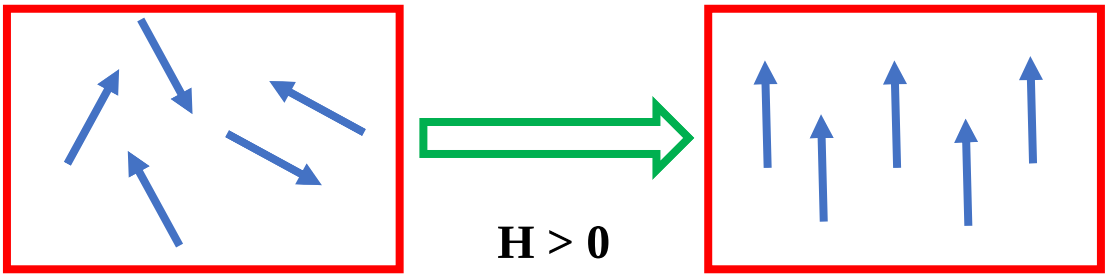

Figure 20. Spin angular momenta, *s*, depicted as arrows, are randomly aligned in zero field, $H = 0$ (left), and align with the applied field, $H > 0$ (right), thereby decreasing the magnetic entropy (S_M) of the system.

the lattice entropy ($S_{lattice}$) increases to compensate, which causes the atoms to become less ordered and more energetic, resulting in an increase in temperature. Alternatively, this process can be explained in terms of phonon exchange, where energy is transferred from the spin system to the lattice, raising it to a higher vibrational mode. When the magnetic field is removed, the process is reversible, and the entropy changes are undone, and any heat produced dissipates to the surroundings. Molecular magnetism researchers use the change in magnetic entropy ($-\Delta S_M$) between magnetized ($H > 0$) and zero-field ($H = 0$) states as a parameter to characterize the magnetocaloric effect. This parameter can be obtained indirectly through magnetic measurements of the magnetization or heat capacity, with the former method being more commonly used for practical reasons.

The magnetization of a sample can be determined through the use of a SQUID magnetometer. Typically, measurements are taken at different fields and temperatures, with intervals ranging from 0-7 T and 1.8-300 K, respectively, as per the standard conventions in the literature. These measurements are then utilized in conjunction with the following Maxwell Equation (Equation 2.4.2). [112] In Equation 2.4.2, T represents temperature, while H_f and H_i denote the final and initial magnetic fields ($H_f > H_i$).

$$\Delta S_M\,(T, \Delta H) = \int_{H_i}^{H_f} \left(\frac{dM\,(T,H)}{dT}\right)_H dH \qquad (2.4.2)$$

It is possible to determine ΔT_{AD} using heat capacity measurements, along with S_M(T) (Equations 2.4.3a and 2.4.3b). For a comprehensive analysis, the heat capacity of magnetization (C_M) can also be considered.

$$\Delta T_{AD}\,(T, \Delta H) = \int_{H_i}^{H_f} \left(\frac{T}{C\,(T,H)}\right)_H \left(\frac{dM\,(T,H)}{dT}\right)_H dH \qquad (2.4.3a)$$

$$S_M\,(T) = \int_0^T \left(\frac{C_M\,(T)}{T}\right) dT \qquad (2.4.3\text{ b})$$

Figure 21 provides a summary and an example of the entropy and temperature changes that occur while moving from one magnetic field to another. In **Figure 21**, when we move from point A to point B and apply an increased field, the total entropy of the system remains constant under adiabatic conditions but the temperature of the paramagnet increases, which is represented by ΔT_{AD}. However, when we move from point A to point C under isothermal conditions, the temperature of the paramagnet remains the same and $\Delta S_{\mathrm{total}}$ decreases due to an uncompensated fall in the magnetic entropy, ΔS_{M}. We can determine which materials will have a large ΔS_{M} by using Equation 2.4.4, where R is the gas constant, s is the spin of each paramagnetic component, and n is the number of spins of the given s. It's worth noting that we use "*s*" for individual spins and "S" for the total spin to distinguish from the entropy S.

$$S_{\mathrm{M}} = R ln(2s + 1) \qquad (2.4.4)$$

When we are dealing with a heterometallic system, the aforementioned value becomes the total sum of different metals. However, achieving this theoretical maximum is often not possible due to various factors, including but not limited to anisotropy, strong interactions or insufficient magnetic field strength.

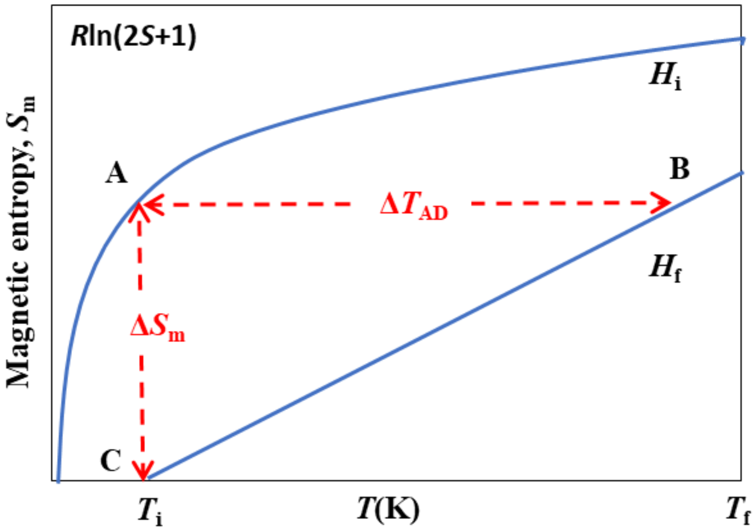

Figure 21. Magnetic entropy versus temperature for a hypothetical paramagnet at two distinct magnetic fields. H_{f} represents the final field and H_{i} the initial, although this nomenclature is arbitrary and there is reversibility between the two ($H_{\mathrm{f}} > H_{\mathrm{i}}$). ΔT_{AD} is the adiabatic temperature change and $-\Delta S_{\mathrm{M}}$ the magnetic entropy change. (Reproduced from Ref. 135, with permission from Royal Society of Chemistry.)

Equation 2.4.4 has two important limitations. Firstly, it only gives the magnetic entropy change (S_M) in joules per kilogram per kelvin, without considering the volume of the material being tested. To take into account the material's density, which is essential for better characterization, we need to combine the density and S_M ($-\rho * \Delta S_M$) to get a more accurate measure in millijoules per cubic centimeter per kelvin. Fortunately, densities can be easily calculated from X-ray crystallographic data. Secondly, it's worth noting that the highest possible spin may not always be achieved, especially in 3d systems where it's challenging to saturate the spin system in moderate fields. Finally, the refrigerant capacity (RC) is occasionally used in the literature, which is given by Equation 5.5. Here, T_1 and T_2 refer to the positions of the full-width-half-maxima in the $-\Delta S_M$ versus Field plots, where $T_1 < T_2$, and S_M is the maximum value found.

$$RC = S_M(T_1 - T_2) \qquad (2.4.5)$$

It can be challenging to practically determine the magnetic entropy change peak value ($-\Delta S_M$) versus temperature, despite being theoretically derived from magnetization data. This is due to the infrequency of observing a maximum in $-\Delta S_M$ versus T in Gd(III) compounds, which can arise from their weak interactions under certain laboratory conditions. Although $-\Delta S_M$ versus T is correlated to the refrigeration capacity (RC) of a material, the latter quantifies the performance of a substance more comprehensively over a broader temperature range.

The potential application of paramagnets is as a magnetic refrigerant, which relies on a process called adiabatic demagnetization. To warm up the material, a magnetic field is applied, and then the heat is exchanged with the surrounding. This results in a paramagnet with an ordered spin system at ambient temperature. The adiabatic demagnetization process then occurs when the paramagnet is removed from the field or when the field is switched off, cooling the material by ΔT_{AD} relative to its initial temperature and surroundings. This lower vibrational state allows the paramagnet to act as a refrigerant, absorbing heat from its surroundings. Phonons are exchanged from the lattice to the spin system during this process, which converts $S_{lattice}$ back to S_M.

Adiabatic coolers, which operate at low temperatures, are used in commercial applications and rely on a compound known as Gd(III)-Ga(III)–garnet, or GGG,[113] with the formula [$Gd^{(III)}{}_5Ga^{(III)}{}_5O_{12}$]. Although the GGG structure can be somewhat customized by substituting Ga(III) atoms for Fe(III) or Al(III),[114] molecular systems are better suited for modification, as Olivier Kahn's vision for molecular magnetism[115] involves specially tailored compounds and extensive chemical engineering. It's important to mention that a molecular cooler is not supposed to replace the common refrigerant systems. Both are useful for different applications.

2.4.3. Prerequisites for a Large Magnetocaloric Effect

The upcoming section examines essential concepts that are crucial for achieving a large magnetocaloric effect. It is revealed that the optimal refrigerant materials are produced by a combination of these factors. Some examples of such materials are $[Gd^{III}(HCO_2)_3]_n$[116]and $[Mn^{II}(H_2O)_6][Gd^{III}Mn^{II}(oda)_3]_2{\cdot}6H_2O$,[117] where oda stands for oxydiacetate ($C_4H_4O_5$).

I. Spin

The relationship between $-\Delta S_M$ and the spin of the metal cage, s, has been observed. To increase $-\Delta S_M$, one direct approach is to create a cage that contains several high-spin ions such as Gd(III). These spins can be easily saturated (provided there are no strong interactions) in magnetic fields that can be generated in a laboratory, increasing the difference between the magnetic entropy under no field and an applied field. Because of their 4f orbitals that can hold up to 14 electrons, Ln(III) ions[14] can have a higher spin than transition metals. As a result, Gd(III) has a maximum spin of $s = 7/2$ when these orbitals are half-filled.

High-nuclearity lanthanide complexes were made by Blagg et al.[118] and Sharples et al.[119] around the same time in 2013. These are made up of metal ions connected by organic ligands. The first is the pentametallic square-based pyramid $[Gd^{(III)}{}_5O(O^iPr)_{13}]$. The second compound is the heptametallic, disc-like $[Gd^{(III)}{}_7(OH)_6(tpa)_6\ (thmeH_2)_5(thmeH)(MeCN)_2](NO_3)_2$ where tpa ($C_{21}H_{18}O_2$) is triphenylacetate, $thmeH_3$ is tris(hydroxymethyl)ethane and MeCN is acetonitrile. Their metal cores are highlighted in **Figure 22** respectively.

The impressive, at the time, ΔS_M figures of 34 and 23 J kg^{-1} K^{-1} for $\{Gd^{(III)}{}_5 2$ and $\{Gd^{(III)}{}_7$ respectively, under applied fields of 7 T and 2 K. However, relying on only a large spin can result in compounds that do not reach their potential. Comparison of the experimental values of $-\Delta S_M$ with the theoretical values reveals that the numbers exceed those expected for simple paramagnets of the appropriate spin. Compared to fully decoupled spin systems, the actual numbers are feeble, with maximum values being 55 and 31.5 J kg^{-1} K^{-1} for {Gd$^{(III)}$$_5$} and {Gd$^{(III)}$$_7$}, respectively.

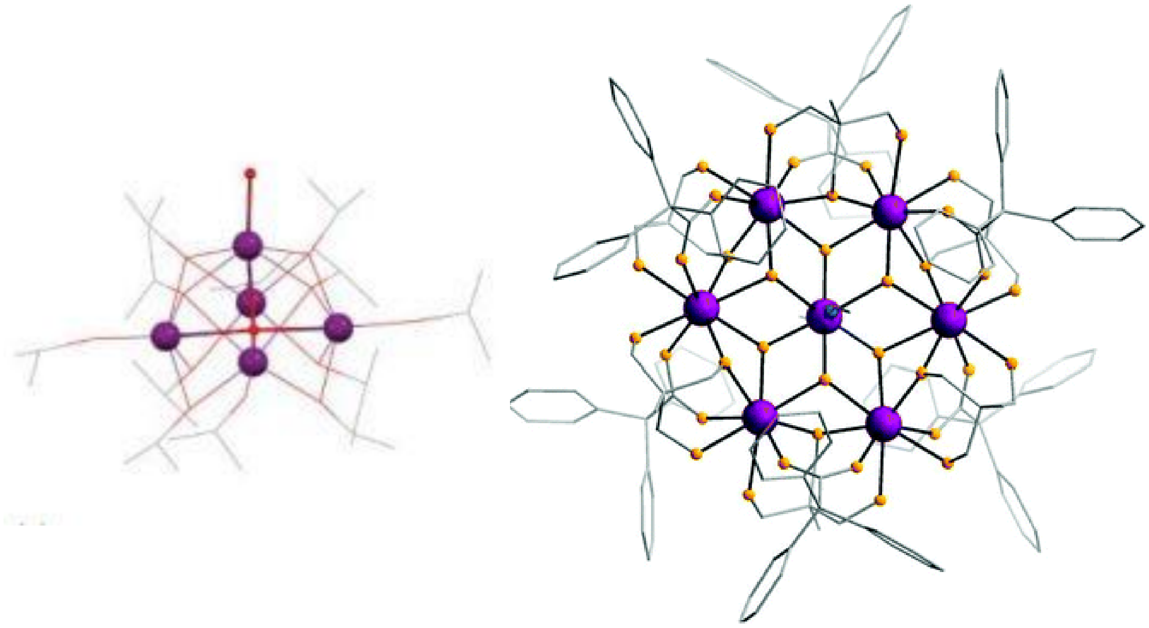

Figure 22. (left) X-ray structure of [$Gd_5O(O^iPr)_{13}$] with permission from the University of Manchester. (b) [Gd$^{(III)}$$_7$$(OH)_6(tpa)_6$ $(thmeH_2)_5(thmeH)(MeCN)_2](NO_3)_2$ with permission from Elsevier core.

To comprehend this, we need to analyze the magnetization data. When examining {Gd$^{(III)}$$_5$}, we observed that the theoretical value of $M(H)$ at 2 K (**Figure 23**) for fully uncoupled spins is significantly higher than the equivalent 2 K experimental data until around 7 T. This, in conjunction with the spin Hamiltonian model, reveals an antiferromagnetic exchange interaction of $J = -0.085$ cm^{-1} between all spins. As a result, the reduced magnetic entropy change is lower in an antiferromagnetic system since the spins are not fully saturated below the conditions of lowest temperature and strongest field. The antiferromagnetic coupling in {Gd$^{(III)}$$_7$} is also a hindrance, with behavior similar to {Gd$^{(III)}$$_5$}, when compared to the relevant Brillouin functions. It is worth noting that the magnetic properties of these compounds were compared to their isostructural Dy(III) SMM (single-molecule magnet) counterparts. Although tuning the magnetic properties of a single structure by simply switching the Ln(III) ion is intriguing from a research standpoint, it is not productive in the search for the best magnetocaloric materials, which can be found in polymeric structures. A large nuclearity cluster, with many high-spin ions, is not necessarily the route to the largest magnetocaloric effect. There are deeper factors, such as exchange interactions, which we now explore.

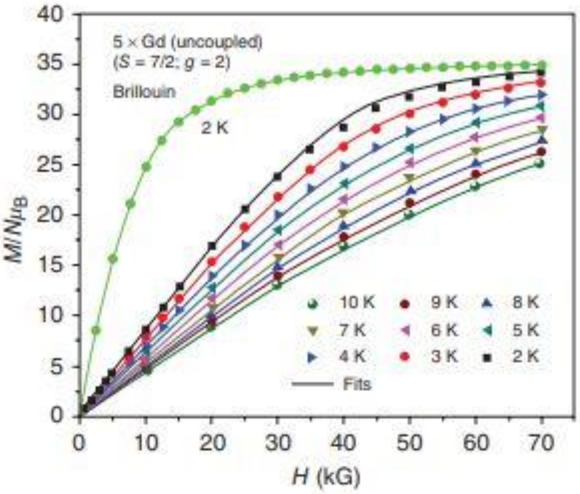

Figure 23. Magnetization versus field plots for $\{Gd^{(III)}{}_5\}$ for a range of temperatures. The green line is the Brillouin function for five uncoupled spins, each of s = 7⁄2 and g = 2.0. (Taken from Ref. 93 with permission from Royal Society of Chemistry.)

II. Nature of Exchange Coupling

It is possible to validate the significance of exchange coupling in magnetocaloric materials by using a model system in which all other factors are fixed. The program PHI, developed by Chilton et al.,[120] was utilized to calculate the $-\Delta S_M$ values of a dimetallic compound consisting of two s = 7⁄2 spins, with g = 2.0, and having a molecular weight of 1300 Da, at 5 and 7 T.

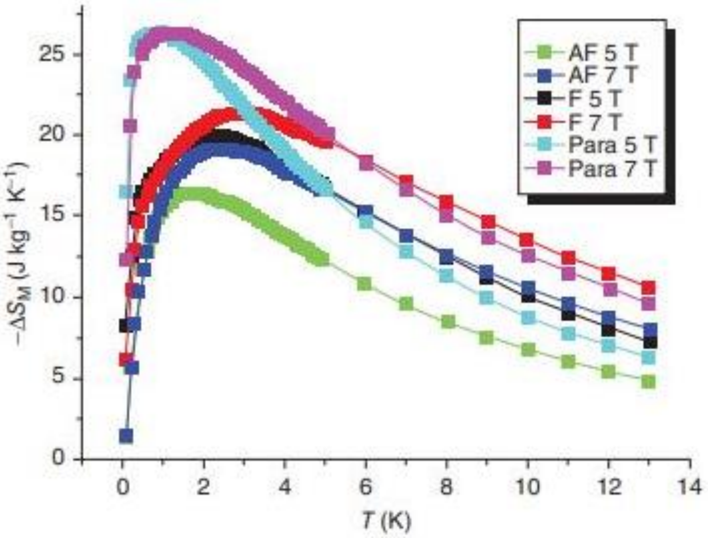

Figure 24. PHI (a computer program designed for the calculation of the magnetic properties of paramagnetic coordination complexes.) simulation of the $-\Delta S_M$ for an arbitrary system of two s = 7⁄2 spins with a MW of 1300 Da. Para is a paramagnetic system, F is a ferromagnetic interaction between spins and AF an antiferromagnetic interaction of ±0.15 cm^{-1}, at 5 and 7 T fields. (Taken from Ref 121 with permission from the University of Manchester.)

Figure 24[121] shows the results obtained. Analyzing the three scenarios at the same field, it becomes apparent that the paramagnetic material exhibits the most significant magnetocaloric effect, followed by the ferromagnetically coupled system, and finally the antiferromagnetic case.

1. Paramagnetism

To achieve the largest magnetocaloric effect (MCE) at the lowest temperatures, it is recommended to prepare systems with uncoupled spins. $Na_9[Gd^{(III)}(W_5O_{18})_2]\cdot35H_2O$ and $K_{12}[Gd^{(III)}(P_5W_{30}O_{110})]\cdot54H_2O$ are excellent examples of such paramagnetic systems[122] that demonstrate the potential of chemical design in this area. The central Gd(III) ion in these systems is enclosed in a diamagnetic coffin made up of a polyoxotungstenate capping group to reduce the interaction between metals. The smallest Gd(III)–Gd(III) distances from the crystal

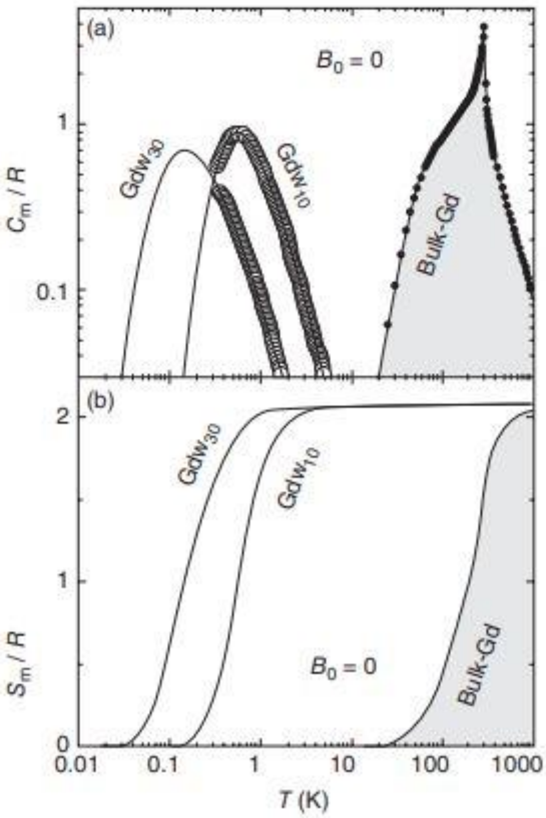

Figure 25. Upper graph (a) showing zero field magnetic contribution to the heat capacity for gadolinium metal, $\{Gd^{(III)}W_{10}\}$ and $\{Gd^{(III)}W_{30}\}$. Lower graph (b) showing zero field magnetic entropy for the same. (Taken from Ref. 122 with permission from Wiley-VCH Verlag GmbH & Co. KGaA.)

structure are 1.12 and 1.56 nm. Both systems exhibit Curie (paramagnetic) behavior down to 0.1 K, with magnetic susceptibility being constant.

From magnetization and heat capacity data (**Figure 25**), it is found that $-\Delta S_M$ for $\{Gd^{(III)}W_{10}\}$ and $\{Gd^{(III)}W_{30}\}$ (1.8 and 1.3 K, $\Delta H = 7$ T) are only 4.7 and 1.9 J kg^{-1} K^{-1}, respectively. Although these values may seem low, it is important to note that below the ordering temperature, the $-\Delta S_M$ of a paramagnet will quickly reduce to zero, thus defining the temperature range in which the material can be usefully employed. The utility of using $\{Gd^{(III)}W_{10}\}$ and $\{Gd^{(III)}W_{30}\}$ extends the working range deep into the millikelvin regime, overcoming the rather low $-\Delta S_M$ in these situations. Gadolinium metal is known to work best at room temperature, and there are already working prototypes that demonstrate this.

2. Ferromagnetism

Despite resulting in a lower MCE, ferromagnetic systems are useful as the spins are more easily aligned with the applied field, saturating in lower fields or at higher temperatures. This makes them usable over a wider range of temperatures and fields, with a potentially larger magnetocaloric effect under less forcing conditions than materials with higher peak $-\Delta S_M$ values. When looked at two similar compounds, gadolinium(III) chains, displaying different exchange interactions.[123] The one with ferromagnetic interactions displays higher $-\Delta S_M$.

3. Antiferromagnetism

Let's explore antiferromagnetic interactions in a fascinating 3d-4f system, $[Gd^{(III)}_4M^{(II)}_8(OH)_8(L)_8(O_2CR)_8]ClO_4$, in this section. The system features Ni(II), Cu(II) or Zn(II) as M(II), Ethyl for Ni(II) and *iso*-propyl for the latter two as R, and 2-(hydroxymethyl)pyridine (found by Hooper et al.) as LH.[123] The metal ions are arranged as a gadolinium(III) square, where each side forms a cubane and two transition metal ions are above and below the lanthanide plane. In the case of the Cu(II) version, there are competing interactions, resulting in a ferrimagnetic compound. In particular, antiferromagnetic coupling exists between the Cu(II) spins (J_{CuCu} = -11.84 cm^{-1}) and Gd(III) spins (J_{GdGd} = -0.2 cm^{-1}), while ferromagnetic coupling exists between heterospins (J_{CuGd} = 1.38 cm^{-1}). This gives a moderate MCE of $-\Delta S_M = 14.6$ J kg^{-1} K^{-1} (5.6 K, $\Delta H = 0 - 7$ T). A higher value of $-\Delta S_M = 18$ J kg^{-1} K^{-1} is found when M(II) = Zn(II), that is, for a diamagnetic metal. The negative impact of antiferromagnetically coupled transition metal ions on the magnetocaloric effect (MCE) is observed in {$\mathrm{Gd^{(III)}}_5$} and {$\mathrm{Gd^{(III)}}_7$}. The low field $-\Delta S_M$ plots in **Figure 26** show that the compound acts as a 'cryogenic heater' at 1 T field and 0.9 K, with $-\Delta S_M = -0.7$ J kg^{-1} K^{-1}. Only with larger fields does the MCE become positive, making the compound behave like a refrigerant. The Cu(II) variant is the only one that displays this behavior. This can be explained by the fact that if the exchange between spins is antiferromagnetic, the applied field must first 'flip' some of the spins to align with the field in order to achieve saturation. The antiferromagnetic coupling between Gd(III) ions in {$\mathrm{Gd^{(III)}}_4(\mathrm{Zn^{(II)}}_8)$} is much weaker, making even the smallest applied field of 1 T sufficient to induce a positive MCE by aligning the spins. The maximum MCE of {$\mathrm{Gd^{(III)}}_4(\mathrm{Zn^{(II)}}_8)$} occurs at a lower temperature than that of the Cu(II) system due to weaker exchange interactions.

It is worth noting that the maximum spin is often not attained in antiferromagnetically coupled systems due to the coupling. M_{sat} can usually be achieved in moderate fields in Gd(III) systems, whereas in transition metal systems, the spin state can be less than the maximum possible. For {$\mathrm{Gd^{(III)}}_4(\mathrm{Cu^{(II)}}_8$), the spin is $S = 18$, the maximum possible (albeit field induced). The difference between paramagnetic, antiferromagnetic, and ferromagnetic exchange can be significant even in homometallic Gd(III) compounds, where this can affect usability at less harsh conditions of field and temperature than those found in the laboratory. The effect is more pronounced in transition metals, where the exchange is stronger, and even negative magnetocaloric effects can be observed. For the largest $-\Delta S_M$ values at the lowest temperatures, a paramagnetic system is preferred.

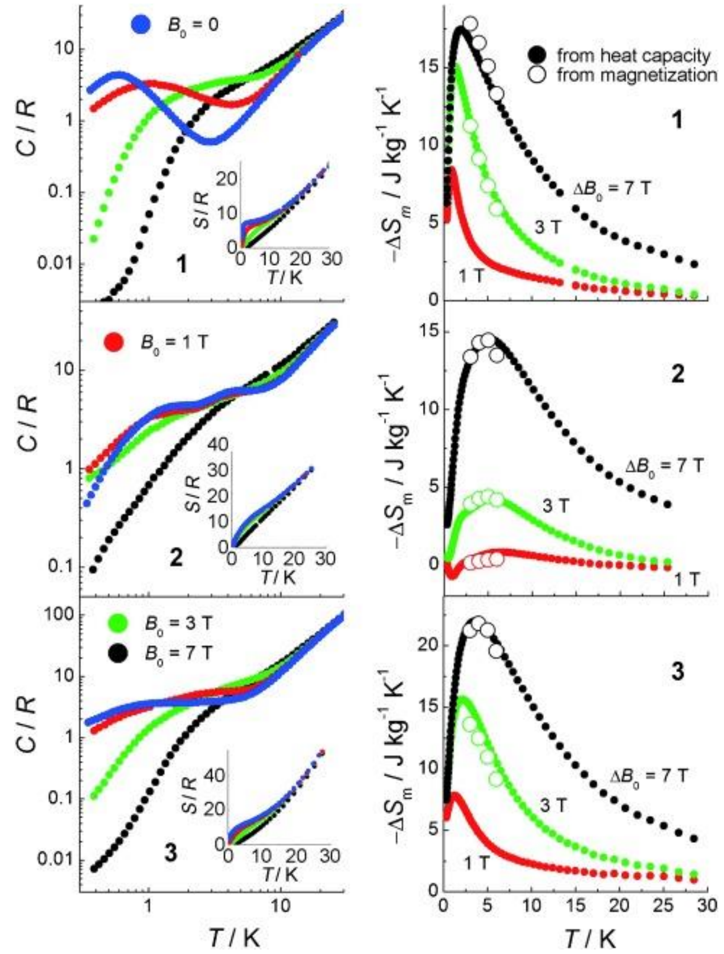

Figure 26. Left: From top to bottom, temperature dependencies of the heat capacities and entropies (insets) of {Gd(III)$_4$Ni(II)$_8$} (**3**), {Gd(III)$_4$Cu(II)$_8$} (**2**) and {Gd(III)$_4$Zn(II)$_8$} (**1**), respectively, for selected applied magnetic fields, as labeled. Right: From top to bottom, temperature dependencies of the magnetic entropy changes, as obtained from C (filled dots) and M data (empty dots), for **1**, **2**, and **3**, respectively, for selected applied magnetic field changes, as labeled. (Taken from Ref.123 with permission from ACS.)

III. Active Metal Percentage

The compound [Gd$^{(III)}$$_7(OH)_6(tpa)_6$(thmeH$_2$)$_5$(thmeH)(MeCN)$_2$](NO$_3$)$_2$ has been found to have only a moderate $-\Delta S_M$ despite containing seven gadolinium(III) ions.[119] This is because the compound has a relatively low percentage of active metal due to the presence of diamagnetic ligands that cannot contribute to the magnetic entropy change. To maximize $-\Delta S_M$, it is necessary to increase the active metal content. This can be achieved by using smaller ligands such as carbonate, formate, and acetate, resulting in structures that have more than double the active content compared to {Gd$^{(III)}$$_7$} and much larger $-\Delta S_M$ values. The effect is more apparent when using units of joule per kilogram per kelvin or similar, which are more relevant to practical work. Examples of such compounds with higher metal content include $Na_9[Gd^{(III)}(W_5O_{18})_2]\cdot 35H_2O$ and lower metal content $K_{12}[Gd^{(III)}(P_5W_{30}O_{110})]\cdot 54H_2O$,[122] which are paramagnetic down to extremely low temperatures and the former has a much higher magnetocaloric effect due to the increased metal percentage.

Table 8 shows magnetic coolers that only use gadolinium(III), along with their respective metal percentage. [111, 116, 118, 119, 122, 124, 125] It's evident that the metal percentage plays a crucial role in determining a material's large $-\Delta S_M$. There's a nearly direct correlation between the two factors, and slight variations can be attributed to exchange factors. As 3d metals are incorporated, the metal percentage becomes less significant, until homometallic 3d compounds are reached, where exchange plays a more significant role.

Table 8. List of selected compounds showing the percentage of metal in each and their $-\Delta S_M$ values.

Compound	**Dimensionality**	**Δ*H* (T)**	***T* (K)**	**−ΔSM (J kg^{-1} K^{-1})**	**Gd$^{(III)}$ (%)**
$[Gd(HCOO)_3]_n$	Three	7	3	55	54
$[Gd(OAc)_3(H_2O)_{0.5}]_n$	One	7	1.8	47.7	46
$[Gd(cit)(H_2O)]_n$	Two	7	2	43.6	43
$[Gd_2(OAc)_6(H_2O)_4]\cdot 4H_2O$	Zero	7	1.8	41.6	39
$[Gd_5(O)(O^iPr)_{13}]$	Zero	7	3	34	39
$[Gd_2(N\text{-}BDC)_3(dmf)_4]$	Three	7	1.8	29	27
$[Gd_7(OH)_6(thmeH_n)_6(tpa)_6(MeCN)_2](NO_3)_2$	Zero	7	3	23	29
$K_{12}[GdP_5W_{30}O_{110}]\cdot 54H_2O$	Zero	7	1.3	1.9	2
OAc, acetate; cit, citrate; N-BDC, 2-amino-1,4-benzenedicarboxylate and dmf, dimethylformamide.					

IV. Density

Good magnetocaloric materials have a commonly overlooked property, which is their density. The amount of a given material that can fit into a particular volume is dictated by its density, and this is an essential practical aspect that cannot be easily controlled. Although the industry standard is GGG[113] which has a $-\Delta S_M$ of 25 J kg^{-1}K^{-1}, this material's extremely high density of 7.1 g cm^{-3} is the reason for its widespread use. However, the majority of lanthanide complexes have densities around 2 g cm^{-3}, which limits their usefulness in practical applications.

Recently, two large complexes, $\{Gd^{(III)}_{38}\}$ and $\{Gd^{(III)}_{48}\}$,[126] have been developed that have abnormally high densities compared to other zero-dimensional structures. These cages rely on the templating of large numbers of metal ions around small anionic ligands such as ClO_4^- in the former and Cl^- and NO_3^- in the latter. Although it is challenging to intentionally engineer increased densities, metal-organic frameworks represent an improvement over molecular complexes, and methods such as anion templating can help. It's essential to note that a large $-\Delta S_M$ without high density is not enough to obtain commercially viable compounds. Therefore, it is crucial to consider both properties when developing magnetocaloric materials for practical applications.

V. Anisotropy

Gadolinium(III) is the only isotropic paramagnetic ion of the lanthanide(III) series and is considered exceptional. Research conducted by Evangelisti and Brechin[126] has shown that anisotropy, D, in 3d systems can hinder a large magnetocaloric effect at low temperatures. In their study, the Schottky heat capacity was calculated for a hypothetical spin of $s = 10$, with an axial anisotropy, $-D$, of −0.5K. **Figure 27** shows that the contribution of this heat capacity decreases with increasing field, and the derived $-\Delta S_M$ values showed the maximum $-\Delta S_M$ shifts and decreases with increasing anisotropy from $D = -0.5$ to −1.5 K and −3.0 K, for $\Delta H = 0 - 7$ T up to 200 K. A larger anisotropy could be desirable for certain applications, as it could provide a possible route to the much sought-after ‘tunability’ promised for molecular magnets in general. By modifying the anisotropy of the metal, either by changing it or by changing its ligand environment,[127] control over the point at which the maximum $-\Delta S_M$ occurs could be achieved. This can be related to Gd(III) in particular, as their anisotropy would be minimal even with engineered ligand changes, and modification of the anisotropy would be hard to achieve. Therefore, this approach would be better suited to 3d chemistry, where the metal ion orbitals can interact more strongly with those of the ligands. According to **Figure 27**, isotropic 3d-metals are better for lower temperature work than anisotropic ones. Empirical evidence by

Zheng et al. has demonstrated the unsuitability of non-gadolinium(III) lanthanide(III) ions.[128] The isostructural pair of compounds $[Ln^{(III)}_8Co^{(II)}_8(OH)_4(NO_3)_4(O_3P^tBu)_8(O_2C^tBu)_{16}]$, where Ln(III) is either Gd(III) or Dy(III), are 3d–4f phosphonates. For the Gd(III) compound, $-\Delta S_M$ is 21.4 J kg^{-1} K^{-1} ($\Delta H = 0 - 7$T, 3 K), whereas for Dy(III) this is only 11.6 J kg^{-1} K^{-1}, which can be accounted for by the lower spin of Dy(III). It is interesting to note that $-\Delta S_M$ has already passed through a maximum at 4 K for Dy(III), while the Gd(III) plot is still rising at 3 K, which is qualitatively in line with the work of Evangelisti and Brechin for 3d metals.[112] Therefore, the best lanthanide(III) for low-temperature MCE is gadolinium(III), and for this same reason there are only a handful of compounds using Dy(III) reported for this application called rotating MCE.[129]

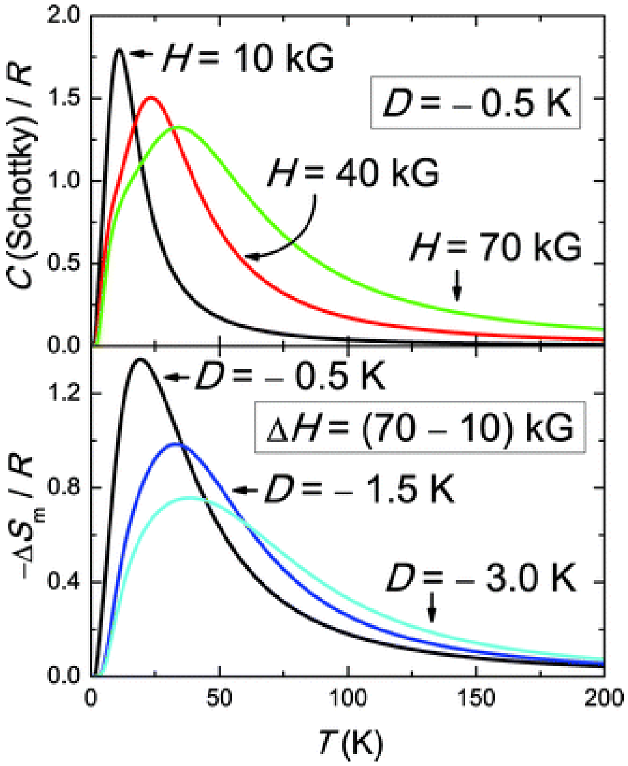

Figure 27. Top: Schottky heat capacities C_{Sch} of an isolated magnetic particle with S = 10 and axial anisotropy $D = -0.5$ K calculated for $H =$ 10, 40 and 70 kG, respectively. Bottom: magnetic entropy changes ΔS_m obtained from the top panel data and equivalent systems with $D = -1.5$ and -3.0 K following an applied field change of $\Delta H = (70–10)$ T. (Taken from Ref. 126 with permission from ACS.)

Currently, molecular-based systems need significant improvements to ensure productive research. However, Gd^{3+} materials have made considerable advancements in this regard. We now have a concise guide to the main points to consider while working with these materials and measuring them.

Chapter 3: Instrumentation

Experimental Techniques

3.1 UV-Visible Spectroscopy

UV-Vis spectroscopy is a technique in the ultraviolet and visible regions of the electromagnetic spectrum, which is typically within the range of 200-800 nm. In a double beam UV-Vis spectrometer, the light is divided into two parallel beams. One of these beams passes through a cell containing the solvent, while the other beam passes through another cell containing the sample dissolved in the same solvent. The detector then measures the intensity of the light transmitted through both cells, and the absorbance (*A*) is calculated using a specific equation:

$$A = log_{10} \frac{I_0}{I}$$

One can use the above equation to calculate the absorption process: ΔE = E2 - E1. This process involves exciting an electron from its lowest electronic energy level (ground state) to a higher energy level. The intensity of the light transmitted through the cell with the dissolved sample (I) and the reference cell with pure solvent (I_0) are used in the equation. The amount of energy required for this transition is determined by ΔE:

$$\Delta E = h.\upsilon = \frac{h.c}{\lambda}$$

The Beer-Lambert law states that the extinction, E_λ, which represents the absorbance of a particular material at a given wavelength, can be described by using certain variables. These variables include *h*, which is the Planck constant (6.626 × 10-34 J·s), c, which is the speed of light (measured at 299792458 ms^{-1}), υ, which represents the frequency, and λ, which represents the wavelength of the electromagnetic wave.

$$E_\lambda = \ log_{10} \frac{I_0}{I} = \ \epsilon.c.l$$

The concentration of the solution (in mol L^{-1}) is represented by *c*, while the length of the cuvette (in cm) is represented by *l*. The extinction coefficient, ϵ, is expressed in units of cm^2 mol^{-1} or dm^3 mol^{-1} cm^{-1}. Generally, transitions from $\pi \rightarrow \pi^*$ tend to have higher ϵ values than transitions from n → π*(**Figure 28**). By utilizing UV-vis spectroscopy, it's possible to analyze different chromophores and estimate the concentration of various solutions.

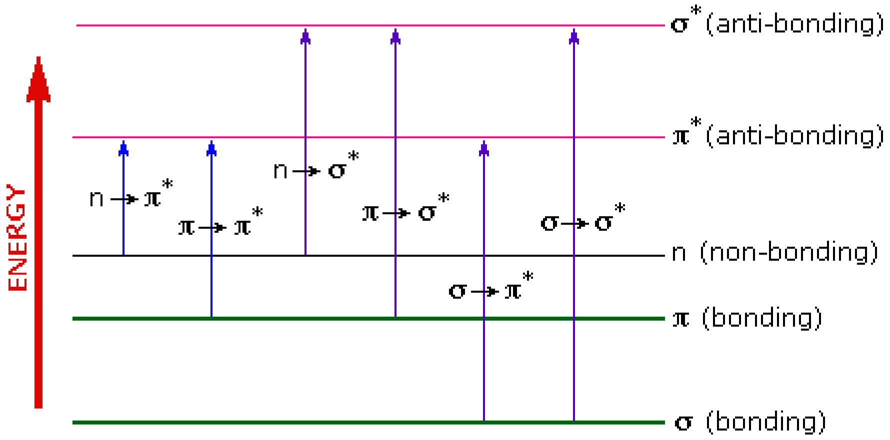

Figure 28. Various possible excitations in a molecule.

3.2 Fluorescence Spectroscopy

When a molecule absorbs energy at a wavelength where it has a transition dipole moment, resulting in radiative emission is also called Fluorescence. When the molecule is in its ground state, excitation energy promotes molecule to an excited singlet state, which then decays to the

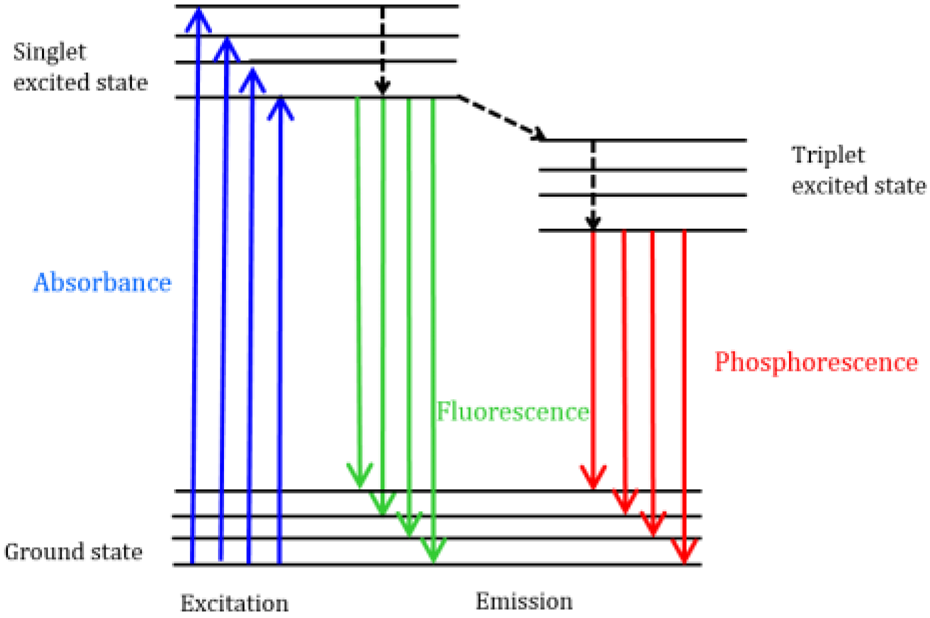

Figure 29. Jablonski diagram illustrating different transitions between a molecule's energy states.

lowest vibrational energy level of this excited singlet state. Finally, the molecule relaxes back to the ground state of the molecule, emitting photons in the process, as illustrated in **Figure 29**.

Fluorescent molecules can experience nonradiative relaxation through three methods: internal conversion, external conversion, and intersystem crossing. Internal conversion occurs when there is a small energy gap between two electronic states and the electrons move from a higher electronic state to one of lower energy, transferring the energy to the vibrational modes of the electronic state. As vibrational processes are thermally driven, an increase in temperature leads to a reduction in fluorescence intensity. Energy is lost through collisional quenching with solute molecules in the fluorophore's surroundings in external conversion. Intersystem crossing arises when the vibrational levels of the singlet and triplet excited states overlap in energy, causing molecule to transition from the lowest singlet excited state to the first excited triplet state. The process of photons emitted upon emission back to the ground state is known as phosphorescence (**Figure 29**). The phosphorescence peaks are at longer wavelengths than fluorescence because the triplet state is lower in energy than the singlet state. Since these transitions are also forbidden, phosphorescence exhibits a longer lifetime (~10^{-4} – 10^{2} seconds) compared with fluorescence (~10^{-9} – 10^{-6} seconds). The longer lifetimes also lead to thermal deactivation via oxygen quenching, solvent movement, and intermolecular collision. Therefore, phosphorescence typically cannot be observed at room temperature, and samples must be cooled at liquid nitrogen temperature to observe it.

Fluorescence intensity is *proportional* to the excitation light intensity:

$$F = 2.303 * K * I * \varepsilon bc$$

The constant K, which is based on instrument geometry, is used in the equation along with the intensity of the excitation light (I_0), the fluorophore's molar absorptivity (ε), the pathlength (b), and the concentration (c). Unlike absorption measurements, where the incident and detected intensities are ratioed, fluorescence intensity is not, resulting in a much greater fluorescence sensitivity that requires smaller concentrations for measurements. However, the equation is linear only when the sample absorbance is less than 0.05 AU. If a sample is too concentrated, the emission light may be reabsorbed by the fluorophore, attenuating the fluorescence signal at shorter wavelengths. In addition, highly concentrated samples may not allow the excitation light to fully penetrate, leading to reduced fluorescence intensities.

3.3 X-Ray Diffraction

The phenomenon of X-ray diffraction occurs when a beam of X-rays is incident on a crystal and interacts with its atomic structure, forming an interference pattern (**Figure 30**). This is similar to how a diffraction grating works with light. When X-rays hit the crystal at an angle θ, they are reflected back at the same angle by atoms that are separated by a distance d. For the interference pattern to form, the difference in path length between the X-rays that reflect off two different planes must be a whole number (n) multiple of wavelengths (λ), or nλ. The Bragg law **nλ = 2d sin θ** is used to calculate this. By analyzing the interference pattern, it is possible to deduce the internal structure of the crystal.

X-ray diffractometers are comprised of three essential components: An X-ray tube, a sample holder, and an X-ray detector. The X-rays are generated in a cathode ray tube by heating a filament to produce electrons, accelerating the electrons towards a target by applying a voltage, and bombarding the target material with electrons. When electrons have enough energy to displace inner shell electrons of the target material, characteristic X-ray spectra are produced, consisting mainly of K_α and K_β components. The most common target materials used are Cu, Fe, Mo, Cr, and Ga and filtering by foils or crystal monochromators is necessary to produce monochromatic X-rays required for diffraction.

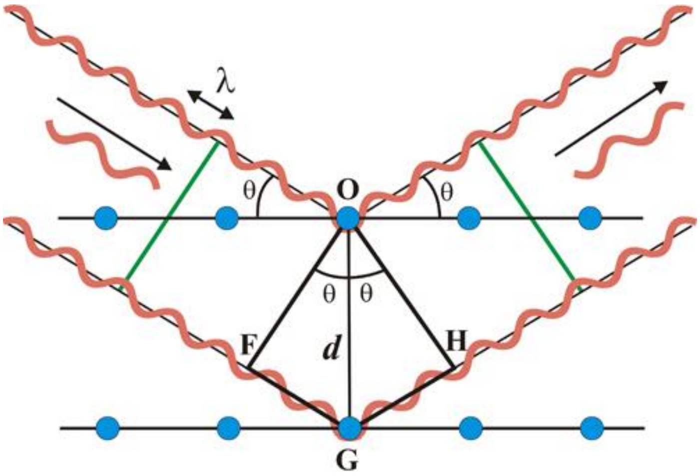

Figure 30. Schematic illustration of Bragg’s Diffraction.

The collimated X-rays are directed onto the sample, and as the sample and detector rotate, the intensity of the reflected X-rays is recorded. When the incident X-rays' geometry satisfies the Bragg Equation, constructive interference occurs and an intensity peak appears (**Figure 31**).

The X-ray signal is detected, processed, and converted to a count rate by the detector, which is then output to a device such as a printer or computer monitor.

The X-ray diffractometer's geometry is such that the sample rotates in the path of the collimated X-ray beam at an angle θ, while the X-ray detector is mounted on an arm to collect the diffracted X-rays and rotates at an angle of 2θ. The goniometer maintains the angle and rotates the sample to collect data at 2θ from ~5° to 70° for typical powder patterns. These angles are preset in the X-ray scan.

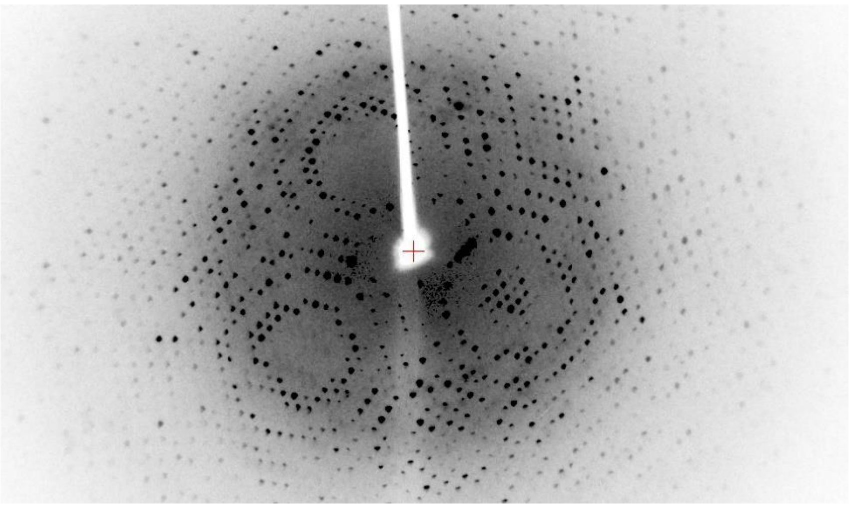

Figure 31. Typical Diffraction Pattern showcased on a detector plate

3.4. Scanning Electron Microscopy

SEM or scanning electron microscopy is a technique that employs the use of a focused beam of electrons to generate images of a sample's microstructure and morphology. These images are produced by capturing signals that result from elastic and inelastic interactions. Thereby, electrons are scattered back in an elastic manner at an angle of over 90°. Inelastic interactions occur when incident electrons interact with the sample's atoms and electrons, transferring energy to the atom through the beam. Secondary electrons (SE) are generated when the electrons of the specimen atom are excited during ionization, and these SE are typically utilized for imaging or sample analysis. SEM can also obtain other signals such as X-rays, Auger electrons, and cathodoluminescence (**Figure 32**). SEM's secondary electrons have energies below 50 eV, indicating that they originate from just a few nanometers below the sample surface. High-resolution images can be obtained with a resolution of up to 1 nm due to their highly localized nature near the electron beam. However, backscattered electrons (BSE) have higher energies, resulting in limited resolution. BSE detection can provide information on sample composition and topography, with heavier elements having more positive charge on their nuclei, leading to more electrons scattering back. Analyzing characteristic x-rays is a widely used method for obtaining chemical information. When a primary electron collides with an inner electron, an outer-shell electron can fill the vacancy created, leading to the emission of an x-ray photon and causing the ionized atom to return to its ground state. Energy-dispersive x-ray spectroscopy (EDS/EDX) is a technique that can be used to determine the chemical composition of a sample by identifying its elements.

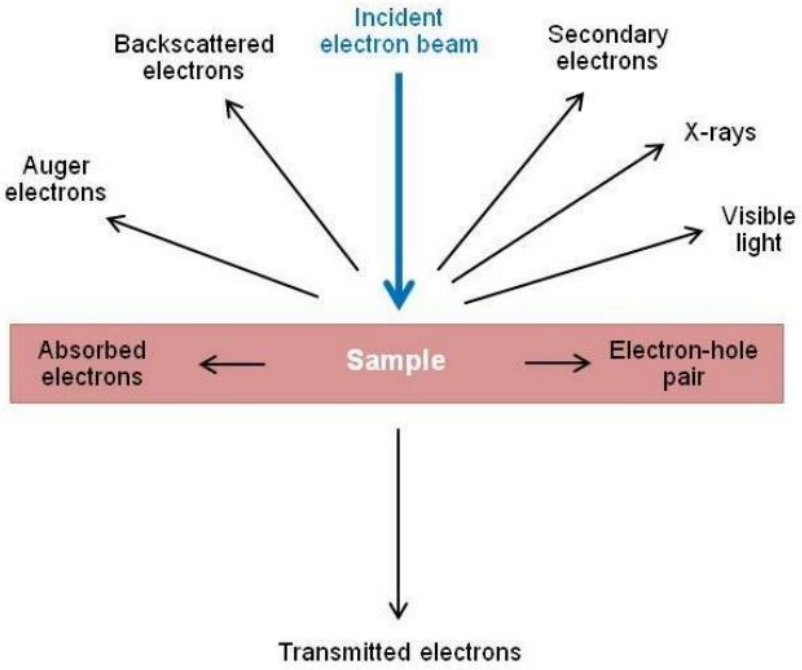

Figure 32. Signals generated by the electron beam. (Reproduced from Alobad, Zoalfokkar. (2018). Designing PU Resins for Fibre Composite Applications).

3.5. Thermogravimetric Analysis (TGA)

During Thermogravimetric Analysis (TGA), a sample is heated while being constantly weighed, while an inert gas atmosphere is introduced. Many solids undergo reactions that produce gaseous byproducts. TGA removes these gaseous byproducts, while recording changes in the remaining mass of the sample. Graphs are commonly used to display data from thermogravimetric analysis, with mass represented as a function of temperature for dynamic

TGA, and as a function of time at a given temperature for static TGA. For quasistatic TGA, multiple mass vs. time plots are produced for different temperatures. To make it easier to identify the points at which different mass changes occur, the derivative of the mass change with temperature is often plotted on the same graph, especially helpful in cases where multiple decomposition reactions occur in close proximity. Generally, mass fluctuations correspond to chemical reactions, with a few exceptions, such as drying, which can be observed as a quick initial drop at the beginning of heating. Depending on the material analyzed, evaporation or sublimation may also appear on the plot. A step-like pattern is common for multistage decomposition. During dynamic TGA, these steps may blend together, which may necessitate either slower heating rates or step-wise methods like quasistatic TGA (**Figure 33**). It is important to note that TGA alone may not be sufficient to identify the decomposition products, and chemical testing of the sample after TGA analysis is often required to ascertain the identities of suspected decomposition products. TGA is not a reliable method to identify substances, and other methods such as chemical testing or differential calorimetry must be performed alongside TGA to verify the identity of products.

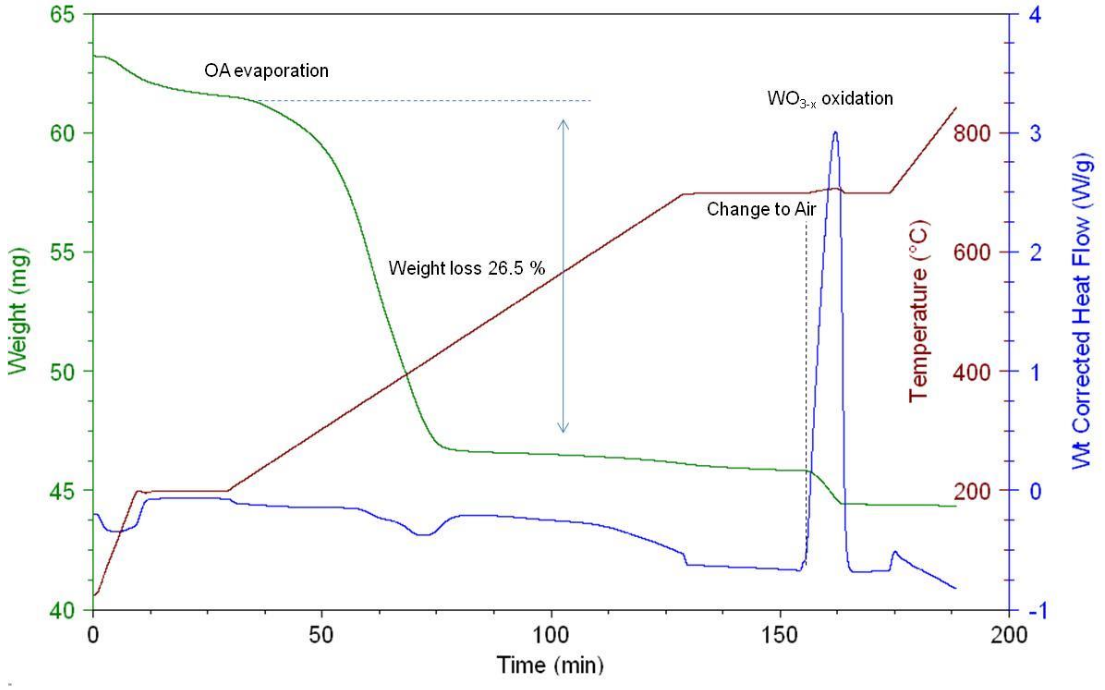

Figure 33. TGA curves showing the correlation of mass loss and heat flow in green. (Figure from Physical Methods in Chemistry and Nanoscience by Pavan M.V. Raja and Andrew R. Barron).

3.6. Mass Spectrometry-Electrospray Ionization

Mass spectrometry is a powerful analytical technique that can provide both qualitative information (structure) and quantitative information (molecular mass or concentration) on analyte molecules, once they are converted to ions. The process begins with the introduction of the molecules of interest into the ionization source of the mass spectrometer. Here, they are ionized to acquire either positive or negative charges. The resulting ions then travel through the mass analyzer and arrive at different parts of the detector based on their mass/charge (m/z) ratio. Electrospray ionization mass spectrometry (ESI-MS) is a powerful analytical technique that uses electrical energy to transfer ions from a solution into a gas phase for subsequent mass spectrometric analysis. ESI-MS allows the detection and analysis of ionic species in solution with increased sensitivity. Neutral compounds can also be converted to ionic form by protonation or cationization or anionization and can be studied by ESI-MS.

The ESI process involves three steps: (1) dispersal of a fine spray of charged droplets, (2) solvent evaporation, and (3) ion ejection from the highly charged droplets. (**Figure 34**) Within an ESI source, a sample solution is passed through a capillary tube that is maintained at a high voltage relative to the surrounding chamber. A mist of highly charged droplets is generated, which passes down a pressure gradient and potential gradient toward the mass spectrometer. With the aid of an elevated ESI-source temperature and/or nitrogen drying gas, the charged

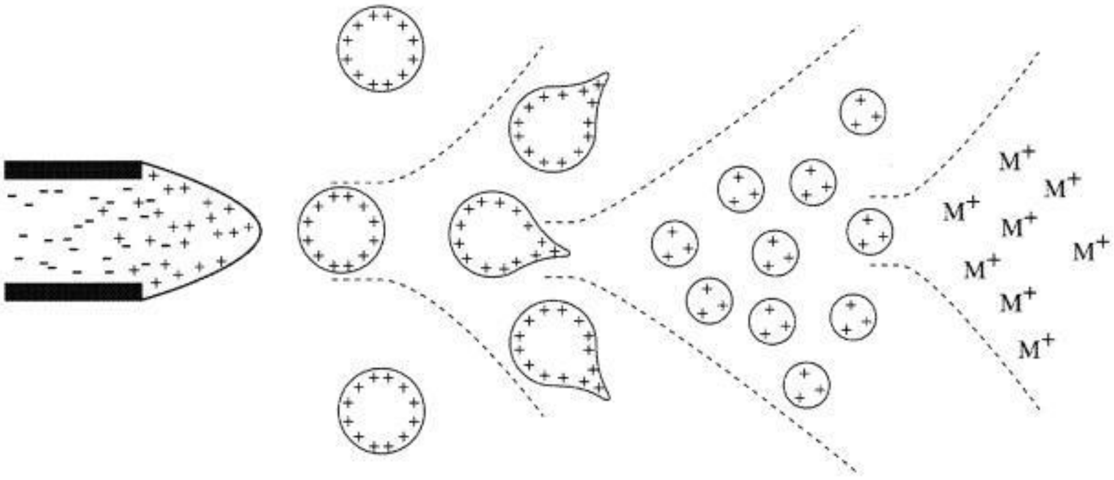

Figure 34. Mechanism of electrospray ionization. (Reproduced from Ho CS, Lam CW, Chan MH, Cheung RC, Law LK, Lit LC, Ng KF, Suen MW, Tai HL. Electrospray ionization mass spectrometry: principles and clinical applications. Clin Biochem Rev. 2003;24(1):3-12. PMID: 18568044; PMCID: PMC1853331).

droplets are continuously reduced in size by solvent evaporation, leading to an increase in surface charge density and a decrease in droplet radius. Finally, ions at the surface of the droplets are ejected into the gas phase, sampled by a skimmer cone, and then accelerated into the mass analyzer for subsequent analysis of molecular mass and ion intensity.

Upon contact with the detector, the ions generate useable signals that are recorded by a computer system. The signals are then graphically displayed as a mass spectrum, which shows the relative abundance of the signals according to their mass/charge (m/z) ratio. ESI-MS is a widely used technique in the fields of chemistry, biology, and medicine for the identification and quantification of a wide range of compounds, including drugs, peptides, proteins, and lipids.

Time-of-flight (TOF) spectrometers are equipped with a fast-electronic data acquisition system and a simple mechanical setup. These devices can provide mass resolutions exceeding 10000, a mass range of up to 500000 Dalton, an ion optical transmission of over 10%, and large acceptance volumes. The working principle of TOF mass spectrometry is based on the correlation between the mass of ions and their velocity when their kinetic energy E is fixed. By measuring the time T taken by ions to travel a fixed distance s, their velocity v can be determined, and consequently, their mass can be calculated from the equation above. The flight path length in commercial TOF spectrometers is typically around 1000-2000 mm, using kinetic energies of approximately 2000 eV, with flight times ranging from 5-100 µs, and individual TOF peak widths of a few ns.

$$m = \frac{2E}{v^2}$$

3.7. Attenuated Total Reflectance Spectroscopy

The ATR spectroscopy technique is utilized for analyzing the infrared (IR) spectra of materials. Unlike FTIR, ATR spectroscopy requires minimal sample preparation. The sample is directly placed in contact with an ATR crystal, which is typically made of materials like diamond, zinc selenide, or germanium. This eliminates the need for complex sample preparation, making ATR spectroscopy more suitable for a variety of applications. Solid or semi-solid samples are the most common cases for ATR, although it can also be utilized for liquids. When compared to

FTIR, it's not as suitable for gas analysis. ATR spectroscopy can be enabled by adding ATR attachments to existing FTIR instruments. The setup's ATR crystal is a critical component. The term "infrared" pertains to the part of the electromagnetic spectrum that lies between the microwave and visible regions. The IR spectrum is categorized into three regions: near, mid, and far IR. Among these regions, the mid IR region is the most useful for organic chemists. It includes wavelengths ranging from 3 x 10^{-4} to 3 x 10^{-3} cm. IR spectra may be reported in µm, although the preferred unit is currently $\bar{v} = 1/\lambda$ (wavenumber) (**Figure 35**).

Organic molecules absorb infrared radiation and use it to the excitation of vibrational levels. IR spectroscopy involves exposing an organic molecule to infrared radiation. When the energy of the radiation matches the energy of a specific molecular vibration, the molecule absorbs it. An IR spectrum is displayed with the wavenumber plotted on the X-axis, which is proportional to energy. Usual notation shows the highest energy vibrations are on the left. On the Y-axis, the percent transmittance (%T) is plotted. An absorption of radiant energy is shown as a "trough" in the curve. Zero transmittance corresponds to 100% absorption of light at that wavelength.

$$E = hc\bar{v}\,;\bar{v} = \frac{1}{\lambda}$$

$$A = \log_{10}\left(\frac{1}{T}\right)$$

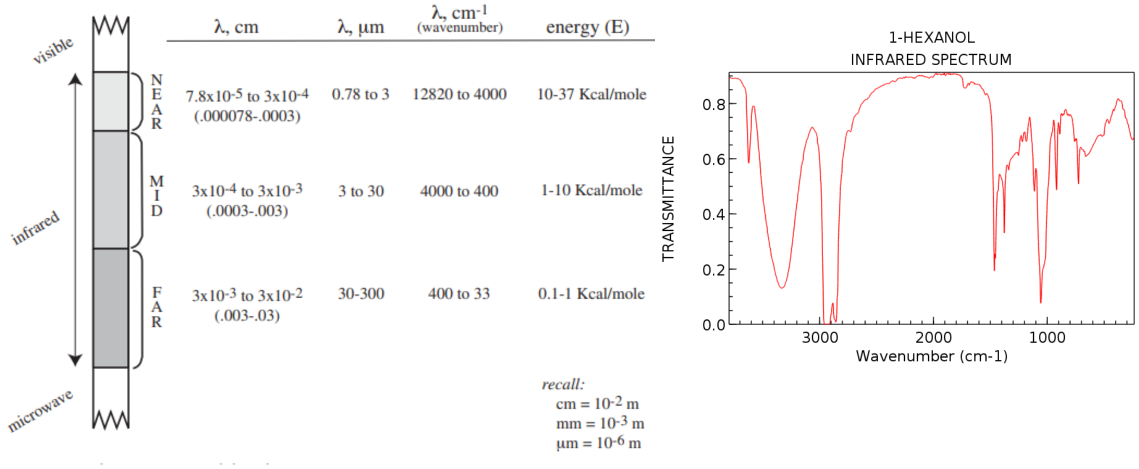

Figure 35. The IR regions of the electromagnetic spectrum and the IR spectrum of 1-Hexanol. (Reproduced from University of Colorado, Boulder, Dept of Chem and Biochem. (2002)).

Chapter 4: Upconversion- Results and Discussion

Cooperative Sensitization Upconversion

4.1. Molecular Upconvertors in Solution State

This chapter is based on the publication titled ”**Yb-to-Eu Cooperative Sensitization Upconversion in a Multifunctional Molecular Nonanuclear Lanthanide Cluster in Solution**”.[130] Sai P. K. Panguluri synthesized and characterized the clusters, performed the experiments, and the writing of the article. Dr. Aline Nonat and Dr. Loïc J. Charbonnière provided invaluable supervision and guidance for the upconversion experiments and analysis. Elsa Jourdain skillfully assisted with the upconversion experiments. Dr. Papri Chakraborthy deftly executed the HRMS-ESI-TOF experiments, and Dr. Svetlana Klyatskaya meticulously conducted EDS measurements.

Upconverting phosphor materials are widely used in medical imaging[131] and energy conversion.[132] However, their relatively large size can cause problems in biodistribution and crossing the blood-brain barrier.[133] Molecular upconverting biolabels could solve these issues by allowing precise control of material size and composition. To achieve molecular upconverting, it is necessary to ensure that the first excited state persists long enough to access the higher lying excited state. However, molecular materials have non-radiative quenching pathways that deactivate the excited state.[134] Metal complexes with vibrations in the near-infrared region have been found to reduce the excited state lifetime and the probability of upconversion.[135]

In 1994, it was proposed that 'ion clusters' were responsible for cooperative upconversion in some doped glasses.[78] These clusters result from ion pairing at very short distances(<5Å) and have been confirmed to be the origin of cooperative upconversion in some doped solids. A family of complexes based on ß-diketonate ligands has attracted attention due to their simple synthesis, versatility [136], and short inter-Ln distances.[137] A controlled doping of these complexes might allow the formation of entities containing up to eight sensitizing ions for one emitting upconversion center, which is considered to be optimum for maximizing energy transfer.[138] The chemical composition of these complexes can be tuned to obtain mixed lanthanide based nonanuclear complexes exhibiting outstanding upconversion properties in solution.

The theory proposed by Förster[139], the improvement of energy transfer efficiency between the energy donor (or sensitizer) and the energy acceptor, W_{SA}, the theory developed by Förster for non-radiative dipole-dipole energy transfer evidenced that the efficiency can be described by the following equation, where R_0 represents the Förster distance (or Förster radius or critical radius) at which the chance of radiative decay and of energy transfer are equiprobable, and r represents the distance between the donor and the acceptor. It is evident that the selection of the donor/acceptor pair is crucial, and the distance between them should be as short as possible. In pairs of Ln cations, R_0 values are rarely greater than a few Å.

$$W_{SA} = \frac{R_0^6}{R_0^6 + r_0^6}$$

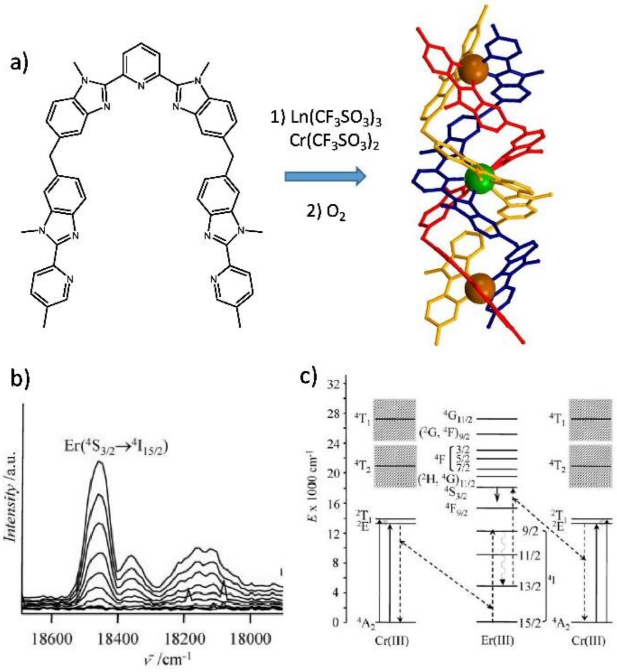

Figure 36. a) Heterotritopic ligand developed by Piguet and coworkers for the formation of heteropolynuclear $[ErCr_2L_3]^{9+}$ triple helicates. b) UC emission spectrum of a 10 mM solution of the helicate in CH_3CN at 30.6 K upon excitation at 748 nm and c) Jablonski energy diagram for the UC excitation of Er by Cr. (Reproduced with permission from reference 76, copyright Elsevier).

Piguet and coworkers developed a heterotritopic ligand for the formation of heteropolynuclear helicates **(Figure 36)**.[76] They designed a ligand composed of a central tridentate unit and two peripheral bidentate sites, bridged by flexible methylene bridges. The ligand was introduced to labile Cr(II) salts and a Ln salt, resulting in the formation of a supramolecular $[Cr_2LnL_3]^{7+}$ heterotrinuclear triple helicate. Oxygen bubbling into the solution led to the oxidation of the labile Cr(II) into inert Cr(III), resulting in the freezing of the helical architecture.[140] The system resulted in the observation of molecular upconversion (UC) with an Energy transfer upconversion mechanism. The only drawback of the system was the rather poor energy transfer efficiency. The thermodynamic, kinetic, and spectroscopic properties of these helicates have also been studied in deep detail.

Research on luminescent Ln complexes for fluoride ion detection led to the discovery of molecular upconversion (UC) in water. Specifically, while investigating these complexes, the formation of dimers in the solid state was serendipitously observed, in which two Ln cations were bridged by a fluoride anion (**Figure 37**).[141, 142] This supramolecular organization was facilitated by the presence of the fluoride bridge, aromatic stacking interactions between the two complexes, and hydrogen bonds between the fluoride bridge and hydrogen atoms of the ligands. However, the dimers could only be observed in the solid state, as they disassembled upon dissolution in water. After further engineering of the ligand structure was engaged to reinforce the different secondary interactions in solution, leading to the design of an indazolyl based ligand that strongly encapsulated the Ln cations and led to the formation of Ln dimers in aqueous solutions in the presence of F^- anions.

The intermetallic Ln distance was found to be very short, less than 4.5 Å, as evidenced by X-ray crystallography of the Yb dimer, which allowed for Tb to Eu energy transfer in the case of the corresponding heterodimer.[143] This short distance is particularly appealing for possible Ln-based energy transfer upconversion (ETU). Notably, the Er complex exhibited interesting spectroscopic properties in D_2O, as it was shown to be a rare case of an Er luminescent complex.[72] Excitation into the ligand absorption bands resulted in the observation of ligand-centered emission, together with admixture of Er-based f-f transitions observable in the visible (at 550 nm, $^4S_{3/2} \rightarrow {}^4I_{15/2}$ transition of Er) and near-infrared (NIR) (at 980 nm for the $^4I_{11/2} \rightarrow$

$^4I_{15/2}$ and around 1550 nm for the $^4I_{13/2} \rightarrow {}^4I_{15/2}$ transitions of Er) regions. Upon excitation of the Er monomer in D_2O at 980 nm, the visible emission spectrum displayed visible emission bands typical of Er at 525 nm ($^2H_{11/2} \rightarrow {}^4I_{15/2}$), 550 nm ($^4S_{3/2} \rightarrow {}^4I_{15/2}$), and 650 nm ($^4F_{9/2} \rightarrow {}^4I_{15/2}$ **Figure 37b**). The observation of this UC is related to an excited-state absorption (ESA) mechanism in the Er monomer. More interesting was the evolution of the UC emission when fluoride anions were added to the solution. The UC dramatically increased up to 0.5 equivalent with a 7.7-fold improvement and slowly decreased for larger excesses, as a result of the formation of a [ErLF] monomer. The UC mechanism was unambiguously demonstrated by a slope of 2.1 of the LogI/LogP plot (**Figure 37c**). The mechanism for UC in the dimer is still not clear as the overall luminescence quantum yield of the complex (obtained upon excitation

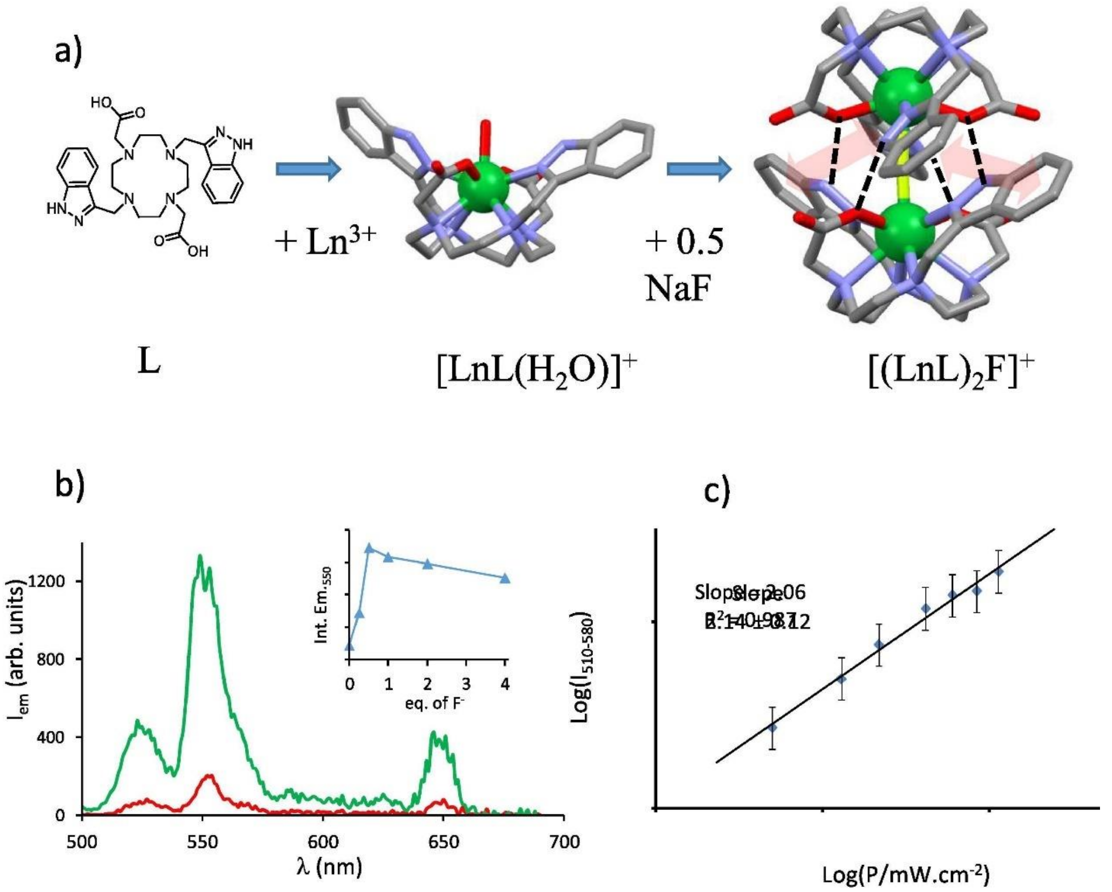

Figure 37. a) Structure of the ligand and complexes for forming fluoride dimers in aqueous solutions. b) UC visible emission spectra (D_2O, λ_{exc} = 980 nm, P = 5 W) of the $[ErL(D_2O)]^+$ complex without fluoride (red) and in the presence of 0.5 equivalent of fluoride anions (Inset: evolution of the UC intensity as a function of the quantity of fluoride anions). c) LogI/LogP plot of the Er dimer in D_2O. (Reproduced with permission from reference 141, copyright Elsevier).

into the ligand-centered band with emission in the NIR region) only displayed a two-fold increase. Assuming the most favorable option in which this increase is entirely due to an increase of the Er-centered luminescence (no change of the sensitization efficiency of the ligand), one would expect a four-fold increase of the UC quantum yield based on an ESA mechanism in the dimer, which is obviously smaller than the almost eight-fold experimentally observed. On this basis, it is not unrealistic to propose that the exact mechanism may be a mixture of ESA and ETU, although time-resolved experiments were unsuccessful in supporting this assumption. These first instances mentioned demonstrate the potential of coordination chemistry and supramolecular chemistry in creating assemblies of polynuclear and heteropolynuclear Ln. These assemblies incorporate multiple donor atoms and an energy accepting atom. In fact, coordination chemistry and supramolecular chemistry are promising tools for constructing polynuclear and heteropolynuclear Ln assemblies. However, Ln cations have similar chemical properties, making it difficult to design heteropolynuclear complexes.[13] Tuning the coordination sites for each of the Ln is one strategy, but the differences in stability are generally modest. Even with elegant and sophisticated synthetic strategies, producing pure heteropolynuclear complexes is challenging. In some cases, simpler ditopic ligands were shown to produce almost pure heterodinuclear complexes in the solid state. For heteropolynuclear complexes with more than three Ln cations, the statistics for pure complexes will be even less favorable.

Dr. Loïc J Charbonnière and colleagues conducted a research on a set of unsubstituted *ß*-diketonates complexes containing homo- and heteronona-nuclear clusters.[46] The research aimed to investigate the properties of these complexes in a solution-state. It was observed that the Yb_9 cluster in CD_3OD exhibited an emission band at 503 nm when exposed to 980 nm irradiation, (**Figure 38c**) which is referred to as cooperative luminescence upconversion. This phenomenon was observed in a solution for the first time. The hetero-nonanuclear complexes Tb_xYb_y showed cooperative sensitization upconversion, which resulted from energy transfer from a doubly excited state of Yb to sensitize Tb. The study also concluded that the most efficient systems had an average donor-acceptor ratio close to one. The results, along with the use of highly deuterated complexes, demonstrated that the Yb_5Tb_4 (D_{Ln}:D_S:D_L) compound had the most efficient molecular UC in a solution to date.

Based on the above-mentioned Ln-based upconversion studies, we turned towards a another family based on substituted *ß*-diketonate ligands as a result of their straightforward synthesis, versatility in nuclearity and composition, and short inter-Ln distances. The simple case of benzoylacetonate (BA) ligands forming nonanuclear complexes particularly piqued our interest with the close proximity of up to nine Ln atoms in a very small volume and intermetallic distances shorter than 4 Å. It is noteworthy that a controlled doping of such complexes might allow the formation of entities containing up to eight sensitizing ions for one emitting UC center, a situation considered to be optimum for maximizing energy transfer UC. Here, we present the synthesis of the a mixed Eu^{III}: Yb^{III} nonanuclear $[Eu_8Yb(BA)_{16}OH_{10}]Cl$ cluster with BA ligands (**Figure 39**), and its characterization in the solid state and, in solution, its magnetic properties as a Yb-SMM (Chapter 6) as well as its luminescent properties in the visible (Eu^{III}) and in the NIR (Yb^{III}) upon excitation in the BA antenna. Last but not least, direct CS

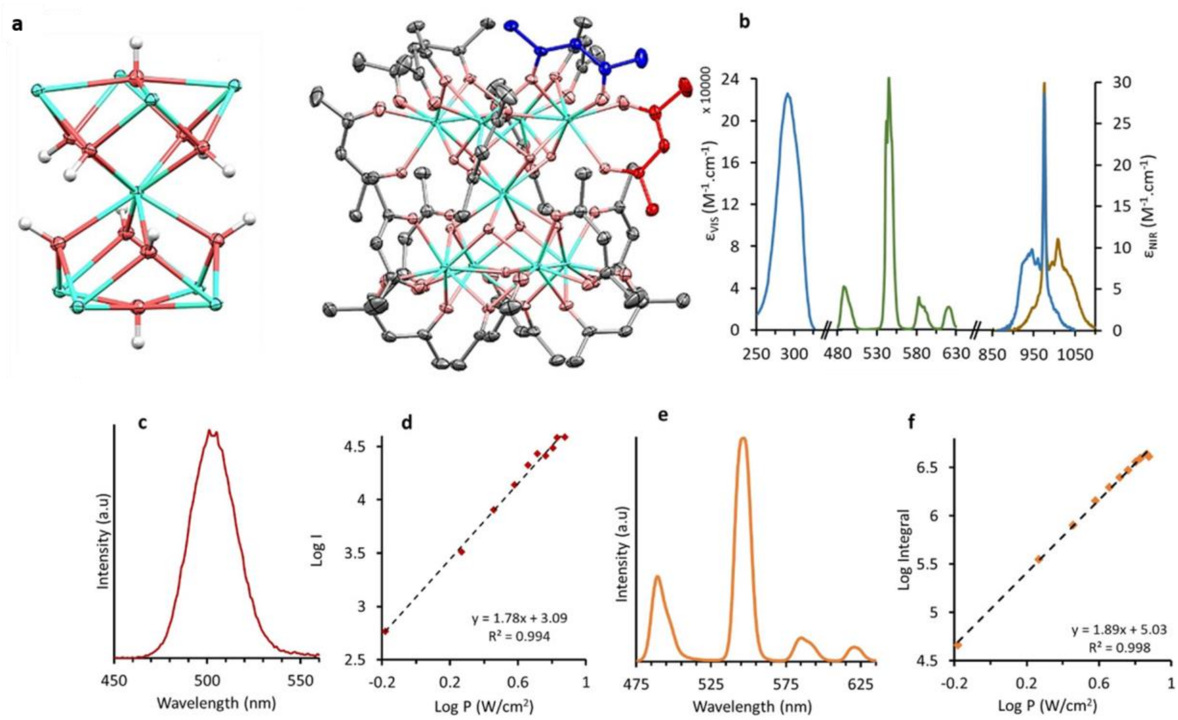

Figure 38. a) Single-crystal X-ray structure of $[Tb_4Yb_5L_{16}(OD)_{10}](OD)$ L= acac. b) Main spectroscopic properties of the $[Tb_4Yb_5(acac)_{16}(OD)_{10}](OD)$ (D_{Ln}:D_S:D_L) complex in CD_3OD representing the absorption spectrum of the acac ligands in the UV (light blue) and of Yb in the NIR (dark blue), the Tb centred emission (green) and the Yb centred emission (brown) upon ligand excitation at 350 nm c) Cooperative luminescence emission of the Yb_9 complex (D_{Ln}:D_S:H_L, [c]=2.04 mM, CD_3OD, λ_{exc}=980 nm, P=10.8 W cm^{-2}). d) UC intensity as a function of the incident pump power in a Log/Log scale. The black straight line represents the linear regression of the data. e) CL UC emission of the Tb_4Yb_5 complex (D_{Ln}:D_S:D_L, [c]=1.4 mM, CD_3OD, λ_{exc}=980 nm, P=2.86 W cm^{-2}). f) CL UC intensity as a function of the incident pump power in a Log/Log scale. (Reproduced from the reference 46)

upconversion of Eu^{III} is also achieved while irradiating Yb at 980 nm. Although indirect photosensitization was reported from Tb to Eu, UC on the other hand has only been reported once in a recent study for a Eu^{III}: Yb^{III} pair in a molecular complex and in solution through an excited multimer process.[144] Isostructural clusters with other lanthanides (Eu, Gd, Tb, Ho, Yb, Dy) and Y have also been synthesized and examined for comparison and understanding the UC mechanism in the heteronuclear complexes.

4.2 Synthesis and Crystal Structure

This chapter mainly focuses on the **$[Eu_8Yb(BA)_{16}(OH)_{10}]Cl\cdot3(C_2H_5OH)\cdot4(H_2O)$** referred to as **$Eu_8Yb$.** The synthesis and the characterization of all the other complexes mentioned in this chapter can be found in the experimental section (Chapter 7).

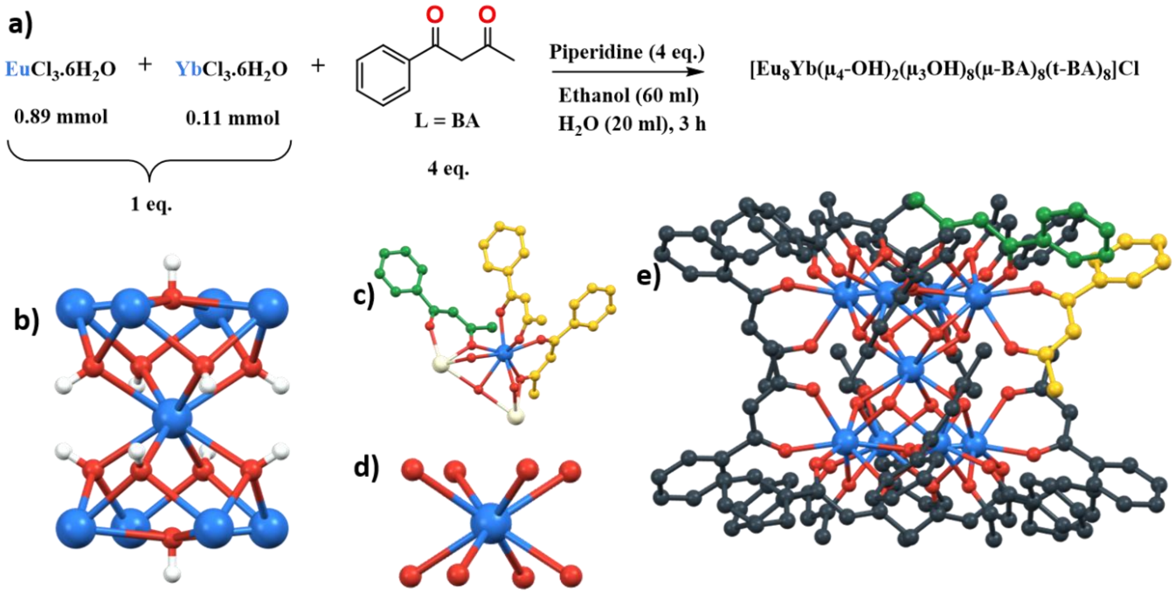

Figure 39. a) Synthetic protocol for preparing the nonanuclear Eu_8Yb complex. b) Single crystal X-ray structure of $[Eu_8Yb(BA)_{16}(OH)_{10}]^+$ showcasing the hourglass arrangement of the nine Ln (blue) and ten hydroxyl groups (O in red and H in white). c) $Ln_{Peripheral}$ coordination sphere: endo ligands (yellow), exo ligands (green), neighboring metal ions(white), oxygens (red). d) $Ln_{Central}$ coordination sphere. e) Single crystal structure of $[Eu_8Yb(BA)_{16}OH_{10}]^+$ ion showcasing BA ligands in grey, with endo and exo BA positions in yellow and green, respectively (hydrogens omitted for clarity).

A series of eight clusters were synthesized using modified procedures from existing literature.[137] They consist of five homonuclear nonanuclear clusters, with the general composition of $[Ln_9(BA)_{16}(OH)_{10}]Cl$ (Ln = Eu, Gd, Tb, Ho, Yb), and three heteronuclear clusters, with the respective formulas of $[Eu_8Yb(BA)_{16}(OH)_{10}]Cl$, $[Dy_8Yb(BA)_{16}(OH)_{10}]Cl$, and $[Y_8Dy(BA)_{16}(OH)_{10}]Cl$. These clusters were obtained in yields ranging from 59% to 70%. The clusters' synthetic methodology and crystal structures were determined using X-ray crystallography and are presented in chapter 7. The clusters were also characterized using XRD, ESI-TOF mass spectrometry, P-XRD, IR, EDS, TGA, and elemental analysis.

The nonanuclear clusters crystallize in the cubic space group with unit cell parameters of $a = b = c = 33.6739(6)$ Å, $\alpha = \beta = \gamma = 90°$, $V = 38183.9$ Å^3, $Pn3n$ (222). $Ln_{Peripheral}$ (**Figure 39c**) are the lanthanides at the corners of the two square planes with BA ligands and μ_3, μ_4 -hydroxy ligands coordination whereas, the central lanthanide ($Ln_{central}$ **Figure 39d**) is octacoordinated with eight μ_3-OH hydroxy ligands.

The eight triangular faces of the pyramids are capped by μ_3-OH groups linked to the three Ln at the edges of the triangles, while μ_4-OH bonds connect the four Ln atoms of the two square faces. All Ln atoms except the central one are linked to three β-diketonate ligands through two coordination modes (*t*-BA in yellow and μ-BA in green) (**Figure 39c**). The peripheral Ln ions are coordinated by 16 bidentate BA ligands. Eight of them (shown in yellow) (**Figure 39e**) present an endo environment with a bidentate coordination mode to a single metal center (*t*-BA), while the eight others (shown in green) are placed in an exo environment and coordinate two metal centers in a bridging mode (μ-BA), while being bidentate coordinated to one of the two metals. The coordination sphere of Ln atoms (CN = 8) is completed by the aforementioned hydroxyl ligands. Two μ_3-OH hydroxy ligands in the triangular face and μ_4-OH ligands in the square face complete the coordination sphere.

This high symmetric cubic packing creates hexagonal channels that run along the body diagonal directions inside the unit cell. These channels have a minimum diameter of approximately 7 Å and can accommodate 24 ethanol molecules in each unitcell and anions (Cl^-). (**Figure 40**).

However, the channels cause significant disorder among smaller components. Even at 120 K, X-ray analysis cannot resolve this disorder. The solid-state structure of the Ln_9 complexes is made up of two pentanuclear square pyramids sharing the apical Ln atom. This results in square anti-prismatic geometry at the central Ln. Refining the occupancy of each lanthanide site as a superposition of x Ln_1 and (1-x) Ln_2, using SC-XRD data, did not reveal notable site preferences in the cases of Eu/Yb, Dy/Yb, and Y/Dy due to the minimal difference in their ionic radii. In the case of Eu_8Yb the refined values were: $Ln_{Central}$: 96 ± 5% Eu, 4 ± 5% Yb; $Ln_{Peripheral}$: 92 ± 4% Eu, 8 ± 4% Yb.

The two distinct coordination environments, $Ln_{Peripheral}$ and $Ln_{central}$, can be used to promote site selectivity for heteronuclear lanthanide clusters. The central pocket size is the largest, and previous studies have shown that such distinct coordination environments are useful for promoting site selectivity, with a tendency for the largest ion to occupy the central position.[145]

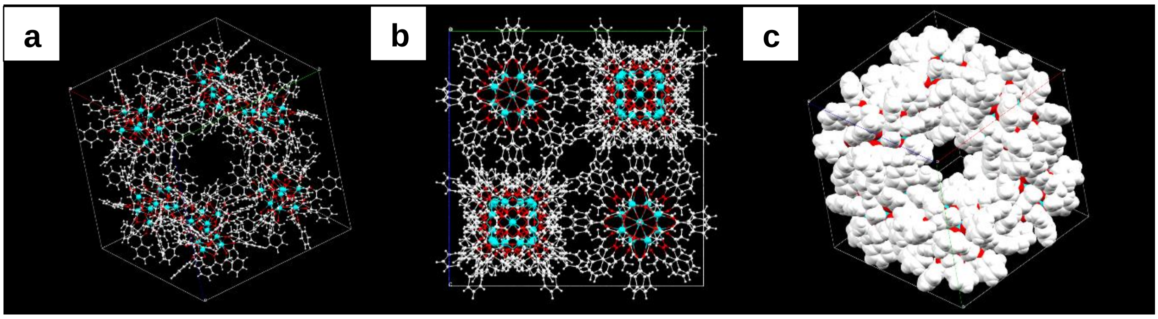

Figure 40. a, b) The Packing of the nonanuclear cations in a unit cell shows the hexagonal channel along the body diagonal in the lattice. c) The huge void in the unit cell of 17,300 Å^{3,} which is about 45% of the unit cell. Colors used Grey for C, Red for O, and Blue for Ln.

Table 9. Continuous Shape Measures (CShMs) for $Ln_{central}$ (case in point Eu_8Yb complex)

Central Ln (Eu_8Yb)	**Geometry/Polyhedron**	**Symmetry**		**CShMs**
1	Octagon	D_{8h}	OP-8	27.856
2	Heptagonal pyramid	C_{7v}	HPY-8	23.923
3	Elongated trigonal bipyramid	D_{3h}	ETBPY-8	24.266
4	Cube	O_h	CU-8	10.599
5	**Square antiprism**	D_{4d}	SAPR-8	0.044

6	Triangular dodecahedron	D_{2d}	TDD-8	2.659
7	Johnson gyrobifastigium J26	D_{2d}	JGBF-8	17.087
8	Johnson elongated triangular bipyramid	D_{3h}	JETBPY-8	28.775
9	Biaugmented trigonal prism J50	C_{2v}	JBTPR-8	2.783
10	Biaugmented trigonal prism	C_{2v}	BTPR-8	2.183
11	Snub diphenoid J84	D_{2d}	JSD-8	5.282
12	Triakis tetrahedron	T_d	TT-8	11.405

Table 10. Continuous Shape Measures (CShMs) for Ln$_{Peripheral}$ (case in point Eu$_8$Yb complex)

Ln$_{Peripheral}$	**Shape**	**Symmetry**		**CShMs**
1	Octagon	D_{8h}	OP-8	32.226
2	Heptagonal pyramid	C_{7v}	HPY-8	22.040
3	Elongated trigonal bipyramid	D_{3h}	ETBPY-8	23.043
4	Cube	O_h	CU-8	13.381
5	Square antiprism	D_{4d}	SAPR-8	3.491
6	Triangular dodecahedron	D_{2d}	TDD-8	2.526
7	Johnson gyrobifastigium J26	D_{2d}	JGBF-8	11.836
8	Johnson elongated triangular bipyramid	D_{3h}	JETBPY-8	26.591
9	Biaugmented trigonal prism J50	C_{2v}	JBTPR-8	1.929
10	**Biaugmented trigonal prism**	**C_{2v}**	**BTPR-8**	**1.417**
11	Snub diphenoid J84	D_{2d}	JSD-8	3.843
12	Triakis tetrahedron	T_d	TT-8	13.792

To test if site selectivity was also present in the BA-clusters, a set of eight homo- and heterometallic nonanuclear clusters was synthesized and crystallized. Continuous shape measures (CShMs) were conducted on X-ray crystallographic data within series, revealing that the $Ln_{central}$ site exhibits a nearly perfect square antiprismatic geometry with D_{4d} symmetry (**Table 9**), while the $Ln_{peripheral}$ site is a biaugmented trigonal prism with C_{2v} symmetry (**Table 10**) confirming the presence of two different coordination sites.

The "coordination site cavity" or "pocket size" for the two different environments was determined by averaging the Ln-O bond lengths for each site. The study demonstrated that the central pocket size is the largest (**Table 11**) (**Figures 41-50**). However, Ln-O bond lengths at each site across the set of complexes were calculated and analyzed for the distinction of the site selectivity suggesting larger lanthanide ion goes to the central site and the smaller lanthanide ion goes to the peripheral site.

Table 11. Pocket size parameters (Av. Ln_{cent}-O, Av. Ln_{peri}-O) and ionic radii difference (Δr) within the homo- and hetero-nonanuclear complexes series of general formula $[(Ln_1)_x(Ln_2)_{9-x}(BA)_{16}OH_{10}]Cl$.

Ln_1	Ln_2	Δr (Å)	Av. Ln_{cent}-O (Å)	Av. Ln_{peri}-O (Å)
Eu	Eu	-	2.429	2.4017
Gd	Gd	-	2.432	2.3928
Tb	Tb	-	2.422	2.3844
Ho	Ho	-	2.409	2.354
Yb	Yb	-	2.388	2.3354
Dy	Yb	0.05	2.419	2.3644
Eu	Yb	0.08	2.455	2.3954
Y	Dy	0.02	2.411	2.356

Table 12. Crystallographic Information of the complexes

Name	**Eu_8Yb**	**Yb_9**	**DyY_8**	**Ho_9**	**$YbDy_8$**	**Tb_9**	**Gd_9**
Chemical Formula	$[Eu_8Yb(BA)_{16}(OH)_{10}]^+$	$[Yb_9(BA)_{16}(OH)_{10}]^+$	$[Y_8Dy(BA)_{16}(OH)_{10}]^+$	$[Ho_9(BA)_{16}(OH)_{10}]^+$	$[Dy_8Yb(BA)_{16}(OH)_{10}]^+$	$[Tb_9(BA)_{16}(OH)_{10}]^+$	$[Gd_9(BA)_{16}(OH)_{10}]^+$
Fw	4137.66	4306.26	3549.01	4233.19	4221.94	4179.19	4164.07
***T*(K)**	150	180	180	180	180	180	180
crystal system	Cubic	Cubic	Cubic	Cubic	Cubic	Cubic	Cubic
space group	P*n*-3*n*	P*n*-3*n*	P*n*-3*n*	P*n*-3*n*	P*n*-3*n*	P*n*-3*n*	P*n*-3*n*
***a*, Å**	33.6739	33.50570 (18)	33.5883 (7)	37887.4	33.5458(4)	33.76869	33.7221 (10)
***b*, Å**	33.6739	33.50570 (18)	33.5883 (7)	37887.4	33.5458(4)	33.76869	33.7221 (10)
***c*, Å**	33.6739	33.50570 (18)	33.5883 (7)	37887.4	33.5458(4)	33.76869	33.7221 (10)
***α*, deg**	90	90	90	90	90	90	90
***β*, deg**	90	90	90	90	90	90	90
***γ*, deg**	90	90	90	90	90	90	90
V (Å^3)	38184 (2)	37614.6	37893 (2)	37887.4 (14)	37749.8(14)	38507.3(17)	38348(3)
Z	6	6	6	6	6	6	6
$\rho_{Calcd.}$ (g·cm^{-3})	1.076	1.140	0.933	1.113	1.134	1.081	1.081
μ (mm^{-1})	2.281	3.369	2.034	12.713	3.357	2.491	12.263
R_1(all data)	0.0504(4751)	0.0358(4890)	0.044785705)	0.0353(5264)	0.0351(6856)	0.0262	0.0485
wR_2(all data)	0.1640(6704)	0.0938(5760)	0.1366(7749)	0.1039(6603)	0.1323(8409)	0.0683	0.1330

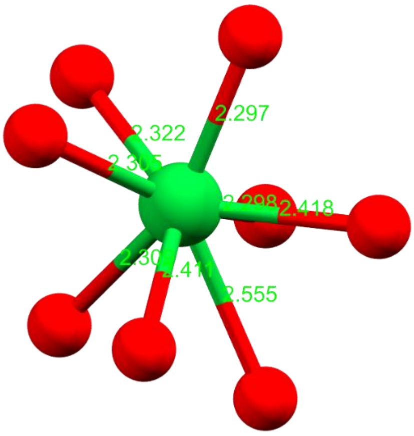

Figure 41 Dy_8Yb-$Ln_{Peripheral}$ Site Ln-O bond distances (Å)

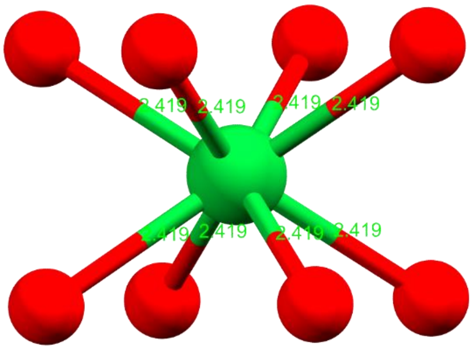

Figure 42 Dy_8Yb-$Ln_{Central}$ Site Ln-O bond distances (Å)

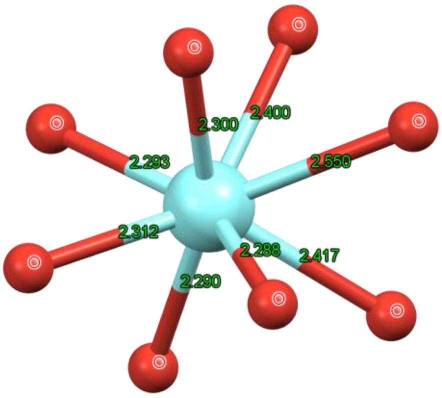

Figure 43. DyY_8-$Ln_{Peripheral}$ Site Ln-O bond distances (Å).

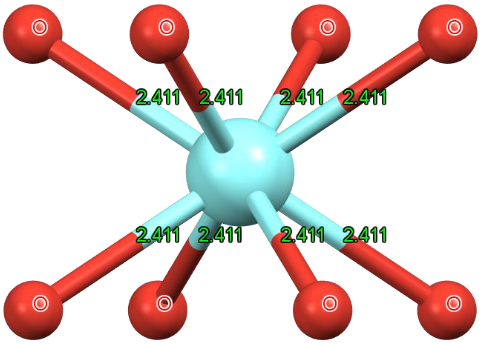

Figure 44 . DyY_8- $Ln_{Central}$ Site Ln-O bond distances (Å).

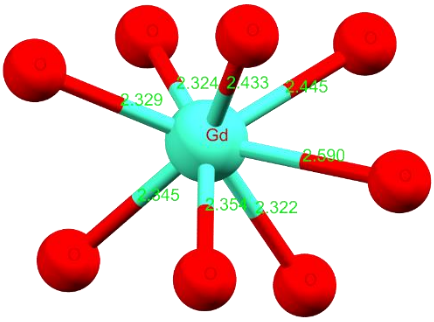

Figure 45. Gd_9-$Ln_{Peripheral}$ Site Ln-O bond distances (Å)

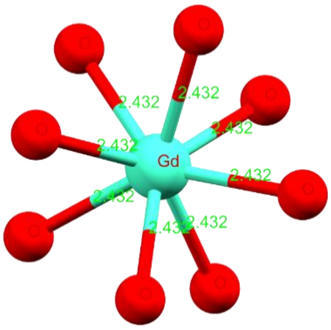

Figure 46. Gd_9-$Ln_{Central}$ Site Ln-O bond distances (Å).

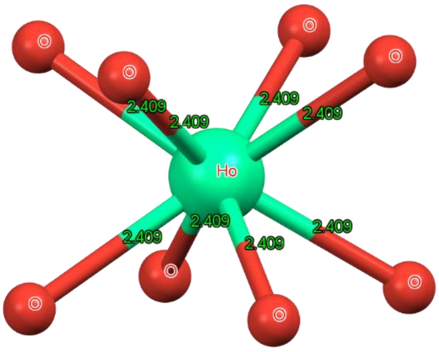

Figure 47. Ho9-Ln_{Central} Site Ln-O bond distances (Å).

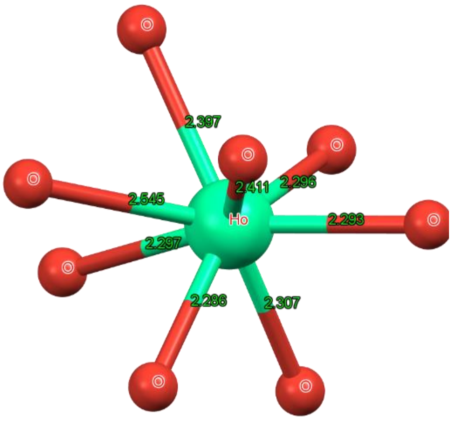

Figure 48. Ho9-Ln_{Peripheral} Site Ln-O bond distances (Å).

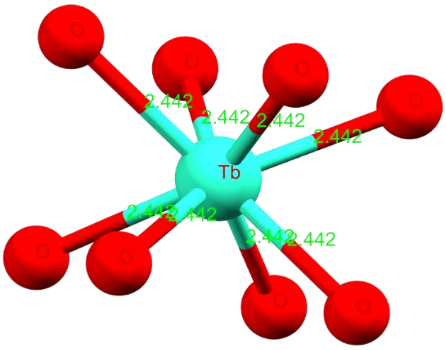

Figure 49. Tb9-Ln_{Central} site Ln-O distances (A).

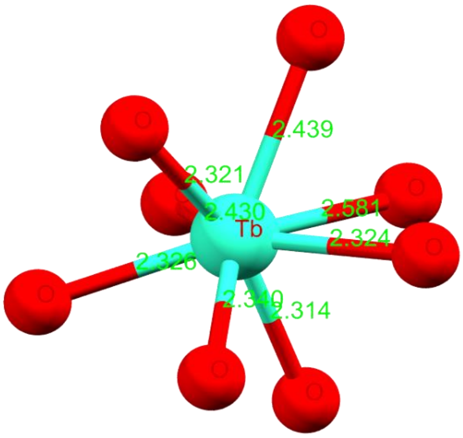

Figure 50. Tb9-Ln_{Peripheral} site Ln-O distances (A).

The nonanuclear clusters have a high cubic symmetry packing which creates hexagonal channels that run along the body diagonal directions inside the unit cell. The solid-state structure of the Ln_9 complexes is made up of two pentanuclear square pyramids sharing the apical Ln atom and resulting in a square anti-prismatic geometry at the central Ln. The two distinct coordination environments, $Ln_{Peripheral}$ and $Ln_{central}$, can be used to promote site selectivity for heteronuclear lanthanide clusters, with a tendency for the largest ion to occupy the central position.

SEM-EDS analysis gave an atomic composition of 81.3% Eu, 9.6% Yb, and 9.2% Cl, in good agreement with the predicted values of 80% Eu, 10% Yb, and 10% Cl (**Figure 51**). The phase purity was also confirmed by measuring the PXRD of fresh crystals taken from the mother liquor (**Figure 52**).

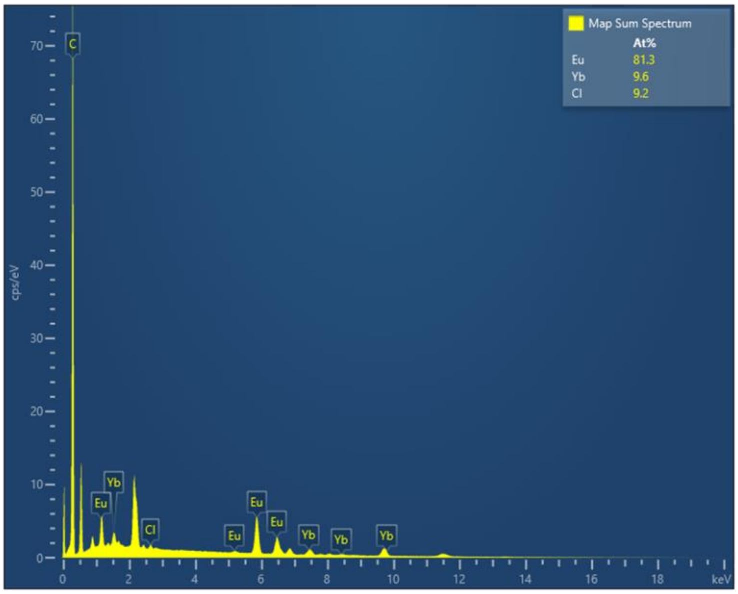

Figure 52. Energy-dispersive X-Ray Spectroscopy graph showing the relative atomic percentages of Eu, Yb and Cl in 8:1:1 ratio. Confirming the presence of Cl^- ion.

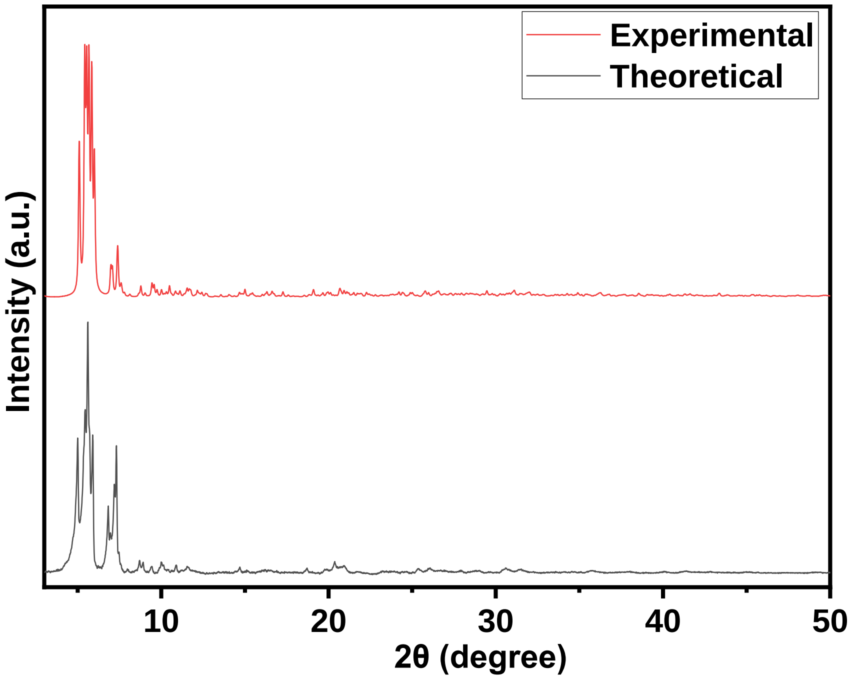

Figure 51. PXRD comparison of Experimental data vs Sc-XRD simulated pattern of Eu_8Yb.

Upon drying in the vaccum, the crystals lost the order (**Figure 53.**). However, a thermal stability study by thermogravimetric analysis (**Figure 54**) confirmed that the compounds remain stable up to 150°C and a weight loss of approximately 5% was measured in the temperature range 0 - 100°C, which corresponds to the loss of lattice solvent (three EtOH and four H_2O molecules), in perfect agreement with PXRD studies. At temperatures above 210°C, decomposition of the cluster is observed.

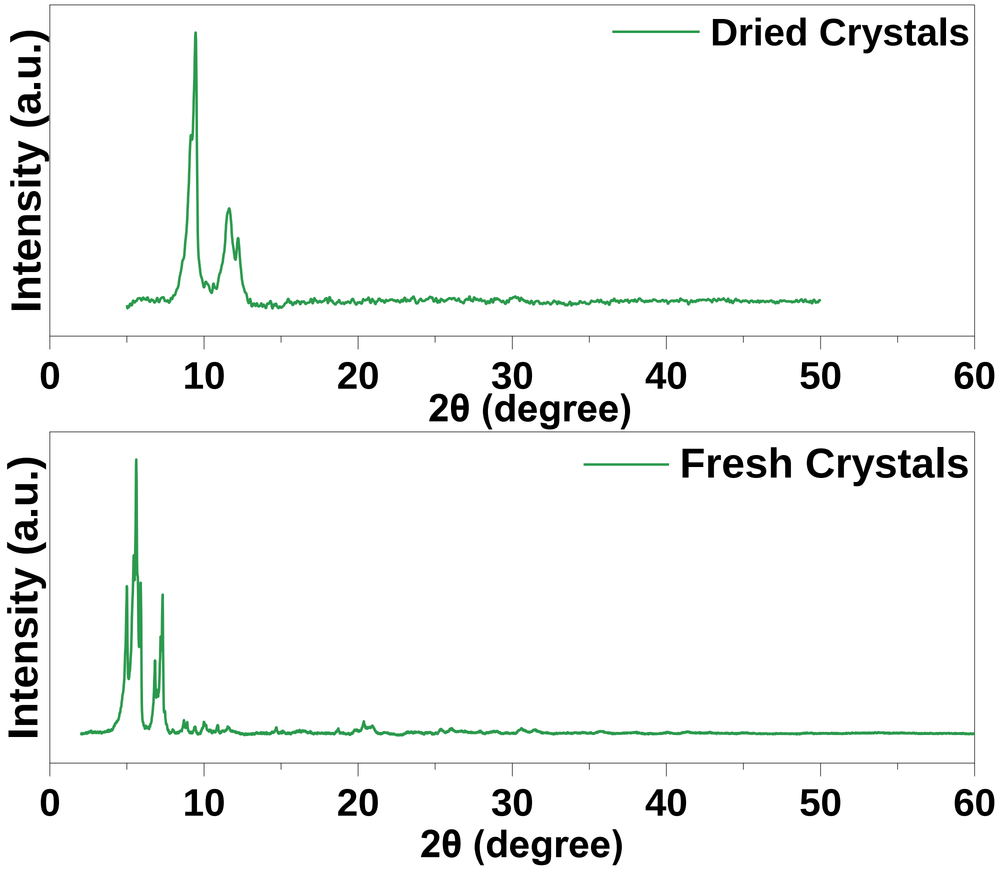

Figure 53. PXRD comparison of dried crystals vs fresh crystals of Eu_8Yb.

To confirm for the homogeneity of the bulk, SEM-EDS analysis was performed on both crystals and powder samples of Eu_8Yb complex at five different sites, giving an atomic composition of 88.6% of Eu and 11.4% of Yb, in good agreement with the 88.9% of Eu and 11.1% of Yb, introduced in the synthesis (**Figure 55**). The atomic composition in C and H was also verified by elemental analysis.

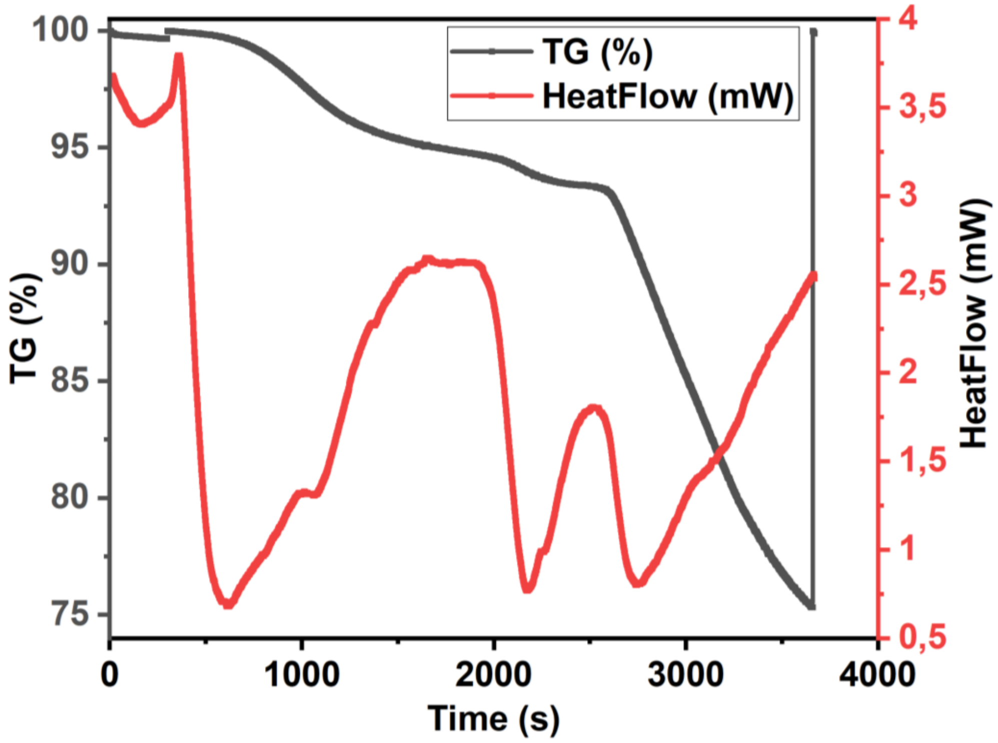

Figure 54. TG-DSC graph of Eu_8Yb

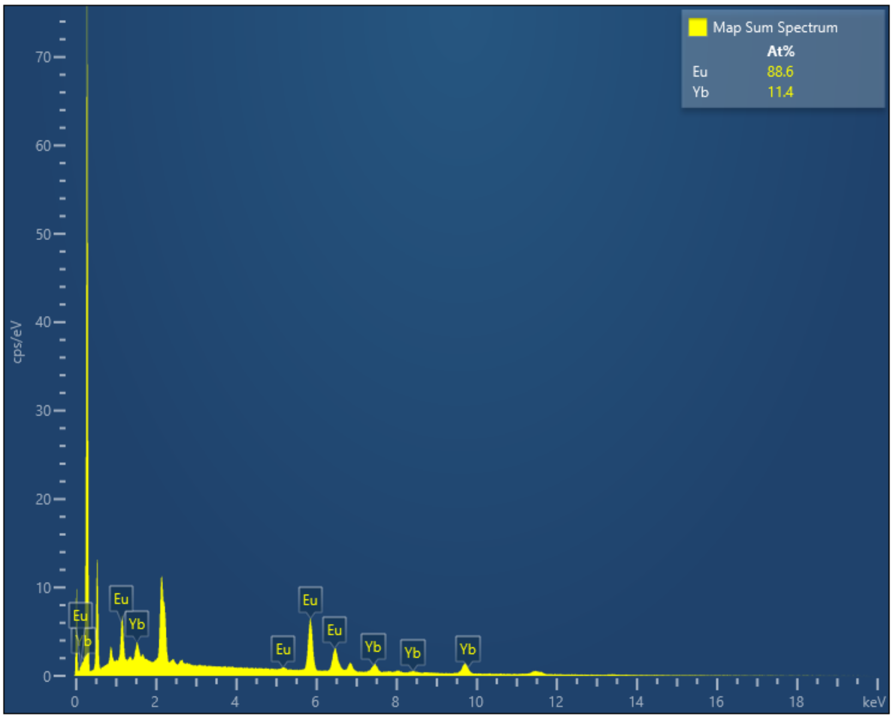

Figure 55. The EDS graph shows the relative atomic percentages of Eu and Yb. 8:1 ratio is the same as used in the synthesis.

Attenuated-Infrared Spectroscopy

The polycrystalline sample has been analyzed using the IR spectroscopy to support the claims of the solvent in the crystal lattice. The major peaks in the spectrum are at 3330m, 1593s, 1566s, 1506s, 1483m, 1448m, 1368s, 1306w, 1275m, 998w, 960m, 843m, 754m, 709m, 687m. the broad peak at 3330 cm^{-1}, the typical stretching of alcohol hydroxyl, also confirms the presence of ethanol and supporting the presence of the solvent molecules. (**Figure 56**)

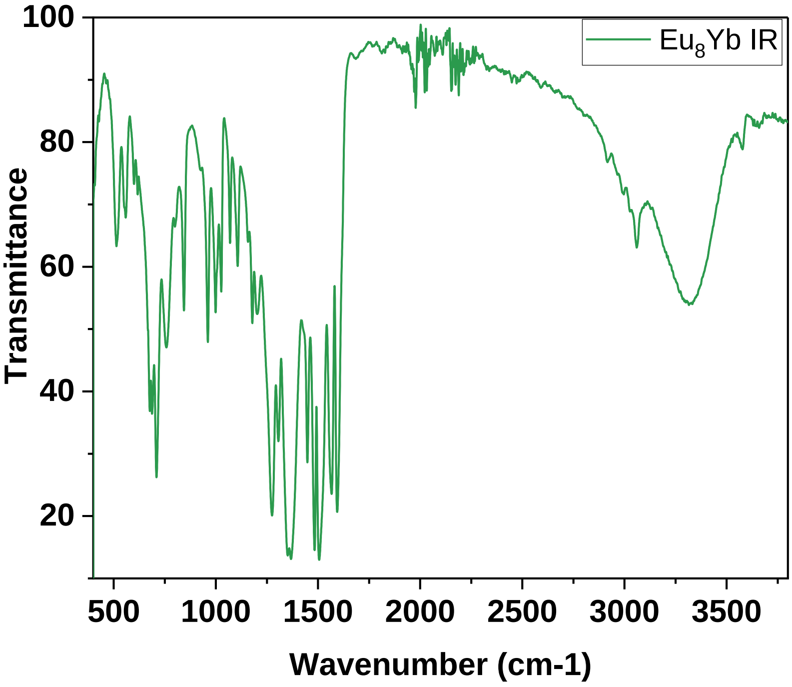

Figure 56. ATR-IR spectra of Eu$_8$Yb. (s = strong, m = medium, w = weak).

4.3. ESI-TOF Mass Analysis

The analysis of the composition of the cluster in solution was conducted through the utilization of electrospray ionization mass spectrometry (ESI-MS). The resulting spectrum obtained from this procedure (**Figure 57**) displayed primary peaks at m/z 4116, 4137, and 4158, which corresponded to the monocharged Eu_9, Eu_8Yb, and Eu_7Yb_2 complexes, respectively. Other peaks present on the higher m/z side, which had an intensity less than 10% of the most abundant Eu_9 peak, were due to complexes that had higher Yb replacing Eu in the metal core (such as Eu_6Yb_3 and Eu_5Yb_4). The full range ESI MS spectrum is presented in the **Figure 59**.

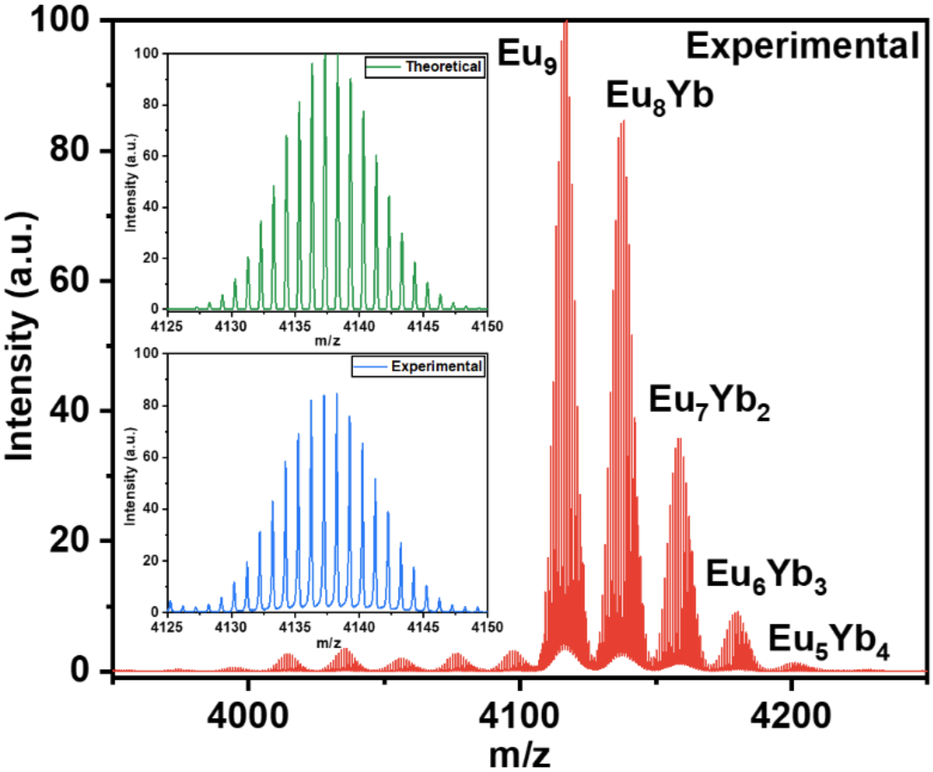

Figure 57. ESI mass spectrum in positive ion mode of the $[Eu_8Yb(BA)_{16}(OH)_{10}]^+$ complex sprayed from a methanol solution. Insets show theoretical (green) and experimental (blue) isotopic pattern of the molecular peak $[Eu_8Yb(BA)_{16}OH_{10}]^+$.

Calculation of the proportions of each polynuclear compound for a complex having n ions starting from a mixture of two different M ions (Yb and Eu)

Although our case is not a perfect example, we assume that all M ions in the M_9 complex are identical. We have defined x as the molar fraction of M^1, while y = (1-x) is the molar fraction of M^2. We assume that all M ions (M^1 or M^2) are chemically indistinguishable, which is a valid assumption for M=Ln ions.

This leads to identical stability constants regardless of the composition of the polynuclear complex. The formation of complexes can be expressed as n M → $[M_n]$, and more generally, i M^1 + (n-i) M^2 → $[M^1{}_i M^2{}_{(n-i)}]$.

The probability P_i of the $M^1{}_i M^2{}_{(n-i)}$ species at a molar fraction x of M^1 is given by:

$$\boldsymbol{P_i = \frac{n!}{i!(n-i)!} * x^i(1-x)^{n-i}} \qquad \textbf{(3)}$$

In the example of the formation of a nonanuclear Eu complex (n = 9), starting from a composition of 1 Yb ion (M^1) and 8 Eu ions (M^2), the molar fraction x of Yb will be x = 1/(1 +8) = 1/9. The probabilities of the different resulting heteropolynuclear complexes are as follows:

For $[Eu_9]$: $\boldsymbol{P_0 = \frac{9!}{0!(9-0)!} * \left(\frac{1}{9}\right)^0 \left(1-\frac{1}{9}\right)^9 = (\frac{8}{9})^9 = 0.346}$

For $[YbEu_8]$: $\boldsymbol{P_1 = \frac{9!}{1!(9-1)!} * \left(\frac{1}{9}\right)^1 \left(1-\frac{1}{9}\right)^8 = 9 * \left(\frac{1}{9}\right) (\frac{8}{9})^8 = 0.389}$

For $[Yb_2Eu_7]$: $\boldsymbol{P_2 = \frac{9!}{2!(9-2)!} * \left(\frac{1}{9}\right)^2 \left(1-\frac{1}{9}\right)^7 = 9 * 4 * \left(\frac{1}{9}\right)^2 \left(\frac{8}{9}\right)^7 = 0.195}$

For $[Yb_3Eu_6]$: $\boldsymbol{P_3 = \frac{9!}{3!(9-3)!} * \left(\frac{1}{9}\right)^3 \left(1-\frac{1}{9}\right)^6 = \frac{9*8*7}{3} * \left(\frac{1}{9}\right)^3 \left(\frac{8}{9}\right)^6 = 0.057}$

For $[Yb_4Eu_5]$: $\boldsymbol{P_4 = \frac{9!}{4!(9-4)!} * \left(\frac{1}{9}\right)^4 \left(1-\frac{1}{9}\right)^5 = \frac{9*8*7*6}{2*3*4} * \left(\frac{1}{9}\right)^4 \left(\frac{8}{9}\right)^5 = 0.011}$

Complexes with higher amounts of Yb have a probability lower than 1%. This example shows that for a mixture of one Yb and eight Eu ions, complexes containing at least two Yb atoms represent more than 26% (19.5% + 5.7% + 1.1% = 26.3%) of all possible nonanuclear complexes formed, which explains the bright UC observed even at this mixing ratio of 1/9 Yb : 8/9 Eu.

The analysis of relative integrals of isotopic patterns was conducted to determine the proportion of two species, Ln^1 and Ln^2, at different mole fractions of Ln^1. The relative integrals of the isotopic patterns were used to calculate the proportion (**Figure 58**) ($\boldsymbol{P_i}$) of the Ln^1 and Ln^2 species at a mole fraction $\boldsymbol{x}$ of Ln^1. The Experimental values are ($P_{0,\text{exp}} = 0.41$ for $[Eu_9]$; $P_{1,\text{exp}} = 0.37$ for $[YbEu_8]$; $P_{2,\text{exp}} = 0.17$ for $[Yb_2Eu_7]$; $P_{3,\text{exp}} = 0.05$ for $[Yb_3Eu_6]$ and

$P_{4,\mathrm{exp}} = 0.008$), respectively. These values are in good agreement with the perfect statistical distribution obtained by Equation (3).

The analysis also revealed that complexes with a higher molar fraction of Yb have a probability lower than 1%. Furthermore, for a Yb:Eu stoichiometric ratio of 1:8, the complexes containing at least two Yb atoms account for more than 22% (17% + 5% + 0.08% = 22.08%) of all possible nonanuclear complexes formed. These findings provide valuable insights into the distribution of Ln^1 and Ln^2 species at different mole fractions of Ln^1 and help to better understand the stoichiometric ratios in related chemical reactions.

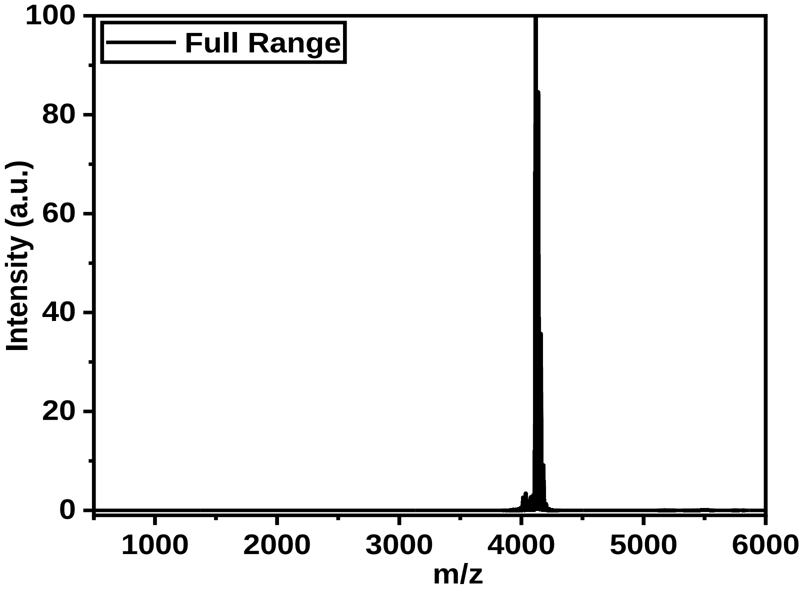

Figure 59. ESI-TOF Full Range Mass spectra of Eu_8Yb complex in CH_3OH.

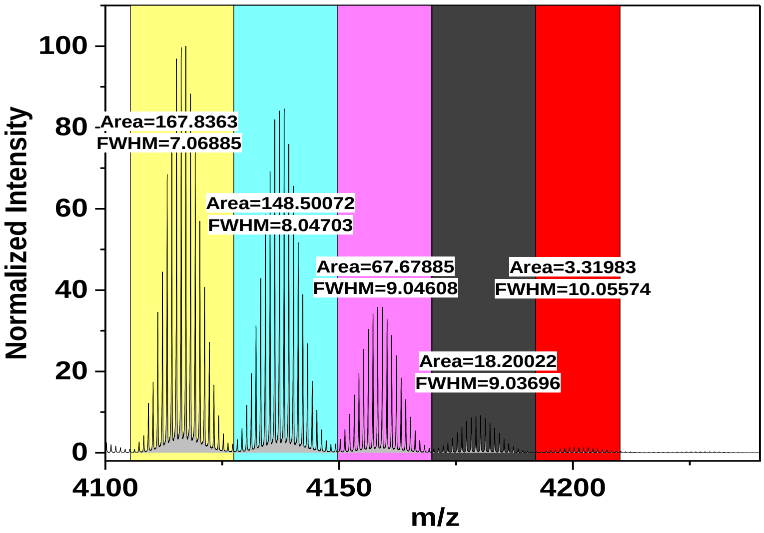

Figure 58 ESI-TOF Mass spectra showing the abundance ratios after integrating the peak intensities and averaging out each peak.

4.4. Photophysical Studies

UV-Vis-NIR Absorption & Emission

The photophysical properties of the $[Eu_8Yb(BA)_{16}(OH)_{10}]Cl$ cluster were examined in CD_3OD solutions at room temperature. The UV-VIS-NIR absorption spectrum (shown in **Figure 60**) revealed a broad band in the UV region with a peak at 306 nm ($\varepsilon = 28.4 \times 10^4$ $M^{-1}cm^{-1}$), which is attributed to transitions centered on the BA ligands. Additionally, there was a broad absorption band at 976 nm ($\varepsilon = 12.95$ $M^{-1}cm^{-1}$ in CD_3OD), which results from the $^2F_{5/2} \leftarrow {}^2F_{7/2}$ transition of Yb^{III}. Upon excitation into the BA absorption band (326 nm), the cluster displayed two sets of emission bands (**Figure 62**). Those in the visible region correspond to the $^5D_0 \rightarrow {}^7F_J$ ($J = 0$ to 4) transitions of Eu ($\Phi_{Eu} = 0.13\%$ in CD_3OD), and the broad emission band peaking at 974 nm corresponds to the $^2F_{5/2} \rightarrow {}^2F_{7/2}$ transition of Yb ($\Phi_{Yb} = 0.26\%$ in CD_3OD). The corresponding luminescence lifetime of Yb in CD_3OD was 13.9 ± 0.1 µs at 974 nm. Lifetime and quantum yield values are similar to those reported for the Tb_1Yb_8 cluster with acac antennae.[46] According to the formalism of Werts and co-workers,[146] the radiative lifetime was estimated from the integral of the Yb absorption spectrum (**Figure 61**) to amount to 810 μs,

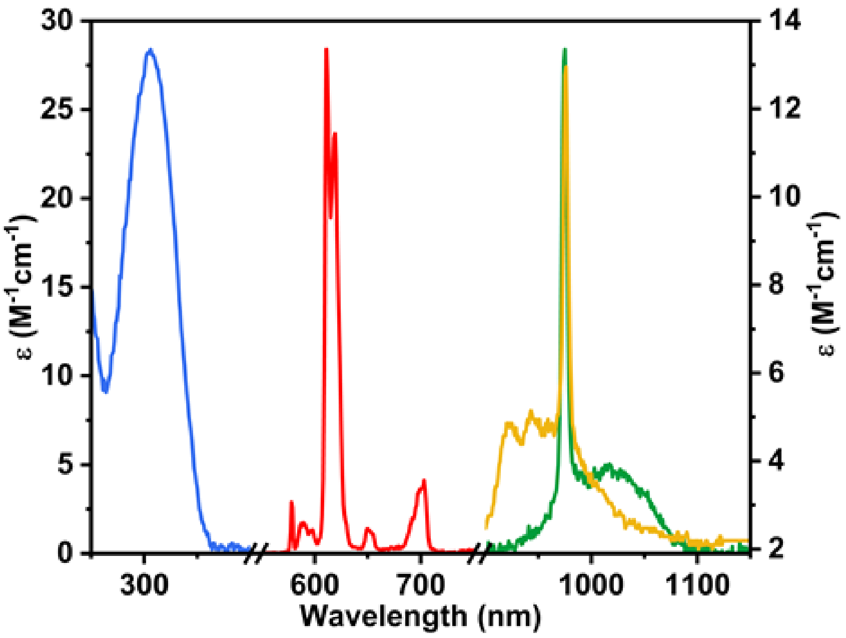

Figure 60. UV-Vis and NIR absorption spectra (blue (45 µM) and yellow (1 mM), respectively) and normalized emission spectra (λ_{exc} = 326 nm) in the visible (red: Eu, 45 µM, 399 nm Filter) and NIR (green: Yb, 45 µM, 800 nm Filter) domains for the Eu_8Yb cluster in CD_3OH.

which is in line with literature data on other Yb clusters.[46] With these values, the intrinsic quantum yield of Yb was calculated to be 1.7%, and the sensitization efficiency amounted to 16%, a result similar to the previously obtained value of 22% for unsubstituted acac-d^7 ligands.

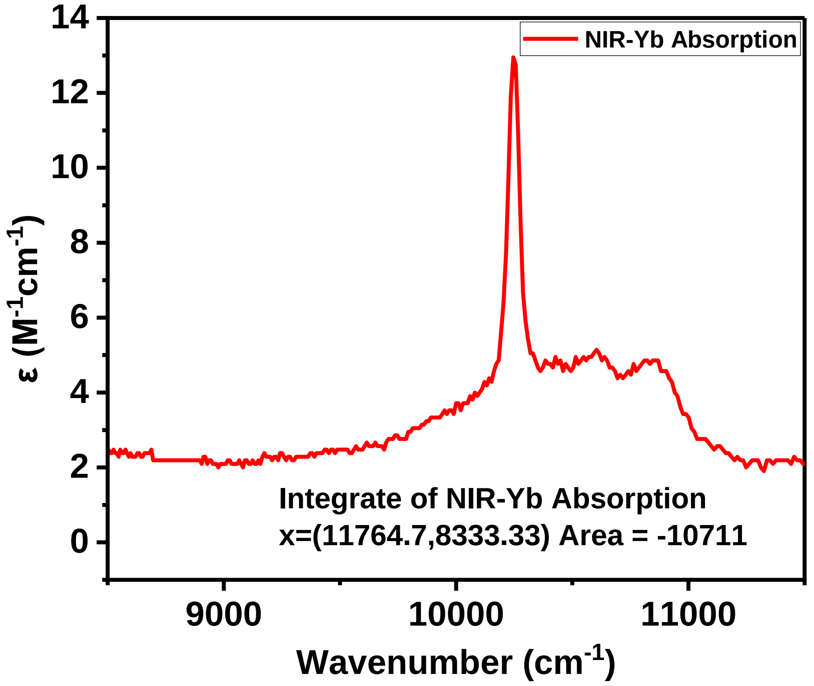

Figure 61. Integral value on NIR-Yb absorption spectra.

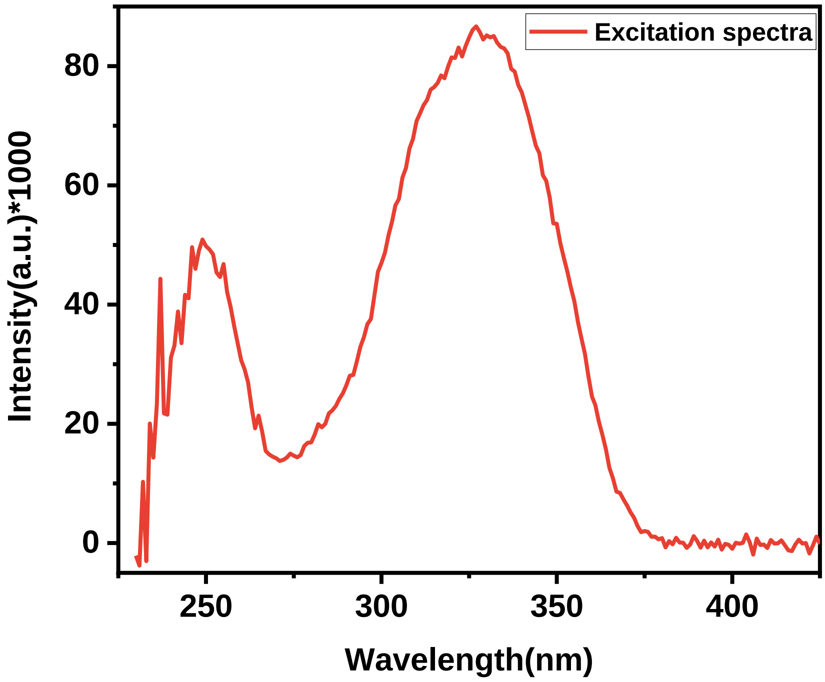

Figure 62. Excitation spectra of Eu_8Yb, λ_{max} = 326 nm.

The experimental measurements of time-dependent luminescence decay profiles were conducted to study the luminescence characteristics of Eu^{3+} emission, with an excitation wavelength of 326 nm. The analysis was based on fitting the obtained data to bi-exponential curves, which led to the identification of two corresponding lifetimes, τ_1 and τ_2. The first lifetime, τ_1, was determined to be 0.196 ± 0.001 ms (B_1 = 85 %) at 578 nm (**Figure 63**) and 0.189 ± 0.001 ms (B_1 = 84 %) at 612 nm (**Figure 64**), respectively. This lifetime mainly reflects the presence of the Eu^{3+} ions in the peripheral site, where the direct photosensitization from the BA antennae contributes significantly. The second lifetime, τ_2, was found to be 1.265 ± 0.002 ms (B_2 = 15 %) at 578 nm and 1.256 ± 0.002 ms (B_2 = 16 %) at 612 nm, respectively. This lifetime indicates the presence of the Eu^{3+} ions in the central site, which is present in a smaller proportion but exhibits a longer lifetime due to enhanced protection against non-radiative quenching by solvent molecules.[68, 134, 146]

The analysis of the luminescence decay profiles showed that the Eu^{3+} emission quantum yield was measured to be $\Phi_{Eu} = 0.13\%$ in CD_3OD ($\lambda_{exc} = 326$ nm). Additionally, the radiative lifetime of Eu was estimated using the formalism of Werts et. al. and was found to be 1.32 ms, which is in relatively good agreement with the value found for Yb, considering the uncertainties inherent in the method. It is important to note that the values obtained for the Eu^{III} emission

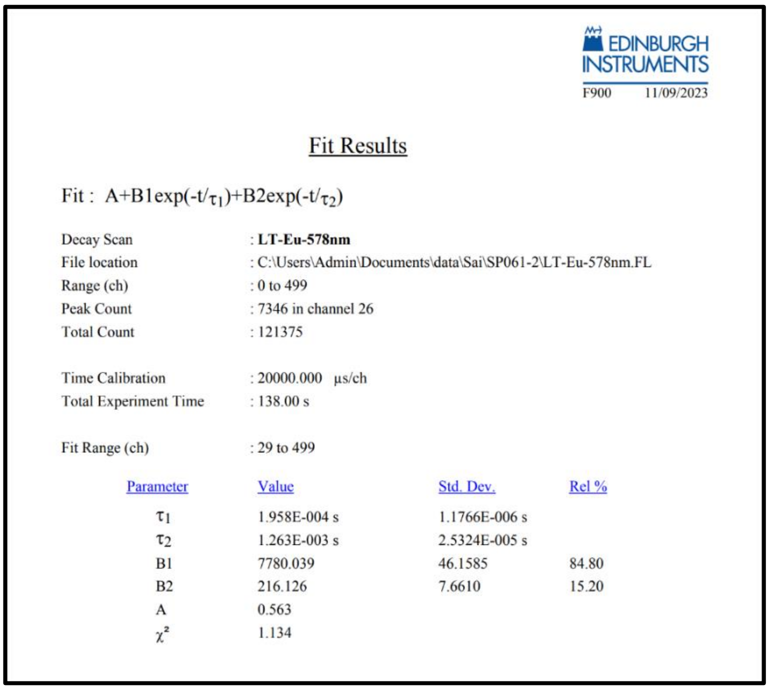

EDINBURGH INSTRUMENTS
F900 11/09/2023

Fit Results

Fit : $A+B1\exp(-t/\tau_1)+B2\exp(-t/\tau_2)$

Decay Scan : **LT-Eu-578nm**
File location : C:\Users\Admin\Documents\data\Sai\SP061-2\LT-Eu-578nm.FL
Range (ch) : 0 to 499
Peak Count : 7346 in channel 26
Total Count : 121375

Time Calibration : 20000.000 µs/ch
Total Experiment Time : 138.00 s

Fit Range (ch) : 29 to 499

Parameter	Value	Std. Dev.	Rel %
τ_1	1.958E-004 s	1.1766E-006 s	
τ_2	1.263E-003 s	2.5324E-005 s	
B1	7780.039	46.1585	84.80
B2	216.126	7.6610	15.20
A	0.563		
χ^2	1.134		

Figure 63. Lifetime values of 578 nm peak of Eu_8Yb.

characteristics are significantly smaller than common values observed for Eu complexes with β-diketonate ligands. The obtained results suggest the presence of two distinct chemical

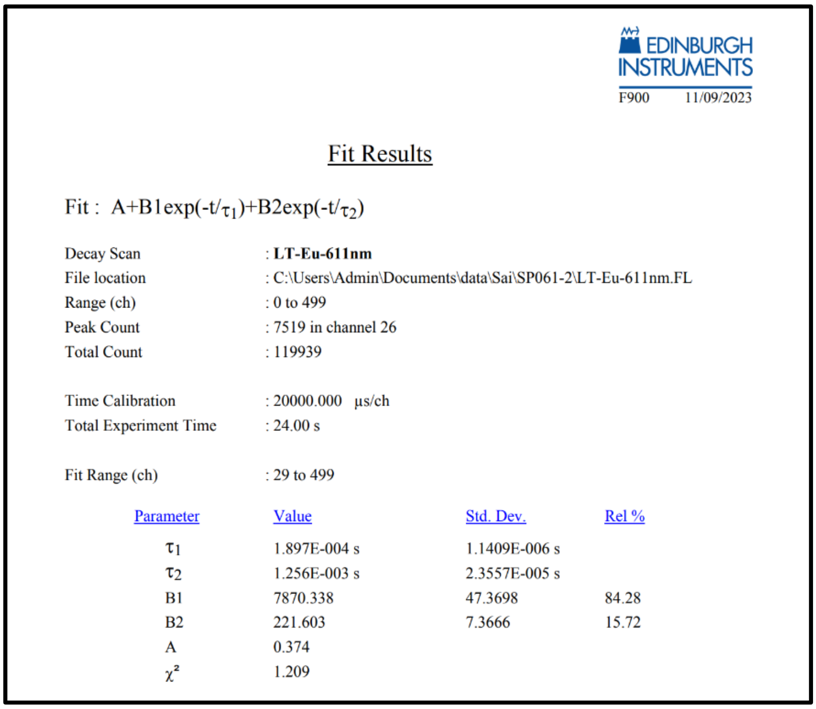

```
                                                          EDINBURGH
                                                          INSTRUMENTS
                                                          F900      11/09/2023

                              Fit Results

  Fit :  A+B1exp(-t/τ1)+B2exp(-t/τ2)

  Decay Scan                 : LT-Eu-611nm
  File location              : C:\Users\Admin\Documents\data\Sai\SP061-2\LT-Eu-611nm.FL
  Range (ch)                 : 0 to 499
  Peak Count                 : 7519 in channel 26
  Total Count                : 119939

  Time Calibration           : 20000.000   µs/ch
  Total Experiment Time      : 24.00 s

  Fit Range (ch)             : 29 to 499

          Parameter          Value                Std. Dev.          Rel %

              τ1             1.897E-004 s         1.1409E-006 s
              τ2             1.256E-003 s         2.3557E-005 s
              B1             7870.338             47.3698            84.28
              B2             221.603              7.3666             15.72
              A              0.374
              χ²             1.209
```

Figure 64. lifetime values of 612 nm peak of Eu₈Yb.

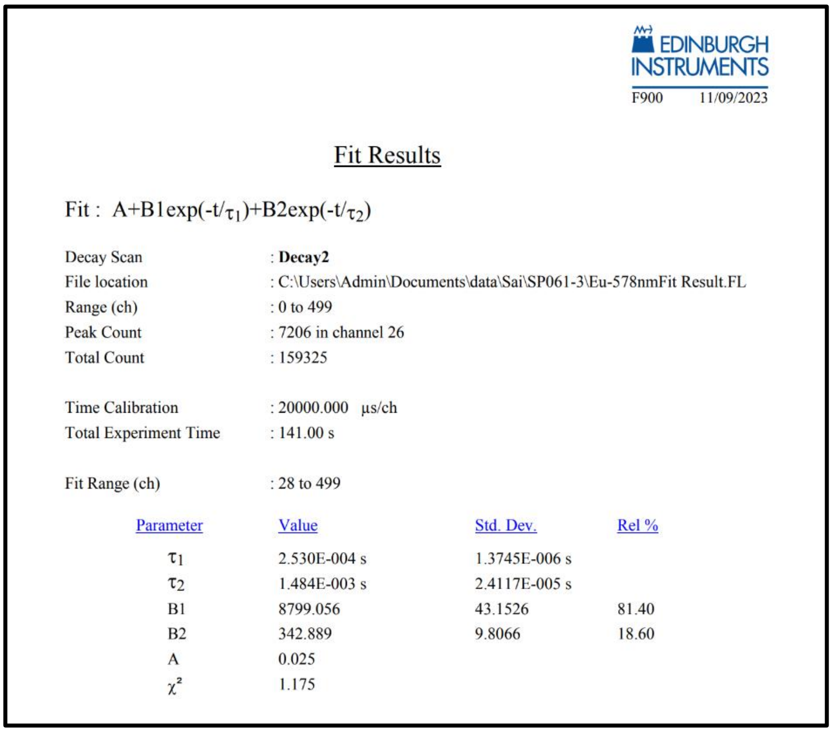

```
                                                          EDINBURGH
                                                          INSTRUMENTS
                                                          F900      11/09/2023

                              Fit Results

  Fit :  A+B1exp(-t/τ1)+B2exp(-t/τ2)

  Decay Scan                 : Decay2
  File location              : C:\Users\Admin\Documents\data\Sai\SP061-3\Eu-578nmFit Result.FL
  Range (ch)                 : 0 to 499
  Peak Count                 : 7206 in channel 26
  Total Count                : 159325

  Time Calibration           : 20000.000   µs/ch
  Total Experiment Time      : 141.00 s

  Fit Range (ch)             : 28 to 499

          Parameter          Value                Std. Dev.          Rel %

              τ1             2.530E-004 s         1.3745E-006 s
              τ2             1.484E-003 s         2.4117E-005 s
              B1             8799.056             43.1526            81.40
              B2             342.889              9.8066             18.60
              A              0.025
              χ²             1.175
```

Figure 65. lifetime values of 578 nm peak of Eu₉.

environments for the Eu^{III} ions, which could have potential applications in luminescence-based sensing and imaging.

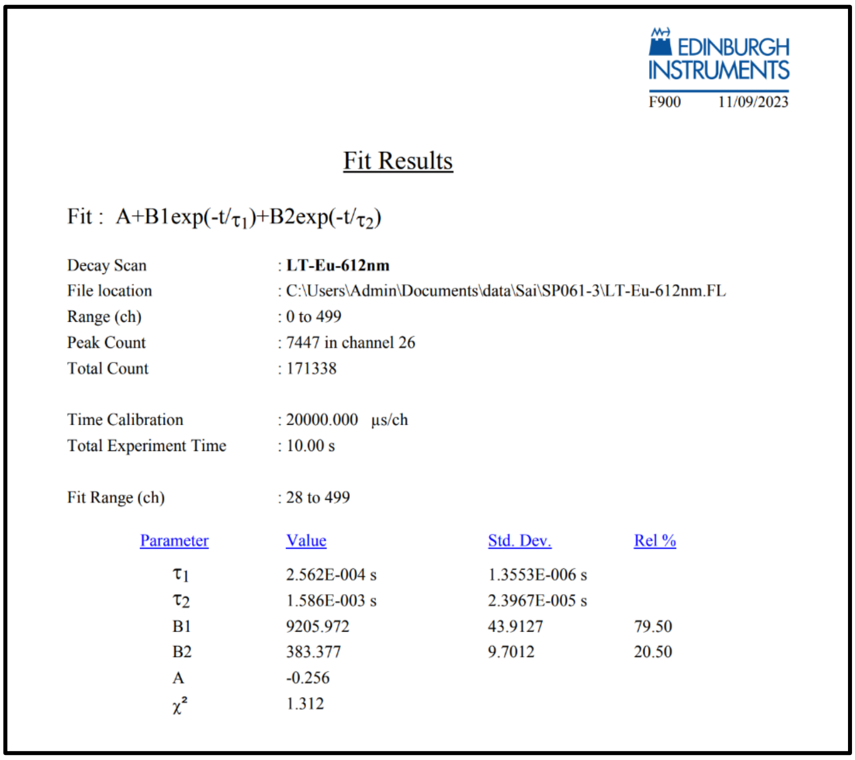

EDINBURGH INSTRUMENTS
F900 11/09/2023

Fit Results

Fit : $A+B1\exp(-t/\tau_1)+B2\exp(-t/\tau_2)$

Decay Scan : **LT-Eu-612nm**
File location : C:\Users\Admin\Documents\data\Sai\SP061-3\LT-Eu-612nm.FL
Range (ch) : 0 to 499
Peak Count : 7447 in channel 26
Total Count : 171338

Time Calibration : 20000.000 µs/ch
Total Experiment Time : 10.00 s

Fit Range (ch) : 28 to 499

Parameter	Value	Std. Dev.	Rel %
τ_1	2.562E-004 s	1.3553E-006 s	
τ_2	1.586E-003 s	2.3967E-005 s	
B1	9205.972	43.9127	79.50
B2	383.377	9.7012	20.50
A	-0.256		
χ^2	1.312		

Figure 67. lifetime values of 612 nm peak of Eu$_9$.

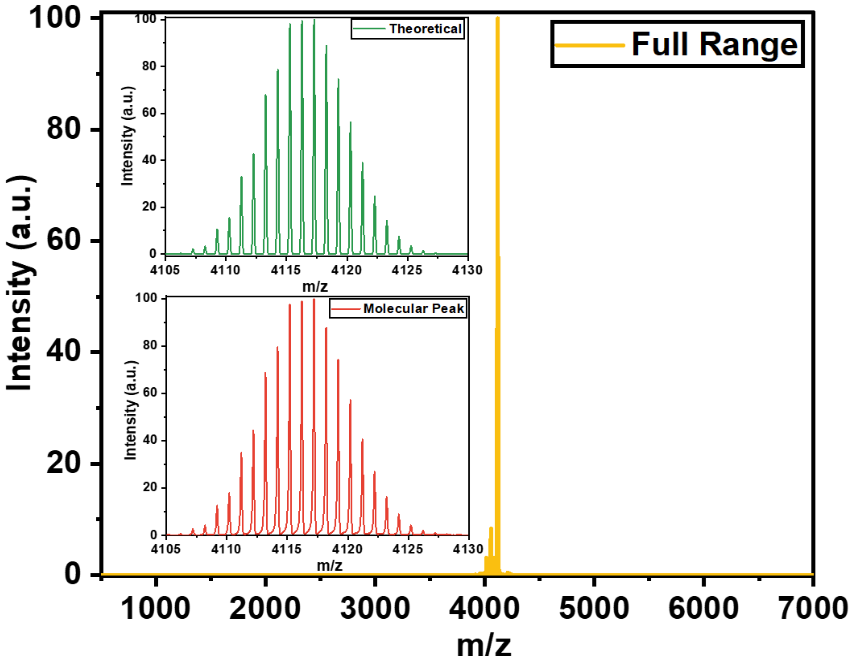

Figure 66. ESI-TOF Mass spectra of Eu$_9$ complex in CH_3OH. $[Eu_9(BA)_{16}OH_{10}]^+$ peak at 4117.2 m/z. Inset showing Experimental and simulated Molecular peak.

The relatively low quantum yield of Eu suggests either inefficient sensitization by the BA ligands or the occurrence of non-radiative quenching processes due to vibrations, concentration quenching,[63] or energy transfer to the Yb $^2F_{5/2}$ excited state. Quantification of the Eu → Yb energy transfer has been achieved by measuring the Eu luminescence lifetimes of the Eu_9 cluster. The corresponding values are τ_1 = 0.253 ± 0.001 ms (B_1 = 81.40%), τ_2 = 1.484 ± 0.002 ms (B_2 = 18.6%) for 578 nm emission peak (**Figure 65**) and τ_1 = 0.256 ± 0.001 ms (B_1 = 79.5%), τ_2 =1.586 ± 0.002 ms (B_2 = 20.5%) at 612 nm (**Figure 67**). A decrease of approximately 24% in the τ_1 lifetime of Yb, as well as a 15% shortening of τ_2, were observed following the incorporation of Eu into the Yb_9 structure. This decrease of the average lifetime amounts to 18% and is ascribed to the energy transfer from Eu to Yb within Eu_8Yb. Consequently, the efficiency of this energy transfer was estimated to be 18%. In addition, a radiative lifetime of 1.65 ms was determined for this cluster, consistent with other values measured within this study.

Eu_8Yb: Downshifting Measurements

Further findings reveal that in the same cluster, a phenomenon known as Stokes downshifted photo-luminescence of Ytterbium (Yb) in the near-infrared (NIR) was observed, when excited in the visible absorption band of Europium (Eu) at 578 nm ($^5D_0 \leftarrow {}^7F_0$) in CD_3OD. This is illustrated in **Figure 68**. The characteristic $^2F_{5/2} \rightarrow {}^2F_{7/2}$ Yb emission is clearly visible, pointing

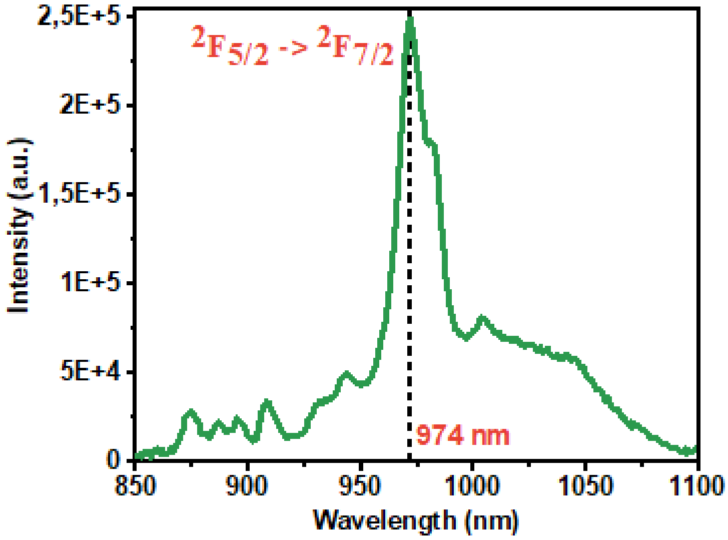

Figure 68. Downshifted PL emission of the Eu_8Yb complex ([c] = 0.5 mM, CD_3OD, λ_{exc} = 578 nm).

towards the occurrence of Yb sensitization as a result of the transfer of energy from the $^5D_0$ energy level of Eu to the $^2F_{5/2}$ excited state of Yb. With these findings we then focused on the reverse mechanism, which is the cooperative sensitization of Eu by Yb, based on this intermetallic communication.

Eu_8Yb: Upconversion Experiments

Experimental investigations were conducted at room temperature in CD_3OD solutions to carry out upconversion experiments, similar to the downshifting measurements. During the experiment, the Eu_8Yb cluster was subjected to excitation in the NIR $^2F_{5/2} \leftarrow {}^2F_{7/2}$ absorption band of Yb at 980 nm. The spectrum of the cluster exhibited a remarkable feature, which was a strong emission in the visible region (cooperative sensitization). This emission had the typical spectral signature of the Eu emission (**Figure 69**) with maxima at 612 nm and the five $^5D_0 \rightarrow {}^7F_J$ ($J = 0 - 4$) transitions. The observation was depicted in **Figure 70**.

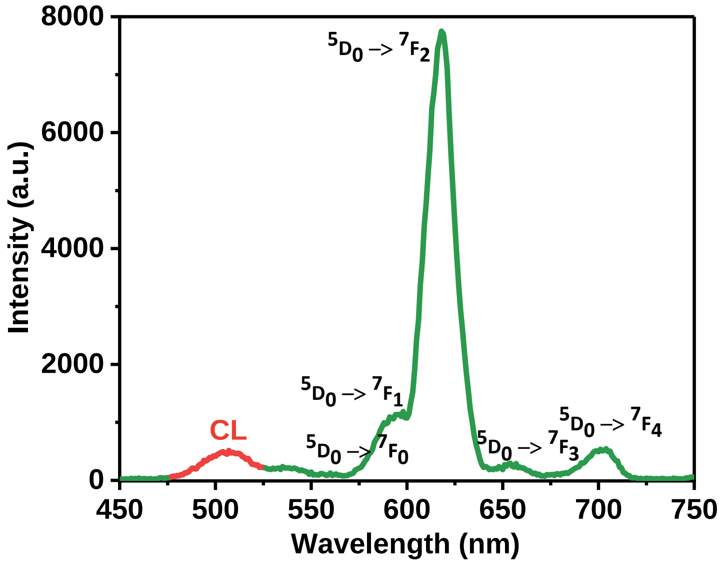

Figure 69. UC emission of the Eu_8Yb complex ([c] = 45 µM, CD_3OD, λ_{exc} = 980 nm, P = 2.86 W cm^{-2}).

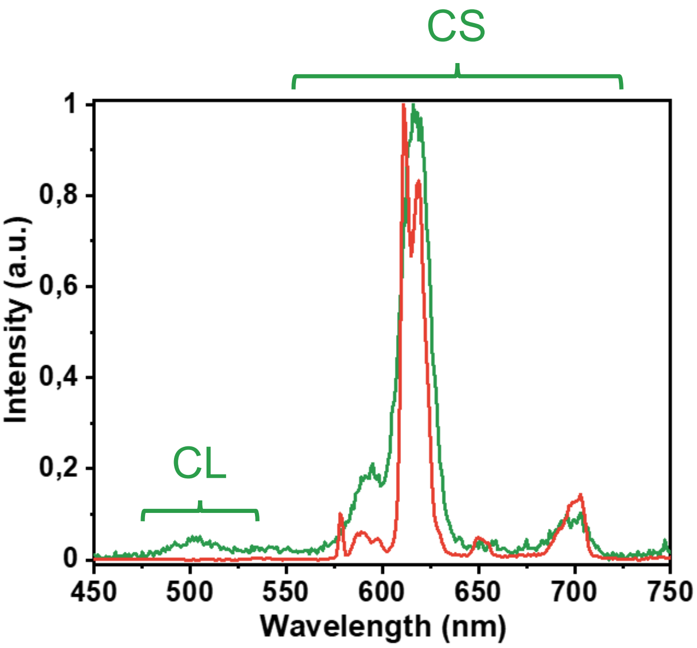

Figure 70. Emission (Red, [c] = 0.5 mM, CD_3OD, λ_{exc} = 326 nm, slits 2/2) *vs* UC spectra (Green, [c] = 45 µM, CD_3OD, λ_{exc} = 980 nm, *P* = 2.86 W cm^{-2}, slit 20) of Eu_8Yb complex. UC shows both CL from Yb and CS from Eu metal centers, respectively.

Furthermore, a minor peak at 505 nm was also present, which was assigned to the cooperative luminescence between two Yb centers, as previously observed in homonuclear Yb_9 clusters.[42, 46] This was demonstrated in **Figure 71**. Upon close observation, a weak and broad emission

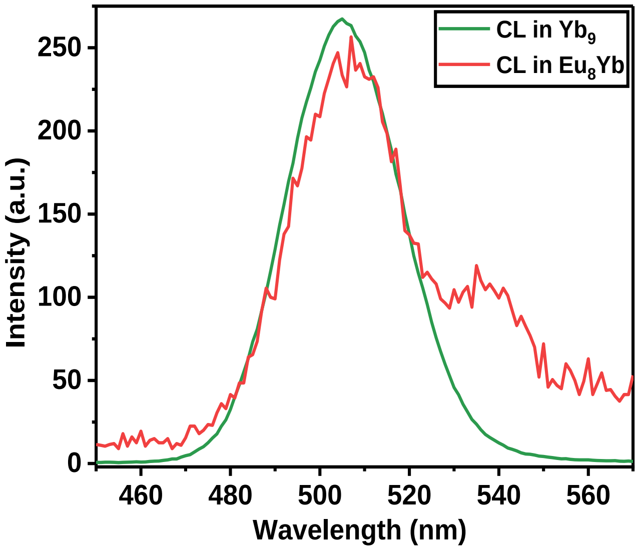

Figure 71. Cooperative luminescence (CL) emission of the Yb_9 complex (Green, [c] = 2.04 mM, CD_3OD, λ_{exc} = 980 nm, P = 10.8 W cm^{-2}) *vs* CL emission of the Eu_8Yb complex (Red, [c] = 45 µM, CD_3OD, λ_{exc} = 980 nm, P = 10.8 W cm^{-2}), normalized according to the concentration of Yb^{3+} in the sample.

band at 535-540 nm was also detected, which was attributed to the contribution of the $^5D_1$ → $^7F_0$ emission. This emission is often observed in Eu β-diketonate complexes. [147] The observation of the weak and broad emission band was depicted in **Figure 71**, red curve. This is a strong argument to propose that the cooperative sensitization occurs from the doubly excited state of Yb to the $^5D_1$ level of Eu, followed by the population of the $^5D_0$ state. In order to gain deeper insights into the impact of Yb doping ratios on CL efficiency, the CL intensity from Eu_8Yb and Yb_9 was compared and analyzed. This comparison was done by measuring the weak signal from Eu_8Yb in comparison to Yb_9. However, it should be noted that this difference could mostly be ascribed to the variations in the Yb^{3+} concentrations of the two samples, which were 9 µM and 18.4 mM, respectively.

It is worth noting that according to theoretical calculations, CL can occur in clusters with a Yb:Eu 1:8 composition due to the statistical presence of clusters containing two or more Yb centers (22%, as explained above). Therefore, considering the smaller concentration of the Eu_8Yb sample in comparison to the Yb_9 cluster and the fact that only 22% of molecules are capable of CL, it can be suggested that CL might be more efficient in Eu_8Yb than in Yb_9. This could be explained by the reduction of the non-radiative Yb-Yb interactions. Taking into account the smaller concentration of the Eu_8Yb sample in comparison to the Yb_9 cluster and

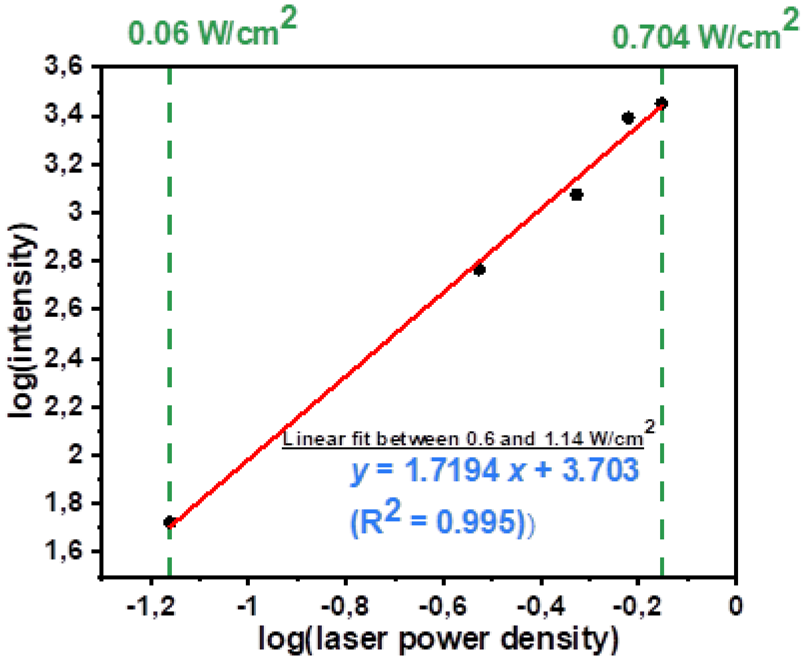

Figure 72. UC intensity as a function of the incident pump power density in a log/log scale.

the fact that only 22% of molecules are capable of CL, **Figure 71** suggests that CL might be more efficient in Eu_8Yb than in Yb_9, which could be explained by the reduction of concentration quenching.

To gain further insight into the upconversion luminescence mechanisms, a comprehensive analysis of the overall upconversion luminescent intensity (CS + CL) was performed in relation to the incident pump power density. The results revealed that the logarithmic representation of the data presented a quasi-linear profile with a slope of two, which attested to the quadratic dependence of a two photon UC process. This finding is illustrated in **Figure 72**.

Moreover, the slopes of the Log/Log plots were calculated to be 1.72 for CS at 612 nm (**Figure 72**) and 1.61 for CL at 505 nm, respectively, as shown in **Figure 73**.[79, 148] These values indicate that the upconversion luminescence intensity of the CS and CL emissions increases with the incident pump power density in a nonlinear fashion, providing further support for the two photon UC process. The results of this study offer valuable insights into the underlying mechanisms governing the upconversion luminescence phenomenon.

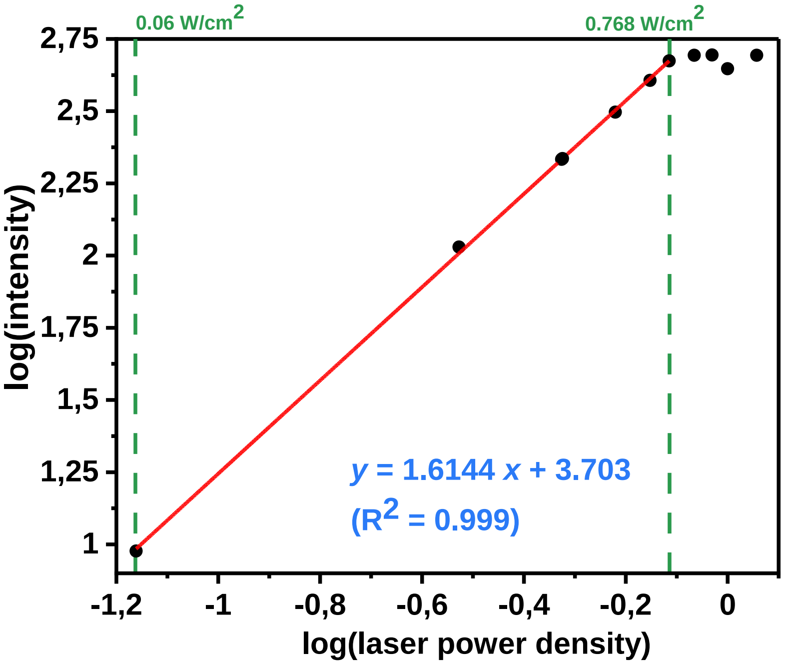

Figure 73. log-log plot of CL peak at 505 nm in the Eu_8Yb in the range between 450-550 nm.

UC Mechanism in Eu_8Yb

The proposed mechanism in a prototype complex (**Figure 74**), such as $Eu_{9-x}Yb_x$ (where x > 1), entails a major contribution of CS and a minor contribution of CL of Yb. As previously described, CS involves a first absorption of a photon by one Yb atom leading to a $[Eu_{9-x}Yb^*Yb_{x-1}]$ excited species, followed by the absorption of a second photon by a neighboring Yb ion, hence forming the $[Yb_2^{**}Eu_{9-x}Yb_{x-2}]$ intermediate which transfers its energy to $^5D_1$ and $^5D_0$ levels of Eu creating the $[Eu_{8-x}Eu^*Yb_x]$ excited states, which then decays to the ground state by emission of visible light. As for CL, two photon absorption by two Yb ions in the same cluster results in a doubly Yb_2^{**} excited state, which decays in the visible, showing a transition at 505 nm. As expected, a $[Eu_9(BA)_{16}(OH)_{10}]Cl$ cluster without any Yb did not show any upconversion luminescence in the visible region when irradiated at 980 nm.

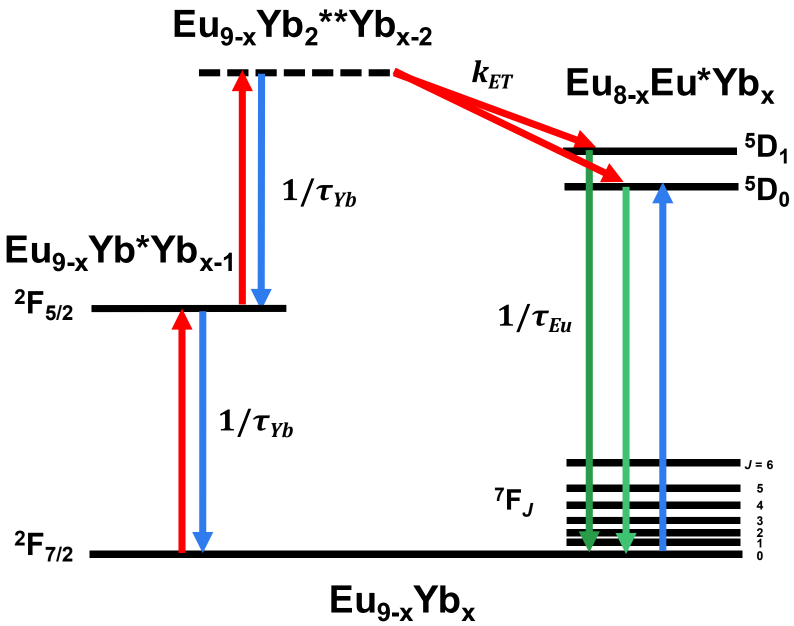

Figure 74. Schematic representation of proposed cooperative photosensitization process UC mechanism in Eu_9Yb_{9-x}.

Using established procedures,[41] we have calculated the UC quantum yield (Φ_{UC}) of the $YbEu_8$ cluster in CD_3OD solution at room temperature. By exciting at 980 nm (1.13 W cm^{-2}), we obtained a quantum yield value of 4.84×10^{-8}. This value is comparable to previously reported data for UC quantum yields, indicating the accuracy of our measurements. Moreover, it is noteworthy that the UC quantum yield value for $YbEu_8$ is higher than that for the best UC Er complexes (ranging from 1.95×10^{-9} to 8×10^{-9} at P= 21 W cm^{-2})[79] and the first heteropolynuclear Yb/Tb UC complexes (1.4 x 10^{-8} at P= 10.3 W cm^{-2}). However, it is still lower than the quantum yields recently reported for Yb:Tb clusters.[42, 46] This difference could be due to the increased propensity of Eu to be quenched by non-radiative deactivations.

Furthermore, it is interesting to note that the lower spectral overlap of the CL emission of Yb** with the $^5D_1$ absorption band of Eu around 535 nm, as compared to that of the $^5D_4$ absorption band of Tb at 485 nm, may also contribute to the reduced UC efficiency.

Our findings highlight the importance of supramolecular clusters in achieving efficient upconversion in solution. The scaffold provided by supramolecular clusters allows for the incorporation of a unique lanthanide (Yb for CL) and/or donor/acceptor pairs (for CS) with appropriate Ln-Ln distances and a tunable statistical distribution. Importantly, our study provides evidence of the potential to achieve cooperative sensitization (CS) upconversion in a molecular cluster containing Eu and Yb. This is the first time such evidence has been presented. This discovery has opened up new avenues for research into the development of more efficient upconversion materials.

4.5. UC Systems with Other Lanthanides

After the findings with Eu/Yb system we looked further down in the lanthanide series and stumbled upon Er and Ho to look out for similar cooperative sensitization. So, we prepared a few combinations of Er and Ho with Yb respectively.

Yb_6Ho_3:

With Yb_6Ho_3, we increased the composition of Yb as it is one of the limiting factors in Eu_8Yb UC efficiency with only 22% contribution of Yb_2 units. However, as one can see from (**Figure 75**) the looming $^5F_{5/2}$ -> $^5F_{7/2}$ shields the expected weak Ho peaks ($^5F_3$ -> $^5I_8$, $^5F_4$ -> $^5I_8$) in the region between 450-550 nm. On the other hand, supporting the claim of CS from Yb to Ho we see the signature emission peaks of Ho in the region between 650-900 nm. $^5F_5$ -> $^5I_8$ at 650 nm, $^5I_4$ -> $^5I_8$ at 750 nm, and a broad peak $^5I_5$ -> $^5I_8$ expanding from 825 all the way to 900 and above nm. After analyzing the weak peaks, we conclude the CS behavior. However, the weak intensities mean an inefficient transfer and therefore did not proceed any further in investigating the system.

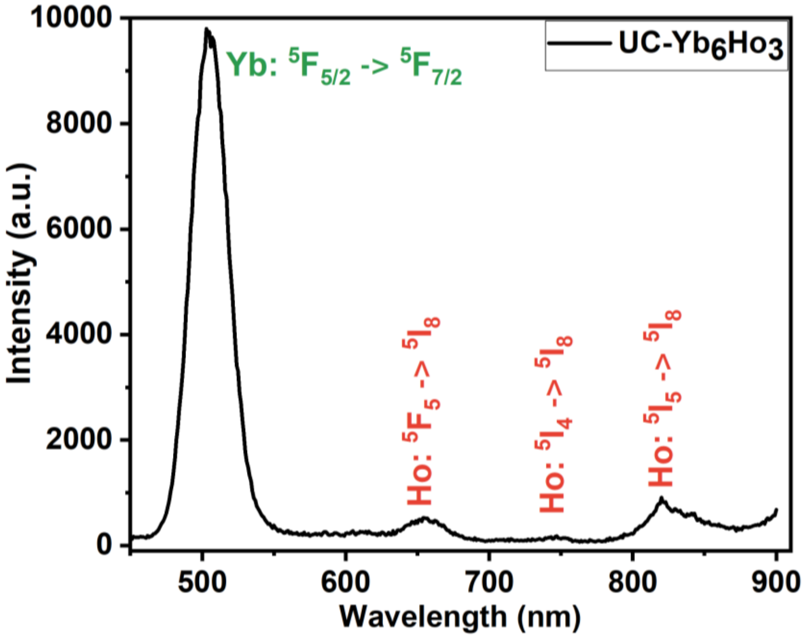

Figure 75. Yb_6Ho_3 UC spectrum showcasing CL and CS in Yb and Ho respectively (λ_{exc} = 978 nm) .

Yb_5Er_4 and Yb_6Er_3:

A typical Er^{3+} emission spectrum, when excited at 980nm, exhibits two green emissions around 525 nm and 548 nm assigned to the radiative transition of $^2H_{11/2} \rightarrow {}^4I_{15/2}$ and $^4S_{3/2} \rightarrow {}^4I_{15/2}$,

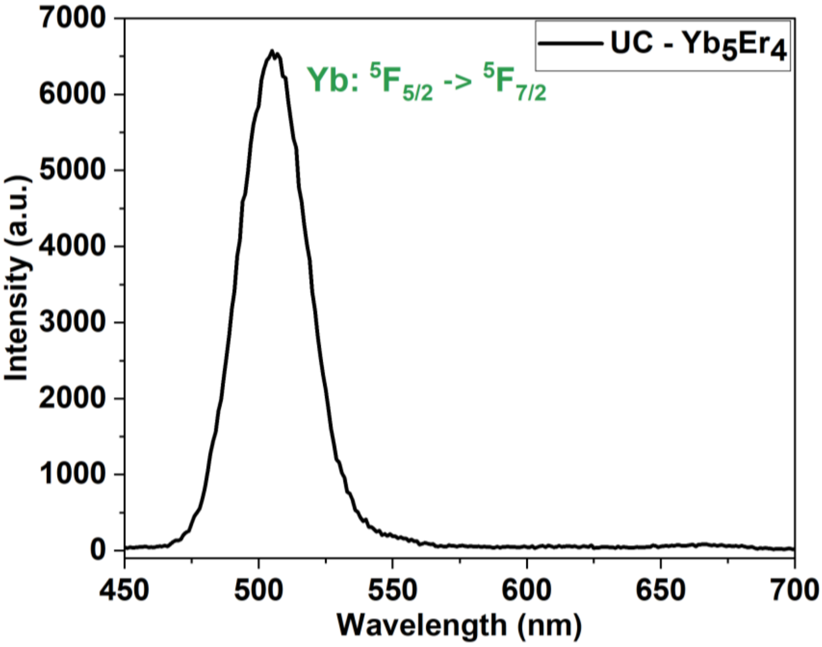

Figure 76. Yb_6Er_4 UC spectrum showcasing CL in Yb (λ_{exc} = 978 nm).

respectively and a red emission band from 638 to 688 nm attributed to the $^4F_{9/2} \rightarrow {}^4I_{15/2}$ transition of Er^{3+} ions. However, in the spectra (**Figures 76,77**) no such peaks are to be noticeable ruling out any CS from Yb^{3+} to Er^{3+}. On a positive note we do observe the quintessential CL peak corresponding to the $^5F_{5/2}$ -> $^5F_{7/2}$ transition of Yb^{3+}. The reason behind the absence of CS could be due to concentration quenching between Er^{3+} and Yb^{3+} ions, the energy transfer process of Er^{3+} ($^4I_{11/2}$) + Yb^{3+} ($^2F_{5/2}$) → Er^{3+} ($^4F_{7/2}$) + Yb^{3+} ($^2F_{7/2}$) reduced accordingly, which leads to the reduction of the population of $^4F_{7/2}$ state of Er^{3+} ions and results in the absence of 525 nm and 548 nm emissions. The red emission $^4F_{9/2} \rightarrow {}^4I_{15/2}$ is only possible when the photon relax from higher energy $^4F_{7/2}$ levels. Seeing the lack of energy transfer to Er higher energy levels there is no possibility for the aforementioned emission.

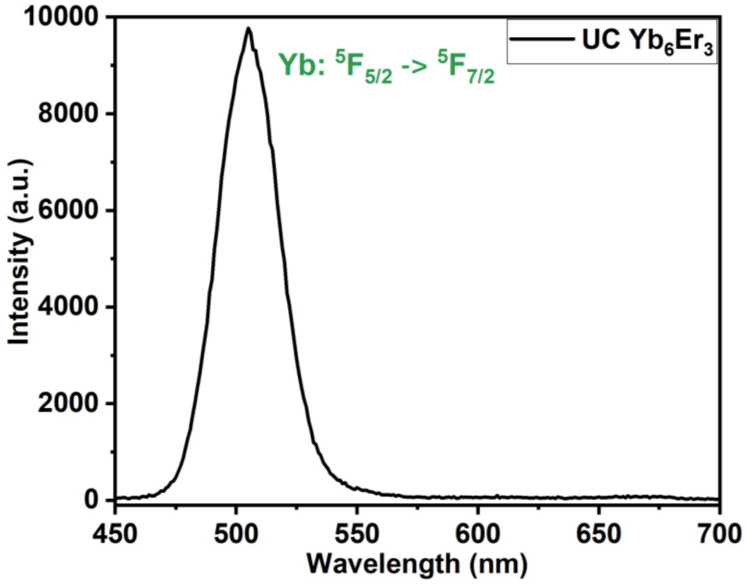

Figure 77. Yb_6Er_3 UC spectrum showcasing CL in Yb (λ_{exc} = 978 nm).

Yb_8Tb

The upconversion properties of the hetero-nonanuclear Yb/Tb clusters were subsequently studied in CD_3OD. Irradiation of the $^5F_{5/2} \leftarrow {}^5F_{7/2}$ Yb absorption band (λ_{exc} = 980 nm) gave rise to signals in the visible region, with the characteristic digitated visible emission of Tb ($^5D_4 \rightarrow {}^7F_J$ with J = 6 to 3) with a maximum at 505 nm next to the peaks at 550 nm, 580nm, and 625nm (**Figure 78**). The two photon behavior of the UC emission was confirmed using Log/Log plots, whereby the intensity was found to have a quadratic dependence on the intensity of the incident light (**Figure 79**). The slope of the Log/ Log plot was similar across the series and found to be

1.86, pointing to the same mechanistic origins across all complexes—two excited ytterbium donors cooperatively sensitizing one terbium acceptor, via the upconverted quasi-virtual Yb_2** excited state.

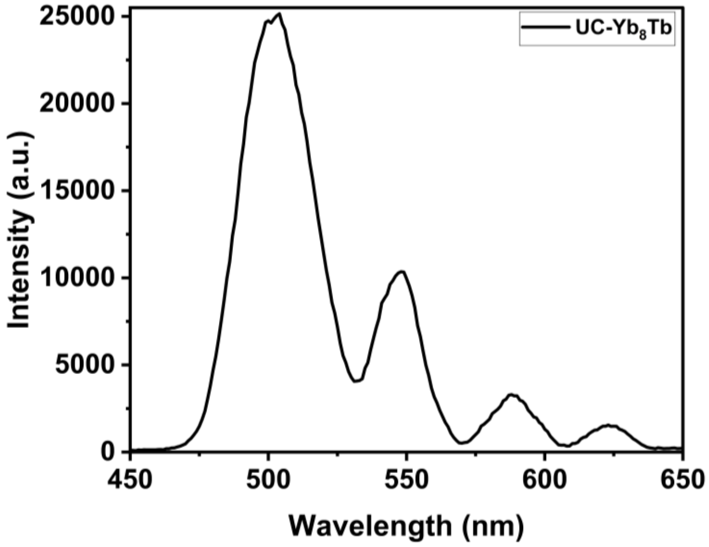

Figure 78. UC CS in Yb/Tb 1mM CD_3OD solution (λ_{exc} = 978 nm).

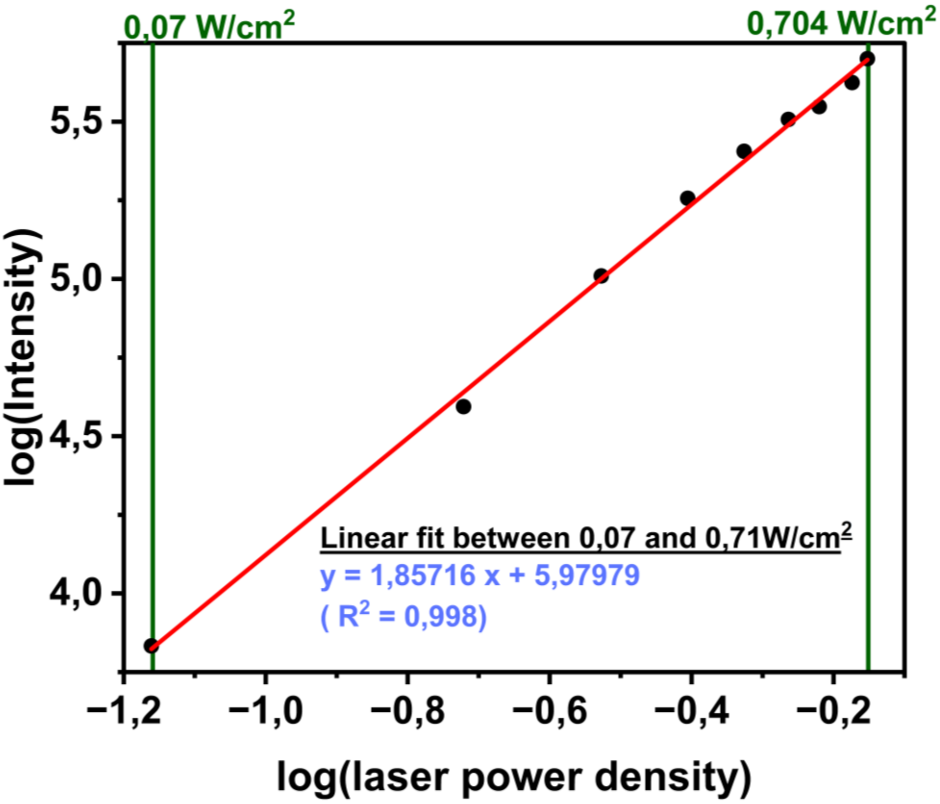

Figure 79. UC intensity as a function of the incident pump power density in a log/log scale.

4.6. Conclusion

We have successfully created a multifunctional heteronuclear complex called $[Eu_8Yb(BA)_{16}(OH)_{10}]Cl$ by doping Yb ions into Europium nonanuclear complexes. This complex exhibits highly efficient cooperative UC luminescence in solution due to the Yb/Eu donor/acceptor pair, making it one of the most efficient molecular or supramolecular UC probes reported to date. [41, 76, 79] The UC process can be observed in solution at concentrations as low as 100 nM, and it marks the first instance of direct cooperative sensitization (CS) upconversion within a molecular cluster that incorporates both Eu and Yb (**Figure 80**).

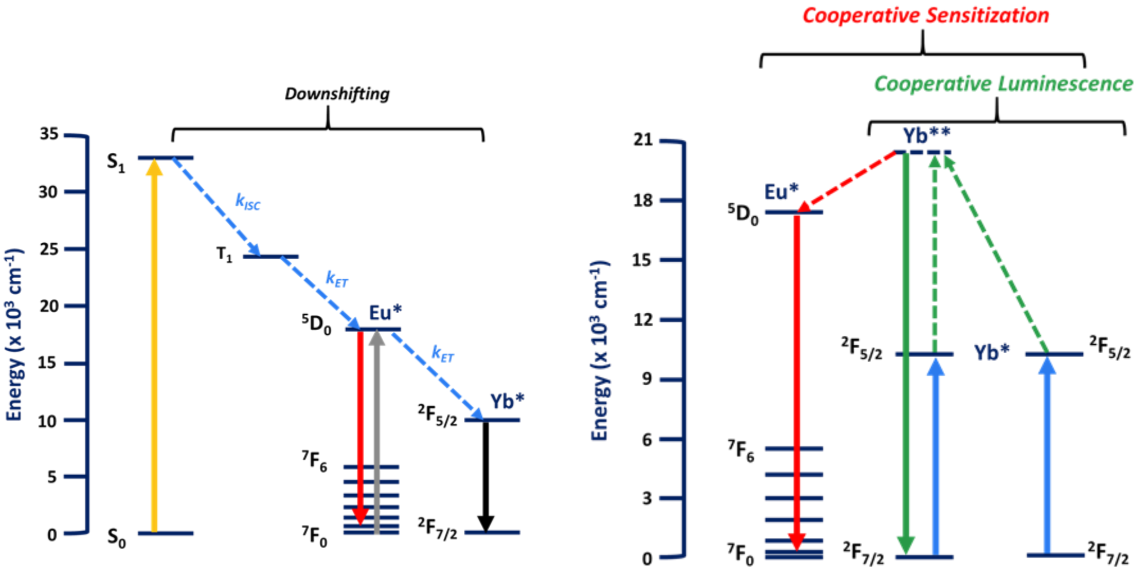

Figure 80. (left) Schematic representation of the absorption (yellow) and downshifting (black). (right) Schematic representation of cooperative luminescence (green) and cooperative sensitization (red) process.

By using readily accessible β-diketonate ligands and a diverse range of Ln donor-acceptor dyads and structures, we expect to achieve even more efficient upconversion (UC) systems. Moreover, we believe that developing UC luminescent Ln-SMMs is a promising field of research with many corners still unexplored. The incorporation of multiple functionalities into a single molecule can potentially enhance our understanding of SMM behavior. SMMs are intended for implementation in next-generation nanocircuits for quantum computation.

In addition to the attractiveness of UC systems for bio-analytical applications, [149] we anticipate developing UC luminescent Ln-SMMs with multiple functionalities, that could potentially revolutionize the field of quantum computation and enhance our understanding of SMM behavior.

Chapter 5: Magnetocaloric Effect- Results and Discussion

Investigating the Physical Properties and Effects in a Highly Symmetric Gd_9 Cluster

5.1. Recent Advances with Gd Complexes

Recent experiments on a {Gd_7} molecule (**Figure 81**) have demonstrated its potential for magnetic cooling applications, achieving cooling to temperatures as low as ~200 mK in adiabatic demagnetization experiments.[150] The molecule's centered-hexagonal array of metal

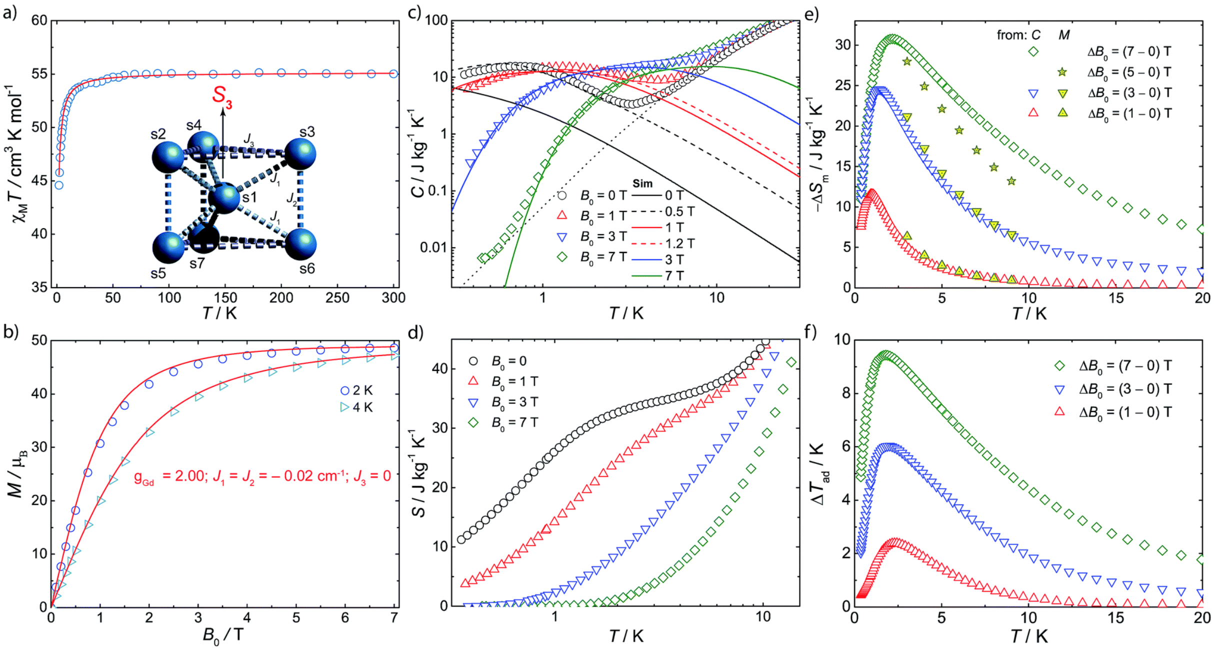

Figure 81. Magnetic properties of a **Gd_7 complex**. (a) Molar magnetic susceptibility (χ_M), in the form of $\chi_M T(T)$, measured in an applied magnetic field of 0.1 T, and fit (solid line) to spin Hamiltonian appropriate for the spin system in the insert. (b) Magnetization (M) as a function of applied field (B_0) and temperature (T = 2, 4 K), and fits (solid lines) from spin Hamiltonian (1). (c) Specific heat (C) as a function of temperature at B_0 = 0 (black symbols), 1 T (red), 3 T (blue) and 7 T (green), and lattice contribution (dotted line). Solid lines show the results that follow from Hamiltonian (1), dashed lines those including an effective internal field, see text. (d) Entropy, as obtained from $C(T)$ data. (e) Magnetic entropy change obtained from $C(T,B_0)$ and $M(T,B_0)$. (f) Adiabatic temperature change obtained from $C(T,B_0)$. (Taken from the reference 150).

ions, with antiferromagnetic exchange coupling, shows signature of a geometric spin frustration, which also leads to an enhanced MCE due to increased density of states at critical fields and is a sign for the complex's potential application as a magnetic coolant.

The concept of "frustration" was initially introduced in the field of magnetism to describe the inability to satisfy all exchange processes simultaneously in spin glasses. However, our current focus is on periodic Hamiltonian systems without any disorder. In such cases, frustration is more accurately described as geometrical frustration. It refers to a condition where a local pattern is unable to produce a simple structure for an extended system. We will be focusing on two models of magnetism for the most part.: the Ising model

$H = \sum_{(i,j)} J_{ij} S_i S_j \quad S_i, S_j = \pm 1 \; or \; \uparrow, \downarrow$

and the Heisenberg model $H = \sum_{(i,j)} J_{ij} \; \vec{S_i}.\vec{S_j}$

where the spins $\vec{S_i}$ are unit vectors in the classical case, and components of a quantum spin in the quantum case: $\left[S_i^{\alpha}, S_i^{\beta}\right] = i\varepsilon^{\alpha\beta\gamma} S_i^{\gamma}, and \; \vec{S_i^2}$ = S(S +1). In both cases, i and j are sites of a periodic lattice, and *Jij* is assumed to depend only on their relative position. Geometrical frustration is a condition that arises when at least some exchange paths are antiferromagnetic, meaning that the exchange integrals J_{ij} are positive. If all exchange paths are ferromagnetic with negative exchange integrals, the ground state is the configuration with all spins parallel. However, even when all bonds are antiferromagnetic, geometrical frustration doesn't necessarily happen. For bipartite lattices like the square lattice that can be divided into two

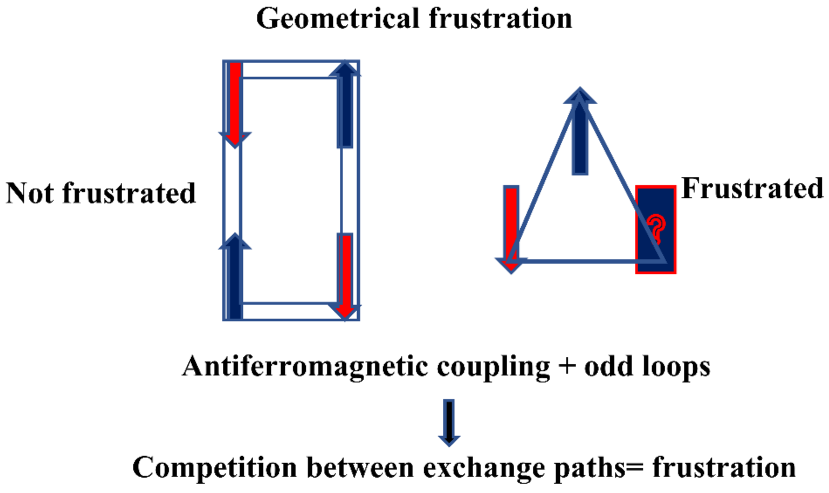

Figure 82. showing systems with and without frustration

sublattices, the energy of the Ising or Heisenberg model is minimized by the Neel configuration, where the spins of one sublattice are parallel to each other and antiparallel to all spins of the other sublattice. Loops of odd length are a necessary condition to satisfy the general condition of geometrical frustration with only antiferromagnetic exchange interactions, but this is not sufficient. In some cases, such as the triangular lattice with nearest-neighbor interactions, the energy of the classical antiferromagnetic Heisenberg model can be minimized with a simple helical arrangement of spins. If this defines a unique ground state, the system is not geometrically frustrated. Geometrical frustration occurs when there is no unique way to minimize the energy, but there are other ways to reach the ground-state energy with less simple structures. If we try to understand the physical consequences of this degeneracy from a theoretical perspective. For example, Ising spins, degeneracy can lead to various zero-temperature behaviors such as long-range order, algebraic order, dipolar correlations, or complete disorder. For Heisenberg models, fluctuations (thermal or quantum) play a significant role. They can order the system by selecting one ordered state out of the ground-state manifold, but they can also destroy any kind of magnetic long-range order. This leads to new types of ground states such as spin nematics, valence-bond crystals, or quantum spin liquids where both the rotational SU (2) symmetry in spin space and the translation symmetry in real space are preserved. Frustration caused by geometric spin can result in areas of high density of states (and zero-temperature entropy), leading to the possibility of achieving very high cooling rates. This is particularly true when sweeping across the saturation field in a one-dimensional (1D) antiferromagnetic (AF) s = 1/2 chain. Low-dimensional frustrated magnetic materials, [151-153] such as the well-known 2D kagome or triangular AF lattices or the 1D saw-tooth AF chain, are attractive targets for achieving enhanced MCE and low-temperature refrigeration due to the combination of these features. It is worth noting that such effects can also be observed in certain 0 D systems, namely molecular clusters of spins in frustrated geometries. These systems are part of the broader class of molecules known as molecular nanomagnets.

As mentioned above, It is possible to reach temperatures below Kelvin using adiabatic demagnetization of paramagnetic salts. This technique exploits the magnetocaloric effect, which can be assessed by analyzing the adiabatic temperature change that occurs when the system is driven along an isentrope, a curve of constant entropy (S).

$$\left(\frac{dT}{dB}\right)_S = -\frac{T}{C}\left(\frac{dS}{dB}\right)_T$$

where C is the heat capacity, T is the temperature and B is the applied magnetic field. In the realm of magnetism, paramagnets and interacting spin systems exhibit distinct characteristics when subjected to magnetic fields. The isentropes, which are curves of constant entropy, for a paramagnet appear as straight lines in a T–B plane[154] that pass through the origin. However, the isentropes for interacting spin systems can display a much more diverse response to magnetic fields, resulting in a wide range of shapes and curves (**Figure 82**).[150]

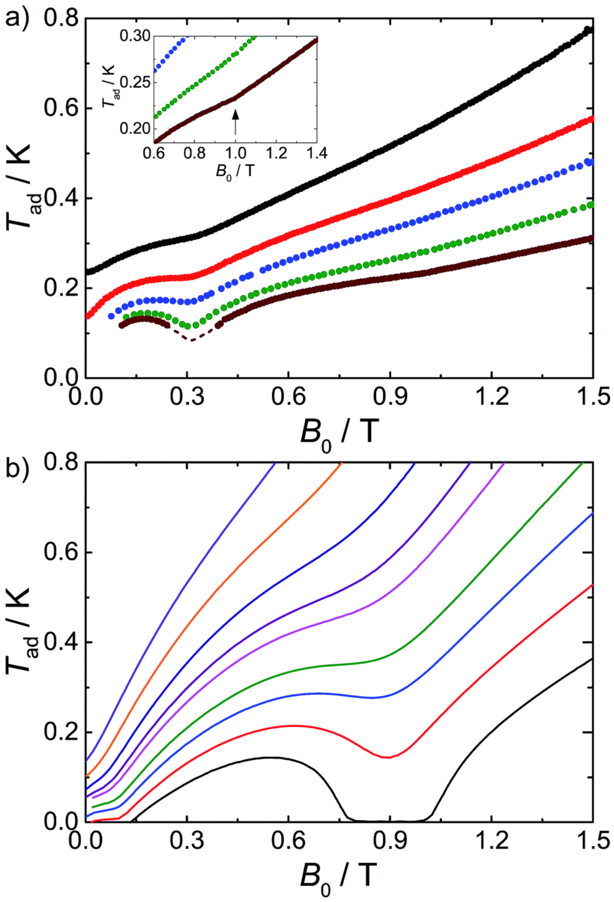

Figure 82. Adiabatic temperature, T_{ad}, as a function of applied magnetic field, B_0, along isentropic curves: (a) from experiments and (b) calculated using Hamiltonian. The dashed line in (a) relates to the uncertainty in the correction applied to the experimental data below 0.1 K. Inset: the arrow highlights the experimental enhancement of $T_{ad}(B_0)$, which becomes noticeable for B_0 near *ca.* 1 T and $T < 0.25$ K.[150]

5.2. [$Gd_9(BA)_{16}(OH)_{10}$]Cl

Lanthanide based systems have been extensively studied due to the ferromagnetic interactions exhibited between them. Weak interactions, high spin degeneracy, and negligible anisotropy make Gd(III) ($^8S_{7/2}$) an ideal candidate for magnetic cooling applications. Based on the above mentioned previous studies, we turned towards our nonanuclear [$Gd_9(BA)_{16}OH_{10}$]Cl cluster with benzoylacetonate (BA) ligands possessing D_{4d} and C_{2v} symmetry. Here we report the magnetic behavior of this system and explore the possibility of the application of such compounds in magnetic cooling. We have modeled the magnetic behavior of the Gd^{3+}-containing systems despite the gigantic Hilbert space involved. Quasi-exact methods allow the determination of the exchange interaction for [$Gd_9(BA)_{16}OH_{10}$]Cl, we have taken advantage of the symmetry to model the magnetic data. Here, we also present its characterization in the solid state and, in solution, its magnetic properties as a prospective MCE material as well as its luminescent properties in both solid and solution states upon excitation of the BA antenna.

[$Gd_9(BA)_{16}(OH)_{10}$]Cl·3(C_2H_5OH)·4(H_2O). Anal. Found: C, 45.43; H, 3.44. Calcd for $C_{160}H_{154}ClO_{42}Gd_9$; C, 45,50; H, 3.76. FTIR (cm^{-1}): 3579m, 3342m, 3058m, 1593s, 1567s, 1507s, 1483m, 1447m, 1370s, 1308w, 1275m, 1108m, 1071m, 999w, 962m, 845m, 760m, 711m, 690m, 560m, 518m. ESI-TOF: m/z 4164.29 [$Gd_9(BA)_{16}OH_{10}$]$^+$. μ_{eff}^{300K} 67.9 cm^3 K mol^{-1}, calcd 70.92 cm^3 K mol^{-1} (300 K), 33.7% of active metal percentage.

Structural Characterization

The nonanuclear complex is of general composition [$Gd_9(BA)_{16}(OH)_{10}$]Cl. The solid-state structure of the Ln_9 complexes can be viewed as two pentanuclear square pyramids sharing the apical Ln atom, with a torsion angle of approximately 45° between the two pyramids, resulting in square anti-prismatic geometry at the central Ln (**Figure 83b**). The eight triangular faces of the pyramids are capped by μ_3-OH groups linked to the three Ln at the edges of the triangles, while μ_4-OH bonds connect the four Ln atoms of the two square faces. All Ln atoms except the central one are linked to three acetylacetonate ligands (**Figure 83d**) through two coordination modes of BA ligands (bridging and terminal). The coordinative saturation of the peripheral Ln ions (Coordination Number = 8) is provided by 16 bidentate acetylacetonate ligands present as endo and exo environments, shown in yellow and blue, respectively (**Figure 83e**) eight endo bidentate ligands are bound to a single metal center (*t*-BA). In contrast, the eight exo ligands display bridging between two metal centers (μ-BA). Upon analyzing the two coordination environments within the cluster, we designated them as the central site, with only eight μ_3-OH hydroxy ligands in the first coordination sphere, and peripheral site, coordinating with one terminal BA ligand, two bridged BA ligands, two μ_3-OH hydroxy ligands in the triangular face and μ_4-OH ligand in the square face. Based on continuous shape measures (CShMs), we determined that the $\text{Ln}_{\text{central}}$ site is nearly a perfect square antiprismatic with D_{4d} symmetry, while the $\text{Ln}_{\text{peripheral}}$ site is a biaugmented trigonal prism with C_{2v} symmetry.

The high cubic symmetry packing (a=b=c = 33.6739(6) Å, $\alpha = \beta = \gamma = 90^{\circ}$, $V = 38183.9$ Å^3, $Pn\bar{3}n$ (222)) arrangement results in hexagonal channels (voids) along the body diagonal directions inside the massive unit cell. The diameter of the channel changes as it runs, with a minimum diameter of approximately 7 Å, not including the van der Waals volume. The channel is spacious enough for solvent molecules and anions (Cl^-) to move freely. Within the lattice, the channels stretch along the four-body diagonal directions of the unit cell, causing significant

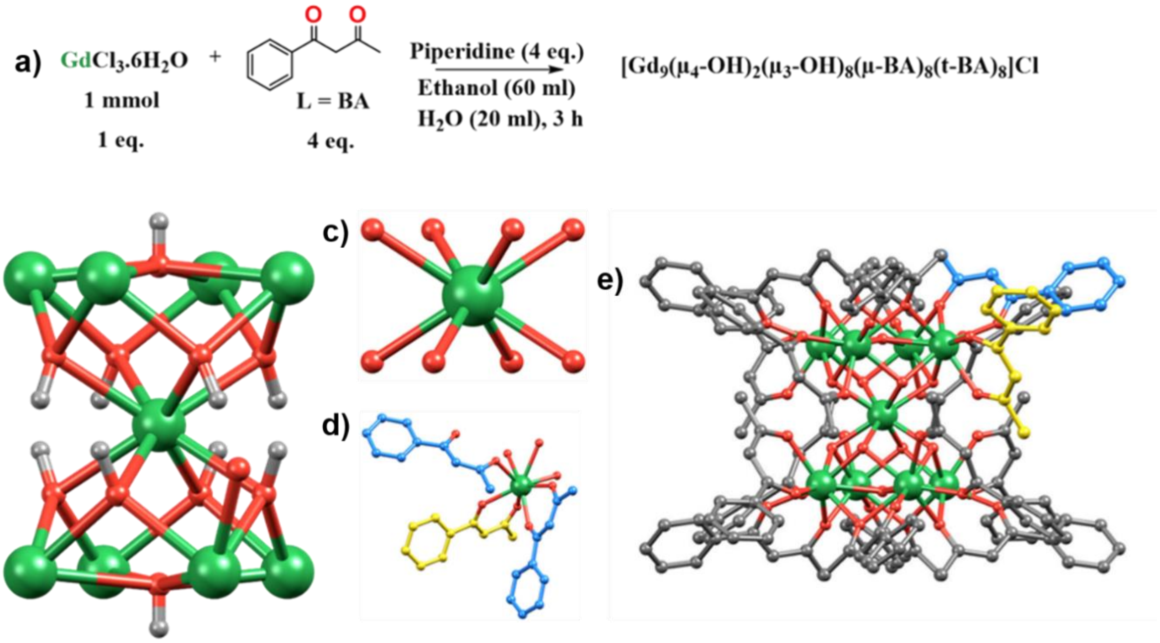

Figure 83. a) Synthetic protocol for preparing the nonanuclear $[Gd_9(BA)_{16}(OH)_{10}]Cl$ complex. b) single crystal X-ray structure of $[Gd_9(BA)_{16}(OH)_{10}]Cl$ showcasing the hour glass core of the nine Gd (green), ten oxygen (red), and ten hydroxyl H atoms (grey) the hour-glass shaped core. c) Single crystal X-ray structure of $\text{Ln}_{\text{Central}}$ coordination sphere. d) Single crystal X-ray structure of $\text{Ln}_{\text{Periphery}}$ coordination sphere. e) Single crystal structure of $[Gd_9(BA)_{16}(OH)_{10}]^+$ ion showcasing BA ligands in grey, with endo and exco BA positions in yellow and green, respectively (hydrogens and Cl ion omitted for clarity).

disorder among smaller components. Even at 120 K, this disorder cannot be resolved through X-ray analysis. The phase purity is also confirmed by measuring the PXRD of fresh crystals taken from the mother liquor. The crystals that are dried and taken from the vacuum lost the order and did not match the SC-XRD simulated pattern due to the loss of solvent molecules from the lattice. After leaving the mother liquid, the crystals lose solvent quickly. However, a thermal stability study confirms that the compounds remain stable. To determine the amount of solvent in the lattice, we measured TGA. The complex doesn't undergo chemical decomposition at temperatures up to 150°C. At temperatures above 210°C, the complex begins to decompose. Therefore, the nonanuclear complex remains stable up to 150°C and experiences a weight loss of approximately 5% until 100°C. This corresponds to the loss of lattice solvent, which includes three ethanol molecules and four water molecules. SEM-EDS analysis was performed on both crystals and powder samples of Gd_9 complex at five different sites, giving an atomic composition of 90% of Gd and 10% of Cl, in good agreement with the 88.9% of Gd and 11.1% of Cl, expected in the final product.

Cell	a=b=c= 33.9869(2) Å, $\alpha=\beta=\gamma= 90^{\circ}$
Temperature	180 K
Wavelength (nm)	0.71073
Space group	$P\,n\,\bar{3}n$
Moiety formula	$C_{160}H_{154}Gd_9O_{42}$, 24[C_2H_6O], [Cl]
Sum formula	$C_{208}H_{298}ClGd_9O_{66}$
Mr (g/mol)	5305.15
D/g cm^{-3}	**1.346**
Z	6
μ (mm^{-1})	2.325
F000	16002.0
h,k,lmax	43, 43, 39
N_{ref}	7230
Tmin, Tmax	0.892, 1.000
AbsCorr	MULTI-SCAN
Data completeness	0.997
Theta(max)	27.099
R(reflections)	0.0296(5868)
wR2(reflections)	0.0680(7230)
N_{par}	264

ESI-TOF Mass Characterization

To analyze the compound in the solution state, which is also the working medium for photoluminescence experiments, we dissolved it in DCM and recorded the electrospray mass spectrometry (**Figure 84**).

The resulting spectrum showed a primary peak at 4164.28 m/z units, which corresponds to the monocharged $[Gd_9(BA)_{16}OH_{10}]^+$ complex. The minor peaks on the right side of the spectrum are due to the adduct formed with the monocharged Gd_9 complex with two ethanol molecules, and the one at 750 m/z units is the fragment of $[Gd(BA)_2]^+$

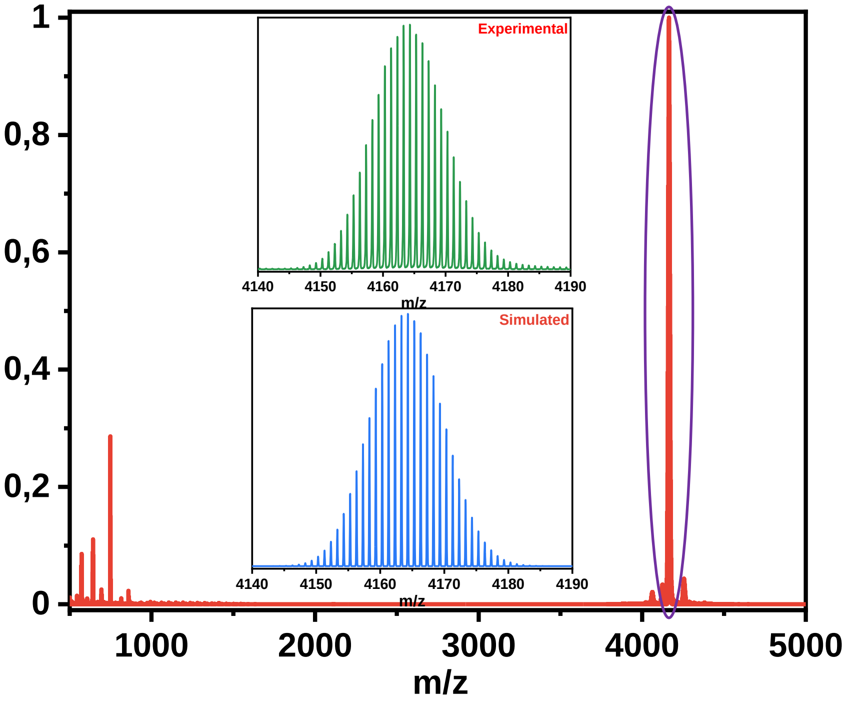

Figure 84. ESI mass spectrum in positive ion mode of the $[Gd_9(BA)_{16}OH_{10}]^+$ complex sprayed from a CH_2Cl_2 solution. (SYNAPT G2S HDMS, Waters). Inset: Experimental M^+ peak (green) 4164.28 m/z; Simulated M^+ peak (blue) 4164.31 m/z.

Photophysical Studies

The solution state UV-vis absorption spectrum of the Gd_9 complex in CD_2Cl_2 is presented in **Figure 85**. The Gd_9 complex in CD_2Cl_2 displays a strong $S_1 \leftarrow S_0$ absorption band in the UV region corresponding to the $S_1 \leftarrow S_0$ transition of the BA ligands (λ_{max} = 322 nm, ε = 18.49 x 10^4 $M^{-1}cm^{-1}$). A way to probe the ligand-based levels' energy and assess the likelihood of their involvement is to measure the phosphorescence spectrum of the Gd_9 compound.[155-157] Gd(III) cannot provide an appropriate acceptor state for antennas in the near-UV/vis range because its first excited state ($^6P_{7/2}$) lies at 32000 cm^{-1} above its ground state. The measurement performed on $[Gd_9(BA)_{16}(OH)_{10}]Cl$ (λ_{exc} = 356 nm, c = 3.8 µM) shows a strong emission band extending from about 400 to 650 nm (**Figure 85 left**) and is attributed to phosphorescence from the lowest triplet state T_1 of the ligand. We note that such structure may reflect the two topologically different BA ligands or may be caused by excitonic states, indicating strongly coupled ligands.[158-160] Figure 84b displays the comparable solid-state broad absorption band in the UV region with maxima around 344 nm. The usual redshift (stokes shift) in the solid state measurement is attributed to more significant intermolecular interactions in the solid state. The measurement performed on $[Gd_9(BA)_{16}(OH)_{10}]Cl$ (λ_{exc} = 365 nm) shows a strong emission band extending from about 450 to 620 nm (**Figure 85**) and is attributed to phosphorescence from the lowest triplet state T_1 of the ligand. Using the solution state emission profile of Gd_9 we calculated the triplet state's energy to be 24,271 cm^{-1}. The resemblance in the emission profile between the solid state and the solution state is noticeable. The shoulder peaks at higher wavelengths (468

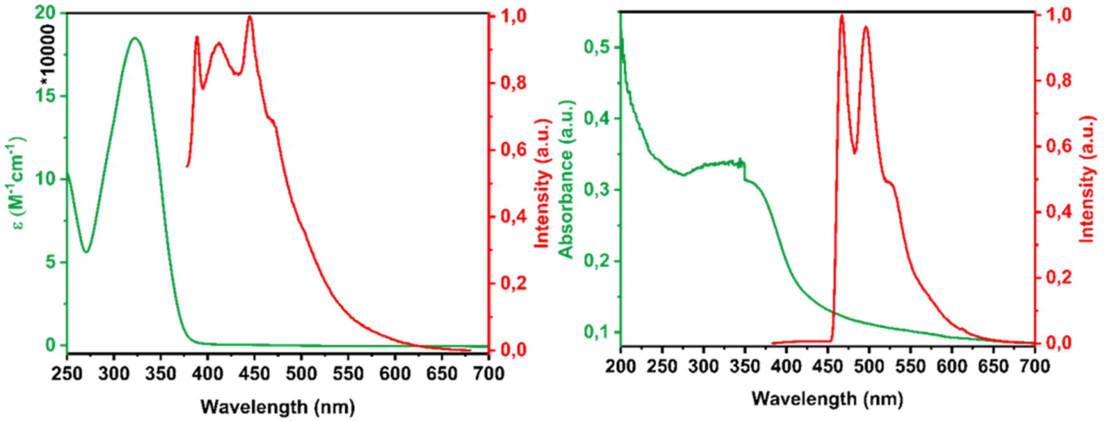

Figure 85. a) Solution state absorption spectrum (green) (λ_{max} = 322 nm) and normalized emission spectra (λ_{exc} = 356 nm) in the visible region (red) for the Gd_9 cluster in CD_2Cl_2, c = 3.8 µM. b) Solid state normalised absorption spectrum (green) ((λ_{max} = 346 nm) and normalized emission spectrum (λ_{exc} = 365 nm) in the visible (red) region for the Gd_9 cluster in CD_2Cl_2.

nm and 526 nm, respectively), and the sharp peaks at the lower wavelengths (412 nm, 444 nm and 467 nm, 496 nm, respectively). The ligand S_1 emission band is the peak at 389 nm in the solution state.

In order to further characterize the emission of the $[Gd_9(BA)_{16}(OH)_{10}]Cl$ complexes, we performed luminescence lifetime measurements in the solid and solution states. Typical luminescence lifetime measurements for the $[Gd_9(BA)_{16}(OH)_{10}]Cl$ complex are shown in **Figure 86**. The corresponding luminescence lifetimes at 2 K are τ_{Gd}= 10.08 ± 0.008 ms. The one order of magnitude higher than that of analogues based on other lanthanides (Chapter 4) longer phosphorescence lifetime measured for the Gd(III) complex supports our interpretation of efficient $(BA)S_1 \rightarrow (BA)T_1 \rightarrow (Ln^{3+})$ excited state energy transfer in the case of the Ln^{3+} complex at cryogenic temperatures. In contrast, the Gd(III)complex has no such relaxation path available and the BA-based triplet state lives correspondingly longer before decaying by phosphorescence. Meanwhile, the phosphorescence lifetime of the complex in the solution state at 300 K is 6.6 ± 0.2 μs. The meagre lifetime in the solution state is expected due to the many relaxation pathways through the surrounding solvent molecules.

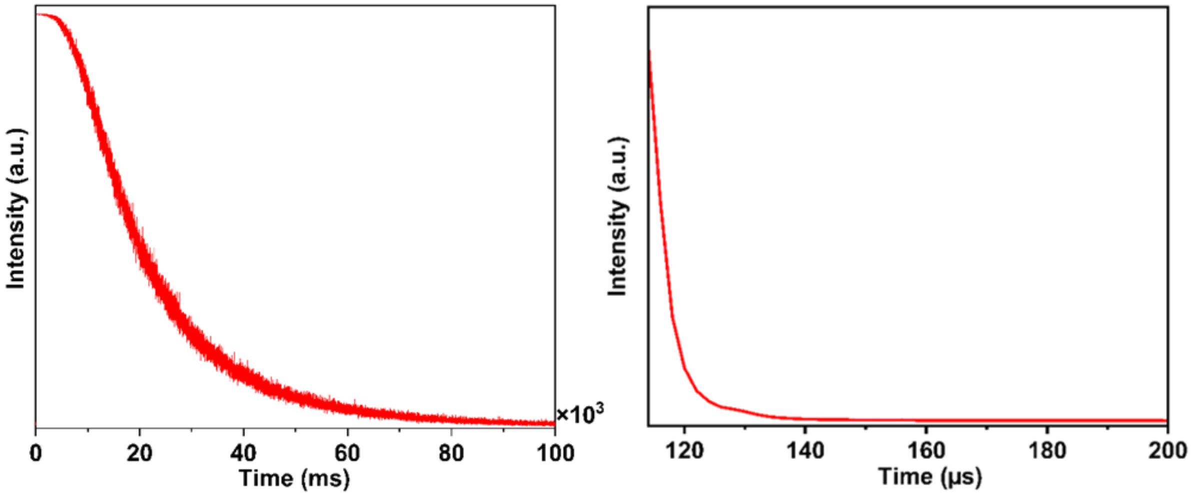

Figure 86. Luminescence lifetime measurements (Red) of $[Gd_9(BA)_{16}(OH)_{10}]Cl$. (left) Solid state measurement at 2 K (λ_{exc} = 365 nm). (right) solution state measurement at 300 K (λ_{exc} = 356 nm, CD_2Cl_2, c = 3.8 µM).

Magnetic Studies

We conducted magnetic susceptibility studies on polycrystalline samples of $[Gd_9(BA)_{16}(OH)_{10}]Cl$ in the temperature range of 2−300 K. We applied a dc magnetic field (*H*) of 0.1 T. Our investigation focused on the magnetization changes in the field and temperature ranges of 0−7 T and 2−12 K, respectively.

The room temperature $\chi_M T$ value (68.22 cm^3 K mol^{-1}) (where χ_M represents the molar susceptibility) for $[Gd_9(BA)_{16}(OH)_{10}]Cl$ is close to the expected value (70.92 cm^3 K mol^{-1})for nine non-interacting Gd ions. There is a minimum in $\chi_M T$ at a 4 Ke, which could indicate weak intramolecular magnetic interactions. As the temperature decreases, we observed a gradual decrease in $\chi_M T$ due to the depopulation of the Stark levels and/or the possible presence of antiferromagnetic interactions (**Figure 87**).

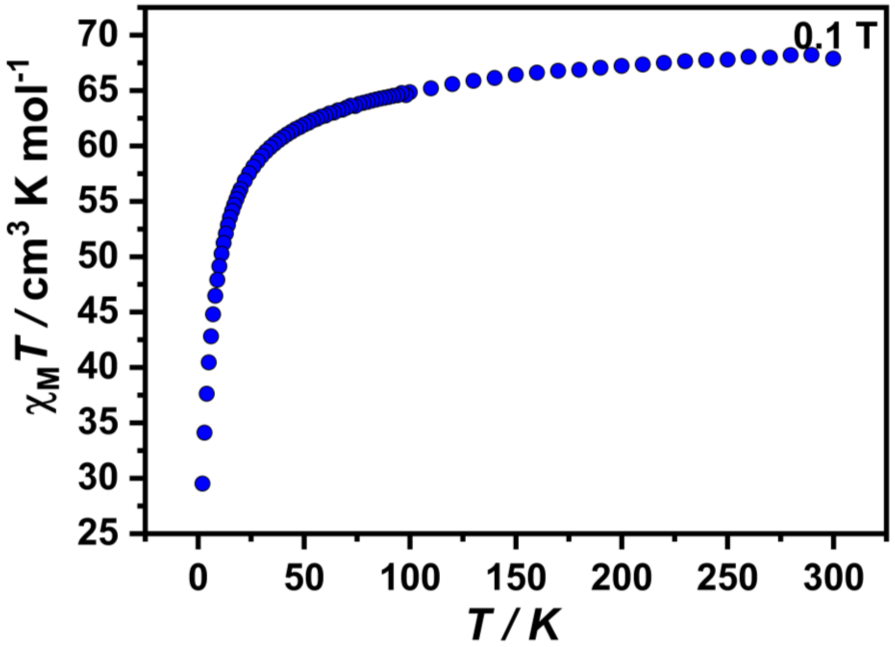

Figure 87. Temperature-product of the molar magnetic susceptibility versus temperature for Gd_9.

Due to their anisotropic character, it is challenging to understand the magnetic behavior of polymetallic compounds containing Tb^{3+}, Dy^{3+}, Ho^{3+}, and Er^{3+}. The depopulation of the Stark levels has a similar effect on the variable temperature magnetic properties as antiferromagnetic exchange interactions. However, modeling the magnetic behavior of complexes containing the isotropic Gd^{3+} is far easier, although still challenging due to the size of the problem. For $[Gd_9(BA)_{16}(OH)_{10}]Cl$, the exp room temperature value 68.22 cm^3 K mol^{-1} is consistent with nine Gd(III), $^8S_{7/2}$ ions ($\chi_M T$ = 70.92 cm^3 K mol^{-1} for nine non-interacting s = 7/2 with g = 2.00). Upon cooling, the χ_MT slowly decreases up to about 40 K, Thereafter $\chi_M T$ sharply decreases. The $M(H)$ curves for Gd$_9$ at low temperature show rapid increases of M with applied magnetic field, reaching a maximum value of 59.2 μ_B at 7 T and 2 K, which is slightly below compared

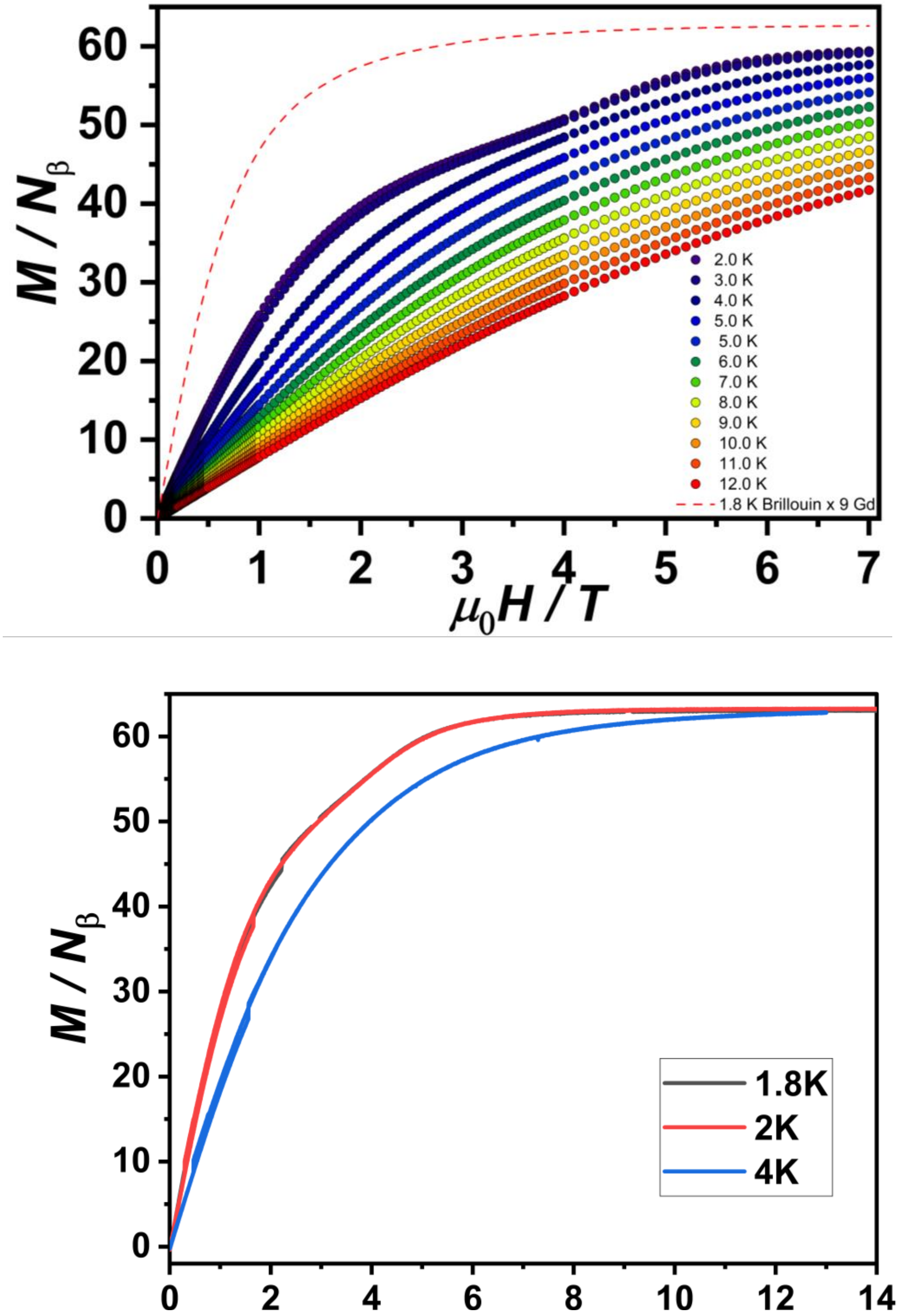

Figure 88. (top) M(H) plots of Gd$_9$ until 7 T across 2 to12 K range. (bottom) M(H) plots of Gd$_9$ until 14 T across 1.8 – 4 K range.

with complete polarization of the spin system (maximum possible M is 63 μ_B for nine s = 7/2 with g = 2.00). The $M(H)$ for Gd_9 was investigated at different applied fields and temperatures, revealing saturation at the highest field and lowest temperatures, i.e., 14 T and 2 K (**Figure 88**). Here the M is consistent with the complete polarization of the spin system (maximum possible M is 63 μ_B for nine s = 7/2. However, the most unique feature of the magnetization studies has been the plateau between 2 and 4 T at low temperatures like 1.8 K, 2 K and 3 K. We suspected this could be due to the spin frustration in the Gd_9.

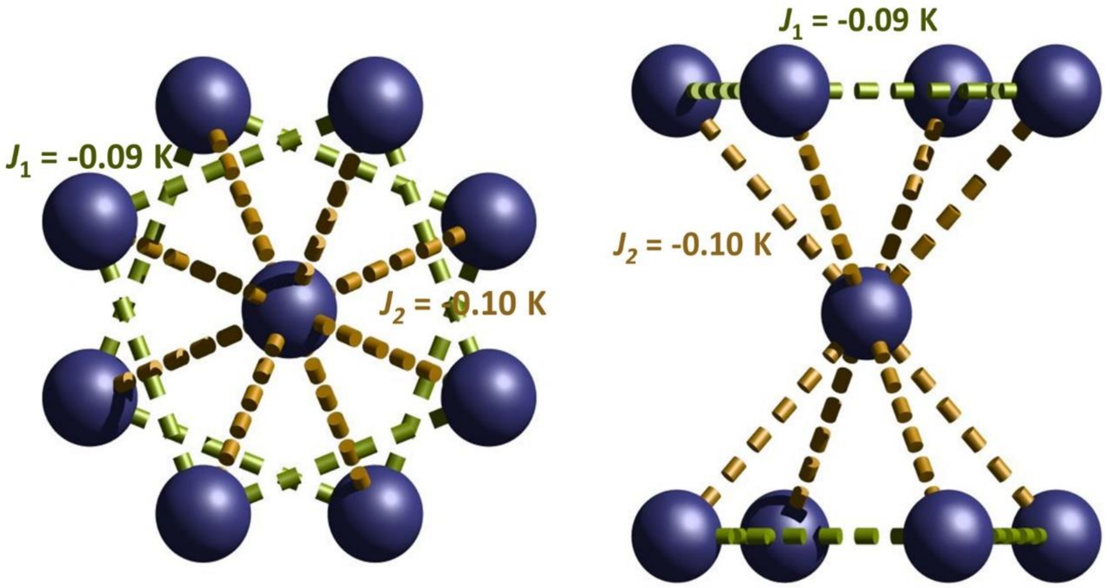

Figure 89. (Left)Top view of the Gd_9 core structure. (Right) The hour-glass structure of Gd_9.The J_1 and J_2 are the antiferromagnetic interactions among the Gds in the square and the apex, respectively.

{Gd_9} as two pentanuclear square pyramids sharing the apical Gd^{III} atom, with a torsion angle of approximately 45° between the two pyramids, resulting in square anti-prismatic geometry at the central Gd^{III} (**Figure 89**).

When the magnetic data (experimental $\chi_M T$ vs T and MH plots) were modelled by Prof. Dr.Jürgen Schnack (**Figure 90**) using a Hamiltonian (H = -2J) where -2J is the interaction between the spin pairs involved in the exchange. J_1 is the interaction between the Gd^{III}s along the corners of both the squares; J_2 is the interaction between the central Gd^{III} ion and all the other 8 Gds situated at the corners of both the square planes (**Figure 89**). The best agreement

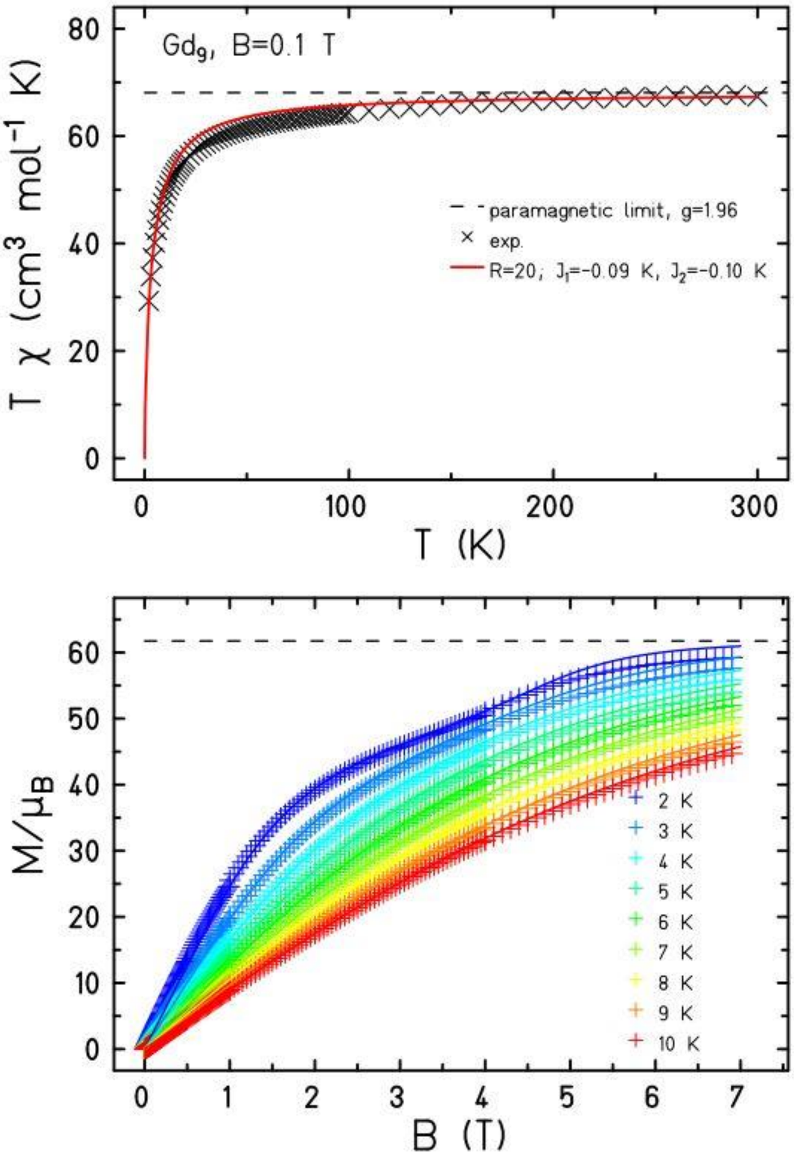

Figure 90. Fits of the (Top) Temperature-product of the molar magnetic susceptibility versus temperature (Bottom) *M(H)* plots of Gd_9 until 7 T across 2 to12 K range for Gd_9.

between experimental data and simulations for $\chi_M T(T)$ and $M(B_0)$ is achieved with J_1 = -0.09 K and J_2 = -0.1 K, assuming g = 1.96. With the interactions being negative values, they are of antiferromagnetic nature. With antiferromagnetic exchange coupling and the highly symmetric motif (equilateral triangles), this nonanuclear structure suffers geometric spin frustration. The *M*(*H*) curves are very sensitive to the exchange, making it an interesting system in the context of spin frustration. As one can see in **Figure 91** already, very small variations of the *J*s lead to drastic changes of the observables. This is an important phenomenon in extended lattices, and is associated with having many degenerate ground state configurations, leading to exotic magnetic behaviors such as spin glasses and spin ice.[161-163] It can also lead to enhanced MCE because of the increased density of states at critical fields.

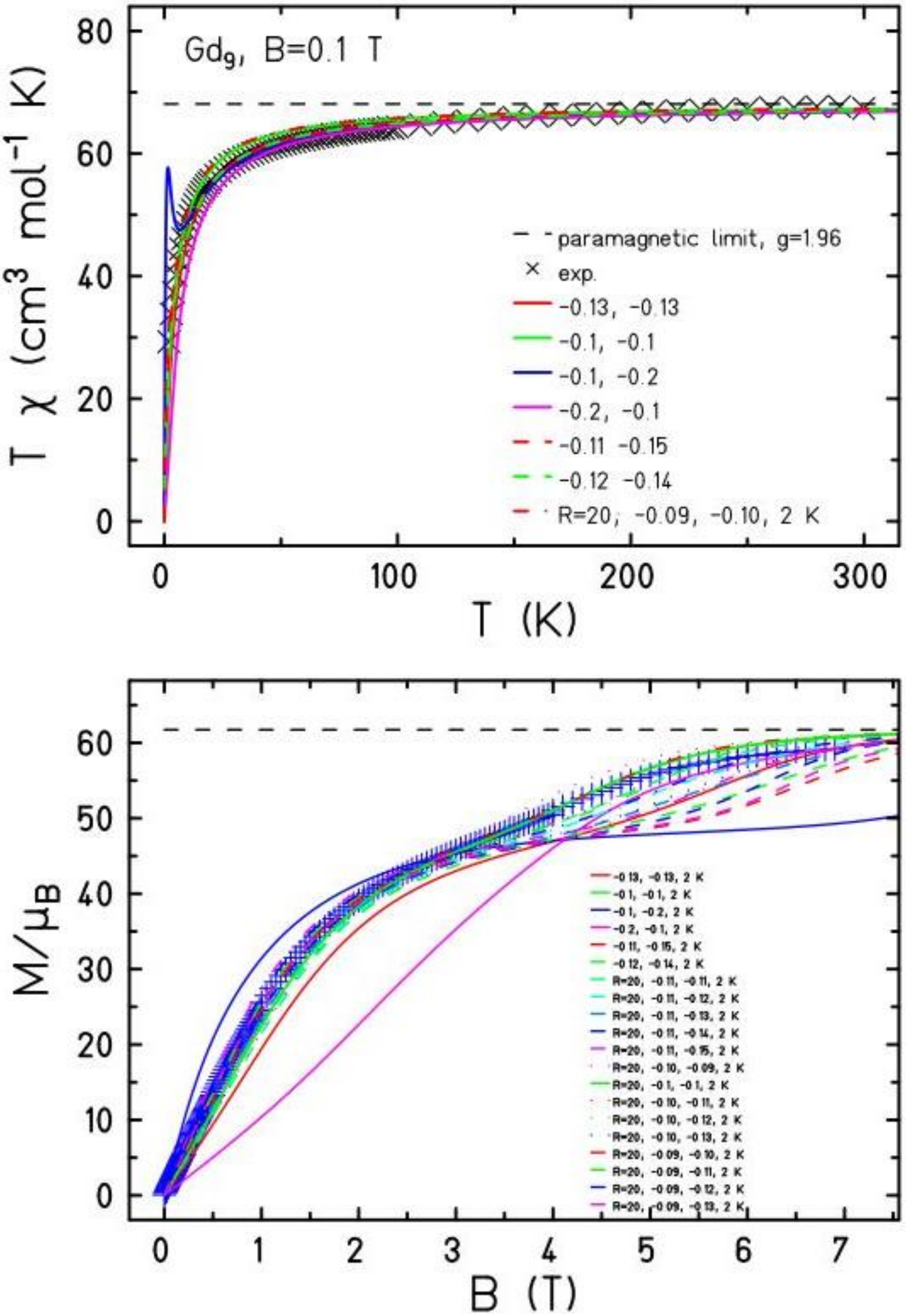

Figure 91. Fits varying the exchange constants of the (Top) Temperature-product of the molar magnetic susceptibility versus temperature (Bottom) *M(H)* plots of Gd_9 until 7 T at 2 K range for Gd_9.

Magnetocaloric Effect Studies

Molecular magnetism researchers as mentioned in the section 5.2. measure the change in magnetic entropy ($-\Delta S_M$) between magnetized ($H > 0$) and zero-field ($H = 0$) states as a parameter to characterize the magnetocaloric effect. This parameter can be obtained indirectly through measurements of the magnetization or heat capacity, with the former method being more commonly used for practical reasons. The high nuclearity, the isotropic nature of Gd(III), and the relatively small exchange interaction led us to examine compounds Gd_9 for possible magnetocaloric applications. The magnetic entropy changes of Gd_9 were obtained from isothermal magnetization measurements from 0 to 7 T in the temperature range 2−12 K (**Figure 88**) and extracted the $-\Delta S_M$ value by plotting the magnetization curves using the Maxwell equation 5.2.(**Figure 92**)

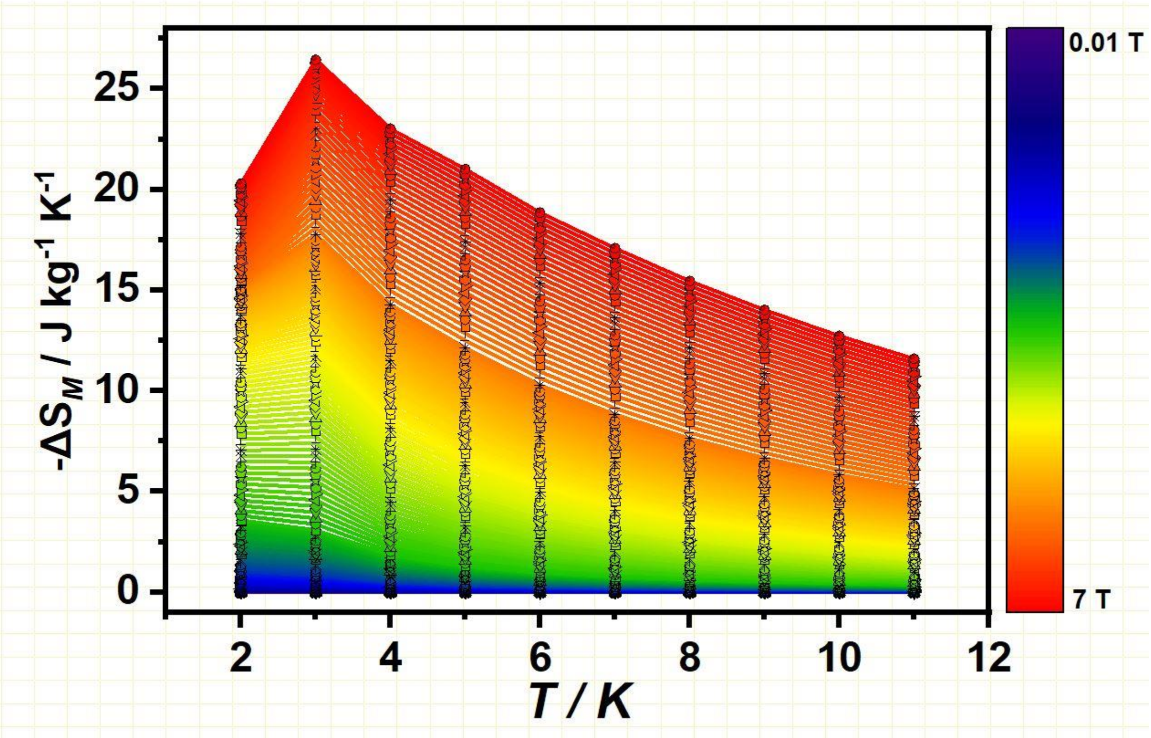

Figure 92. Magnetic entropy change from isothermal magnetization measurements from 0 to 7 T in the temperature range 2−12 K.

The maximum value observed for Gd_9 at 3 K and 7 T is $-\Delta S_M = 26.44$. The magnetic entropy for non-interacting centers is given by $\sum nR\ln(2s + 1)$ (R being the gas constant), leading to values of 18.72R (36.35 J kg^{-1} K^{-1} , for nine Gd(III)s. Comparison of the experimental $-\Delta S_M$

with the theoretical value clearly shows that 73% (at 3 K and 7 T) of the total magnetic entropy is accessed. This fact is most likely attributable to the antiferromagnetic exchange operating within the molecules.

μ-SQUID Studies

To investigate the existence of magnetic anisotropy, we turn to μ-SQUID measurements. Given that Gd presents a very small anisotropy, sub-Kelvin temperatures offered by μ-SQUID were deemed necessary to analyze the anisotropy. Although the information obtained from commercial SQUID magnetometers about the magnetization's dynamics is valuable, their sensitivity is not as high as that of μ-SQUIDs arrays (**Figure 93**).[164] These micro-SQUID magnetometers are highly sensitive instruments that can accurately measure the magnetic properties of microcrystals and explore the dynamics of SMMs down to 30mK. As a result, they can observe quantum effects like quantum tunneling of the magnetization. Traditional devices are unable to monitor quantum tunneling of the magnetization that often occurs between S_z states due to inter and intramolecular interactions, level crossing between ground and excited

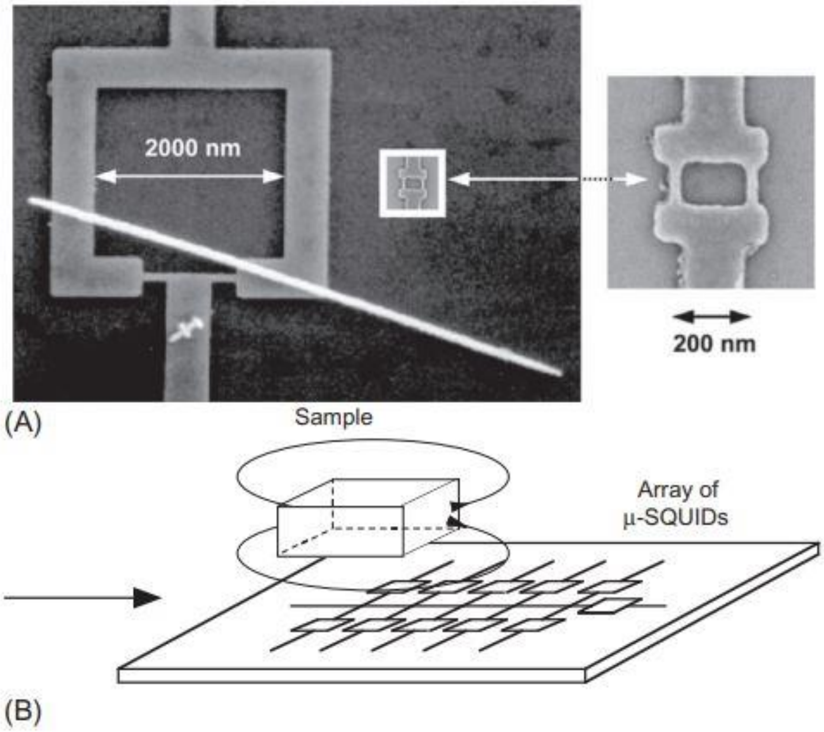

Figure 93. (A) Micrographic image of a Nb μ-SQUID and a Ni wire of diameter of about 90 nm, deposited on the μ-SQUID and (B) an array of μ-SQUIDs used for macroscopic crystal studies. (Reproduced with permission from W. Wernsdorfer, From micro-to nano-SQUIDs: applications to nanomagnetism, Supercond. Sci. Technol. 22 (2009) 64013)

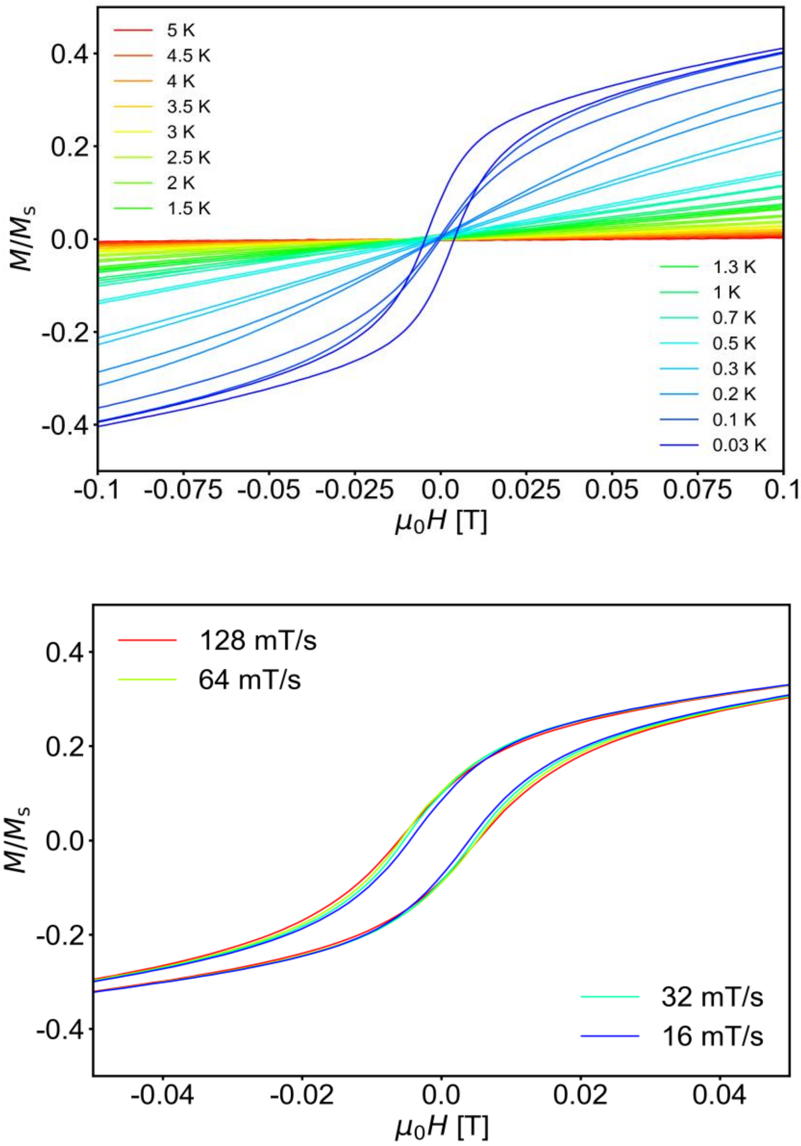

Figure 94. MicroSQUID hysteresis loop dependence with (top) temperature (16 mT/s) and (bottom) sweep rate at 30 mK for Gd_9.

states, and/or hyperfine-based tunneling. However, micro-SQUID instruments can detect such events with a high degree of sensitivity. These instruments operate at milli-Kelvin temperatures, enabling them to determine the U_{eff} values of weak SMMs with greater accuracy than commercial SQUID devices.

The magnetization of Gd_9 was measured using an array of microSQUIDs to investigate its magnetic behavior at very low temperatures (**Figure 94**). Below 0.3 K, slightly open hysteresis loops were observed for a complex that contains isotropic Gd^{III} ions in a Gd_9 complex, with a coercive field of 10 mT at 30 mK. These loops saturate at 1.4 T, where the magnetization is known to have reached at least 34 μ_B at 2 K. Although these loops are temperature-dependent, they are nearly sweep-rate-independent. This behavior is likely due to the non-collinear nature of the single-ion anisotropies. At low temperatures, dipolar ordering might also be possible due to the large ground-state spin.

5.3 Conclusion

The synthesis and characterization of a homometallic 4f complex have been achieved through a series of experiments. The approach involved the use of acetylacetonate-based ligands as scaffolds for Gd-based nonanuclear complexes, which were synthesized under reflux conditions. The use of acetylacetonates as ligands was found to be successful in bringing several paramagnetic ions(Eu, Gd, Tb, Dy, Ho, Er, Yb) together in a single entity.

Furthermore, the hydrolysis of the solvent into hydroxy group was used as an extra bridging group, leading to the formation of a family of nonanuclear complexes (Chapter 4 and 6). These families possessed highly symmetric motifs, with an hourglass structure comprising two different Gds, in a Gd_9 complex, based on the coordination environments. The complexes exhibited D_{4d} and C_3v symmetries at the center and periphery, respectively, forming a metallic core that resembled two vertex-shared pyramids.

The resulting complex had two distinct Gd ions in the crystal structure, with only two different Gd-Gd distances. The shortest distances were shown in green (3.670 Å) while the longest was shown in yellow (3.765 Å) (**Figure 89**). The magnetic properties of Gd_9 were studied, with a focus on their application in magnetocalorics.

Simulation of the isotropic systems revealed antiferromagnetic interactions operating within the system. This led to a diminished magnetic entropy change compared to that of the non-interacting ions. The antiferromagnetic exchange interactions are deciding whether or not these compounds are of interest for magnetic cooling.

Summarizing the findings, it was observed that signs of geometric spin frustration were evident in magnetization experiments of a molecular nanomagnet. The *M(H)* did not show any saturation until 14 T, which could be a sign of some frustrated systems. More puzzling was the fact that the *M(H)* traces at 1.8 K and 2.0 K showed a plateau between 3 and 4 T. In the present investigation, adiabatic demagnetization experiments are still required through which ΔT_{ad} could be achieved, which is an ongoing work, and which in turn, would decide if this molecule is of any interest as a magnetic coolant.

In general, dipolar interactions limit the temperatures that can be reached in such experiments. These results highlight the importance of the relative magnitudes of the interaction parameters in molecular clusters in terms of their use for MCE. The antiferromagnetic interactions are necessary for spin frustration, which gives rise to large entropy changes. However, if the interactions are too large, then the full magnetic entropy will not be available on (de)magnetization. If, on the other hand, the interactions are too weak, then the MCE will be limited by dipolar interactions.[150] Most studies of the MCE in molecular systems have simply relied on indirect determination of MCE parameters and are blind to these effects.

Chapter 6: Molecular Magnetism- Results and Discussion

Magnetic Properties of Ln-based Nonanuclear Clusters

6.1. Magnetism in Polynuclear SMMs

The current focus of research groups worldwide is on creating multifunctional molecular materials that exhibit more than one physical property within the same molecule or family of compounds.[165] Polynuclear lanthanide complexes, known as 4f metal clusters, are promising candidates for this aim, given their potential contributions to various research areas such as molecular magnetism, optics, catalysis, and medicine.[166] These clusters have the ability to function as single-molecule magnets[167] and photo-luminescence sensitizers,[168] making them particularly interesting for their potential applications in high-density information storage, spintronics, [169] display devices, luminescent sensors, and probes for clinical use.[170]

The magnetic and photophysical properties of these clusters depend on their organic ligands. To synthesize hybrid molecular materials, the choice of the organic ligand becomes particularly important. The organic ligand should contain O-donor atoms to bind to the oxophilic Ln^{3+} ions, have the ability to bridge many metal centers but prevent polymer formation, and contain aromatic groups for enhancing the luminescence intensities. The chances of identifying new 4f metal clusters exhibiting simultaneously interesting magnetic and photophysical properties will benefit from the development of new reaction schemes with suitable organic ligands.

With all of the above in mind, we decided to use benzoylacetone (BA), 9-hydroxyphenalen-1-one (PLN) and 1-pyrenebutane-1,3-dione (PA) for the synthesis of 4f metal clusters possessing large-spin ground states and SMM behavior. Herein we present the Variable-temperature dc and ac magnetic susceptibility studies of families of polynuclear complexes. Some of them display both SMM and upconversion properties (Chapter 4) therefore, the described work represents important steps toward multifunctional SMMs as the work is extended.

6.2. Magnetic Properties of Benzoylacetone (BA) Complexes

Magnetic properties of $[Yb(BA)_3H_2O]$

Ytterbium is the lanthanide element with the highest atomic weight that possesses a trivalent ion exhibiting paramagnetism. The ground state of Yb(III) is represented by ${}^2F_{7/2}$. It has been observed that coordination complexes containing Yb(III) display delayed magnetic relaxation.[171] The temperature dependency of the magnetic response of samples of **$[Yb(BA)_3H_2O]$** referred to as **Yb-Monomer** has been measured in an external magnetic field of 1800 Oe upon cooling from room temperature to 2 K.

The obtained room temperature values of $\chi_{mol}T$ are 2.22 cm^3 K mol^{-1} for **Yb-Monomer** (**Figure 95**). Which is a little smaller than the theoretically expected value of 2.57 cm^3 K mol^{-1} for a single Yb(III) ion at 300 K although within the acceptable 10% error range. There is a consistent decrease in $\chi_{mol}T$ for all Yb containing complexes. This can be attributed to the depopulation of the m_j levels split by the crystal field and the weak antiferromagnetic intermolecular interactions between Yb^{3+} ions. Comparison of the recorded behavior to *ab initio* simulations of the susceptibility, shows a higher, but similar decrease of the experimental data, while the room temperature values are matching nicely. This gradual type of decrease has been reported for other Yb(III)-based compound.[172]

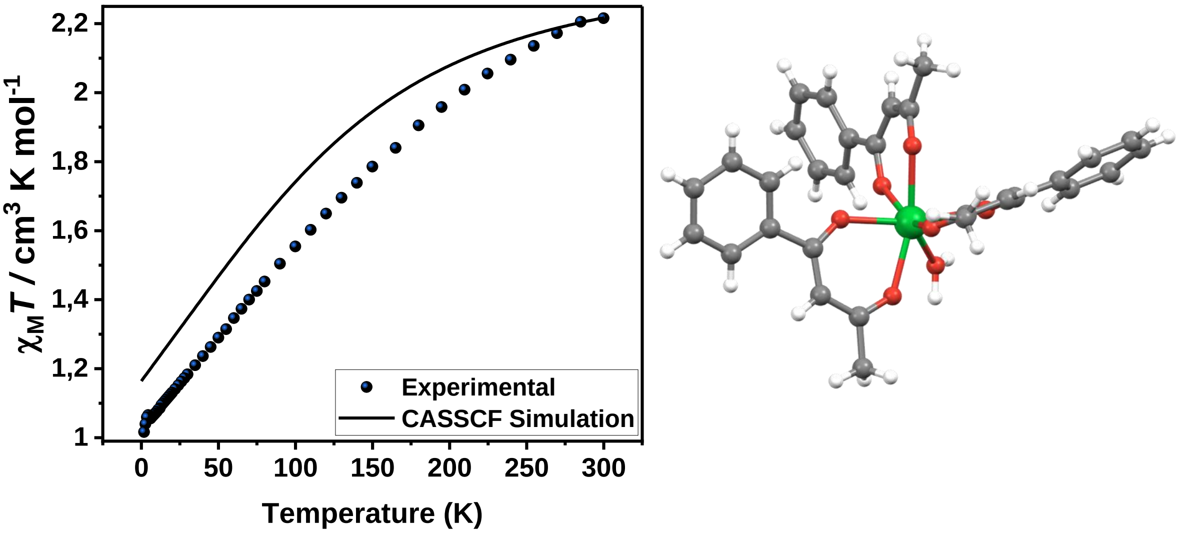

Figure 95. (left) Temperature-product of the molar magnetic susceptibility versus temperature for **Yb-Monomer** (right) crystal structure of **Yb-Monomer.**

Since Yb^{3+} has a prolate electron density and, therefore, is anisotropic, we investigated the magnetization dynamics by *ac* susceptibility measurements on the same sample under an applied dc field of 1800 Oe, in order to establish whether the properties of the single molecule magnets (SMMs) are exhibited. The slow relaxation magnetic behavior, which may originate from the significant separation between the ground and the first excited state, was investigated. No out-of-phase signal was observed at zero dc field, likely due to quantum tunneling of the magnetization (QTM), which is enabled by the mixture of the m_j levels in the ground state. However, a clear out-of-phase signal was observed upon applying a small dc field. Under a static dc field of 1800 Oe, the signal of the ac magnetic susceptibility was optimized in the frequency range of 1 to 1500 Hz, where an out-of-phase signal was observed up to 4.8 K.

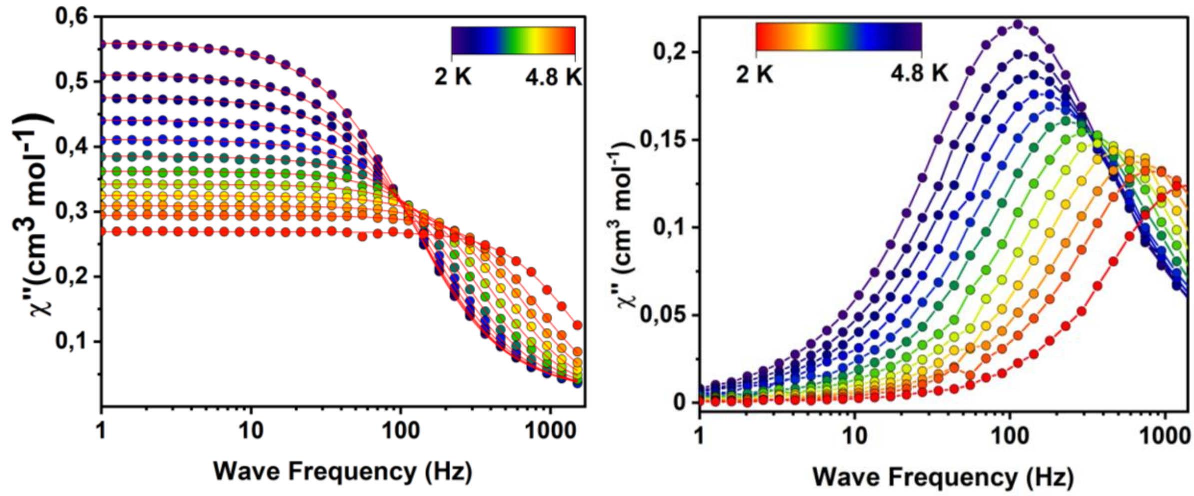

Figure 96. Frequency dependency of the in-phase (left) and out-of-phase (right) components of the magnetic susceptibility for **Yb-Monomer.** The solid lines are the best fits to a generalized Debeye model.

The AC susceptibility data of **Yb-Monomer** (**Figure 96**) show a single relaxation maximum in the out-of-phase component. It is observable in a temperature range from 2 K to 4.8 K, shifting from 121.5 Hz to 1500 Hz in the process. The plots suggest Raman relaxation at low *T*, due to a visible change in the intensity of the frequency shift. Further insights into the magnetic relaxation processes of the complex were achieved by evaluating the ln(τ) vs. T^{-1} plot (**Figure 97**). The distribution of active magnetic relaxation mechanisms is characterized by the α parameters obtained from fits to a generalized Debeye model. The α values obtained for **Yb-Monomer** are found between 13.5 % at 2 K and 1.5 % at 4.8 K, signaling pure Orbach-type relaxation at higher *T*, with other processes, most likely Raman, active at low T. The temperature-dependent relaxation times τ(T) obtained from the Debeye fits were fit using the following equation, employing Raman- and Orbach-type relaxation mechanisms.

$$\tau^{-1} = \tau_0^{-1} \exp(-U_{eff}/k_B T) + CT^m + \tau_{QTM}^{-1}$$

The fitting yielded the relaxation parameters τ_0 = (3.13 ± 0.37) x 10^{-7} s, U_{eff} = (29.46 ± 1.4) K (20.16 cm^{-1}), C = (11.85 ± 8.3) s $\mathrm{K}^{-3.90}$, and m = 3.90 ± 0.6 for **Yb-Monomer.**

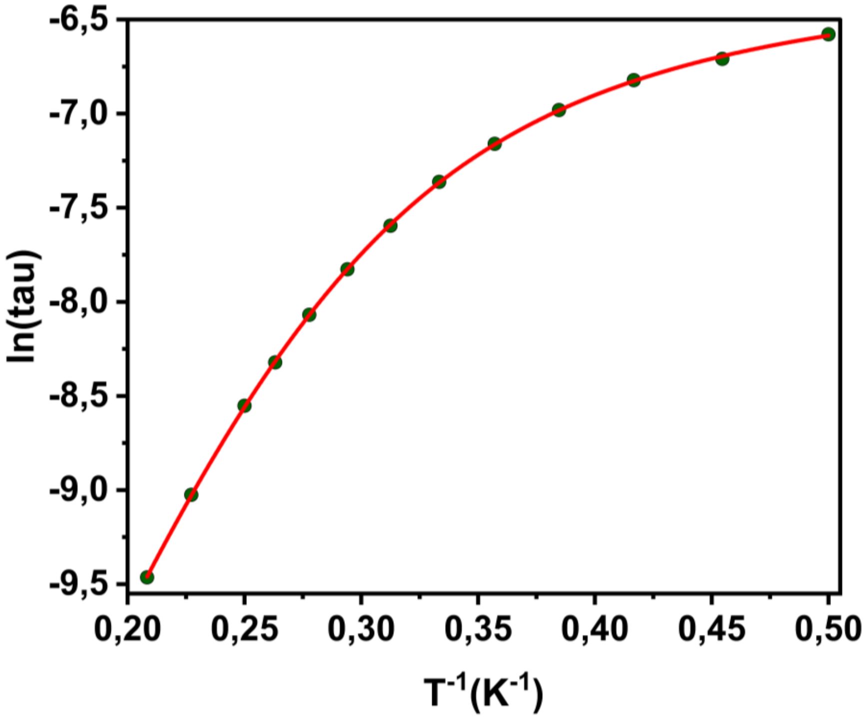

Figure 97. Arrhenius plot for **Yb-Monomer.**

Magnetic properties of $[Eu_8Yb(BA)_{16}(OH)_{10}]Cl$

$[Yb_9(BA)_{16}(OH)_{10}]Cl$ did not show any slow relaxation magnetic behavior when investigated the magnetic properties through the ac susceptibility measurements. Therefore, We moved on to the **$[Eu_8Yb(BA)_{16}(OH)_{10}]Cl$** (will be addressed as **Eu_8Yb** from here on). Despite the lack of magnetic interest in Eu(III) due to the spin-orbit coupled $J = 0$ ground state, materials and molecular complexes based on Eu(III) have found extensive application as emissive components in optical devices. These materials exhibit bright emission throughout the visible spectrum with lifetimes that are significantly longer than those observed for other Ln(III) ions.

We synthesized a **Eu_8Yb** complex to take advantage of a system with both Eu(III) and Yb(III) ions. This is interesting from both magnetic and optical perspectives. For SMMs based on Yb,

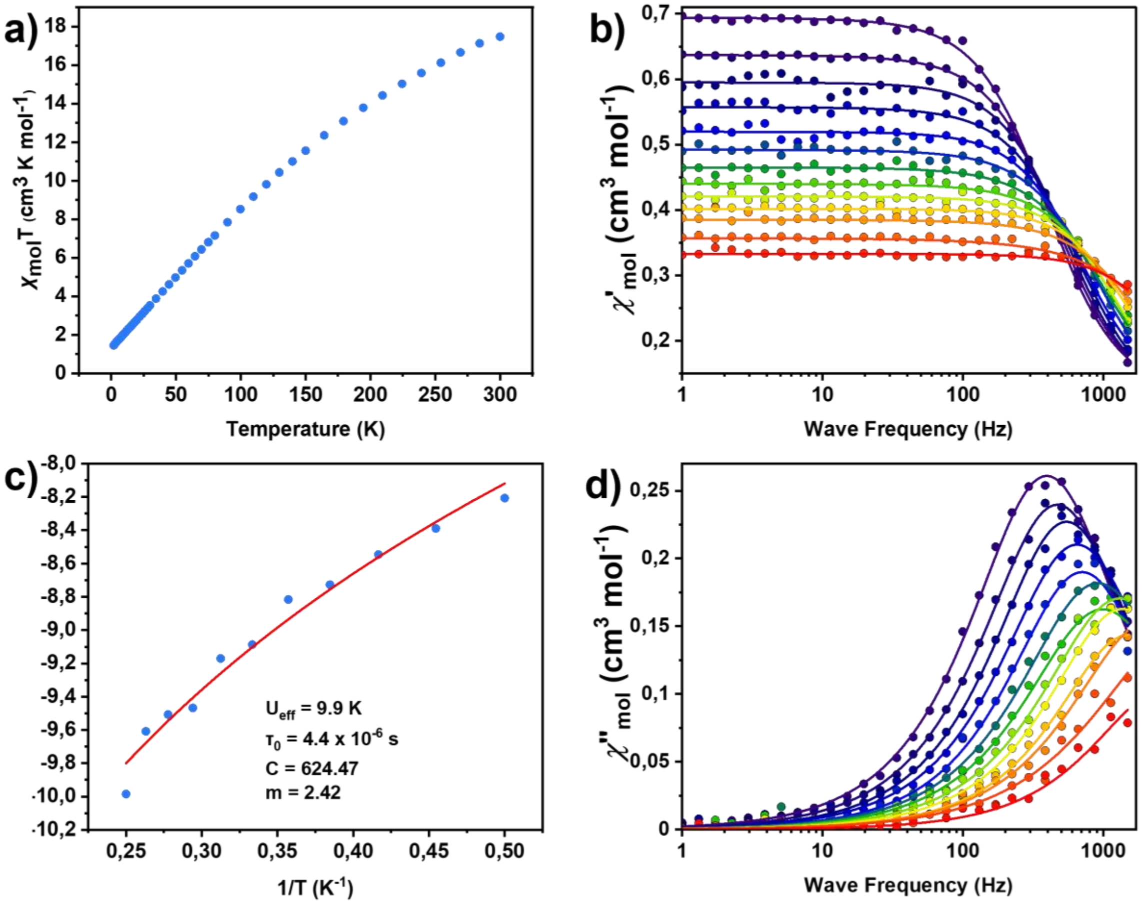

Figure 98. a) **Eu_8Yb** DC Fit: Temperature product of the molar susceptibility vs. Temperature. c) Temperature dependence of the magnetization relaxation times (s), with the solid line representing the best fit using eqn above; (b, d) in-phase and out of phase susceptibilities vs. frequency fits of Eu_8Yb under 1750 Oe applied dc field (Debeye model).

a strong axial magnetic anisotropy would be required, and with appropriate system designs, the energy barriers of magnetization reversal can reach as high as 45 cm^{-1}. Additionally, Yb complexes that emit in the Near Infrared (NIR) region are particularly fascinating due to the potential for combining magnetic properties with luminescence, providing prospects for advanced information storage and quantum computing applications.

We analyzed the dc magnetic behavior of **Eu_8Yb** (using a weighted average of all the clusters as MW found in the Mass spectrum under a 1000 Oe magnetic field in the temperature range of 2-300 K. (**Figure 98a**) shows the corresponding $\chi_m T$ vs. T dependencies. As the temperature decreases from 300 K to 2 K, there is a consistent decrease in $\chi_m T$ for all nonisotropic lanthanide containing complexes. This can be attributed to the depopulation of the m_j levels split by the crystal field and the weak antiferromagnetic intermolecular interactions between Ln^{3+} ions. The dependencies of $\chi_m T$ vs. T, especially the low value at low T, indicate the incorporated Eu^{3+} ion's absence of thermally populated excited states (J = 1) and highlight their decisive effect on the dc magnetic behavior. Therefore, the sole contributor of $\chi_m T$ at 2 K is Yb^{3+}, which explains the very low value, as Eu^{3+} has no contribution at such low temperatures. In contrast, at 300 K, the $\chi_m T$ value is 17.47 cm^3 K mol^{-1}, and the calculated value is eight times 1.7 (Eu^{3+}) and 2.57 (Yb^{3+}) = 16.14 cm^3 K mol^{-1} for nine non-interacting ions. The small discrepancy is within the acceptable range of a 10% error. Since Yb^{3+} has a prolate electron density and, therefore, is anisotropic, we investigated the magnetization dynamics by ac susceptibility measurements on the same sample under an applied dc field of 1750 Oe, in order to establish whether the properties of the single molecule magnets (SMMs) are exhibited (**Figure 98b, d**). The slow relaxation magnetic behavior, which may originate from the significant separation between the ground and the first excited state, was investigated. No out-of-phase signal was observed at zero dc field, likely due to quantum tunneling of the magnetization (QTM), which is enabled by the mixture of the m_j levels in the ground state. However, a clear out-of-phase signal was observed upon applying a small dc field. Under a static dc field of 1750 Oe, the signal of the ac magnetic susceptibility was optimized in the frequency range of 1 to 1500 Hz, where an out-of-phase signal was observed up to 4 K (**Figure 98d**). These data were fit to a generalized Debye model from which a distribution (α) of relaxation times (τ) can be extracted. Further insights into the magnetic relaxation processes of the complex were achieved by evaluating the ln(τ^-) vs. T^{-1} plot (**Figure 98c**). Considerable deviation from the linear course of the dependencies evidences the occurrence of the relaxation mechanisms additional or different from the Orbach one. The fittings by the sets of mechanisms other than the Raman and Orbach fit were unsatisfactory and/or led to overparameterization. As a consequence, we approximated the relaxation data in the entire temperature range by the Raman and Orbach relaxation mechanism. The fitting yielded the relaxation parameters $\tau_0 = (4.4 \pm 0.4) \times 10^{-6}$ s, $U_{\text{eff}} = (9.9 \pm 1.5)$ K (7 cm^{-1}), C = 624.47 s $\text{K}^{-2.27}$, and m = 2.27 ± 0.14 for **Eu$_8$Yb**.

The Cole-Cole plots give a proper visual representation (**Figure 99**), showing the symmetric (circular arcs) but more asymmetric behavior (broken circular arcs) of Eu$_8$Yb, suggesting a narrow distribution of relaxation processes.

These parameters indicate that the **Eu$_8$Yb** cluster exhibits SMM behavior, characterized by a relatively short relaxation time and a moderate energy barrier, especially when compared to other SMMs based on Yb$^{\text{III}}$ reported in the literature.[173] This is, to the best of our knowledge, the first example of a Yb$^{\text{III}}$-based SMM that also possesses upconversion properties (as illustrated in chapter 4). Throughout the temperature range (2 – 4 K), the temperature dependency of the tau confirms the presence of a Raman relaxation process. Finally, at high temperatures, deviation from this exponential behavior might suggest the onset of an Orbach

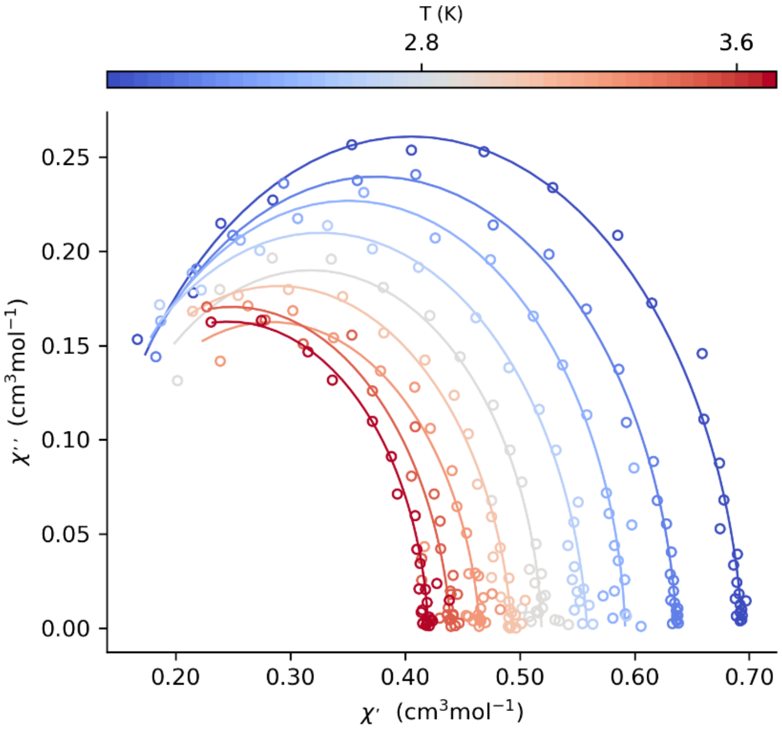

Figure 99. Cole-Cole plots for Eu$_8$Yb. The solid lines are the best fits to a generalized Debeye model.

relaxation mechanism, which has been observed in a limited number of Yb^{III}-based complexes. [174-176]

Since $[Yb_9(BA)_{16}(OH)_{10}]Cl$ is not an SMM but **Eu_8Yb** is one. we suspected strong anti-ferromagnetic interactions between the Ln^{3+} ions within the nonanuclear moiety as the Ln-Ln distances are less than 4Å. Keeping this in mind we synthesiszed a series of complexes diluted with Y to see the impact and effect of dilution on the slow relaxation magnetic behavior.

Magnetic Properties of $[Tb_{0.5}Y_{8.5}(BA)_{16}(OH)_{10}]Cl$

$[Tb_{0.5}Y_{8.5}(BA)_{16}(OH)_{10}]Cl$ will be referred as **$Tb_{0.5}Y_{8.5}$-BA**. Generally non-Kramers ions are less likely to exhibit SMM behavior, due to the bistability of the ground state not being an intrinsic feature. Tb(III) is the most studied non-Kramers ion in molecular magnetism, based on the discovery of lanthanide based SMM behavior in $TbPc_2$ and many following studies. [177-179] The DC magnetic behavior is shown in (**Figure 100**). It was measured upon cooling polycrystalline sample of **$Tb_{0.5}Y_{8.5}$-BA** from 300 K to 2 K in an external field of 1000 Oe.

The observed room temperature value is 11.54 cm^3 K mol^{-1}(normalized by a factor of 2 to adjust the scale to one the scale to one Tb ion) for **$Tb_{0.5}Y_{8.5}$-BA** in good agreement with the

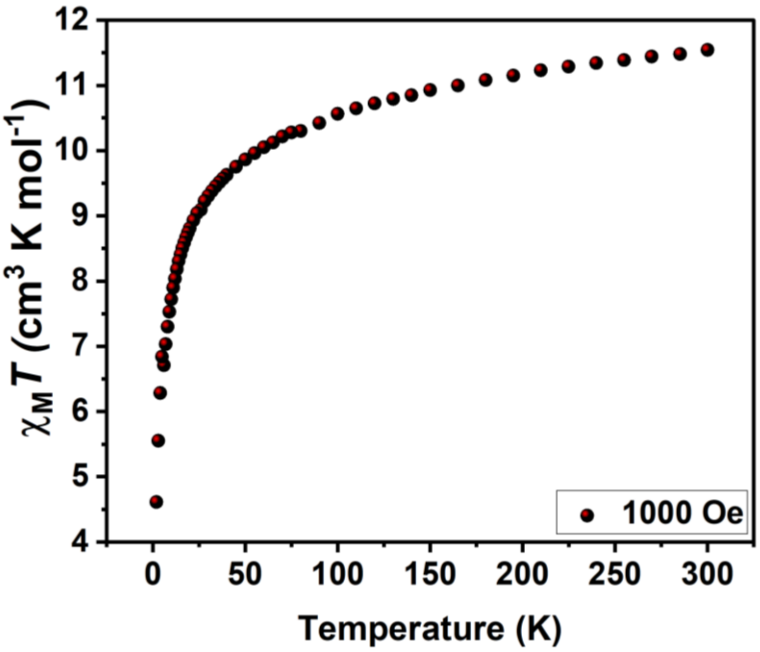

Figure 100. Temperature-product of the molar magnetic susceptibility versus temperature for **$Tb_{0.5}Y_{8.5}$-BA**.

theoretical value of 11.82 cm^3 K mol^{-1} for a single Tb(III) ion with J = 6 and g$_J$ = 3/2. The experimental $\chi_m T$ remains constantly depleted upon cooling until 50 K and then a sharp nose-dive all the way until 2K related to the intermolecular magnetic coupling including the usual depopulation of the Stark levels for **Tb$_{0.5}$Y$_{8.5}$-BA**.

The dynamic magnetic relaxation behavior has been studied using AC susceptibility techniques (**Figure 101**). **Tb$_{0.5}$Y$_{8.5}$-BA** did not exhibit any out-of-phase signal with or without an external magnetic field within the frequency range of 0 to 1500 Hz. Tb(III) is a non-Kramers ion, meaning the degeneracy of the m$_J$ -states of opposing magnetization is an intrinsic feature. However, the AC curves at 2 K over various fields did show a traces of the slow relaxation magnetic behavior outside the frequency range of 1500 Hz. The absence of strong slow relaxation magnetic behavior is most likely a result of a non degenerate ground state and a lack of proper ligand field to maximize the oblate anisotropy of a Tb(III) ion.

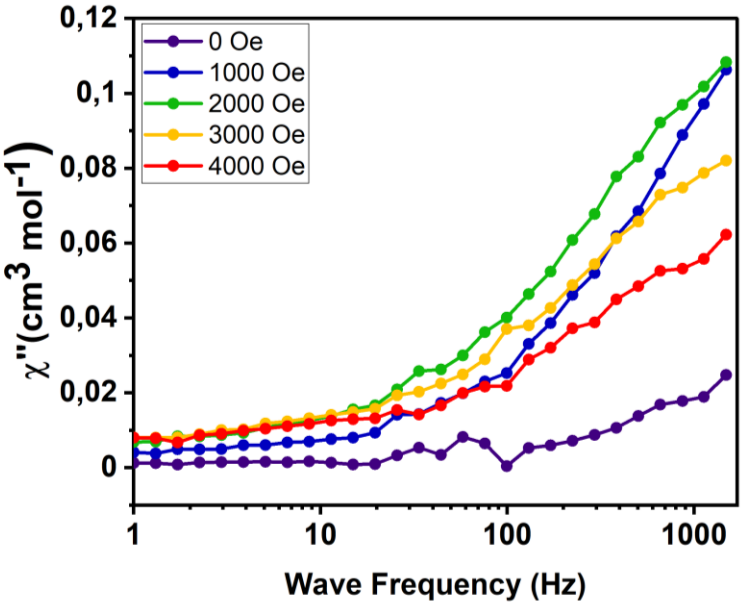

Figure 101. Frequency dependency of the out-of-phase components of the magnetic susceptibility at 2K over different external fields for **Tb$_{0.5}$Y$_{8.5}$-BA**.

The field dependence of magnetization of **$Tb_{0.5}Y_{8.5}$-BA** was evaluated at different temperatures 2, 3, 4, and 5 K in the magnetic field range of 0−7 T (**Figure 102**). The sharp increase of magnetization at low field at low temperatures reveals a significant energy difference between the ground and excited states. Additionally, as the external field is increased, the magnetization value increases and reaches 2.7 μ_B for complex $Tb_{0.5}Y_{8.5}$ at 7 T and shows signs of saturation at the higher fields. The *M*(*H*) value is consistent with the expected one (2.25 μ_B) for a half equivalent Tb(III) ion with a $J = 6$ ground state in the lower field (H< 3.5 T) region.

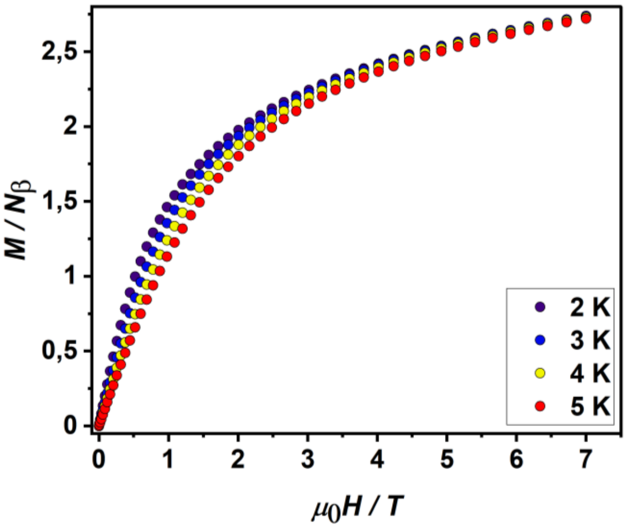

Figure 102. Plots of M vs. H at different temperatures

Magnetic Properties of $[Dy_{0.5}Y_{8.5}(BA)_{16}(OH)_{10}]Cl$

$[Dy_{0.5}Y_{8.5}(BA)_{16}(OH)_{10}]Cl$ will be referred to as **$Dy_{0.5}Y_{8.5}$-BA** from here on. Dy(III) is the most commonly used Ln(III) ion in molecular magnetism. This is because of its highly magnetic (J = 15/2) and anisotropic ground state. The ground state bistability is guaranteed because Dy(III) is also a Kramers ion. For a long time, Dy(III)- based compounds have held the record for being the most effective SMMs in terms of their effective energy barrier.[180-182] In an external magnetic field of 1000 Oe, the temperature dependent DC susceptibility was recorded upon cooling **$Dy_{0.5}Y_{8.5}$-BA** from 300 K to 2 K.

The room temperature $\chi_m T$ value for **Dy$_{0.5}$Y$_{8.5}$-BA** was found at 14.12 cm^3 K mol^{-1} (normalized by a factor of 2 to adjust the scale to one to one Dy ion) (**Figure 103**) which is in good agreement to the theoretical value expected for a single Dy(III) ion of 14.17 cm^3 K mol^{-1}. The temperature dependence is characterized by a constant dwindling of $\chi_m T$ upon cooling related to the intermolecular magnetic coupling including with the depopulation of the Stark levels for **Dy$_{0.5}$Y$_{8.5}$-BA**.

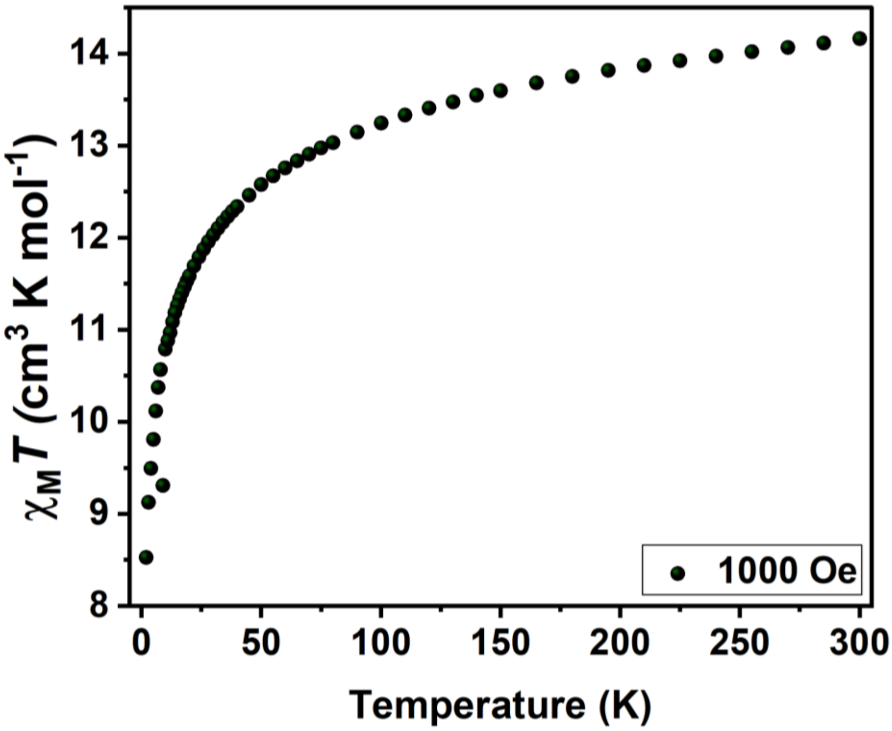

Figure 103. Temperature-product of the molar magnetic susceptibility versus temperature for **Dy$_{0.5}$Y$_{8.5}$-BA**.

The dynamic magnetic relaxation behavior has been studied using AC susceptibility techniques (**Figure 105**). **Dy$_{0.5}$Y$_{8.5}$-BA** did not exhibit any out-of-phase signal with or without an external magnetic field within the frequency range of 0 to 1500 Hz. However, the AC curves at 2 K over various fields did show a traces of the slow relaxation magnetic behavior outside the frequency range of 1400 Hz. This suggests a rather poor stability of the oblate distribution of the ground state and a lack of proper ligand field to maximize the oblate anisotropy of a Dy(III) ion.

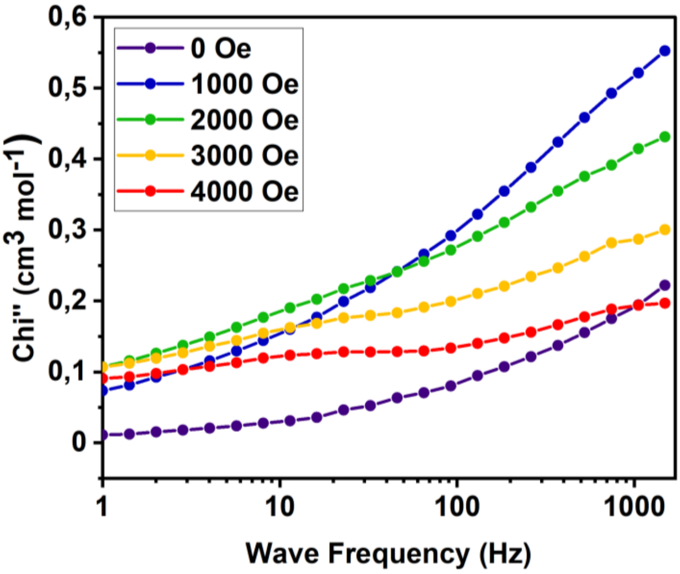

Figure 104. Frequency dependency of the out-of-phase components of the magnetic susceptibility at 2K over different external fields for **Dy$_{0.5}$Y$_{8.5}$-BA.**

The field dependence of magnetization of **Dy$_{0.5}$Y$_{8.5}$-BA** was evaluated at different temperatures 2, 3, 4, and 5 K in the magnetic field range of 0−7 T (**Figure 104**). The sharp increase of magnetization at low field at low temperatures reveals a significant energy difference between the ground and excited states. Additionally, as the external field is increased, the magnetization value increases and reaches saturation at 2.23 μ_B for complex **Dy$_{0.5}$Y$_{8.5}$-BA** at 7 T. The M (H) value is consistent with the expected one (2.5 μ_B) for a half equivalent Dy(III) ion with a well-defined J = 15/2 ground doublet.

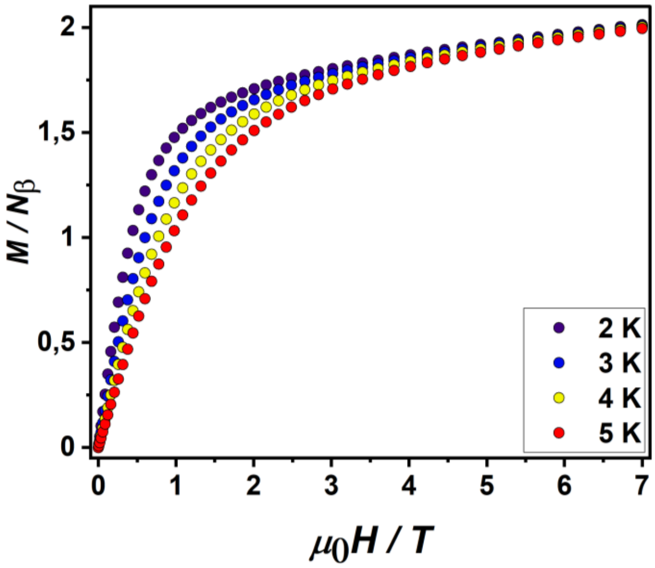

Figure 105. Plots of M vs. H at different temperatures.

Magnetic Properties of $[Ho_{0.5}Y_{8.5}(BA)_{16}(OH)_{10}]Cl$

$[Ho_{0.5}Y_{8.5}(BA)_{16}(OH)_{10}]Cl$ is referred as **$Ho_{0.5}Y_{8.5}$-BA**. Ho(III) is the lanthanide element that has been observed to possess the highest total angular momentum $J = 8$. Apart from Dy(III), which has the highest magnetic moment, Ho(III) is the lanthanide ion with the second-highest magnetic moment. Numerous Ho(III) single-molecule magnets have been reported, showcasing a broad spectrum of observed energy barriers.[183, 184] The magnetic response of **$Ho_{0.5}Y_{8.5}$-BA** was tested upon cooling from 300 K to 2 K in an applied magnetic field of 1000 Oe. The magnetic response of **$Ho_{0.5}Y_{8.5}$-BA** was tested upon cooling from 300 K to 2 K in an applied magnetic field of 1000 Oe.

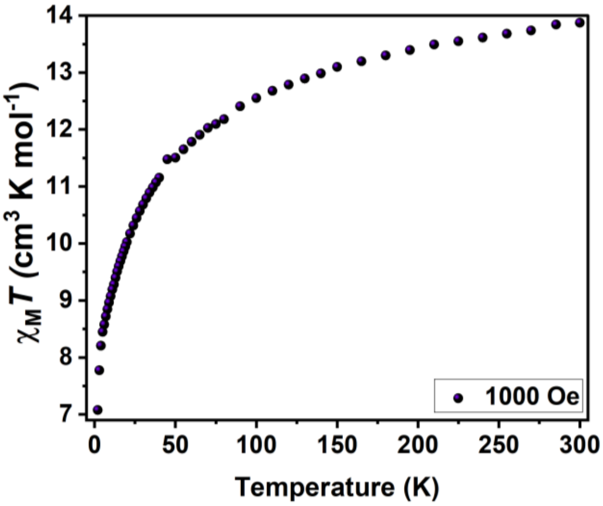

Figure 106. Temperature-product of the molar magnetic susceptibility versus temperature for **$Ho_{0.5}Y_{8.5}$-BA**.

The room temperature $\chi_m T$ value for **$Ho_{0.5}Y_{8.5}$-BA** was found at 13.87 cm^3 K mol^{-1} (normalized by a factor of 2 to adjust the scale to one to one Ho ion) (**Figure 106**) which is in good agreement to the theoretical value expected for a single Ho(III) ion of 14.07 cm^3 K mol^{-1}. The temperature dependence is characterized by a constant tail-off of $\chi_m T$ upon cooling related to the intermolecular magnetic coupling including with the depopulation of the Stark levels for **$Ho_{0.5}Y_{8.5}$-BA**.

Performing dynamic AC susceptibility studies (**Figure 107**), no out-of-phase signal was observed for **$Ho_{0.5}Y_{8.5}$-BA**. Also, the application of an external field, did not result in an observable χ ″ signal. Ho(III) is a non-Kramers ion, meaning the degeneracy of the m_J -states of opposing magnetization is an intrinsic feature. However, the AC curves at 2 K over various fields did show a traces of the slow relaxation magnetic behavior outside the frequency range of 1500 Hz. The abscence of strong slow relaxation magnetic behavior is most likely a result of a non-degenerate ground state and a lack of a proper ligand field to maximize the oblate anisotropy of a Ho(III) ion.

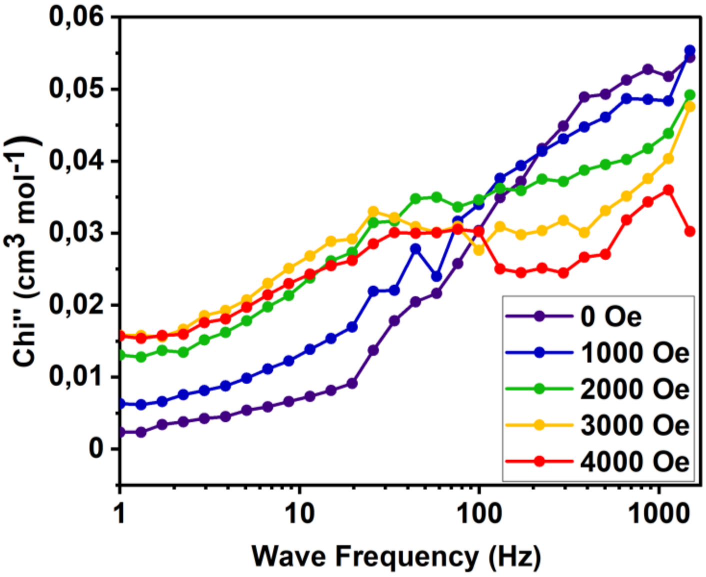

Figure 107. Frequency dependency of the out-of-phase components of the magnetic susceptibility at 2K over different external fields for **$Ho_{0.5}Y_{8.5}$-BA**.

The field dependence of magnetization of **$Ho_{0.5}Y_{8.5}$-BA** was evaluated at different temperatures 2, 3, 4, and 5 K in the magnetic field range of 0−7 T (**Figure 108**). The sharp increase of magnetization at low field at low temperatures reveals a significant energy difference between the ground and excited states. Additionally, as the external field is increased, the magnetization value increases and reaches at 2.34 μ_B for complex **$Ho_{0.5}Y_{8.5}$-BA** at 7 T. The *M*(*H*) value is consistent with the expected one (2.5 μ_B) for a half equivalent of Ho(III) ion with a well-defined *J* = 8 ground doublet.

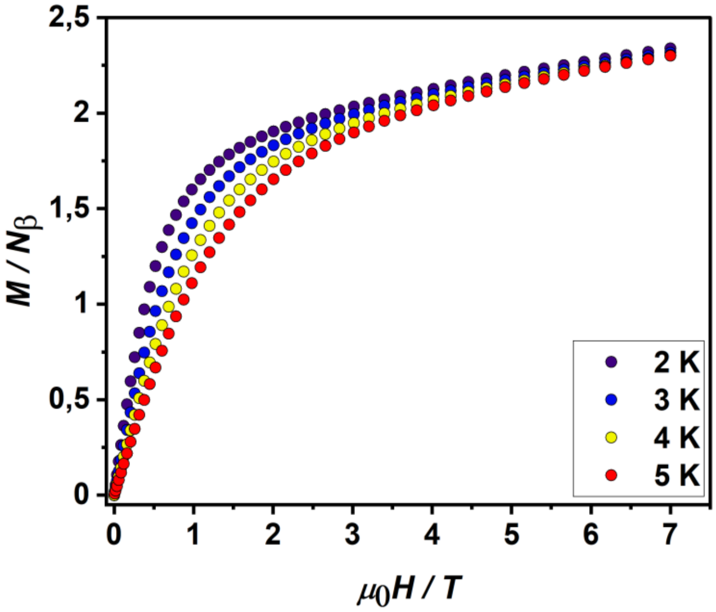

Figure 108. Plots of M vs. H at different temperatures

Magnetic Properties of [$Er_{0.5}Y_{8.5}(BA)_{16}(OH)_{10}$]Cl

[$Er_{0.5}Y_{8.5}(BA)_{16}(OH)_{10}$]Cl is referred to as **$Er_{0.5}Y_{8.5}$-BA**. Er(III) ions are frequently used for creating single-molecule magnets, alongside dysprosium-based compounds. The angular momentum of Er(III) ions is the same as that of dysprosium ions, with a value of J = 15/2. However, the gyromagnetic constant g_J = 6/5 of erbium causes their observed magnetic moment to be lower than that of Tb(III), Dy(III), and Ho(III) ions. it has been mentioned in the introduction that the electron density distribution of Er(III) is strongly prolate, indicating that equatorial ligand arrangements are advantageous for observing high energy barriers to slow magnetic relaxation.[98, 185, 186] Interestingly, since the electron density distribution of Dy(III) is oblate, the Er(III) counterpart of a high-performance Dy(III)-SMM often exhibits a low energy barrier, and vice versa.

Being a Kramers ion, Er(III) is guaranteed to have doubly degenerate m_J states, making slow relaxation highly probable. The static DC magnetic response of **$Er_{0.5}Y_{8.5}$-BA** was analyzed in an external field of 1000 Oe over a temperature range of 300 K to 2 K, with the T-dependent $\chi_{mol}T$ shown in **Figure 109**.

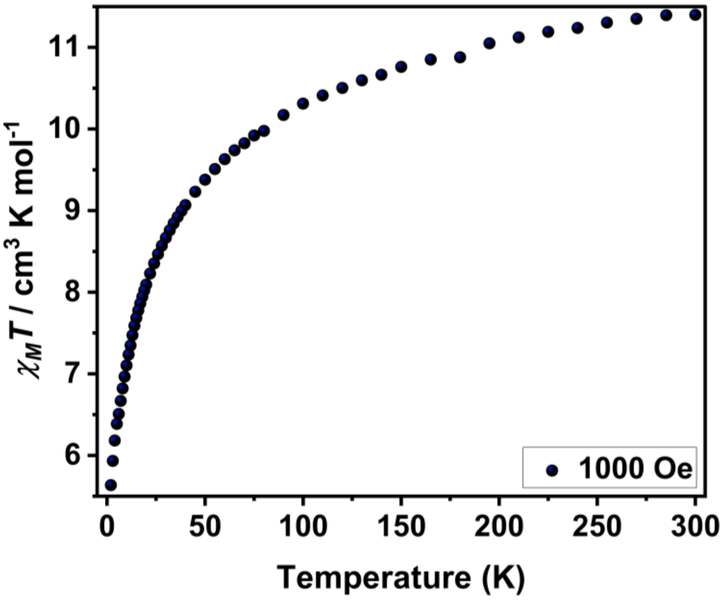

Figure 109. Temperature-product of the molar magnetic susceptibility versus temperature for **Er$_{0.5}$Y$_{8.5}$**.

At room temperature the observed $\chi_{mol}T$ value is 11.39 cm^3 K mol^{-1} for **Er$_{0.5}$Y$_{8.5}$-BA**, respectively (normalized by a factor of 2 to adjust the scale to one to one Er ion). The measured values are in good agreement with the theoretical value of 11.48 cm^3 K mol^{-1} for a single Er(III) ion. The temperature dependence is characterized by a constant dwindling of $\chi_m T$ upon cooling related to the intermolecular magnetic coupling including the depopulation of the Stark levels for **Er$_{0.5}$Y$_{8.5}$-BA**.

Testing the dynamic behavior through *ac* susceptibility measurements, **Er$_{0.5}$Y$_{8.5}$-BA** did not show any signal in the out-of-phase component of the susceptibility that could be linked to slow magnetic relaxation under zero field. Under the application of an external field, a signal appeared and the optimal field was found to be 1600 Oe (**Figure 110**). The absence of any signal at zero field suggests efficient quantum tunneling within the ground state Kramers doublet, allowing fast relaxation and, therefore, quenching zero-field SMM behavior. The frequency-dependent in-phase and out-of-phase components of **Er$_{0.5}$Y$_{8.5}$-BA** is given in **Figure 113**. **Er$_{0.5}$Y$_{8.5}$-BA** reveals a single maximum in the out-of-phase component around 1400 Hz at the lowest temperature of 2 K. It decreases in intensity and very slowly shifts to higher frequencies until 2.5 K, where the frequency shift gets more pronounced and moves out of the range. This behavior is typical for magnetic relaxation, that is dominated by Raman processes at low T. Fits of the ac susceptibilities of **Er$_{0.5}$Y$_{8.5}$-BA** to a generalized Debeye model have been performed. The α parameters obtained are in the range between 22 % at 2 K and 37 % at 2.5 K. The decrease in both cases indicates the onset of active Raman relaxation at low T.

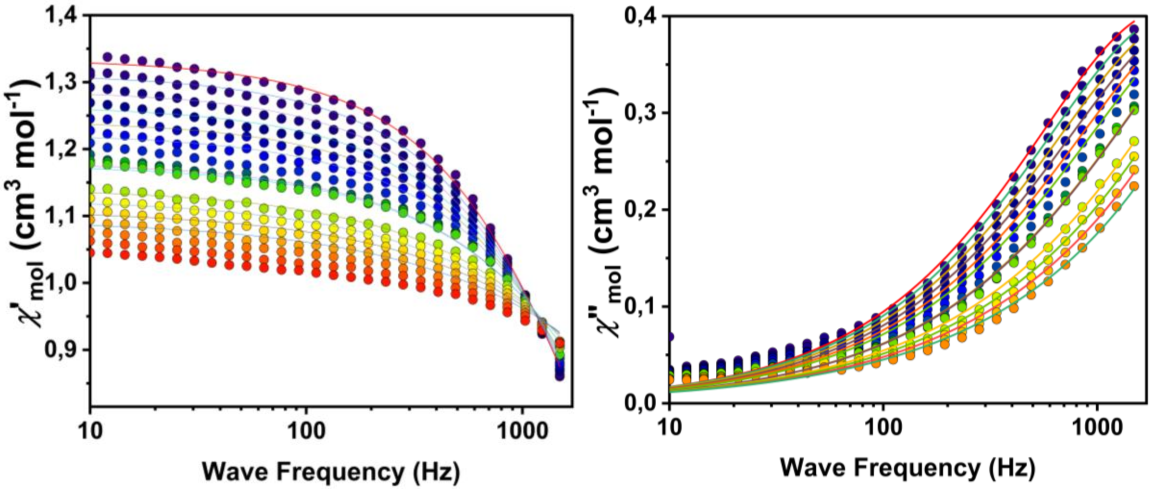

Figure 110. Frequency dependency of the in-phase (left) and out-of-phase (right) components of the magnetic susceptibility for **$Er_{0.5}Y_{8.5}$-BA**. The solid lines are the best fits to a generalized Debeye model.

The temperature-dependent relaxation times for **$Er_{0.5}Y_{8.5}$-BA** were fitted obtaining good agreements employing Raman and Orbach relaxation processes (**Figure 111**). The best fits for Er were obtained using a combination of Direct and Raman relaxation. The best fit parameters for **$Er_{0.5}Y_{8.5}$-BA** were τ_0 = (1.73 ± 0.18) x 10^{-7} s, U_{eff} = 12.23 K (8.43 cm^{-1}), C = 1117.48 s

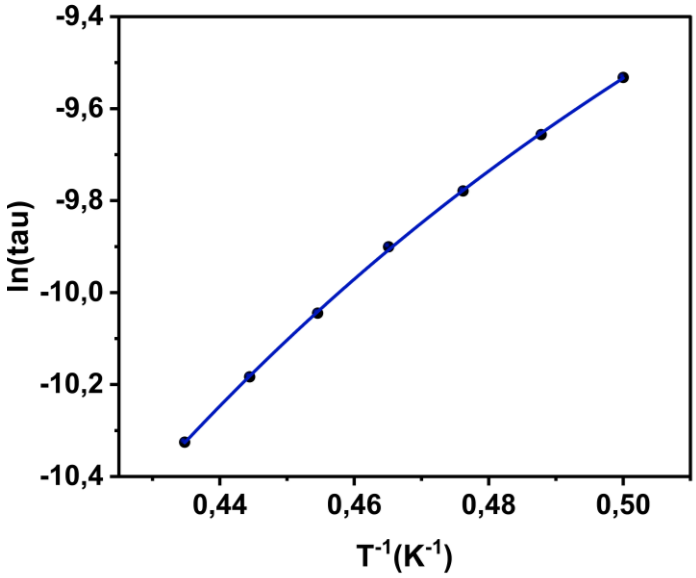

Figure 111. Arrhenius plots for **$Er_{0.5}Y_{8.5}$-BA**.

$K^{-3.46}$ and n = 3.46. Being a prolate anisotropy ion, **$Er_{0.5}Y_{8.5}$-BA** following our hypothesis is a field induced SMM. Even if it is not the best performing SMM as we had expected.

The field dependence of magnetization of **$Er_{0.5}Y_{8.5}$-BA** was evaluated at different temperatures 2, 3, 4, and 5 K in the magnetic field range of 0−7 T (**Figure 112**). The sharp increase of magnetization at low field at low temperatures reveals a significant energy difference between the ground and excited states. Additionally, as the external field is increased, the magnetization value increases and reaches saturation at 2,245 μ_B for complex $Er_{0.5}Y_{8.5}$ at 7 T. The $M(H)$ value is consistent with the expected one (2.25 μ_B) for a half equivalent Er(III) ion with a well-defined J = 15/2 ground doublet.

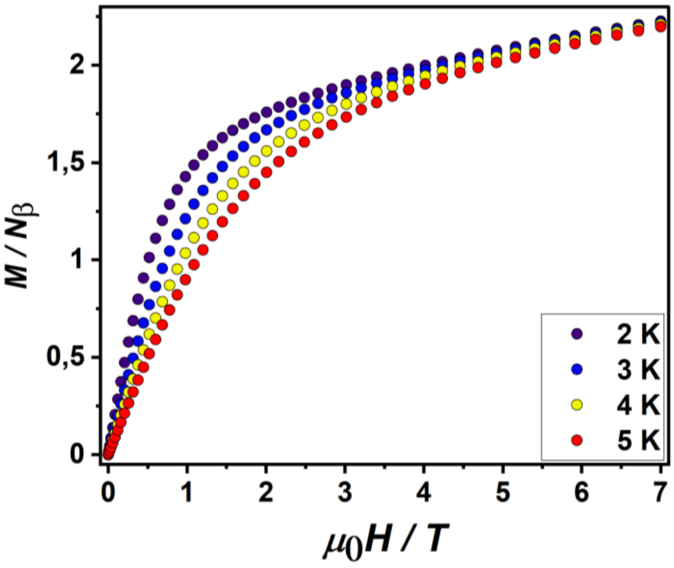

Figure 112. Plots of M vs. H at different temperatures.

Magnetic Properties of $[Tm_{0.5}Y_{8.5}(BA)_{16}(OH)_{10}]Cl$

$[Tm_{0.5}Y_{8.5}(BA)_{16}(OH)_{10}]Cl$ is referred to as **$Tm_{0.5}Y_{8.5}$-BA**. Tm(III) complexes are not often studied in the literature because thulium is the rarest of the Lanthanides. The ground state produced by SOC for Tm(III) is $^4H_6$, which has a gyromagnetic constant of g_J = 7/6. Tm(III) has a relatively strong magnetic moment due to this. However, the reports of Tm(III)-based SMMs are rare because trivalent thulium ions are non-Kramers in nature.[173, 183] The temperature dependence of the magnetic susceptibilities of **$Tm_{0.5}Y_{8.5}$-BA** was measured in an external field

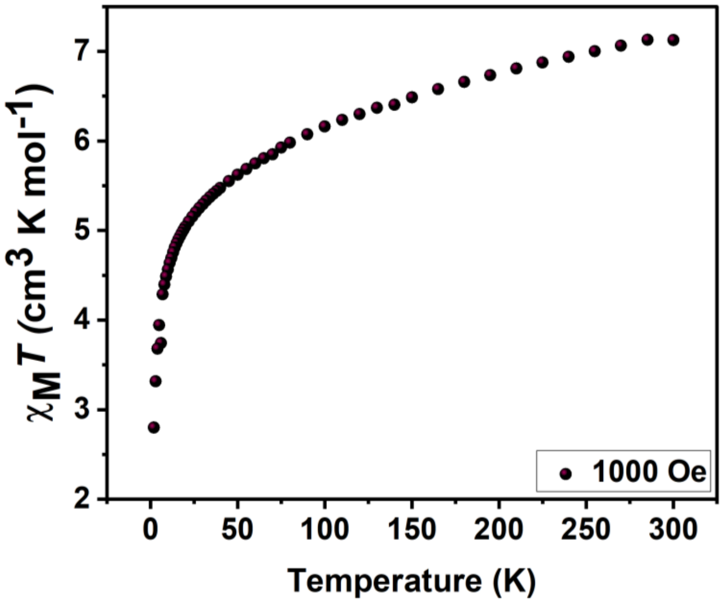

Figure 113. Temperature-product of the molar magnetic susceptibility versus temperature for **Tm$_{0.5}$Y$_{8.5}$-BA**.

of 1000 Oe upon cooling the samples from room temperature to 2 K. **Figure 113** shows the recorded behavior.

At room temperature the $\chi_{mol}T$ value has been found at 7.04 cm^3 K mol^{-1} for **Tm$_{0.5}$Y$_{8.5}$-BA** (normalized by a factor of 2 to adjust the scale to one Tm ion). which is in good agreement with the value predicted by Curie's law of 7.17 cm^3 K mol^{-1} for a single Tm(III) ion. Upon cooling, the observed $\chi_{mol}T$ values decrease increasingly strong reaching the lowest value of 2.74 cm^3 K

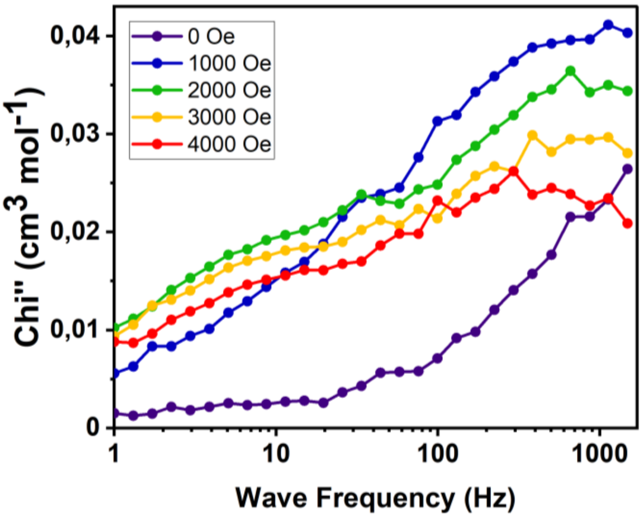

Figure 114. Frequency dependency of the out-of-phase components of the magnetic susceptibility at 2K over different external fields for **Tm$_{0.5}$Y$_{8.5}$-BA**.

mol^{-1}. Generally, $\chi_{mol}T$ values close to zero can suggest the presence on antiferromagnetic interactions between neighbouring Ln(III) ions.

In order to probe the samples for SMM characteristics, dynamic AC susceptibility measurements have been performed (**Figure 114**). **Tm$_{0.5}$Y$_{8.5}$-BA** did not reveal an observable signal in χ'' mol(ν) at zero field, as well as under the application of an external magnetic field. We know that the smaller Tm(III) prefers the peripheral site and the larger Y(III) the central site. The coordination that is exerted by the benzoylacetone ligands and the OH$^-$ groups are highly asymmetric in the peripheral site as measured from the shape analysis, C_{2v}. With that, the ZFS induced by the ligand field is unlikely to yield degeneracy of the ground state, as it is not a guaranteed property, similar to Kramers ions.

Magnetic properties of [Yb$_{0.5}$Y$_{8.5}$(BA)$_{16}$(OH)$_{10}$]Cl

[Yb$_{0.5}$Y$_{8.5}$(BA)$_{16}$(OH)$_{10}$]Cl is referred to as **Yb$_{0.5}$Y$_{8.5}$-BA**. The heaviest element of the lanthanides with a paramagnetic trivalent ion is ytterbium, with the $^2F_{7/2}$ ground state. It is a prolate ion and also a Kramers ion.. Coordination complexes of Yb(III) have been reported to show slow magnetic relaxation as well as photoluminescent emission in the IR-region of the electromagnetic spectrum.[61, 173, 183] The temperature dependency of the magnetic response of **Yb$_{0.5}$Y$_{8.5}$-BA** has been measured in an external magnetic field of 1000 Oe upon cooling from room temperature to 2 K. (**Figure 116**)

The obtained room temperature values of $\chi_{mol}T$ are 2.68 cm^3 K mol^{-1} for **Yb$_{0.5}$Y$_{8.5}$-BA** (normalized by a factor of 2 to adjust the scale to one to one Yb ion). Which is in very good agreement with the theoretically expected value of 2.57 cm^3 K mol^{-1} for a single Yb(III) ion at 300 K. The T-dependency of **Yb$_{0.5}$Y$_{8.5}$-BA** is characterized by a very steady decrease. This gradual type of decrease has been reported for other Yb(III)-based compounds.[172] As it has been observed for the samples of the other Kramers ion complexes. A small drop is observed at 4 K, possibly due to weak intermolecular antiferromagnetic interactions.

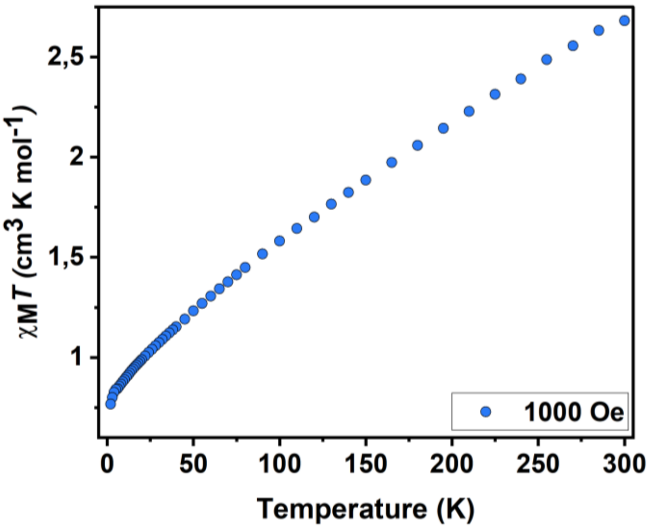

Figure 115. Temperature-product of the molar magnetic susceptibility versus temperature for **Yb$_{0.5}$Y$_{8.5}$-BA**.

No out-of-phase signal was observed in the absence of an external magnetic field, but slow relaxation has been observed once an external field is applied supporting the claim of ligand field ideal for prolate anisotropy. The optimal field was found at 2400 Oe, for **Yb$_{0.5}$Y$_{8.5}$-BA**. The in-phase and out-of-phase components of the magnetic susceptibility recorded at different temperatures are given in **Figure 117**.

The *ac* susceptibility data of **Yb$_{0.5}$Y$_{8.5}$-BA** shows a single relaxation maximum in the out-of-phase component. It is observable in a temperature range from 2 K to 4 K, shifting from 110 Hz to 1500 Hz in the process. The dataset suggests Raman relaxation at low T, due to a visible

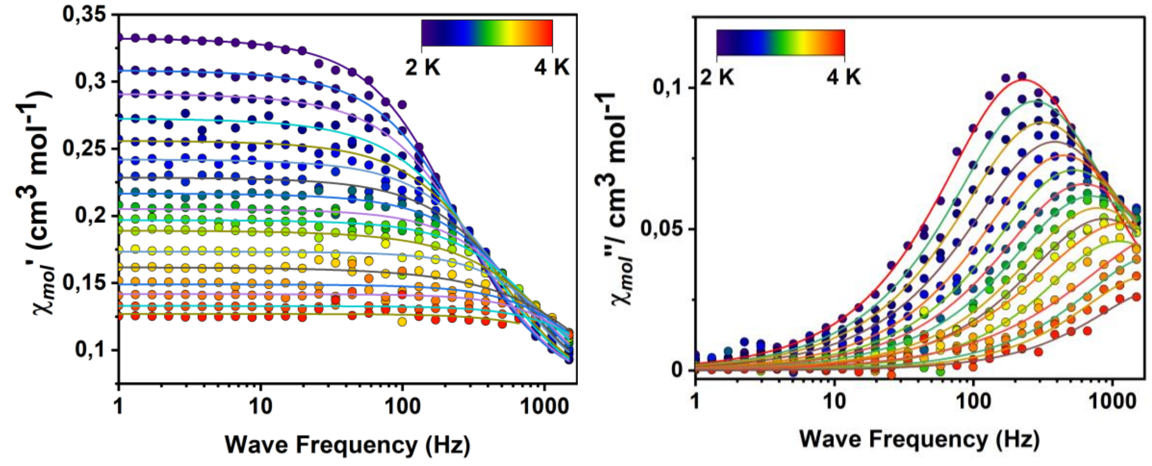

Figure 116. Frequency dependency of the in-phase (left) and out-of-phase (right) components of the magnetic susceptibility for **Yb$_{0.5}$Y$_{8.5}$-BA**. The solid lines are the best fits to a generalized Debeye model.

change in the intensity and the peak shift to the right with the increase in frequency. The distribution of active magnetic relaxation mechanisms is characterized by the α parameters obtained from fits to a generalized Debeye model. The α values obtained for **Yb$_{0.5}$Y$_{8.5}$-BA** are found between 14 % at 2 K and 19 % at 4 K, signaling likely Raman relaxation mechanism. The temperature-dependent relaxation times ln(τ) *vs* (T^{-1}) obtained from the Debeye fits were fit using equation above, employing Raman-relaxation mechanisms (**Figure 117**).

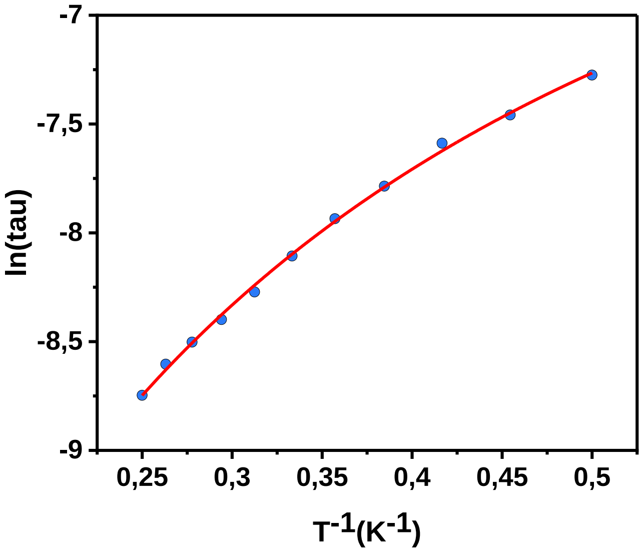

Figure 117. Arhenius plot for **Yb$_{0.5}$Y$_{8.5}$.**

The best fit parameters for **Yb$_{0.5}$Y$_{8.5}$-BA** after fitting yielded the following relaxation parameters C = (202.81±12) s $K^{-3.46}$ and n = (2.43±0.03). The observed energy barrier is in good agreement, with what is commonly reported for Yb(III) based SMMs, for which relaxation below the energy of the first excited state has been reported.[172]

The field dependence of magnetization of **Yb$_{0.5}$Y$_{8.5}$-BA** was evaluated at different temperatures 2, 3, 4, and 5 K in the magnetic field range of 0−7 T (**Figure 118**). The sharp increase of magnetization at low field at low temperatures reveals a significant energy difference between the ground and excited states. Additionally, as the external field is increased, the magnetization value increases and approaches saturation at 0.78 μ_B for complex **Yb$_{0.5}$Y$_{8.5}$-BA** at 7 T. The $M(H)$ value is consistent with the expected one (0.825 μ_B) for a Yb(III) ion with a well-defined J = 7/2 ground doublet at 7 T.

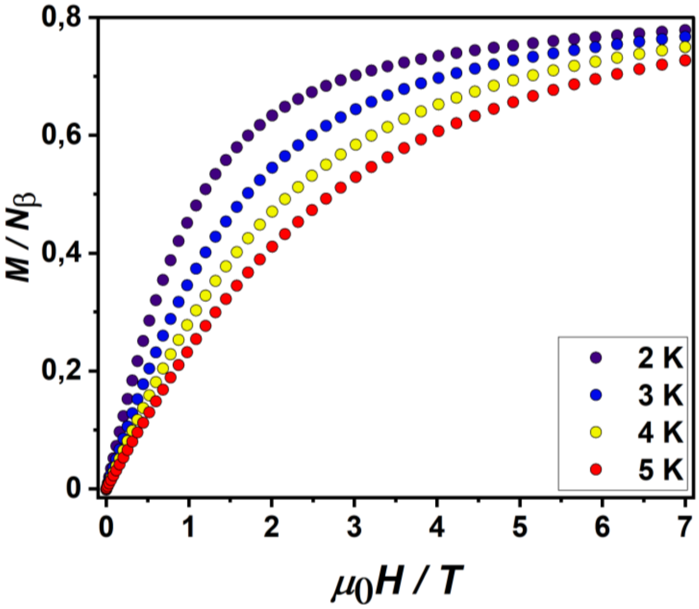

Figure 118. Plots of M vs. H at different temperatures.

6.3. Magnetic Properties of 9-hydroxyphenalen-1-one (PLN) Complexes

The deprotonated 9-hydroxyphenalen-1-one ligand (PLN$^-$) has light harvesting properties, which are used to sensitize Ln(III) ions effectively. This sensitization was achieved over a wide range of wavelengths, extending from the UV to the visible region. Interestingly, these complexes also exhibit slow relaxation magnetic behavior. A list of such complexes has been presented in this section.

Magnetic Properties of [$Tb_{0.5}Y_{8.5}(PLN)_{16}(OH)_{10}$]Cl

[$Tb_{0.5}Y_{8.5}(PLN)_{16}(OH)_{10}$]Cl is referred to as **$Tb_{0.5}Y_{8.5}$-PLN**. The temperature dependent DC susceptibility has been recorded upon cooling **$Tb_{0.5}Y_{8.5}$-PLN** from 300 K to 2 K in an external magnetic field of 1000 Oe (**Figure 119**).

The observed room temperature values are 11.07 cm^3 K mol^{-1} for **$Tb_{0.5}Y_{8.5}$-PLN** (normalized by a factor of 2 to adjust the scale to one to one Tb ion), which is in good agreement with the theoretical value of 11.82 cm^3 K mol^{-1} for a single Tb(III) ion with J = 6 and g_J = 3/2. The experimental $\chi_{mol}T$ steadily declines with the temperature going down almost linearly implying depopulation of the excited m_j states. A small dip around 5 K indicates strong anti-ferromagnetic interactions matches the distance between Tb-Tb ions (< 4 Å) even with 5.5% dilution.

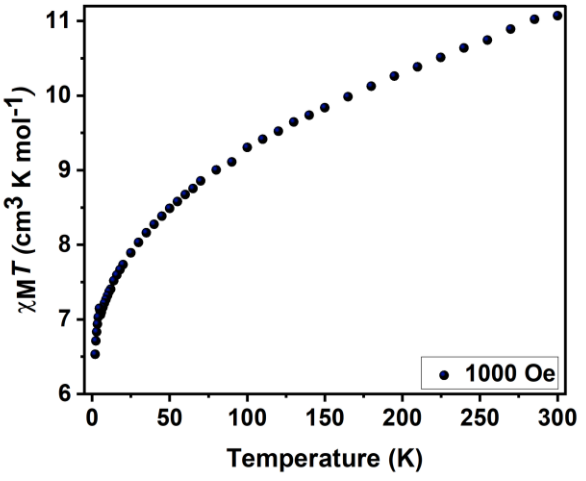

Figure 119. Temperature-product of the molar magnetic susceptibility versus temperature for **$Tb_{0.5}Y_{8.5}$-PLN.**

As stated previously, Tb(III) is not a Kramers ion, which means that it is less likely to exhibit slow magnetic relaxation in comparison to other analogues of Kramers ions. To investigate its dynamic magnetic behavior, AC susceptibility measurement techniques were employed at low temperatures. As anticipated and consistent with previous observations in other lanthanide analogues, no out-of-phase signal was detected in the absence of an external field. However,

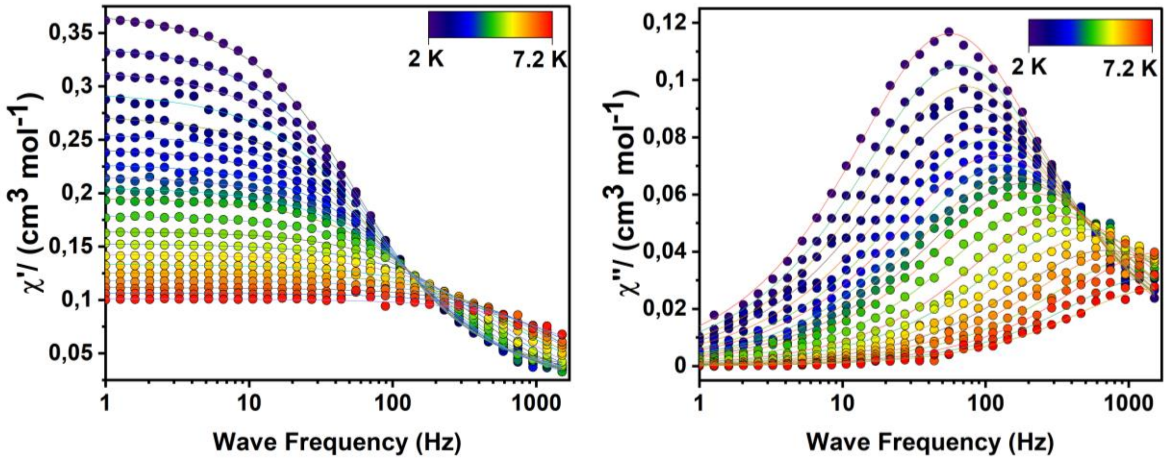

Figure 120. Frequency dependency of the in-phase (left) and out-of-phase (right) components of the magnetic susceptibility for **$Tb_{0.5}Y_{8.5}$-PLN.** The solid lines are the best fits to a generalized Debeye model.

upon the application of an external DC field, a strong signal was observed, as depicted in the **Figure 120**.

The optimal DC field has been found to be 1000 Oe for **$Tb_{0.5}Y_{8.5}$-PLN**. It should be stated that the applied field is comparably less than the optimal fields that have been found for the other benzoylacetone analogues. The observed signals are found around 50 Hz. Upon increasing the temperature, the maximum is shifting to higher frequencies while a decreasing intensity of the signal is also observed. The shifting nature of the out-of-phase signal with temperature is a clear sign of SMM behavior. The maximum is observed close to the highest observable frequency of 1500 Hz at 8 K. In order to quantitatively assess the SMM properties, the in-phase and out-of-phase data were simulatneously fitted to a generalized Debeye model. The obtained α values decrease with T, which is a typical behavior, as the high temperature relaxation is dominated by the Orbach process (see section 6.2.4). The α value observed at 2 K is 0.23 and at 7.2 K is 0.19 for **$Tb_{0.5}Y_{8.5}$-PLN**. The values make it apparent that significant contributions of Raman relaxation are present in the overall relaxation behavior of the complex. Arrhenius analysis has been performed on the temperature dependent τ values obtained. Good fits of the relaxation data were obtained employing Orbach and Raman terms for **$Tb_{0.5}Y_{8.5}$-PLN**.(**Figure 121**)

The best fits yielded the relaxation parameters $\tau_0 = (1.07 \pm 0.34) \times 10^{-6}$ s, $U_{eff} = 35.76 \pm 2.4$ K ($24.85\ cm^{-1}$), C = 103.83 ± 8.9 s K^{-n}, n = 1.7 ± 0.04 for **$Tb_{0.5}Y_{8.5}$-PLN**, The observed effective

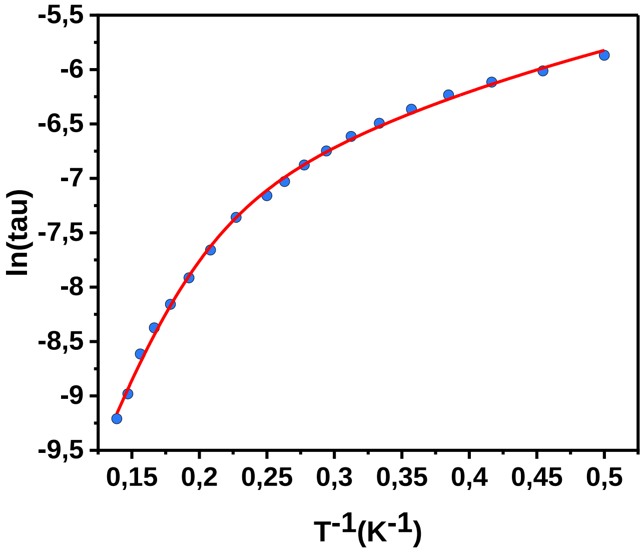

Figure 121. Arrhenius plots for **$Tb_{0.5}Y_{8.5}$-PLN**.

energy barriers are rather small in respect to what has been observed for Tb(III)-based SMMs featuring axial ligand fields. This is again a direct consequence of the low symmetry environment which is not ideal for stabilizing the m_J states of the central Tb(III) ion.

The field dependence of magnetization of **$Tb_{0.5}Y_{8.5}$-PLN** was evaluated at different temperatures 2, 3, 4, and 5 K in the magnetic field range of 0−7 T (**Figure 122**). The sharp increase of magnetization at low field at low temperatures reveals a significant energy difference between the ground and excited states. Additionally, as the external field is increased, the magnetization value increases and reaches saturation at 2.23 μ_B for **$Tb_{0.5}Y_{8.5}$-PLN** at 7 T. The $M(H)$ value is consistent with the expected one (2.25 μ_B) for a half equivalent Tb(III) ion with a $J = 6$ ground state.

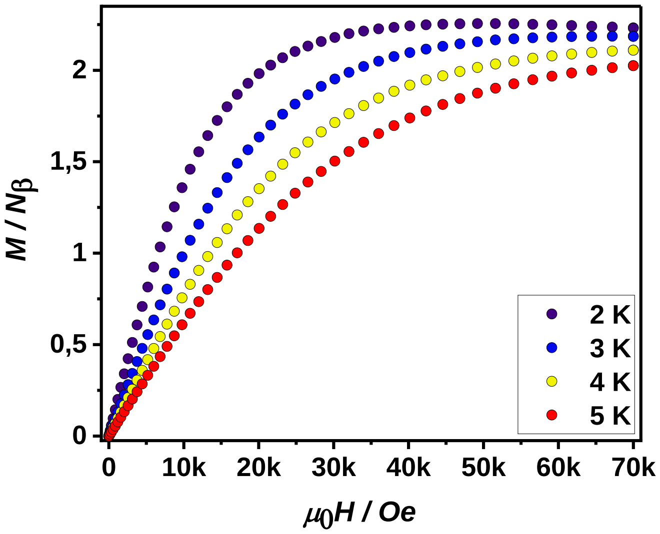

Figure 122. Plots of M vs. H at different temperatures

Magnetic Properties of $[Dy_{0.5}Y_{8.5}(PLN)_{16}(OH)_{10}]Cl$

$[Dy_{0.5}Y_{8.5}(PLN)_{16}(OH)_{10}]Cl$ is referred to as **$Dy_{0.5}Y_{8.5}$-PLN**. The temperature dependent DC susceptibility has been recorded upon cooling **$Dy_{0.5}Y_{8.5}$-PLN** from 300 K to 2 K in an external magnetic field of 1000 Oe (**Figure 123**).

The observed room temperature values are 14.02 cm^3 K mol^{-1} for **$Dy_{0.5}Y_{8.5}$-PLN** (normalized by a factor of 2 to adjust the scale to one to one Dy ion), which is in good agreement with the theoretical value of 14.17 cm^3 K mol^{-1} for a single Dy(III) ion with $J = 15/2$ and $g_J = 3/2$. The temperature dependence is characterized by a constant dwindling of $\chi_m T$ upon cooling related to the intermolecular magnetic coupling including with the depopulation of the Stark levels for **Dy$_{0.5}$Y$_{8.5}$-PLN**.

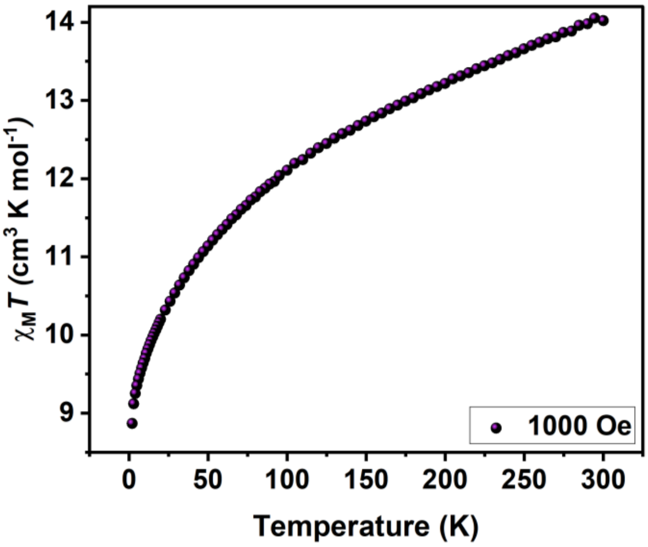

Figure 123. Temperature-product of the molar magnetic susceptibility versus temperature for **Dy$_{0.5}$Y$_{8.5}$-PLN**.

The dynamic magnetic relaxation behavior has been studied using AC susceptibility techniques as described in section 6.3. Without the application of an external field, **Dy$_{0.5}$Y$_{8.5}$-PLN** did not show any out-of-phase signal, which can be qualitatively explained by the low symmetry environment(C_{2v}) around the Dy(III). Low symmetry enhances QTM, therefore, allowing efficient magnetic relaxation between the two orientations of the ground state doublet.

Upon the application of an external magnetic field, slow relaxation was observed in both samples. The optimal fields for the relaxation were determined to be 1000 Oe. **Figure 124** shows the frequency dependent in-phase and out-of-phase components of the magnetic susceptibility for the samples of **Dy$_{0.5}$Y$_{8.5}$-PLN**.

The optimal DC field has been found to be 1000 Oe for **Dy$_{0.5}$Y$_{8.5}$-PLN**. Similar to the **Tb$_{0.5}$Y$_{8.5}$-PLN** the applied field is comparably less than the optimal fields that have been found for the other BA analogues. The observed signals are found around 40 Hz. Upon increasing the temperature, there is only a decrease in the intensity and peaks remains at 40 Hz and above 4 K

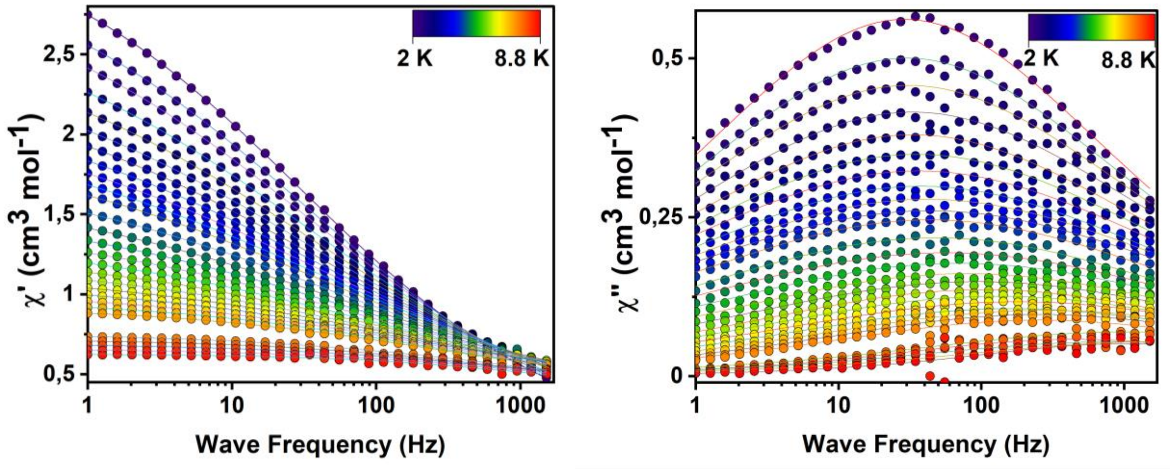

Figure 124. Frequency dependency of the in-phase (left) and out-of-phase (right) components of the magnetic susceptibility for **$Dy_{0.5}Y_{8.5}$-PLN**. The solid lines are the best fits to a generalized Debeye model.

the maximum is shifting to higher frequencies while a decreasing intensity of the signal is also observed. The shifting nature of the out-of-phase signal with temperature is a clear sign of SMM behavior. The maximum is observed close to the highest observable frequency of 1500 Hz at 8.8 K.

In order to quantitatively assess the SMM properties, the in-phase and out-of-phase data were simultaneously fitted to a generalized Debeye model. The obtained α values remain fairly constant with T, which is a typical behavior, as the high temperature relaxation is dominated by the Direct process (see section 2.4.2). The **α** value observed at 2 K is a significantly higher

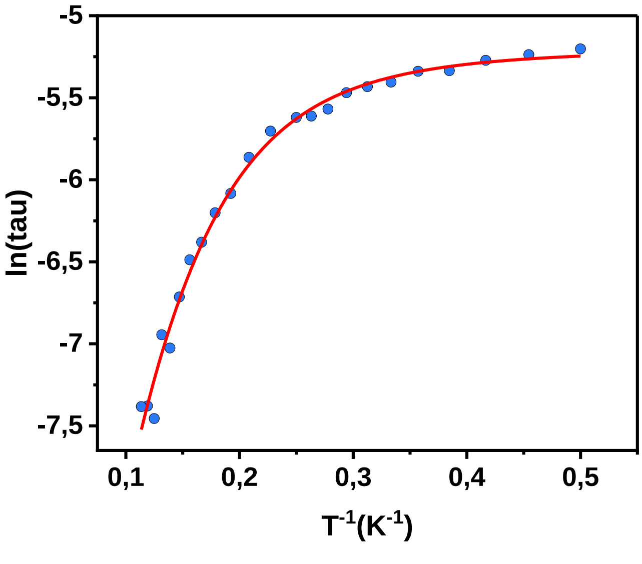

Figure 125. Arrhenius plots for **$Dy_{0.5}Y_{8.5}$-PLN**.

0.59 than Tb analogue, indicating a range of relaxation mechanisms and also at 8.8 K is 0.59 for **$Dy_{0.5}Y_{8.5}$-PLN**. The values make it apparent that significant contributions of Direct and Raman relaxation are present in the overall relaxation behavior of the complex. Arrhenius analysis has been performed on the temperature dependent τ values obtained. Good fits of the relaxation data were obtained employing Direct and Raman terms for **$Dy_{0.5}Y_{8.5}$-PLN**.(**Figure 125**)

The best fits yielded the relaxation parameters $\tau_0 = (1.36 \pm 0.14) \times 10^{-6}$ s, $U_{eff} = 51.74 \pm 10.4$ K ($24.85\ cm^{-1}$), $C = 94.22 \pm 0.24\ s\ K^{-n}$, $n = 1 \pm 0.3$ (confirming the direct process) for **$Dy_{0.5}Y_{8.5}$,** The observed effective energy barriers are rather small in respect to what has been observed for Dy(III)-based SMMs featuring axial ligand fields. This is again a direct consequence of the low symmetry environment which is not ideal for stabilizing the m_J states of the central Dy(III) ion.

The field dependence of magnetization of **$Dy_{0.5}Y_{8.5}$-PLN** was evaluated at different temperatures 2, 3, 4, and 5 K in the magnetic field range of 0−7 T (**Figure 126**). The sharp increase of magnetization at low field at low temperatures reveals a significant energy difference between the ground and excited states. Additionally, as the external field is increased, the magnetization value increases and approaches saturation at 2.48 μ_B for complex **$Dy_{0.5}Y_{8.5}$-PLN** at 7 T. The *M*(*H*) value is consistent with the expected one (2.5 μ_B) for a half equivalent Dy(III) ion with a well-defined $J = 15/2$ ground doublet.

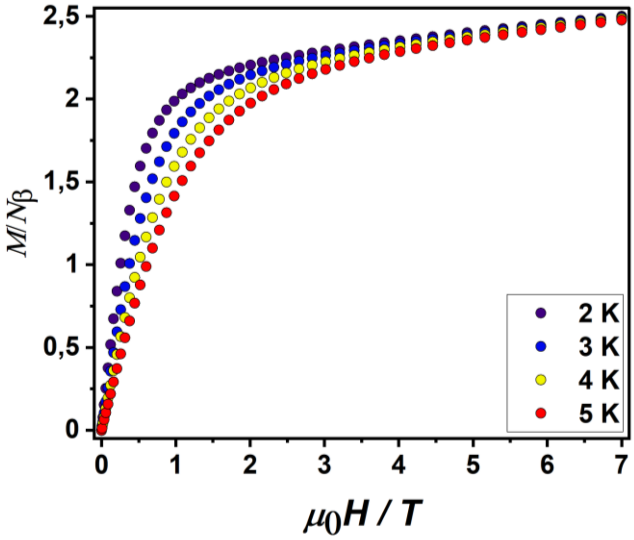

Figure 126. Plots of M vs. H at different temperatures.

Magnetic Properties of [Yb$_{0.5}$Y$_{8.5}$(PLN)$_{16}$(OH)$_{10}$]Cl

[Yb$_{0.5}$Y$_{8.5}$(PLN)$_{16}$(OH)$_{10}$]Cl is referred to as **Yb$_{0.5}$Y$_{8.5}$-PLN**. The temperature dependent DC susceptibility has been recorded upon cooling **Yb$_{0.5}$Y$_{8.5}$-PLN** from 300 K to 2 K in an external magnetic field of 1000 Oe (**Figure 127**).

The obtained room temperature values of $\chi_{mol}T$ are 2.49 cm^3 K mol^{-1} for **Yb$_{0.5}$Y$_{8.5}$-PLN**. Which is in very good agreement with the theoretically expected value of 2.57 cm^3 K mol^{-1} for a single Yb(III) ion at 300 K. The T-dependency of **Yb$_{0.5}$Y$_{8.5}$-PLN** is characterized by a very steady decrease. This gradual type of decrease has been reported for other Yb(III)-based compounds.[172] This can be attributed to the depopulation of the m$_j$ levels split by the crystal field and the weak antiferromagnetic intermolecular interactions between Ln^{3+} ions.

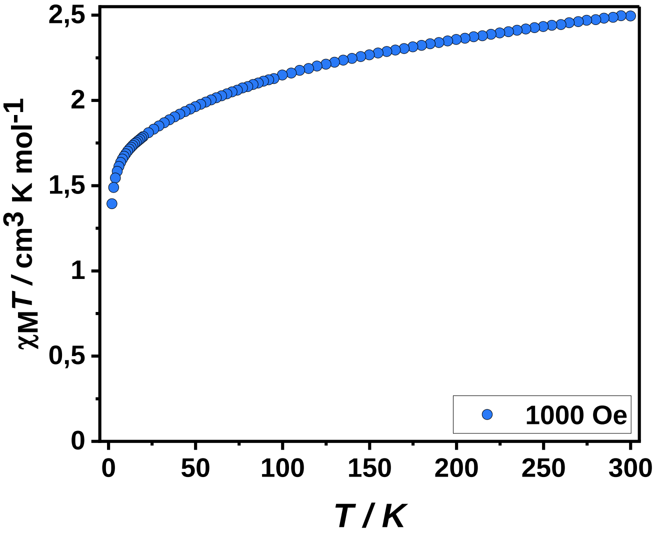

Figure 127. Temperature-product of the molar magnetic susceptibility versus temperature for **Yb$_{0.5}$Y$_{8.5}$-PLN.**

Performing dynamic *ac* susceptibility studies (**Figure 128**), no out-of-phase signal was observed for **Yb$_{0.5}$Y$_{8.5}$-PLN** under zero field. Also, the application of an external field, did not result in an observable χ'' signal. As mentioned above, Yb(III) has a prolate electron density which is different from Dy and Tb, both of which have oblate electron density. When viewed in the context of crystal packing, it is seen that Phenalenone ligands have a bulky phenalene moiety in an axial crystal field fashion, whereas the phenyl rings from Benzoylacetone ligands coordinate in an equatorial plane. As explained in section 6.2, Lanthanide ions that have oblate electron density require axial crystal field type for better performing Single-Molecule Magnets (SMMs), while prolate ions require an equatorial crystal type. This could be the reason why **$Yb_{0.5}Y_{8.5}$-PLN** does not exhibit any slow relaxation magnetic behavior within the 1500 Hz range.

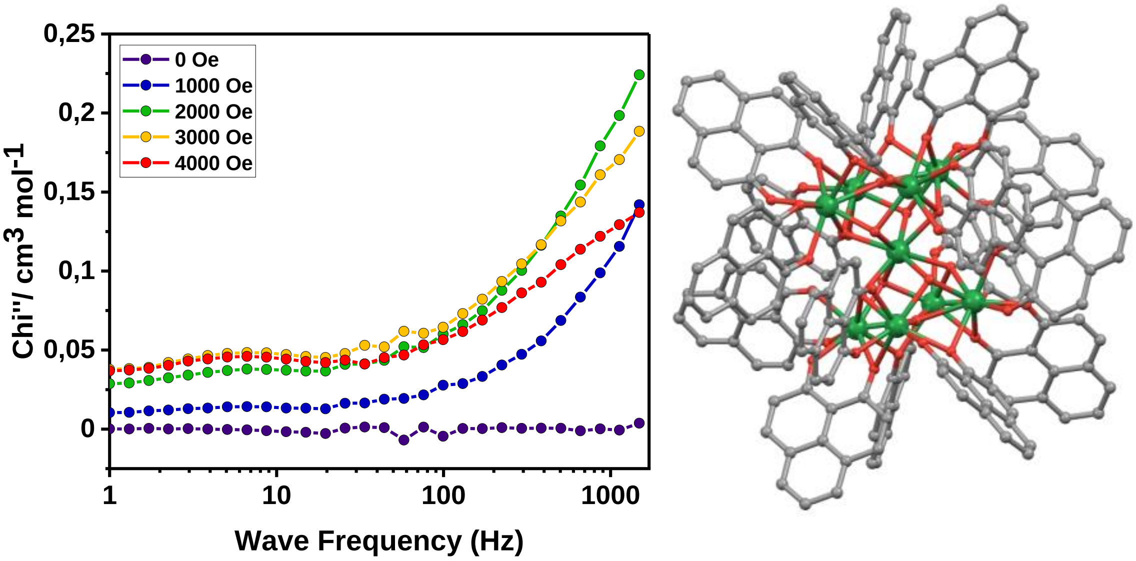

Figure 128. (left) Frequency dependency of the out-of-phase components of the magnetic susceptibility at 2K over different external fields for **$Yb_{0.5}Y_{8.5}$-PLN**. (right) The crystal packing of **9-hydroxyphenalen-1-one (PLN)** complexes (Reproduced from J. Phys. Chem. Lett. 2014, 5, 1727−1731).

The field dependence of magnetization of **$Yb_{0.5}Y_{8.5}$-PLN** was evaluated at different temperatures 2, 3, 4, and 5 K in the magnetic field range of 0−7 T (**Figure 129**). The sharp

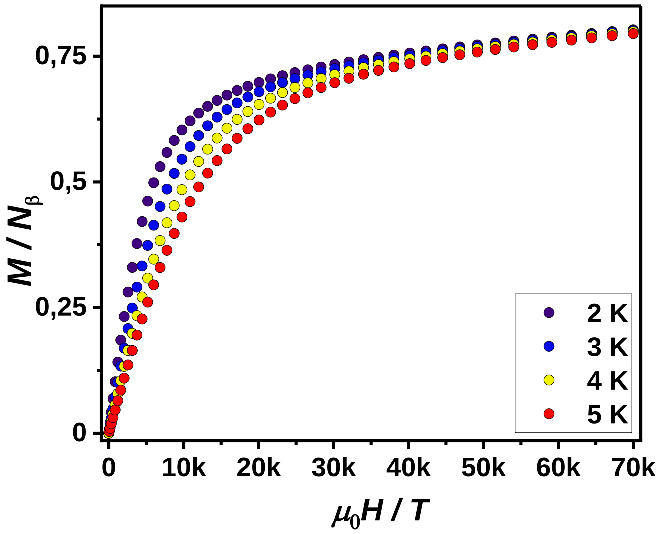

Figure 129. Plots of M vs. H at different temperatures.

increase of magnetization at low field at low temperatures reveals a significant energy difference between

the ground and excited states. Additionally, as the external field is increased, the magnetization value increases and reaches saturation at 0.80 μ_B for complex **$Yb_{0.5}Y_{8.5}$-PLN** at 7 T. The $M(H)$ value is consistent with the expected one (0.825 μ_B) for a Yb(III) ion with a well-defined J = 7/2 ground doublet at 7T.

6.4. Magnetic Properties of 1-pyrenebutane-1,3-dione (PA) Complex

The 1-pyrenebutane-1,3-dione (PA) (Pyrene-acac) has light harvesting properties, which are used to sensitize Ln(III) effectively. due to its extensive conjugation it can sensitize over a wide range of wavelengths, extending from the UV to the visible region. The idea was to obtain similar nonanuclear complexes for a comparative study. Due to the bulky pyrene group we could never isolate nonanuclear complexes. However, after several tries we could isolate and characterize a monomeric Yb complex. Interestingly, the Yb-Pyrene-acac complex also exhibits slow relaxation magnetic behavior.

Magnetic properties of $[Yb_1(PA)_{16}(CH_3OH)(H_2O)]$

$[Yb_1(PA)_{16}(CH_3OH)(H_2O)]$ is referred to as **Yb-PA**. The temperature dependent DC susceptibility has been recorded upon cooling **Yb-PA** from 300 K to 2 K in an external magnetic field of 1000 Oe (**Figure 130**).

The obtained room temperature value of $\chi_{mol}T$ is 2.53 cm^3 K mol^{-1} for **Yb-PA**. Which is in very good agreement with the theoretically expected value of 2.57 cm^3 K mol^{-1} for a single Yb(III) ion at 300 K. The T-dependency of **Yb-PA** is characterized by an ever-declining behavior down to 200 K, followed by a very steady decrease almost linear fashion and a dip at 8 K suggesting suggesting the depopulation of the higher m_j states and antiferromagnetic inteactions below 8 K.

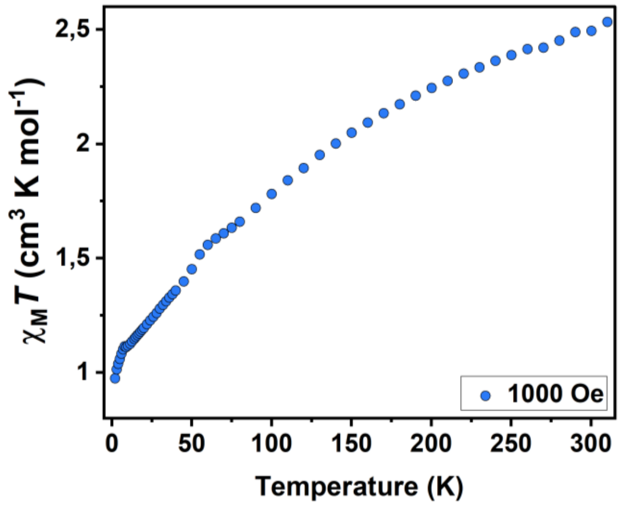

Figure 130. Temperature-product of the molar magnetic susceptibility versus temperature for **Yb-PA**.

Yb(III) is a Kramers ion and with that the observation of slow magnetic relaxation is more likely compared to analogues of non-Kramers ions. The dynamic magnetic behavior was tested using *ac* susceptibility measurement techniques at low T. As expected, and matching what has been observed in the other Yb complexes, no out-of-phase signal was observed without the application of an external field. With the application of an external DC field (2200 Oe), a signal has been observed, as shown in **Figure 131**.

The ac susceptibility data of **Yb-PA** show a single relaxation maximum in the out-of-phase component. It is observable in a temperature range from 2 K to 6 K, shifting from 60 Hz to

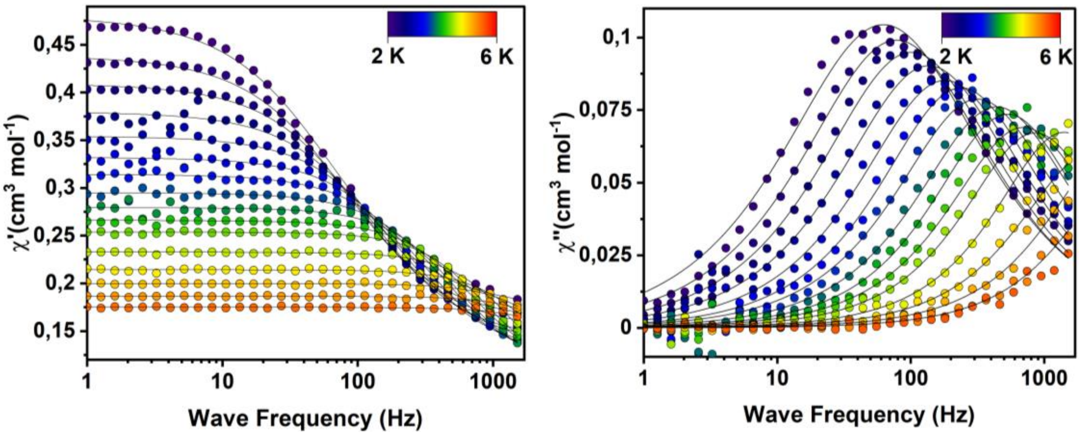

Figure 131. Frequency dependency of the in-phase (left) and out-of-phase (right) components of the magnetic susceptibility for **Yb-PA**. The solid lines are the best fits to a generalized Debeye model.

1500 Hz in the process. The highest observable frequency of 1500 Hz is reached at 6 K. The dataset suggests Raman relaxation throughout the temperature range, due to a visible change in the intensity of the frequency shift.

The distribution of active magnetic relaxation mechanisms is characterized by the α parameters obtained from fits to a generalized Debeye model. The α values obtained for **Yb-PA** are found between 24 % at 2 K and 5.5 % at 6 K, signaling pure Orbach-type relaxation at higher T, with other processes, most likely Raman, active at low T. The temperature-dependent relaxation times $\tau(T)$ obtained from the Debeye fits were fit using the equation above, employing Raman- and Orbach-type relaxation mechanisms (**Figure 132**).

The best fits yielded the relaxation parameters $\tau_0 = (2.94 \pm 0.69) \times 10^{-7}$ s, $U_{eff} = 28.17 \pm 1.6$ K ($19.58\ \mathrm{cm}^{-1}$), $C = 51.99 \pm 12.3\ \mathrm{s\ K}^{-n}$, $n = 2.85 \pm 0.29$ for **Yb-PA**, The observed energy barrier is in good agreement, with what is commonly reported for Yb(III) based SMMs, for which relaxation below the energy of the first excited state has been reported.

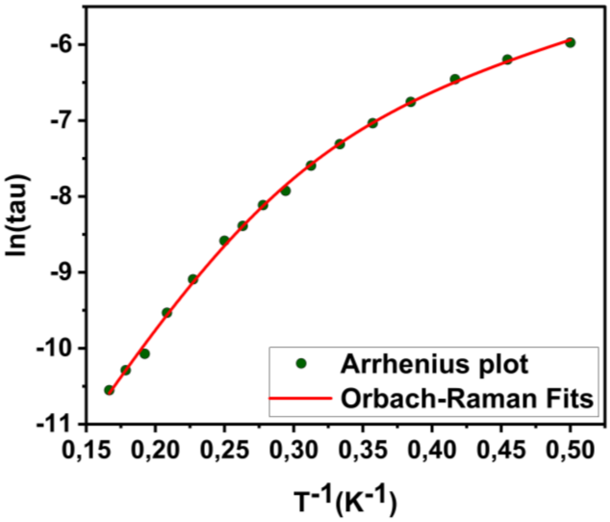

Figure 132. Arrhenius Plot for **Yb-PA.**

Table 13. Summary of the SMM behavior of the ß-diketonate-based lanthanide complexes.

Ligand	Name	Lanthanide	SMM (0-1500 Hz) (DC Field *Oe*)	Kramers/Non-Kramers	Anisotropy
BA	Yb-Monomer	Yb^{3+}	SMM (1800)	Kramers	Prolate
	Yb_9-BA	Yb^{3+}	Not an SMM	Kramers	Prolate
	Eu_8Yb-BA	Yb^{3+}	SMM (1750)	Kramers	Prolate
	$Tb_{0.5}Y_{8.5}$-BA	Tb^{3+}	Not an SMM	Non-Kramers	Oblate
	$Dy_{0.5}Y_{8.5}$-BA	Dy^{3+}	Not an SMM	Kramers	Oblate
	$Ho_{0.5}Y_{8.5}$-BA	Ho^{3+}	Not an SMM	Kramers	Oblate
	$Er_{0.5}Y_{8.5}$-BA	Er^{3+}	SMM (1600)	Kramers	Prolate
	$Tm_{0.5}Y_{8.5}$-BA	Tm^{3+}	Not an SMM	Non-Kramers	Prolate
	$Yb_{0.5}Y_{8.5}$-BA	Yb^{3+}	SMM (2400)	Kramers	Prolate
PLN	$Tb_{0.5}Y_{8.5}$-PLN	Tb^{3+}	SMM (1000)	Non-Kramers	Oblate
	$Dy_{0.5}Y_{8.5}$-PLN	Dy^{3+}	SMM (1000)	Kramers	Oblate
	$Yb_{0.5}Y_{8.5}$-PLN	Yb^{3+}	Not an SMM	Kramers	Prolate
PA	Yb-PA	Yb^{3+}	SMM (2200)	Kramers	Prolate

6.5 Conclusion

In this particular chapter, the focus is on thirteen complexes (**Table 13**), all of which were magnetically characterized. Out of these twelve, ten are nonanuclear complexes, while two are mononuclear Yb complexes. The complexes were synthesized successfully with three different ligands, which were tailored to the ß-diketonate scaffold by modifying the aromatic moiety.

The nonanuclear complexes were diluted with Y in order to minimize intramolecular interactions within the complex, as slow relaxation magnetic behavior was not observed in the Yb_9(BA) complex. The detailed structure of these complexes was explained and characterized in chapters 4 and 7.

It was observed that in the benzoylacetone complexes series, only the ions with prolate electron density (Yb, Er) showed slow magnetic relaxation behavior under an external DC field. This behavior was attributed to the equatorial coordination of the BA ligands, which is ideal for prolate ions. Tm(III), which has a prolate electron density, did not show any slow relaxation behavior, with or without external DC field, as it is a non-kramers ion unlike Er and Yb.

Regarding the Phenalenone series, it was noted that the oblate ions (Dy, Tb) exhibited slow magnetic relaxation behavior, whereas the prolate Yb(III) complex did not. This behavior was attributed to the axial crystal type coordination of the phenalenone ligands, as can be seen in their crystal packing. Axial coordination helps the oblate ions to stabilize the bistability of the ground state, which in turn shows a slow relaxation magnetic behavior.

Furthermore, the Yb-PA complex was magnetically characterized in this study. Although the nonanuclear complexes could not be isolated due to the steric bulkiness of the ligands, a monomeric Yb complex was successfully isolated. This complex exhibited slow relaxation magnetic behavior under an external DC field (2200 Oe).

To summarize, this study shows that the SMM property can be modified by changing the coordination environment resulting from changes in the substituents of *ß*-diketonate ligands. Therefore, careful design of organic ligands can enhance magnetic relaxation with an appropriate crystal field environment. These complexes will be a good reference for SMM properties of Ln-based nonanuclear analogues.

Chapter 7: Polynuclear Ytterbium Complexes- Results and Discussion

Background

The search for effective single-molecule magnets (SMMs) has led to intense study of novel lanthanide-based complexes. These complexes retain residual magnetization after switching off the external magnetic field, making them a potential alternative to commonly used magnetic materials.[187] Among the Ln-based SMM studies, those based on Dy^{3+} complexes are the most common.[188] Dy^{3+} is ideal for SMMs because it is a Kramers ion (has an odd number of f-electrons), fulfilling the requirement of a bistable ground state of the central ion in SMMs.[189] The availability of systematic studies on the effect of nuclearity[190] and auxiliary ligands,[191] as well as the molecules of crystallization[192] on SMM properties of Dy^{3+} complexes, has further expanded the knowledge about SMM behavior. However, the number of known SMMs based on other Ln^{3+}, including those formed by Yb^{3+}, is greatly inferior to that of the Dy derivatives.[173] There is virtually a complete absence of systematic and comparative experimental studies for Yb-based SMMs, making them a promising area for future research. In recent times, there has been a growing interest in using Yb^{3+} ions for the preparation of magnetic systems, despite it being an unusual choice. This is because of the potential of these compounds in generating novel opto-magnetic species.[193] Our approach is to use Yb^{3+} ions, which exhibit near-infrared optical activity, to design and synthesize multifunctional luminescent single-molecule magnets (SMMs). [194] This makes Yb^{3+} SMMs promising multifunctional opto-magnetic species. Additionally, the use of Yb^{3+} complexes has been shown to be a suitable tool to probe environmental changes such as temperature[195] and viscosity variation,[196] which further increases the appeal of these systems from an application standpoint.

7.1. 3d–4f Dinuclear Complex (1) = $[Yb(VO)LCl_3(H_2O)]\cdot 2CH_3CN$

The interaction between 3d and 4f elements in a compound is a fascinating subject due to the strong magnetic exchange that can occur between them.[197] This exchange leads to an additional splitting of energy levels, which can affect the magnetic anisotropy in various ways, given that the magnetic exchange includes both isotropic and anisotropic contributions. Interestingly, it has been found that the magnetic exchange interaction suppresses quantum tunneling of magnetization in the ground state, which improves the single-molecule magnet (SMM) properties.[198] Generally, the exchange interactions are much stronger in polynuclear complexes comprising d-block metals than f-block metals, particularly lanthanides. This is because the valence 6s-orbitals of the lanthanides shield the unpaired electrons in 4f-orbitals. Therefore, combining lanthanides with d-block elements can result in larger magnetic exchange interactions between paramagnetic centers, making it an interesting avenue for further research.

Over the last 15 years, researchers have been actively exploring the potential of paramagnetic molecular complexes as a platform for implementing quantum technologies.[199] These complexes have electronic spins with long coherence times, which make them ideal for spin manipulation using pulsed magnetic resonance techniques.[200] Compared to other architectures, the molecular approach allows fine-tuning of the qubit's chemical and physical properties through rational chemical design.[201] This enables control over the sources of spin decoherence and permits engineering the inter-spin interactions required to build universal quantum gates and organize molecules on a surface. Among the potential spin qubits investigated, molecules containing the vanadyl ion (VO^{2+}) have shown almost universally good coherence times that persist up to room temperature.[202,203] Additionally, thanks to the I = 7/2 nuclear spin of ^{51}V, which has a natural abundance of 99.75%, vanadium(IV) complexes can be operated as nuclear qudits with an electronic spin auxiliary.[204]

For complex 1, we used the "sales type" Schiff bases, which easily form complexes with 3d elements and lanthanides, with $\{N_2O_2\}$ and usually $\{O_4\}$ coordination modes, respectively, depending on other substituents. This type of compound is most abundant with Cu^{2+} and Ni^{2+} and, to a lesser extent, with V^{4+}. Both Cu^{2+} and V^{4+} ions both contribute with $S = 1/2$, making them magnetically isotropic by their nature. The Ni^{2+} ions can be either diamagnetic (in a square planar shape of the coordination polyhedron) or paramagnetic with $S = 1$ contribution (in penta-, hexa-, and hepta-coordinations) and non-negligible magnetic anisotropy.

In Ln^{3+}-Cu^{2+} complexes, the magnetic exchange interactions are ferromagnetic in all the cases found so far. However, in Ln^{3+}-V^{4+} complexes, both ferromagnetic and antiferromagnetic interactions are possible due to the geometry of the central atoms in salen-type complexes.

Unlike Ln^{3+}-Cu^{2+} complexes, there are only a few reported complexes of Ln^{III}-V^{IV} with ligands.[205]

In this subsection a 3d–4f dinuclear complex (**1**) = **[Yb(VO)LCl$_3$(H$_2$O)]·CH$_3$CN** [hfac = hexafluoroacetyl-acetonate; NIT$_2$PhO = 2-(2-hydroxyphenyl)-4,4,5,5-tetra-methyl-imidazoline-1-oxyl-3-oxide; H_2L = N,N′-bis(1-hydroxy-2-benzylidene-6-methoxy)-1,7-diamino-4-azaheptane) has been discussed. As a confirmation of the presence of the Yb we recorded the X-ray fluorescence of the complex **1**. The magnetic properties are investigated by DC and AC magnetometry. We also investigated the energy level structure of **1** using low temperature solid-state luminescence.

7.1.1. Synthesis

As mentioned above we designed a complex with Yb^{3+} and V^{4+} using "salen type" Schiff bases, derived from 2-hydroxy-3-methoxy-benzaldehyde, for their readily coordinating nature with 3d and 4f metal ions. The extensive synthesis is inspired by previously reported methods.[206]

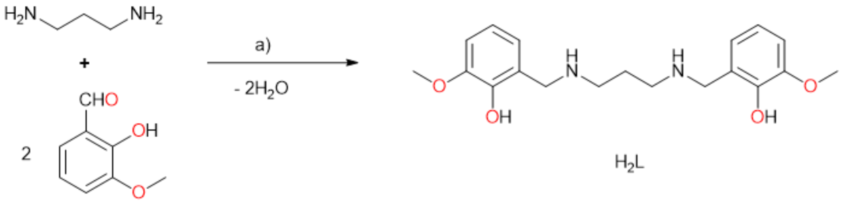

Figure 133. Synthetic pathway of H_2L = N,N′-bis(1-hydroxy-2-benzylidene-6-methoxy)-1,7- diamino-4-azaheptane (a) MeOH, reflux.

The bright yellow H_2L (H_2L = N,N′-bis(1-hydroxy-2-benzylidene-6-methoxy)-1,7- diamino-4-azaheptane) powder was obtained by the condensation reaction of *o*-vaniline and propylenediamine in methanol (**Figure 133**).

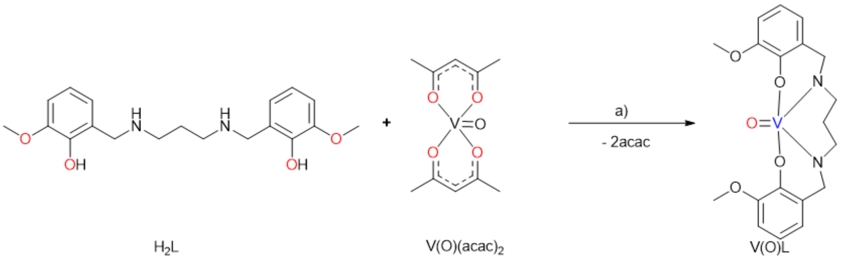

Figure 134. Synthetic pathway of V(O)L a) CH_3OH, reflux.

The green V(O)L precipitate was obtained by coordinating $VO(acac)_2$ salt with H_2L in methanol (**Figure 134**).

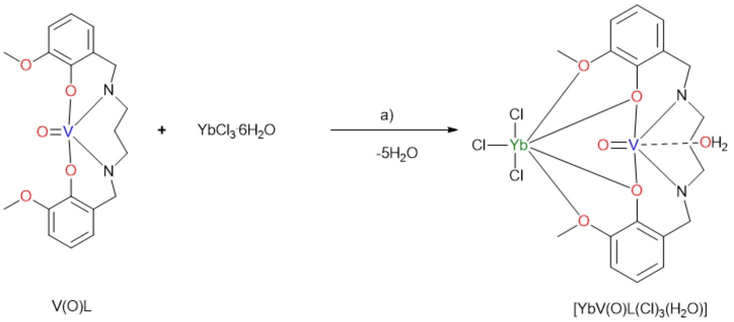

Figure 135. Synthetic pathway of $[YbV(O)L(Cl)_3(H_2O)]$ a) $CH_3CN/CH_3C(O)CH_3$, reflux.

The green $[Yb(VO)L(Cl)_3(H_2O)]$ precipitate was obtained by suspending $YbCl_3{\cdot}6H_2O$ with V(O)L in acetonitrile. After several days we harvested the crystals suitable for SC-XRD to study the structure in detail (**Figure 135**).

7.1.2. Crystal Structure

Complex **1**, $\mathbf{[Yb(VO)LCl_3(H_2O)]{\cdot}2CH_3CN}$**:** crystallizes in the monoclinic space group $P2_1/c$(14) (a = 10.1573(5) Å, b = 16.4364(12) Å, c = 17.2907(19) Å, α = 90°, β = 91.851(7)°, γ = 90°, V = 2885.17 Å^3). The V^{4+} ion is coordinated by two nitrogen and two oxygen atoms of the L_2^- ligand forming an equatorial plane of the deformed octahedron (continuous shape measures indexes for O_h: 0.996), which has two oxygen atoms in the axial positions from the vanadyl group and the aqua ligand (**Figure 136a**). The shortest metal–ligand bond length for the V^{4+} ion is observed in the vanadyl group ((V=O) = 1.590 Å), while the longest ones are observed for the bonds with the aqua ligands ((V–O) = 2.340 Å). The Yb atom is hepta-coordinated by four oxygen donor atoms and three chlorine ligands. Oxygen donor atoms are provided by the outer chelating pocket of the L_2^- ligands (two phenolate and two methoxy oxygen atoms) and the remaining three originate from three chloride ligands. The shortest Yb–O bond lengths are observed in the bonds involving phenolate oxygen atoms (Yb–O = 2.288, 2.292 Å). Whereas, the methoxy oxygen atoms form longer bonds (Yb–O = 2.405, 2.431 Å), the shorter bond length observed for heavier Yb^{3+} is in agreement with the lanthanide contraction. The chloride ligands bonds with Yb in a wide range of bond lengths ranging between 2.532, 2.588 and 2.591 Å. The intradimer Yb···V distance is 3.473 Å.

The packing in the crystal structure can be ascribed to a ladder-like supramolecular substructure of the complex molecules interconnected by strong O–H···O hydrogen bonds (d(O···O) = 3.089–3.261 Å) formed between the hydrogen atoms of the coordinated aqua ligands and the chlorine ligands of the neighboring molecules (**Figure 136c**).

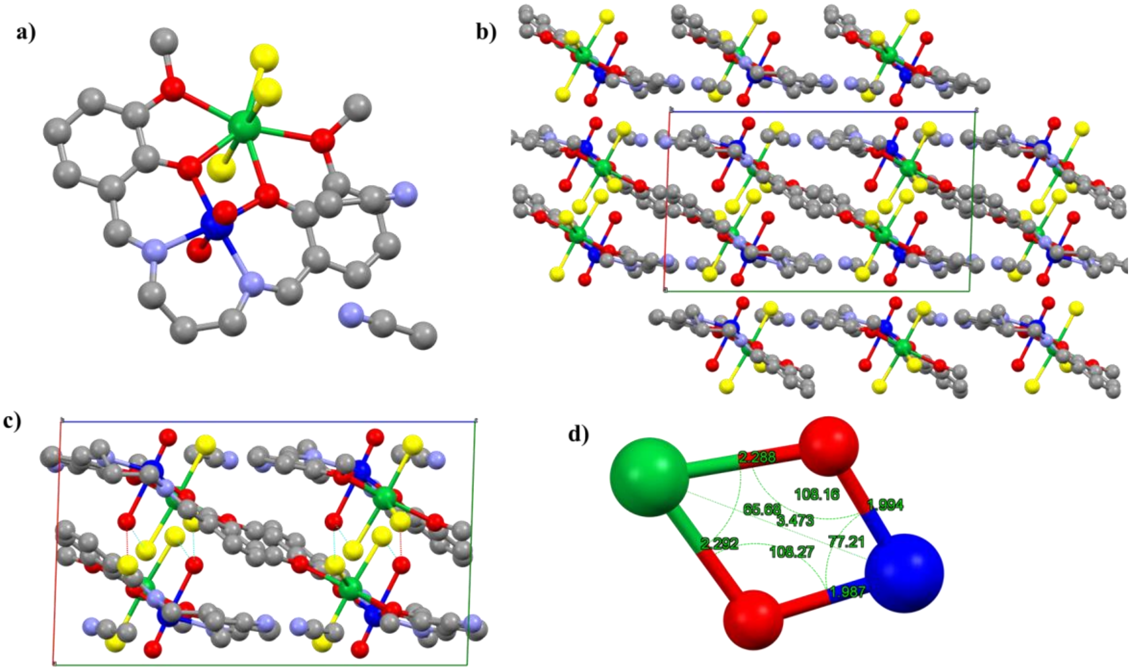

Figure 136. a) Crystal structure of (**1**) hydrogen atoms are omitted for clarity. b) A perspective view down the b crystallographic axis of the packing of the molecules. c) The hydrogen bonding (hydrogen bonding depicted by blue (intramolecular) and red (intermolecular) dashed lines). d) The Yb-V dimer moiety. hydrogens are omitted for clarity. Green (Yb), Blue (V), Red (O), Grey (C), Violet (N), Yellow (Cl).

The Yb–O–V bridge angles are 118.16(10)° and 108.27(10)°, the O–Yb–O bridge angle is 65.68(10)°, the O–V–O bridge angle is 77.21(10)° and related Yb–O distances are in the range of 2.288(2)–2.292(2) Å, the V–O bond lengths are in the range of 1.987(2)- 1.994(2) Å, the Yb–V bond length is 3.473(2) Å, which is comparable to those of the reported data in other lanthanide-vanadium complexes. The central core Yb-V-O_2 appears to be an irregular quadrilateral with different sides, different angles **(Figure 136d)**,

7.1.3. X-Ray Fluorescence (XRF)

Using XRF technique that allows for the identification of elemental composition in a material. based on the following three simple steps: Primary X-rays knock out an electron from one of

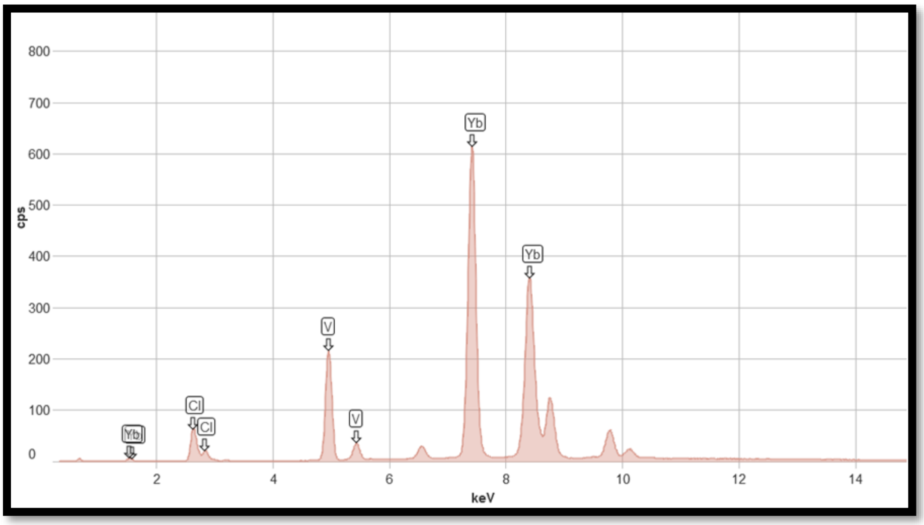

Figure 137. X-Ray Fluorescence spectrum of Complex **1**.

the orbitals surrounding the nucleus within an atom of the material. A hole is produced in the orbital, which results in a high energy and unstable configuration for the atom. To restore equilibrium, an electron from a higher energy, outer orbital falls into the hole. This results in the emission of fluorescent X-rays, which contain energy specific to the element atom being analyzed.

The energy difference between the expelled and replacement electrons is indicative of the element in the material where the fluorescence process is occurring. This makes XRF a fast-analytical tool for identifying an element's composition. Using this we could confirm the stoichiometric ratio of vanadium (4.952- $K_{\alpha1}$, 4.944- $K_{\alpha2}$, 5.427- $K_{\beta1}$), and ytterbium (7.415- $L_{\alpha1}$, 8.4040- $L_{\beta1}$, 8.758- $L_{\beta1}$, 9.780-$L_{\gamma1,}$ 1.521-$M_{\alpha1}$) (**Figure 137**) in the powder sample at room temperature. We also tried to analyze the chlorine atoms. However, the detector works better for the heavier elements and is accurate at the higher KeVs. We can deduce the stoichiometric ratios of Yb and V using the spectral intensities.

Table 14. Stoichiometric ratios from XRF.

Element	Atomic mass	The. Stoichiometry	**wt% measured**	Exp. Stoichiometry
Cl	35.453	3.0	20,5838	1.67
V	50.94	1.0	19,2736	1.09
Yb	173.04	1.0	60,1426	1.0

From the XRF data we can confirm the presence of the Yb, V and from **Table 14** we can also deduce the experimental stoichiometric ratios.

7.1.4. Magnetic Measurements

The magnetism in complex **2** is contributed by both $V^{4+}(d^1)$ and $Yb^{3+}(4f^{13})$ both being a S =1/2 systems. In the case of the complexes containing Yb^{3+} ions, which has a large energetic separation between the ground state and the first excited state, only the ground state is thermally populated at room temperature. This is noticed through the ever decreasing $\chi_M T$ values down to 2 K. The value of effective magnetic moment of the complex **2** at 300 K, (**Figure 138**) is 3.15 $cm^3{\cdot}K{\cdot}mol^{-1}$ and is close to the theoretical values for uncoupled V^{4+}–Yb^{3+} systems, which is 2.938 $cm^3{\cdot}K{\cdot}mol^{-1}$. The $\chi_M T$ value keep decreasing on lowering the temperature down and reaches a minimum 1.9 $cm^3{\cdot}K{\cdot}mol^{-1}$ at 5 K, which is most likely caused by the zero-field splitting induced by the ligand-field, the thermal depopulation of the Yb^{3+} excited states, the spin–orbit interactions, and also due to the possible weak antiferromagnetic magnetic interaction between V^{4+}–Yb^{3+} paramagnetic ions.

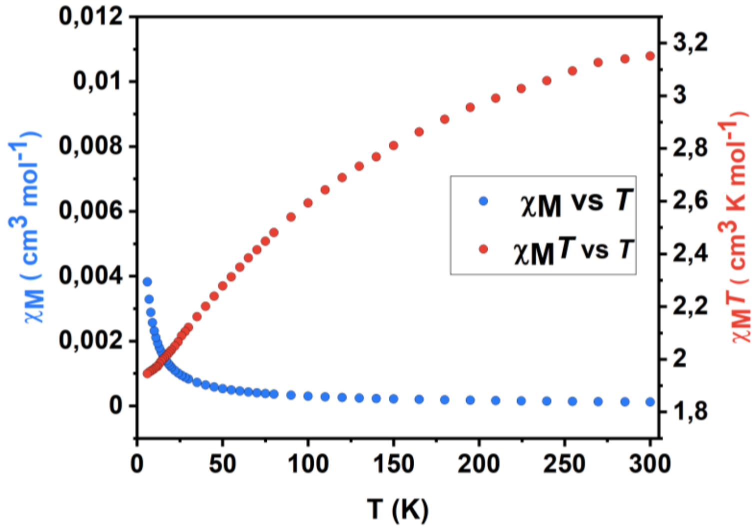

Figure 138. $\chi_M T$ vs. T plot for **1** under 1000 Oe.

Since V^{4+} complexes and Yb^{3+} complexes often display slow relaxation of magnetization in applied fields, we also performed alternating-current magnetic susceptibility measurements on compound **2.** To examine the spin dynamics, the field dependence of the AC magnetic

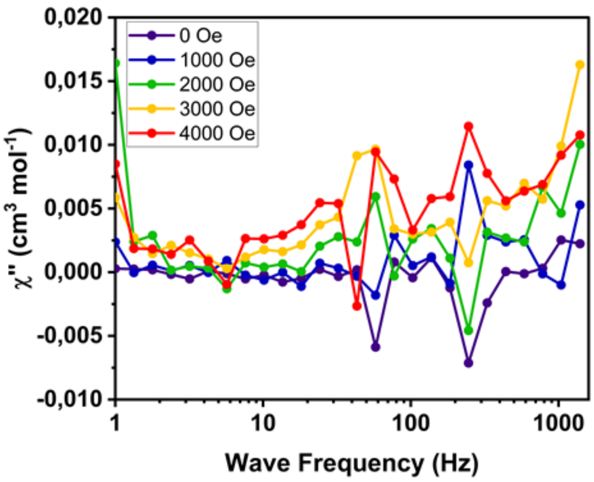

Figure 139. AC susceptibility data of **1.**

susceptibility was collected at 2 K and an ac field of 3.5 Oe across the frequency range of 1 - 1400 Hz for complex **1.** First, the AC susceptibility was measured at the lowest temperature as a function of the magnetic field in order to identify the zero-field or field-induced SMM behavior of the compound (**Figure 139**). Complex **1** showed no out-of-phase susceptibility signal with or without external field. However, we did not observe any imaginary component of the susceptibility, indicating that the possible weak antiferromagnetic coupling observed through dc measurements hampers slow relaxation of magnetization in the solid state.

7.1.5. Low-Temperature Luminescence

Yb^{3+} is supposed to show a single photoluminescent emission band in the NIR region. The emission is related to the $^2F_{5/2} \rightarrow ^2F_{7/2}$ transition of Yb^{3+}. Solid state photoluminescence spectroscopy measurements were performed on complex **2** at 3 K, with an excitation wavelength of 380 nm. As expected, a single emission band is observed between 960 nm and 1050 nm (**Figure 140**), corresponding to $^2F_{5/2} \rightarrow ^2F_{7/2}$. For complex **1** the transition is very clearly composed of three distinct lines and one shoulder peak, the first emission peak is found at 980.5 nm, which corresponds to an energy gap between $^2F_{7/2}$ and $^2F_{5/2}$ of 10198.9 cm^{-1}.

Choosing the first emission as a relative zero energy line, the peak positions for the following peaks of 1000.1 nm, the shoulder peak at 1013.7 nm and 1030.7 nm translate to relative energies of the first, second and third excited Kramers doublet of 109.9 cm^{-1}, 334 cm^{-1} and 496.8 cm^{-1}, respectively. The broad peak at 1140 nm is the third harmonic peak (3*380) which couldn't be removed with a low pass 400 nm filter.

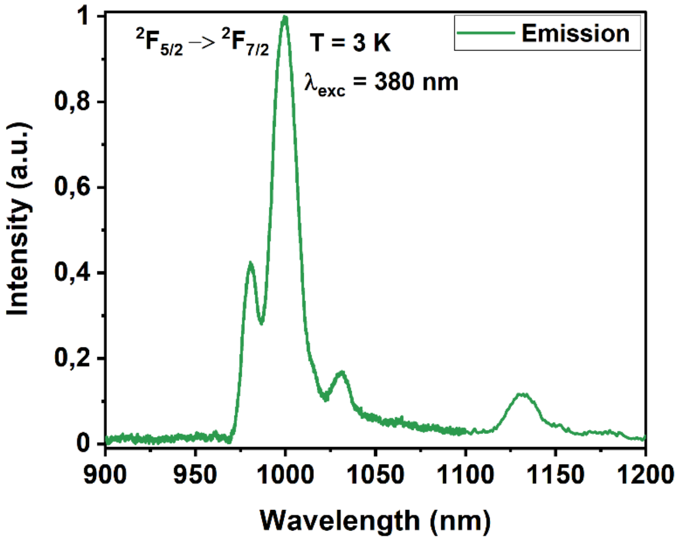

Figure 140. Solid-state emission spectra recorded at 3 K with λ_{exc} = 369 nm for **2**.

The absence of slow relaxation despite of the relatively large energy gap (109.9 cm^{-1}) between the ground and the first excited m$_j$ state suggesting efficient QTM relaxation due to the non-beneficial ligand field.

We find that the highly resolved X-band EPR spectra exhibited by these complexes in frozen solution would allow for the accurate measurement of the superhyperfine coupling with most abundant isotopes of ^{171}Yb (I = 1/2, NA = 14.1%), ^{173}Yb (I = 5/2, NA = 16.1%) in addition to the usual hyperfine interaction with the ^{51}V (I = 7/2, NA = 99.75%) nucleus. To then understand the origin of the superhyperfine coupling with Yb, we would additionally need the DFT calculations .

7.1.6. Conclusion and Outlook

We have successfully synthesized and structurally characterized a heterobimetallic Yb^{3+}–V^{4+} complex (**2**) using XRD, its magnetic properties were scrutinized by experimental DC and AC magnetometry. The DC data shows paramagnetic behavior and AC measurements did not show any slow relaxation behavior neither under external field nor under zero field. For the first time we have recorded a low temperature solid state emission spectrum of a Yb^{3+}–V^{4+} based salen complex and could also deduce the energy gap between the ground and first excited m_j state. Changing the coordination from chloride salts to nitrate salts, acetylacetonate salts to have a complete first coordination sphere nuclear spin free could be the next step in realizing salen-based Yb^{3+}–V^{4+} luminescent SMMs. We have planned EPR studies to further understand and for the accurate measurement of the super hyperfine coupling between Yb^{3+}–V^{4+} centers and to determine the kind of magnetic interaction between these spin centers. The 4f and the 3d binuclear complexes with their unique coordination geometry offer attractive perspectives for functionalization and processing. The assembly of Yb into V complex in the solid state through Yb···O with the fixed Yb···V distance of 3.473 Å is expected to ensure a weak electronic coupling between the VO^{2+} ion and the Yb^{3+}.

In terms of the future outlook, there's a new electrically neutral complex that has been developed. This complex contains a paramagnetic vanadyl ion ($S = 1/2$) situated in a coordination environment with oxygen and nitrogen donors, and an ytterbium ion ($S = 1/2$) situated in a coordination environment with oxygen and chlorine donors. The possible hyperfine interaction with the ^{51}V nucleus ($I = 7/2$) could be accompanied by a further superhyperfine coupling with Yb nuclei with a fixed Yb···V distance of 3.473 Å. As a result, the ^{173}Yb-^{51}V isotopomer could contain one electronic qubit ($S = 1/2$) coupled with a nuclear qudit ($I = 7/2$) and with a nuclear qubit (nuclear spin of Yb). The study of the spin coherence properties in frozen organic solution using EPR could be helpful in understanding and supporting the research of vanadyl-based qubits. It's possible to demonstrate the coherent manipulation of the electronic spin by observing Rabi oscillations in nutation experiments.

7.2. Nitronylnitroxide Dinuclear Complex (2) = [$Yb_2(hfac)_4(NIT_2PhO)_2$]

Here, In ligand selection for Ytterbium complexes, we synthesized a complex with nitronyl nitroxide radicals that can act as both spin carriers and building blocks, specifically as functional organic radicals with different substituent groups, such as an imidazol or a related unit, which are electroneutral.[207] We also considered using an anionic and oxygenic moiety as a coligand, a phenol. The oxygen atom bonds more easily with the lanthanide ion than the nitrogen atom, and the polynuclear lanthanide-nitronyl nitroxide complexes are formed due to the strong coordination ability between lanthanide and oxygen atoms, which is rare in the lanthanide-nitronyl nitroxide system. These halogen substitutions in the face moiety are likely to result in electronic effects to induce SMM behavior by reducing spin phonons compared to CH bonds. Moreover, molecule magnets involving anionic radicals and rare earth ions are not common.[207]

In this sub chapter we report lanthanide-anion nitronylnitroxide dinuclear complex (**2**) = **[$Yb_2(hfac)_4(NIT_2PhO)_2$]** NIT_2PhO = 2-(2_-hydroxyphenyl)-4,4,5,5-tetramethyl-imidazoline-1-oxyl-3-oxide; hfac = hexafluoroacetylacetonate . The compound was structurally characterized by single-crystal X-ray diffraction, X-ray fluorescence, elemental analysis, and IR spectroscopy. The synthetic approach provides an innovative way to synthesize new dinuclear lanthanide-nitroxide-based complexes. Additionally, the magnetic properties are investigated by DC and AC magnetometry.

7.2.1. Synthesis

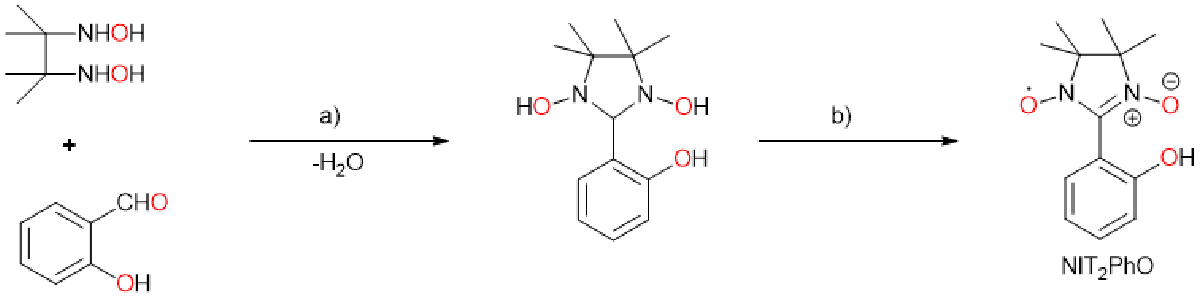

Figure 141. Synthetic pathway of NIT_2PhO nitronyl nitroxide. (a) MeOH, reflux; (b) PbO_2, RT, CH_3OH.

In order to explore the relationship between the magnetic properties and lanthanide ions as well as the substituent groups of radicals, we decide to adopt NIT_2PhO with Yb^{3+} to construct the radical lanthanide system. The phenol-substituted group favors the coordination of the nitroxide to the *Ln* ion and obtaining polynuclear complexes, which is rare in the *Ln*-nitroxide system. NIT_2PhO was obtained by a condensation reaction between salicylaldehyde and 2,3-Bis(hydroxyamino)-2,3-dimethylbutane in methanol and further oxidized by PbO_2 to obtain the radical (**Figure 141**).

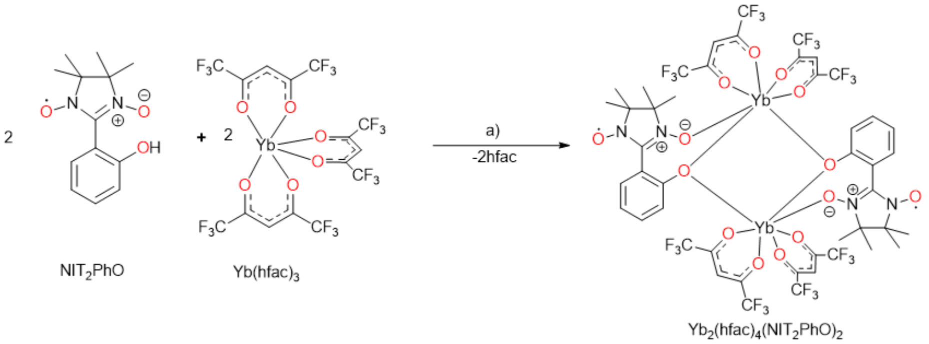

Figure 142. Synthetic pathway of complex **2 [$Yb_2(hfac)_4(NIT_2PhO)_2$]**. (a) heptane/diethylether, RT.

Complex **2** is obtained after coordinating $Yb(hfac)_3$ salt with NIT_2PhO under inert conditions (**Figure 142**). The purple crystals were obtained after several days from the schlenk tube and were not stable in the solution which is indicated by the colour change from purple to orange. Which is why for analysis one needs fresh sample each time. Due to the paramagnetic nature of nitroxide, the use of NMR precludes structural characterization. We characterized the fresh purple crystals for determining the crystal structure using SC-XRD.

7.2.2. Crystal Structures

Complex **2**, **[$Yb_2(hfac)_4(NIT_2PhO)_2$]:** The complex crystallizes in the triclinic packing P-1 (a = 10.3206(6) Å, b = 12.0532(8) Å, c = 13.2532(11) Å, α = 68.792(7)°, β = 75.766(6)°, γ = 69.969(6)°, V = 1429.94 Å^3). As shown in **Figure 143a**, the centrosymmetric dinuclear complex is composed of two [$Yb(hfac)_2(NIT_2PhO)$] units bridged by two phenoxo-O anions, and the oxygen atom of the N–O group is coordinated to a single $Ln(hfac)_2$ unit. Each Yb atom is seven-coordinate, and the coordination spheres of the Yb atoms are completed by four oxygen atoms from two bidentate hfac ligands. The polyhedral shape of the central Yb atom was ascertained by continuous shape measures analysis carried out with SHAPE analysis. The resulting data revealed that the shape around the central metal atom is a capped octahedron (C_{3v}). The Yb–O–Yb bridge angles are 110.98(10)°, the O–Yb–O bridge angles are 69.02(10)° and related Yb–O distances are in the range of 2.234(2)–2.305(2) Å, the Yb-O (phenolic oxygen) bond length is 2.234(2) Å, the Yb–O (nitroxide group) bond length is 2.305(2) Å, which are comparable to those of the reported data in other phenoxo-bridged lanthanide complexes. The central core Yb_2O_2 appears to be nearly rhombic with two different sides, two different angles and the Yb–Yb distance is 3.741(2) Å (**Figure 143b)**, and the Yb–O (hfac) bond lengths are in the range of 2.218(2)–2.317(3) Å. The packing arrangement of the molecules in (**2**) is shown in **Figure 143c**. The shortest separation between the uncoordinated NO groups is 4.473 Å.

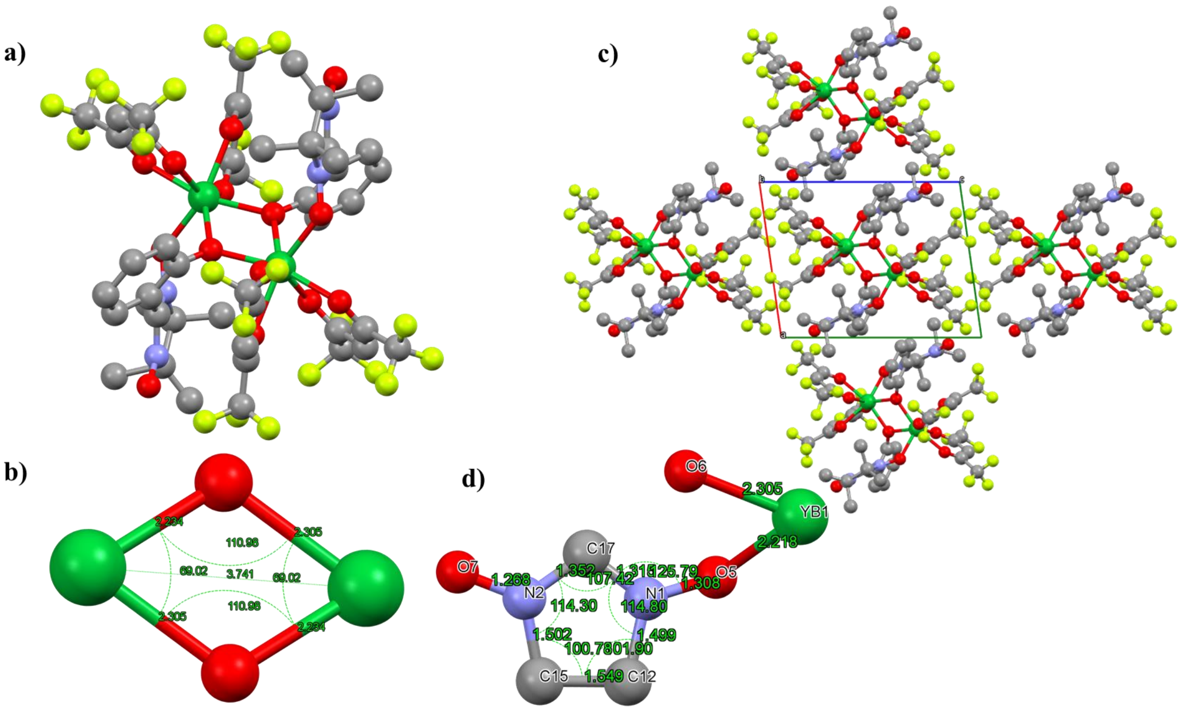

Figure 143. a) Crystal structure of (**2**). b) The Central Yb_2O_2 core of (**2**). c) The packing arrangement of the molecules in (2) d) The NIT_2PhO moiety coordinated to the Yb. Green (Yb), Grey (C), Violet (N), Red (O), Yellow (F), hydrogen atoms are omitted for clarity.

The bond lengths of the two N-O groups in the NIT_2PhO are 1.268 and 1.308 Å. The O coordinated to the Yb is from the N-O with the higher bond length and the one from the smaller N-O is uncoordinated. Based on the bond lengths of the N-O groups, the radical of the NIT_2PhO is on the oxygen that is uncoordinated to the Yb. The electronegative oxygen and the conjugation with the double bond of the imidazole stabilize the radical. Fragment O7–N2–C17–

N1–O5 of nitronyl nitroxide on which the radical is delocalized is mostly planar, with the internal angles of the imidazole ring ranging from 100.71-114.30° and the two similar external O7–N2–C17 and O5–N1–C17 angles being 123.53° and 125.79°, respectively (**Figure 143d**).

7.2.3. X-Ray Fluorescence

Since we do not have any other heavy element in complex **2,** It is harder for us to deduce the stoichiometric ratios of Yb. However, we used the technique for additional confirmation of the presence of Yb (7.415- $L_{\alpha 1}$, 8.4040- $L_{\beta 1}$, 8.758- $L_{\beta 1}$, 9.780-$L_{\gamma 1,}$ 1.521-$M_{\alpha 1}$) element in the complex (**Figure 144**).

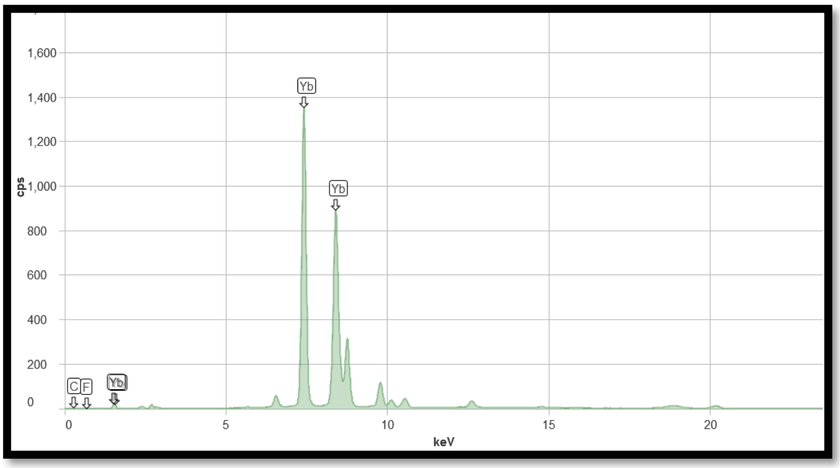

Figure 144. X-Ray Fluorescence of complex **2**.

7.2.4. Magnetic Measurements

The variable-temperature magnetic susceptibilities were measured with a SQUID magnetometer in the temperature range 2–300 K in an applied field of 1000 Oe for the complex **2**. The $\chi_M T$ vs. T plots for **2** is shown in **Figure 145**. At room temperature, the $\chi_M T$ value is 5.56 $cm^3 \cdot K \cdot mol^{-1}$, which is close to 5.86 $cm^3 \cdot K \cdot mol^{-1}$ expected for two uncorrelated Yb^{3+} (a $^2F_{7/2}$ ion) and two uncorrelated $S = 1/2$ spins of the nitronyl nitroxyl radicals. As the temperature is lowered, the $\chi_M T$ value gradually decreases to reach 2.75 $cm^3 \cdot K \cdot mol^{-1}$ at 30 K, due to crystal-field effects on the Yb^{3+} Stark sub-level. Below 30 K, the $\chi_M T$ value decreases rapidly to a minimum of 0.33 $cm^3 \cdot K \cdot mol^{-1}$ at 2 K.

This overall behavior encompasses three processes, namely: (i) the intrinsic behavior of Yb^{3+} due to the crystal field effect, (ii) the magnetic interaction between Yb^{3+} ions, and the (iii) the Yb–Yb interaction mediated by the phenolate bridges. It is therefore difficult to attribute the behavior to a specific contribution. Even so, the interaction between Ln and directly co-ordinated nitroxide group is known to be ferromagnetic for the Ln^{3+} with $4f^7$–$4f^{10}$ electronic configurations.[208] Thus the Yb-nitronyl nitroxide interaction is anticipated to be antiferromagnetic, this claim is also supported by the χ_M *vs.* T plot as it shows the signature dip in the χ_M value at very low temperatures (T<10 K) (**Figure 145**). Due to the separation between the uncoordinated NO groups being too far to influence each other (the shortest separation is 4.473 Å), the magnetic coupling between the uncoordinated nitroxide groups can be ignored.

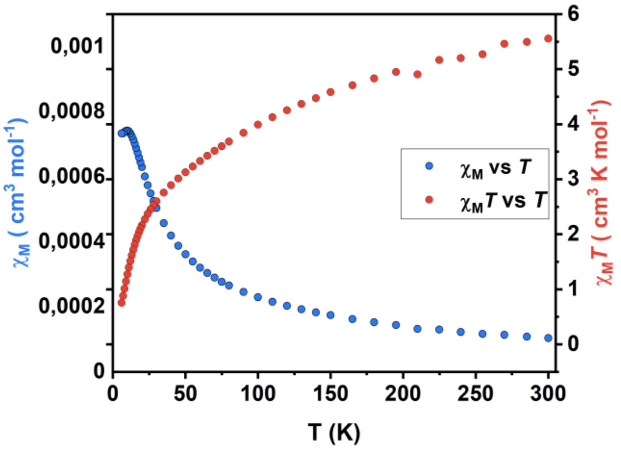

Figure 145. χ_M vs. T (blue) and $\chi_M T$ vs. T (red) plots for **2** under 1000 Oe.

To examine the spin dynamics, the field dependence of the AC magnetic susceptibility was collected at 2 K and an ac field of 3.5 Oe across the frequency range of 1 - 1400 Hz for complex **2**. The out-of-phase signals (χ_M'') are depicted in **Figure 146**, but the signals do not display a considerable frequency-dependence signal at 2.0 K, the minimum operating temperature of our SQUID magnetometer. Nevertheless, this novel chelating anion nitronyl nitroxide radical bridged dinuclear ytterbium structure is first reported in the ytterbium-nitronyl nitroxide system by us. It provides an innovative approach to synthesize new dinuclear ytterbium-nitroxide-based compounds.

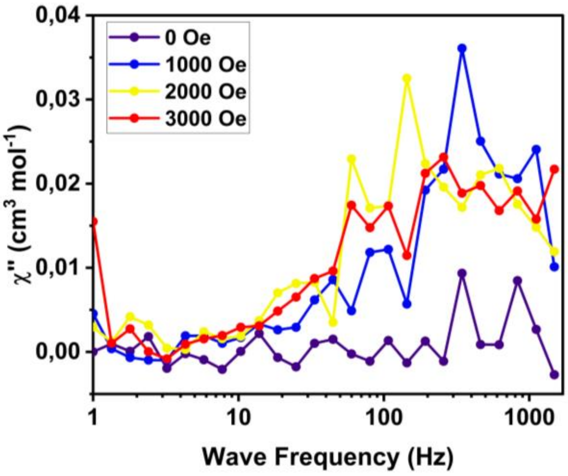

Figure 146. AC susceptibility data of **2**.

7.2.5. Conclusion and Outlook

We have successfully prepared a phenoxo-bridged dinuclear Yb-radical complex (**2**) by using phenol-functionalized anion nitronyl nitroxide radicals. As far as we know, this is the first reported dinuclear Yb system with chelating nitronyl nitroxide radical. The phenol-substituted group favors the coordination of the nitroxide to the Yb ion and obtaining polynuclear complexes, which is rare in the Ln-nitroxide system. It appears to be a very innovative approach to develop dinuclear lanthanide nitroxide-based complexes. In the complex, the central lanthanide atoms are seven-coordinated and the polyhedral shapes are capped octahedron through analysis carried out with SHAPE. This is less common than the octa or nona-coordinated surrounding usually obtained in Ln coordination compounds. DC Magnetic measurements show antiferromagnetic interaction, with the signature dip in the χ_M values from 10 K down to 2 K, between the paramagnetic ions (Yb^{3+}) and radical. AC measurements did not show any slow relaxation behavior with or without an external field. Though no out-of-phase signals were observed, it contributed to the exploration of the relationship between the magnetism and structures based on the NIT2PhO ligand and also gave a promising way to design and synthesize dimeric Ln complexes systematically. Using EPR spectroscopy, and depending on the nature of the nitronyl nitroxide radicals, we could characterize the radical moieties and their interactions with paramagnetic Yb^{3+} ions (S =1/2). These NIT_2PhO ligands are key precursors for the synthesis of dimeric 4f complexes and paramagnetic phthalocyanine and porphyrin macrocycles to be used as open-shell organic building blocks of molecule based magnetic materials. This work is underway and will be continued towards the direction of EPR characterization in order to explore the relationship between the magnetic properties and lanthanide ions as well as the substituent groups of radicals.

Chapter 8: Synthesis and Characterization

Experimental Section

The procedural approach is explained in the experimental section. In the initial section, the synthesis protocols and analytical methods' assessment are highlighted.

8.1. Materials and Equipment

Chemicals

The chemicals that were utilized in the synthesis process were obtained from commercial sources and were used in their original form without any further purification or modification. These chemicals were readily available and procured as per standard industry practices.

Thin-layer Chromatography (TLC)

For the purpose of analyzing the chemical components of a sample, thin-layer chromatography was employed. This process involved using thin sheets of aluminum coated with silica gel, which were provided by, Merck. The specific type of silica gel used in this case is known as 60 $F_2$54. In order to identify the various components, present in the sample, detection was carried out using ultraviolet (UV) light, with a wavelength range of 254 nanometers.

Column Chromatography

During the experiment, the crude products were separated using a technique called flash column chromatography. For the stationary phase, Silica gel Si 60 with a particle size of less than 0.063 nanometers from Merck, or activated basic alumina with a particle size ranging from 0.063 to 0.2 millimeters, also from Merck were used. The choice of which stationary phase to use depended on the specific requirements of the experiment. In determining the appropriate mobile phase, various factors were taken into account, and the details of this process are mentioned in the experiment description.

^{1}H-NMR Spectroscopy

The method employed to perform ^{1}H-NMR measurements involved the use of a Bruker instrument with a frequency of 500 MHz. Solvents such as deuterated chloroform ($CDCl_3$), dichloromethane (CD_2Cl_2) or methanol (CD_3OD) were used. The chemical shift values were reported in ppm and referenced to tetramethylsilane as an internal standard. Furthermore, the coupling constants were reported in hertz [Hz], and the multiplets were abbreviated as s (singlet), d (doublet), t (triplet), q (quartet), and m (multiplet). With respect to the multiplets, the entire range was indicated, whereas for the signal centroid, the chemical shift values were given. The data analysis was performed using TopSpin 4.0.6 software from Bruker.

ATR-IR Spectroscopy

The ATR crystal was used as a base for the sample under investigation. Nicolet's " iS50 FTIR spectrometer" instrument was used to record the IR spectra. OPUS 7.0 software was employed for data analysis. Vibration frequencies were reported in wavenumbers (cm^{-1}), and the range of measurements was from 400-4000 cm^{-1}. Abbreviations such as def (for deformation), sh (for sharp), m (for medium), w (for weak) were used to aid in characterization.

ESI-TOF-MS Spectometry

ESI MS measurements were performed on a commercial Bruker TIMS-TOF instrument, equipped with an electrospray source. The samples for ESI MS measurements were prepared in Methanol or DCM.

The samples were measured in the positive ion mode under the following experimental conditions: capillary voltage: 4 kV, end plate offset: 2200 V, nebulizer: 0.3 Bar, dry gas: 3.5 l/min, dry temperature: 200 °C, flow rate: 100 µL/h.

UV-VIS Spectroscopy

The UV-Vis measurements were performed using the “Cary 500 Scan” instrument from Varian. Solutions with a concentration of approximately 10^{-4} – 10^{-8} M in dichloromethane and

Methanol-d^4 were used. Spectroscopic measurements were performed with 10×10 mm² quartz suprasil certified cells (Helma Analytics). Additionally, UV/Vis absorption spectra were also recorded on a Specord 205 (Analytic Jena) spectrometer and a lambda 950 UV/VIS/NIR absorption spectrometer from Perkin Elmer.

Emission Measurements

The steady-state emission spectra were measured using an Edinburgh Instruments FLP920 with a continuous 450 W Xe lamp. The visible detection (230 to 900 nm) was carried out using a red-sensitive R928 photomultiplier from Hamamatsu in Pelletier housing, and the Vis-NIR part was detected using a Hamamatsu R5 509-72 photomultiplier cooled at 77 K. To eliminate the second order artifacts for the visible part, a 330 nm high pass cut-off filter was used, and an 850 nm high pass cut-off filter was used for the NIR part. Phosphorescence lifetimes were measured using the same instrument in the Multi Channels Spectroscopy mode, with a Xenon flash lamp as the excitation source. Luminescence errors were estimated to be ±10%. Luminescence quantum yields were measured using conventional procedures, [209] with $Ru(bipy)_3Cl_2$ in methanol ($\varphi = 4.0\%$)[210] for Eu and cardiogreen in MeOH ($\varphi = 7.8\%$)[210] for Yb. Diluted solutions (optical density < 0.05) were used for the measurements. The UC_{QY} was measured on concentrated solutions (ca. 1-2 mM) using the luminescence QY definition as the ratio of the number of emitted photons to the number of photons absorbed. The Tb_1Yb_8 D_{Ln}:D_s:HL complex ($\phi_{UC} = 1 \times 10^{-7}$) was used as a reference for comparison with the emitted signals. Steady-state upconversion emission spectra were recorded using an Edinburgh Instrument FLP920 spectrometer. The excitation source was a 980 nm LED, and an 850 nm high pass filter was placed between the source and the sample to remove any potential visible excitation. The power of the LED was calibrated using a FieldMate power meter from Coherent Technology.

EDX Spectroscopy

EDX measurements were conducted using an Oxford Instruments X-MaxN 50 mm^2 Silicon Drift Detector within a Leo Gemini SEM.

Powder X-Ray Diffraction

X-ray diffraction (XRD) patterns of the powders were obtained using a Bruker D8 diffractometer. The measurements were conducted with Bragg-Brentano geometry 89 Experimental Section Materials and Equipment and Cu-Kα radiation. The measurements were performed within the range of 0 to 50 degrees.

TGA-DSC Analysis

The measurements were conducted using a Setaram thermal analyzer SENSYS evo TGA-DSC, coupled with a “Pfeiffer OmniStar” mass spectrometer. The evolved gas during the analysis was analyzed using simultaneous thermogravimetric analysis, differential scanning calorimetry(TGA-DSC). The analyses were carried out under an argon atmosphere, with a heating rate of 10 °C/min.

Elemental Analysis

Elemental analyses were performed using a Vario micro cube instrument in CHNS mode.

Photoluminescence Measurements

Photoluminescence measurements were recorded using a Horiba Fluorolog spectrometer with a 920 photomultiplier tube detector for the visible range and a InGaAs detector for the near-IR region. The solid crystalline samples were placed in between two quartz glass plates with a drop of perfluorinated oil and cooled to 3 K under vacuum.

Crystallography

Single crystal X-ray diffraction measurements were performed on an STOE StadiVadi 25 diffractometer using a GeniX 3D HF microfocus with MoKα-radiation (λ = 0.71073 Å) and a CCD image plate detector. Crystals were mounted using crystallographic oil and placed in a cold nitrogen stream. All data were corrected for absorption using CrysAlisPro.1 The structures were solved by direct methods and refined against F2 using the SHELXL-97 package2 in

Olex2.3 All non-hydrogen atoms were refined anisotropically, and hydrogens were placed based on a riding model approach. Full crystallographic details can be found in CIF format: see the Cambridge Crystallographic Data Centre database 2288023.

8.2. Calculations in Fluorescence and UC measurements

Some of the key calculations in understanding and studying the UC complexes are provided below.

Quantum Yield calculations

$$QY = \frac{Q_{ref} \times d_{comp}^{2} \times A_{ref} \times I_{comp}}{d_{ref}^{2} \times A_{comp} \times I_{ref}}$$

ref is the reference, e.g., cardiogreen and Ru(bipy)$_3$Cl$_2$

comp the cluster

Q_{ref} is 7.8 % for cardogreen and 4.0% for Ru(bipy)$_3$Cl$_2$

d is the Refractive index of the solvent

d(H_2O) = 1.3330, d(D_2O) = 1.3281, d(MeOH) = 1.329, d(CD_3OD) = 1.326

A is the absorbance at the excitation wavelength

I is the integral of the emission intensity

For example for the Yb in Eu$_8$Yb calculation:

Cardiogreen is the ref; so, **Q_{ref}** = 7.8%

Solvent is CD_3OD therefore, d = 1.326

A_{ref} is the absorbance at 765 nm: 0.045291

I_{comp} is the integration of emission band of Yb

The ref was dissolved in methanol d = 1.329

A_{comp} is the absorbance at 326 nm : 0.033823

I_{ref} is the integration of emission band of the reference

$$QY_{Yb} = \frac{0.078 \ \times 1.326^2 \times 0.045291 * 110484}{1.329^2 \times 0.033823 * 4.35E+6} = 0.26\%$$

$$QY_{Eu} = \frac{0.04 \ \times 1.326^2 \times 0.04883 * 72003.8}{1.329^2 \times 0.033823 * 3.27E+6} = 0.13\%$$

Radiative lifetime calculation

Details for the calculation of τ_{rad}.

From the NIR absorption band of Yb and weighting the absorption coefficients by the number of Yb atoms, it was possible to calculate the radiative lifetime of Yb, τ_{rad}, using the equation:

$$\frac{\mathbf{1}}{\boldsymbol{\tau_R}} = \mathbf{2303\ x} \left(\frac{\boldsymbol{8\pi c n^2 v_{ul}^2}}{\boldsymbol{N_A}}\right)\left(\frac{\boldsymbol{g_l}}{\boldsymbol{g_u}}\right)\int \boldsymbol{\varepsilon(v)dv}$$

In this modified Einstein relation, c is the speed of light in vacuo (in cm s^{-1}), $\boldsymbol{v}$ is the frequency of the transition in cm^{-1}, n is the refractive index of the medium, N_A is Avogadro's constant, $\boldsymbol{\varepsilon(v)}$ is the absorption spectrum of the transition (in M^{-1} cm^{-1} vs. wavenumber), g_l and g_u denote the degeneracies of the ground and excited states respectively, in the case of trivalent lanthanide ions 2J + 1. (Yb^{3+}: $g_l = 8$, $g_u = 6$)

If the radiative lifetime, $\boldsymbol{\tau_R}$, is known, Φ_{Ln} can be calculated using the observed luminescence lifetime, $\boldsymbol{\tau_{obs}}$:

$$\Phi_{Ln} = \frac{\boldsymbol{\tau_{obs}}}{\boldsymbol{\tau_R}}$$

Within a general paradigm, the overall luminescence quantum yield of the complex upon excitation of the chromophore is determined by the efficiency of the sensitization (η_{sens}) and by the quantum yield (Φ_{Ln}) of the lanthanide luminescence step.

$$\Phi_{tot} = \eta_{sens}\Phi_{Ln}$$

UC Quantum Yield Calculation

$$\Phi_{UC} = \Phi_{ref} \times \frac{nD_{UC}^2}{nD_{ref}^2} \times \frac{\int I_{UC}}{\int I_{ref}} \times \frac{P_{ref} \times \lambda_{exc-ref} \times A_{ref}}{P_{UC} \times \lambda_{exc-UC} \times A_{UC}}$$

nD Refractive index of the solvent,

$\int I$ Emission spectrum Integral,

P the power of the excitation source

λ Excitation wavelength and

A Absorbance at excitation wavelength

8.3 Ligands

Ligands used

1. **1-phenylbutane-1,3-dione (BA)**

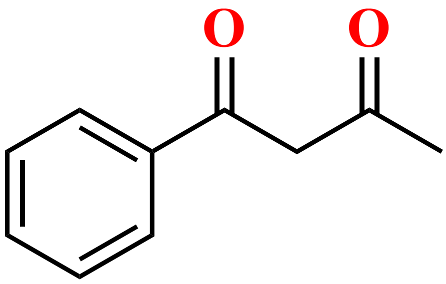

2. **9-hydroxy-phenalen-1-one (PLN)**

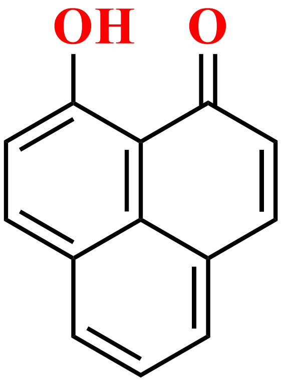

3. **1-pyrenebutane-1,3-dione (PA)**

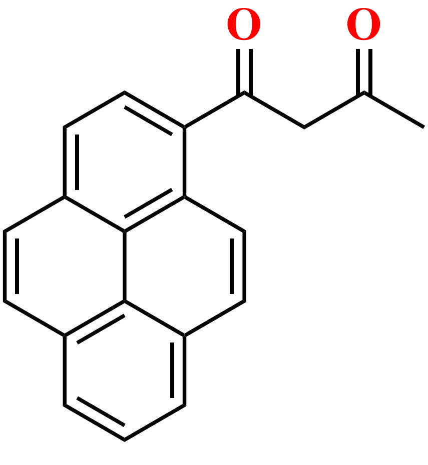

Preparation of 1-pyrenebutane-1,3-dione (PA):

Compound was synthesized modifying the procedures described in the literature.[211] In the experiment, the reaction was carried out in an inert atmosphere. Initially, NaH suspension was mixed, which was in excess, with dry THF (30 mL). The suspension contained 2.5 g (40 mmol) of NaH dispersion in oil. Later, 2-Acetylpyrene was introduced, which is 10 mmol (2.44) g in weight, into the mixture under Ar atmosphere. We let it stir for 30 minutes before carefully adding Ethyl acetate (4 mL) to the mixture. Afterward, we refluxed the solution for 12 hours. We treated the mixture with 10% aqueous NH_4Cl (30 mL) and adjusted its pH to 5 with *dil.*hydrochloric acid. Next, we separated the aqueous phase and extracted it with pure Ethyl acetate. Later, we combined the organic extracts and dried them over anhydrous Na_2SO_4. Finally, we concentrated the extract under reduced pressure. We first purified the crude product by using a flash column with 7 hexane:1 EtOAc. Further purification was carried out by column chromatography using SiO_2 and 1 hexane:1 EtOAc. During this process, we noticed three spots on the TLC slide, and the second one turned out to be the desired product. To obtain crystals, the product is dissolved in hot $CHCl_3$ and layered the solution with hexane through the walls and left it for slow evaporation to get the desired result.

Yield: 48.9% (1.40 g)

^{1}H-NMR: (500 MHz, $CDCl_3$): 8.805 (1H, d, OH), 8.315-8.0174 (9H, m, Pyrene), 6.2337 (1H, s, CH_2), 2.2995 (3H, s, CH_3) ppm.

ESI-TOF-MS: 287.1272 m/z (Simulated $C_{20}H_{14}O_2$ 287.1067).

CHN analysis: Calc C: 83.90, H: 4.93; Exp C: 83.86, H: 4.92.

8.4 Preparation of complexes

Preparation of $Yb(BA)_3{\cdot}H_2O$: (Yb-Monomer)

A solution was prepared by dissolving 1-phenylbutane-1,3-dione (4 mmol, 648 mg) and Piperidine (4 mmol, 0.398 mL) in 20 mL of ethanol. The mixture was then heated to 72°C until everything dissolved, followed by the slow dropwise addition of $YbCl_3{\cdot}6H_2O$ (1 mmol, 387 mg) aqueous solution (10 mL). A cloudy precipitate appeared and disappeared on stirring upon the addition of $YbCl_3{\cdot}6H_2O$ solution increases. The mixture was allowed to stir for 3 h at a refluxing temperature. Once the solution became clear, it was cooled slowly to room temperature and filtered into vials. The filtered solution was left undisturbed to obtain crystals of $Yb(BA)_3{}^{.}H2O$.

Yield: 45.9% (310 mg)

^{1}H-NMR: Paramagnetic

CHN analysis: Calc C: 53.41, H: 4.33; Exp C: 53.51, H: 4.64.

XRD:

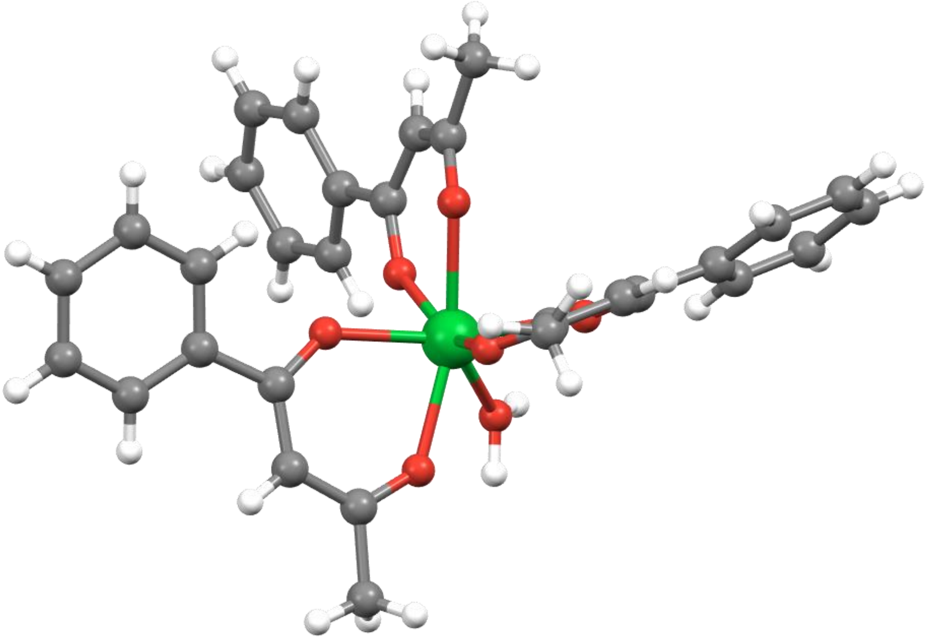

Figure 147. Crystal structure of $Yb(BzAc)_3{}^{.}H_2O$: Green (Yb), Grey (C), Red (O), White (H).

Table 15. Crystal data of $Yb(BA)_3.H_2O$.

CHEMICAL FORMULA	C_{30} H_{29} O_7 Yb
SPACE GROUP	*P* $\bar{1}$ (2)
CRYSTAL SYSTEM	Triclinic
CELL LENGHTS (Å)	**a** 6.1549(9) **b** 12.3812(15) **c** 18.5688(19)
CELL ANGLES (°)	**α** 82.056(9) **β** 86.325(10) **γ** 83.569(11)
CELL VOLUME (Å^3)	1390.94
Z, Z’	**Z**: 2 **Z’**: 1
R-FACTOR(%)	4.86
TEMPERATURE (K)	180

Preparation of $[Yb_9(BA)_{16}(OH)_{10}]Cl$: ($Yb_9$-BA)

A solution was prepared by dissolving 1-phenylbutane-1,3-dione (4 mmol, 648 mg) and Piperidine (4 mmol, 398 µL) in 60 mL of ethanol. The mixture was then heated to 72°C until everything dissolved, followed by the slow dropwise addition of $YbCl_3 \cdot 6H_2O$ (1 mmol, 387 mg) in aqueous solution (10 mL). A cloudy precipitate appears and disappears on stirring as the addition of $YbCl_3 \cdot 6H_2O$ solution increases. The mixture was allowed to stir for 3 h at a refluxing temperature while the ethanol was being refluxed. Once the solution became clear, it was cooled slowly to room temperature and filtered into vials. The filtered solution was left undisturbed to obtain crystals of $[Yb_9(BA)_{16}(OH)_{10}]Cl$.

Yield: 690 mg (70%)

^{1}H-NMR: Paramagnetic

ESI-TOF: *m/z* 4306.41 $[Yb_9(BA)_{16}(OH)_{10}]^+$. Calcd 4306.46.

CHN analysis: $C_{160}H_{154}ClO_{42}Yb_9$; Calc C, 44.37; H, 3.61. Exp C, 44.46; H, 3.59.

XRD:

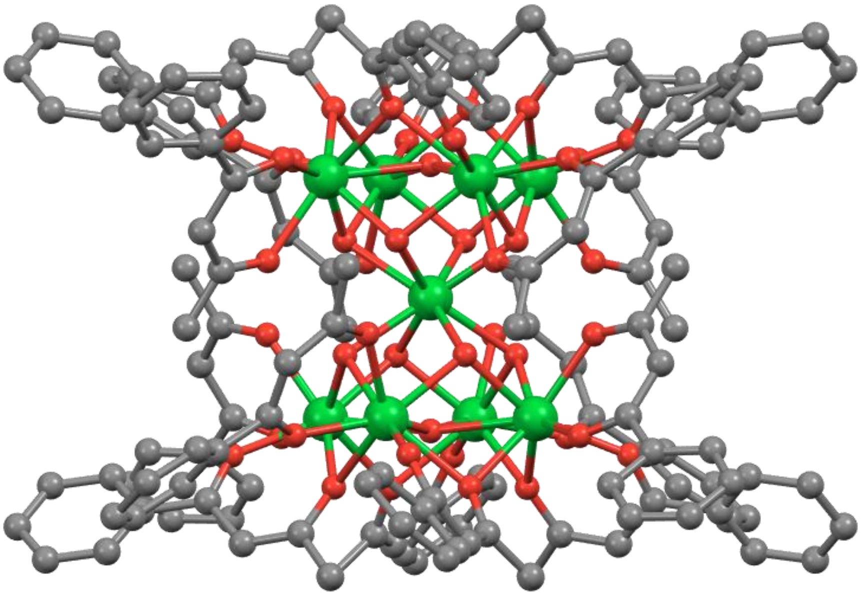

Figure 148. Crystal structure of $[Yb_9(BA)_{16}(OH)_{10}]Cl$: Green (Yb), Grey (C), Red (O).

Table 16. Crystal data of $[Yb_9(BA)_{16}(OH)_{10}]Cl$

CHEMICAL FORMULA	$C_{160}H_{154}ClO_{42}Yb_9$
SPACE GROUP	$P\,n\,\bar{3}\,n$ (222)
CRYSTAL SYSTEM	Cubic
CELL LENGHTS (Å)	***a*** = ***b*** = ***c*** 33.50570(18)
CELL ANGLES (°)	**α = β = γ = 90**
CELL VOLUME (Å^3)	37614.6
Z, Z'	**Z**: 6 **Z'**: 0.11

R-FACTOR(%)	5.26
TEMPERATURE (K)	180

Preparation of [$Gd_9(BA)_{16}(OH)_{10}$]Cl: (Gd_9-BA)

A solution was prepared by dissolving 1-phenylbutane-1,3-dione (4 mmol, 648 mg) and Piperidine (4 mmol, 398 µL) in 60 mL of ethanol. The mixture was then heated to 72°C until everything dissolved, followed by the slow dropwise addition of $GdCl_3{\cdot}6H_2O$ (1 mmol, 371.7 mg) aqueous solution (10 mL). A cloudy precipitate appears and disappears on stirring as the addition of $GdCl_3{\cdot}6H_2O$ solution increases. The mixture was allowed to stir for 3 h at a refluxing temperature. Once the solution became clear, it was cooled slowly to room temperature and filtered into vials. The filtered solution was left undisturbed to obtain crystals of [$Gd_9(BA)_{16}(OH)_{10}$]Cl.

Yield: 640 mg (66%)

CHN analysis: $C_{160}H_{154}ClO_{42}Gd_9$; Calcd C, 45.76; H, 3.70 Exp: C, 45.98; H, 3.66.

ESI-TOF: m/z 4164.15 [$Gd_9(BA)_{16}OH_{10}$]$^+$.

XRD:

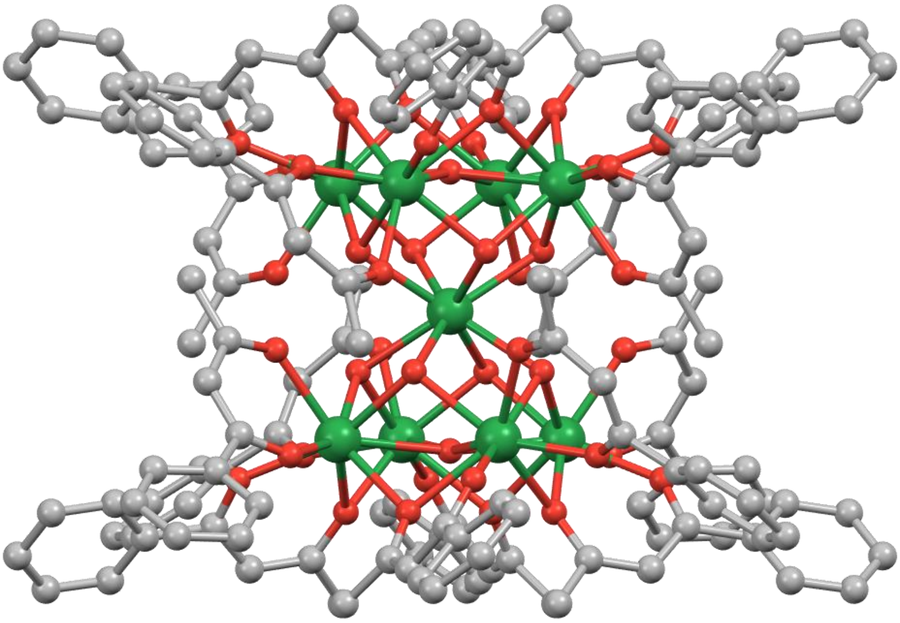

Figure 149. Crystal structure of [$Gd_9(BA)_{16}(OH)_{10}$]Cl: Green (Gd), Grey (C), Red (O).

Table 17. Crystal data of [$Gd_9(BA)_{16}(OH)_{10}$]Cl.

CHEMICAL FORMULA	$C_{160}H_{154}ClO_{42}Gd_9$
SPACE GROUP	$P\ n\ \bar{3}\ n$ (222)

CRYSTAL SYSTEM	Cubic
CELL LENGHTS(Å)	**a** 33.98688(19) **b** 33.98688(19) **c** 33.98688(19)
CELL ANGLES(°)	**$\alpha = \beta = \gamma = 90$**
CELL VOLUME(Å^3)	39258.5
Z, Z'	**Z**: 6 **Z'**: 0.11
R-FACTOR(%)	3.78
TEMPERATURE (K)	180

Preparation of $[Tb_9(BA)_{16}(OH)_{10}]Cl$: ($Tb_9$-BA)

A solution was prepared by dissolving 1-phenylbutane-1,3-dione (4 mmol, 648 mg) and Piperidine (4 mmol, 0.398 mL) in 60 mL of ethanol. The mixture was then heated to 72°C until everything dissolved, followed by the slow dropwise addition of $TbCl_3{\cdot}6H_2O$ (1 mmol, 371.7 mg) aqueous solution (10 mL). A cloudy precipitate appears and disappears on stirring as the addition of $TbCl_3{\cdot}6H_2O$ solution increases. The mixture was allowed to stir for 3 h at a refluxing temperature. Once the solution became clear, it was cooled slowly to room temperature and filtered into vials. The filtered solution was left undisturbed to obtain crystals of $[Tb_9(BA)_{16}(OH)_{10}]Cl$.

Yield: 650 mg (66%)

CHN analysis: $C_{160}H_{154}ClO_{42}Tb_9$; Exp : C, 45.48; H, 3.67. Calcd; C, 45.60; H, 3.68.

XRD:

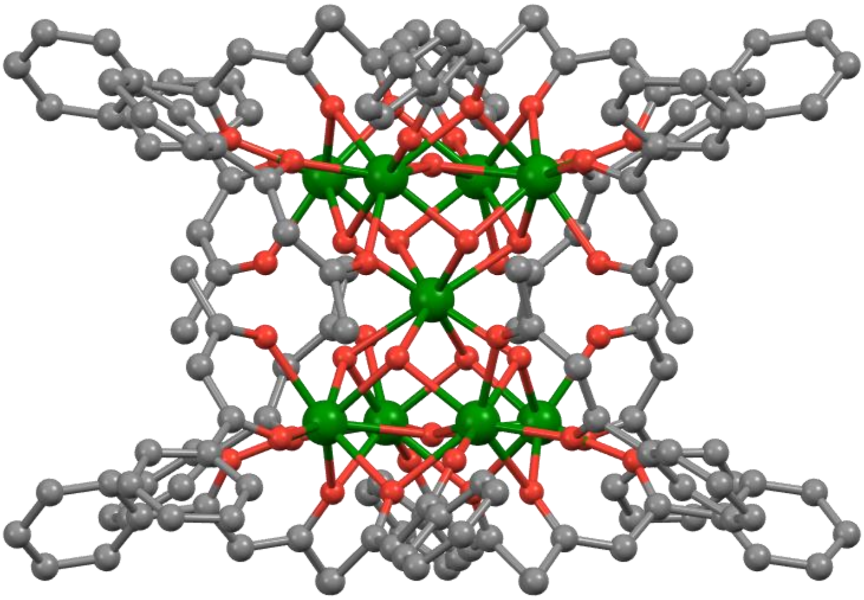

Figure 150. Crystal structure of $[Tb_9(BA)_{16}(OH)_{10}]Cl$: Green (Tb), Grey (C), Red (O).

Table 18. Crystal data of $[Tb_9(BA)_{16}(OH)_{10}]Cl$.

CHEMICAL FORMULA	$C_{160}H_{154}ClO_{42}Tb_9$
SPACE GROUP	*P n* $\bar{3}$ *n* (<u>222</u>)
CRYSTAL SYSTEM	Cubic
CELL LENGHTS(Å)	**a** 33.76869(17) **b** 33.76869(17) **c** 33.76869(17)
CELL ANGLES(°)	**α = β = γ = 90**
CELL VOLUME(Å^3)	38507.3
Z, Z'	**Z**: 6 **Z'**: 0.11
R-FACTOR(%)	3.26
TEMPERATURE (K)	180

Preparation of $[Dy_8Yb(BA)_{16}(OH)_{10}]Cl$: ($Dy_8Yb$-BA)

A solution was prepared by dissolving 1-phenylbutane-1,3-dione (4 mmol, 648 mg) and Piperidine (4 mmol, 0.398 mL) in 60 mL of ethanol. The mixture was then heated to 72°C until everything dissolved, followed by the slow dropwise addition of $DyCl_3{\cdot}6H_2O$ (0.89 mmol, 335.5 mg) and $YbCl_3{\cdot}6H_2O$ (0.11 mmol, 42.6 mg) aqueous solution (10 mL). A cloudy precipitate appears and disappears on stirring as the addition of $DyCl_3.6H_2O$ and $YbCl_3{\cdot}6H_2O$ solution increases. The mixture was allowed to stir for 3 h at a refluxing temperature. Once the solution became clear, it was cooled slowly to room temperature and filtered into vials. The filtered solution was left undisturbed to obtain crystals of $[Dy_8Yb\ (BA)_{16}(OH)_{10}]Cl$.

Yield: 590 mg (60%)

CHN analysis: $C_{160}H_{154}ClO_{42}Dy_8Yb$ Exp: C, 45.18; H, 3.66. Calcd for; C, 45.17; H, 3.65.

XRD:

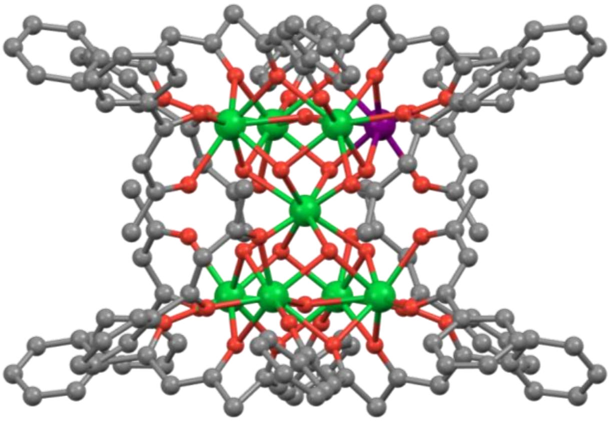

Figure 151. Crystal structure of $[Dy_8Yb(BA)_{16}(OH)_{10}]Cl$: Green (Dy), Purple (Yb), Grey (C), Red (O).

Table 19. Crystal data of $[Dy_8Yb(BA)_{16}(OH)_{10}]Cl$.

CHEMICAL FORMULA	$C_{160}H_{154}ClO_{42}Dy_8Yb$
SPACE GROUP	$P\,n\,\bar{3}\,n$ ($\underline{222}$)
CRYSTAL SYSTEM	Cubic
CELL LENGHTS(Å)	**a** 33.5458(4) **b** 33.5458(4) **c** 33.5458(4)
CELL ANGLES(°)	**α = β = γ = 90**
CELL VOLUME(Å^3)	37749.8
Z, Z’	**Z**: 6 **Z’**: 0.11
R-FACTOR(%)	6.16
TEMPERATURE (K)	150

Preparation of $[Eu_8Yb(BA)_{16}(OH)_{10}]Cl$: Eu_8Yb-BA

A solution was prepared by dissolving 1-phenylbutane-1,3-dione (4 mmol, 648 mg) and Piperidine (4 mmol, 0.398 mL) in 60 mL of ethanol. The mixture was then heated to 72°C until everything dissolved, followed by the slow dropwise addition of $EuCl_3{\cdot}6H_2O$ (0.89 mmol, 326.11 mg) and $YbCl_3{\cdot}6H_2O$ (0.11 mmol, 42.6 mg) aqueous solution (10 mL). A cloudy precipitate appears and disappears on stirring as the addition of $EuCl_3{\cdot}6H_2O$ and $YbCl_3{\cdot}6H_2O$ solution increases. The mixture was allowed to stir for 3 h at a refluxing temperature while the ethanol was being refluxed. Once the solution became clear, it was cooled slowly to room temperature and filtered into vials. The filtered solution was left undisturbed to obtain crystals of $[Eu_8Yb(BA)_{16}(OH)_{10}]Cl$.

Yield: 550 mg (56%)

CHN analysis: $C_{160}H_{154}ClO_{42}Eu_8Yb$ Exp: C, 45.43; H, 3.44. Calcd for; C, 45,50; H, 3.76.

ATR (cm^{-1}): 3330m, 1593s, 1566s, 1506s, 1483m, 1448m, 1368s, 1306w, 1275m, 998w, 960m, 843m, 754m, 709m, 687m.

ESI-TOF: *m/z* 4137.66 $[Eu_8Yb(BA)_{16}(OH)_{10}]^+$. Calcd 4137.32.

μ_{eff}^{300K} 17.47 cm^3 K mol^{-1}, calcd 16.14 cm^3 K mol^{-1} (300 K).

XRD:

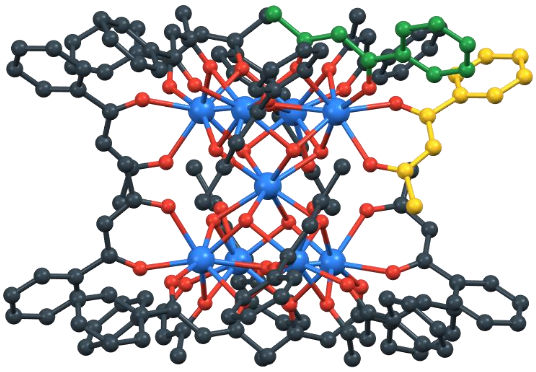

Figure 152. Single crystal structure of $[Eu_8Yb(BA)_{16}OH_{10}]^+$ ion showcasing BA ligands in grey, with endo and exo BA positions in yellow and green, respectively (hydrogens omitted for clarity).

Table 20. Single crystal structure of $[Eu_8Yb(BA)_{16}OH_{10}]Cl$.

CHEMICAL FORMULA	$C_{160}H_{154}ClO_{42}Eu_8Yb$
SPACE GROUP	$P\,n\,\bar{3}\,n$ (222)
CRYSTAL SYSTEM	Cubic
CELL LENGHTS(Å)	**a** 33.6739(6) **b** 33.6739(6) **c** 33.6739(6)
CELL ANGLES(°)	**$\alpha = \beta = \gamma = 90$**
CELL VOLUME(Å^3)	38183.9
Z, Z'	**Z**: 6 **Z'**: 0.11
R-FACTOR(%)	5.04
TEMPERATURE (K)	150

Preparation of $[Eu_9(BA)_{16}(OH)_{10}]Cl$: ($Eu_9$-BA)

A solution was prepared by dissolving 1-phenylbutane-1,3-dione (4 mmol, 648 mg) and Piperidine (4 mmol, 398 µL) in 60 mL of ethanol. The mixture was then heated to 72°C until everything dissolved, followed by the slow dropwise addition of $EuCl_3.6H_2O$ (1 mmol, 366.4 mg) aqueous solution (10 mL). A cloudy precipitate appears and disappears on stirring as the addition of $EuCl_3.6H_2O$ solution increases. The mixture was allowed to stir for 3 h at a refluxing temperature while the ethanol was being refluxed. Once the solution became clear, it was cooled slowly to room temperature and filtered into vials. The filtered solution was left undisturbed to obtain crystals of $[Eu_9(BA)_{16}(OH)_{10}]Cl$.

Yield: 650 mg (66%)

CHN analysis: $C_{160}H_{154}ClO_{42}Eu_9$; Exp: C, 45.98; H, 3.66. Calcd C, 46.28; H, 3.74.

ESI-TOF: m/z 4117.2 $[Eu_9(BA)_{16}OH_{10}]^+$. 4116.58.

XRD:

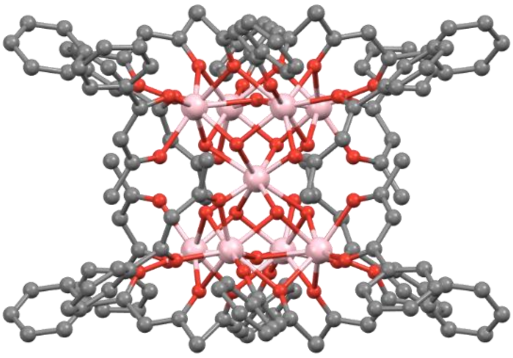

Figure 153. Crystal structure of $[Eu_9(BA)_{16}(OH)_{10}]Cl$: Pink (Eu), Grey (C), Red (O).

Preparation of Complex (1) [Ln(VO)L(Cl)$_3$(H$_2$O)]

H$_2$L (N,N′-bis(1-hydroxy-2-benzylidene-6-methoxy)-1,7-diamino-4azaheptane)ligand). In a 10 ml methanol solution, o-vaniline (6 mmol) and propylenediamine (3 mmol) were mixed and left to reflux overnight. The resulting solution was yellow in color and was evaporated at low pressure to produce a dense reddish oily liquid. This liquid was then treated with 10 ml of diethylether and subjected to ultrasound, resulting in the precipitation of a yellow powder. The powder was filtered under reduced pressure until it was completely free from methanol and washed with diethylether, yielding 81%. The product obtained was used without any further purification.[205]

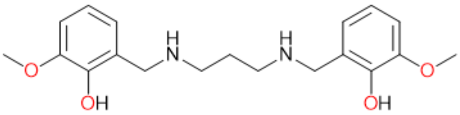

H$_2$L

[VO(L)]. H$_2$L (1 mmol) and VO(acac)$_2$ (1 mmol) were added in 15 ml of methanol. The mixture was left to react for one hour at reflux temperature. Afterward, the resulting precipitate, which was green in color, was filtered under reduced pressure and washed with diethylether. The yield of this process was 77%. The obtained product was used as is, without undergoing any further purification steps.

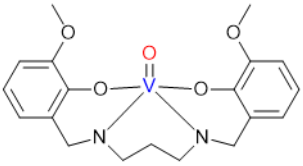

V(O)L

[Ln(VO)LCl$_3$(H$_2$O)] (2). [VO(L)] (0.1 mmol) was suspended in 10 ml of acetonitrile and slightly heated. Next, a dropwise addition of YbCl$_3$·6H$_2$O (0.15 mmol) in 10 ml of acetone was performed. As a result, the yellow solution turned green. The mixture was stirred for an hour, then filtered and left to stand. After several days, green crystals were observed in the solution, which were filtered and washed with diethylether.

CHN analysis: Theo: C 29.49%, H 2.61%, N 9.05% Found: C 29.02%, H 2.78%, N 8.9%.

FTIR-analysis: cm^{-1} (ATR): 3576 (w), 3421 (w), 2951 (w), 1625 (s), 1568(w), 1503 (m), 1466 (s), 1432 (m), 1341 (m), 1275 (s), 1224 (m), 1060 (m), 1026 (m), 988 (m), 939 (m), 856 (m), 735 (m), 636 (w).

$[Yb(VO)LCl_3H_2O]$ (1)

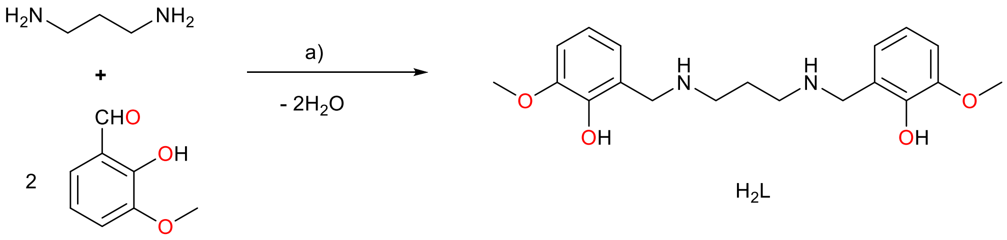

Figure 154. Synthetic pathway of H_2L = N,N′-bis(1-hydroxy-2-benzylidene-6-methoxy)-1,7- diamino-4-azaheptane (a) MeOH, reflux.

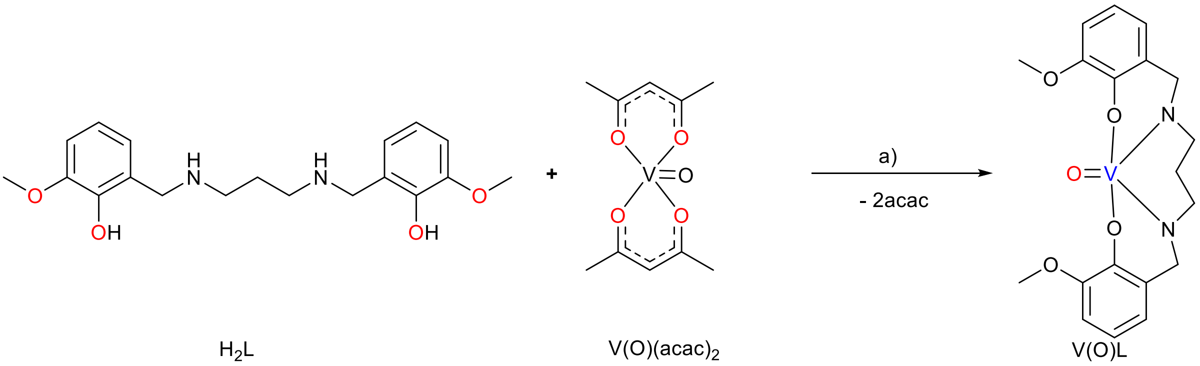

Figure 155. Synthetic pathway of V(O)L a) CH_3OH, reflux.

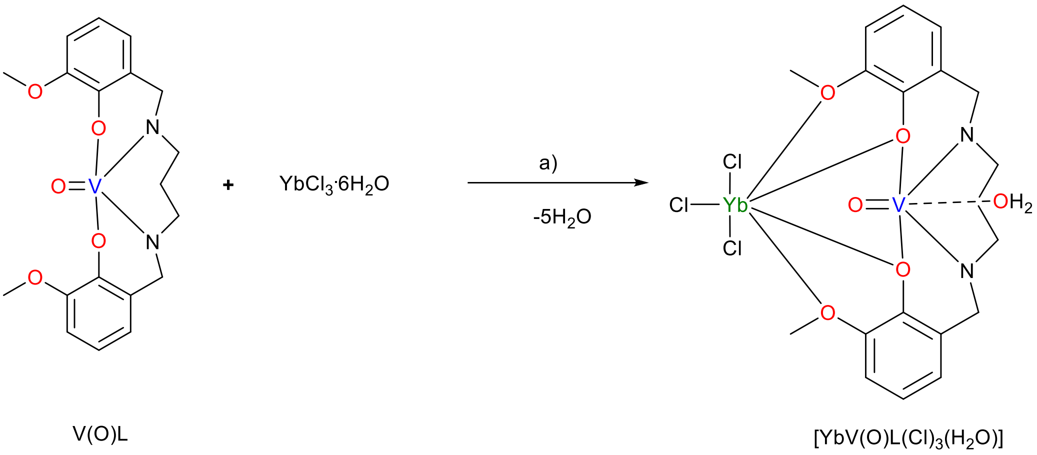

Figure 156. Synthetic pathway of $[YbV(O)L(Cl)_3(H_2O)]$ a) $CH_3CN/CH_3C(O)CH_3$, reflux.

Preparation of [Yb_2(hfac)$_4$(NIT$_2$PhO)$_2$]:[207] (2)

Synthesis of NIT2PhO: Salicylaldehyde (2 mmol, 212 mg) and 2,3-Bis(hydroxyamino)-2,3-dimethylbutane (2 mmol, 296 mg) were added to methanol (10 mL) and reacted for overnight at RT. The filtered precipitate (200 mg) was reacted with PbO_2 (500 mg) for 30 minutes at Rt in methanol (10 mL). The acquired crude product has been purified using column chromatography ($CHCl_3$/CH_3OH: 10:1) and the third spot on the column is our desired product. The product was crystallized in methanol and ether at -20°C. Yield: 240 mg

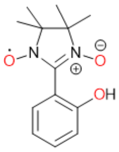

NIT$_2$PhO

Synthesis of [Yb_2(hfac)$_4$(NIT2PhO)$_2$]: Heptane (30 mL) was added to Yb(hfac)$_3$·2H_2O (0.0330 g, 0.04 mmol) and was heated to reflux for 2 hours to eliminate hydration water molecules. The resulting solution was cooled to 90 °C, and a solution of NIT$_2$PhOH (0.01 g, 0.04 mmol) in anhydrous diethyl ether (5 mL) was added. After stirring for 1 minute, the mixture was filtered and cooled to room temperature. The dark blue filtrate was left for slow evaporation, and after 5 days, purple crystals were formed. The crystals were not stable in solution, and both the crystals and filtrate would change to orange after 7 days. Therefore, it was essential to collect the crystals in time. The yield was 38%. The calculated and found percentages of C, H, and N for $C_{46}H_{36}F_{24}N_4O_{14}Yb_2$ were C 33.07; H 2.17; N 3.35% and C 33.12; H 2.24; N 3.38 %, respectively. The ATR values were 1651 (s), 1557 (m), 1472 (m), 1257 (s), 1207 (s), 1148 (s), 803 (m), 662 (m) cm^{-1}.

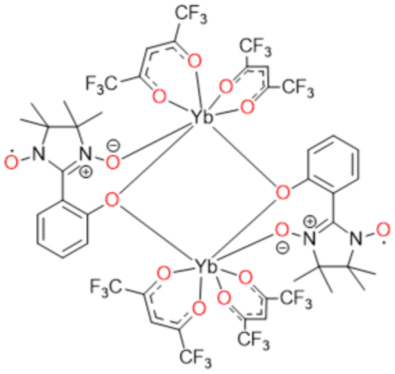

Yb$_2$(hfac)$_4$(NIT$_2$PhO)$_2$

$[Yb_2(hfac)_4(NIT_2PhO)_2]$ (2)

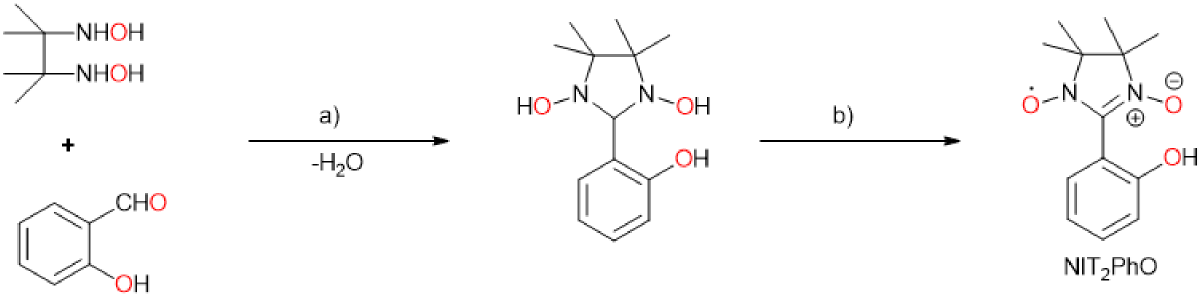

Figure 157. Synthetic pathway of NIT_2PhO nitronyl nitroxide. (a) MeOH, reflux; (b) PbO_2, RT, CH_3OH.

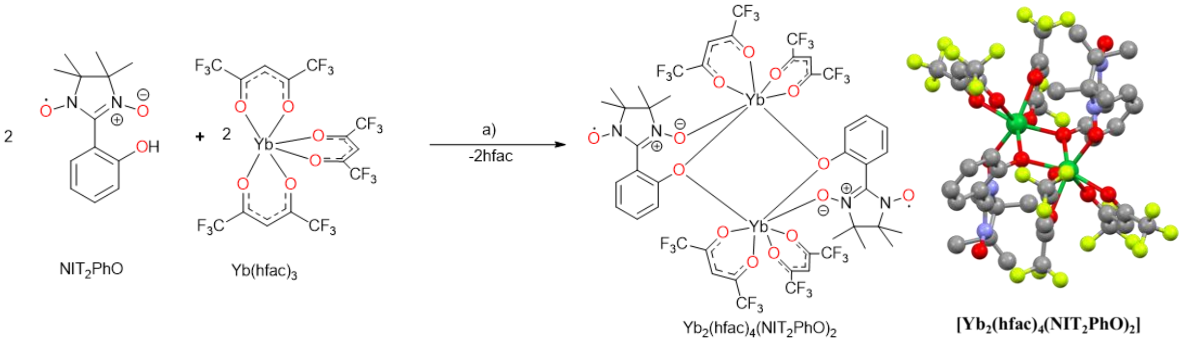

Figure 158. Synthetic pathway of complex **2 $[Yb_2(hfac)_4(NIT_2PhO)_2]$**. (a) heptane/diethylether, RT. Green (Yb), Grey (C), Violet (N), Red (O), Yellow (F). hydrogen atoms are omitted for clarity.

Preparation of $[Y_9(BA)_{16}(OH)_{10}]Cl$: ($Y_9$-BA)

A solution was prepared by dissolving 1-phenylbutane-1,3-dione (4 mmol, 648 mg) and Piperidine (4 mmol, 0.398 mL) in 60 mL of ethanol. The mixture was then heated to 72°C until everything dissolved, followed by the slow dropwise addition of $YCl_3{\cdot}6H_2O$ (1 mmol, 366.4 mg) aqueous solution (10 mL). A cloudy precipitate appears and disappears on stirring as the addition of $YCl_3{\cdot}6H_2O$ solution increases. The mixture was allowed to stir for 3 h at a refluxing temperature. Once the solution became clear, it was cooled slowly to room temperature and filtered into vials. The filtered solution was left undisturbed to obtain crystals of $[Y_9(BA)_{16}(OH)_{10}]Cl$.

Yield: 750 mg (76%)

ESI-TOF-MS: $[Y_9(BA)_{16}(OH)_{10}]^+$ Theo: 3549.06 Exp: 3549.17.

CHN analysis: Calc C 54.15%, H 4.37%, N 9.05% Found: C 54.02%, H 4.47%.

Preparation of $[Yb_8Eu(BA)_{16}(OH)_{10}]Cl$: ($Yb_8Eu$-BA)

A solution was prepared by dissolving 1-phenylbutane-1,3-dione (4 mmol, 648 mg) and Piperidine (4 mmol, 0.398 mL) in 60 mL of ethanol. The mixture was then heated to 72°C until everything dissolved, followed by the slow dropwise addition of $EuCl_3{\cdot}6H_2O$ (0.11 mmol, 40.31 mg) and $YbCl_3{\cdot}6H_2O$ (0.89 mmol, 344 mg) aqueous solution (10 mL). A cloudy precipitate appears and disappears on stirring as the addition of $EuCl_3.6H_2O$ & $YbCl_3.6H_2O$ solution increases. The mixture was allowed to stir for 3 h at a refluxing temperature. Once the solution became clear, it was cooled slowly to room temperature and filtered into vials. The filtered solution was left undisturbed to obtain crystals of $[Yb_8Eu(BA)_{16}(OH)_{10}]Cl$.

XRD:

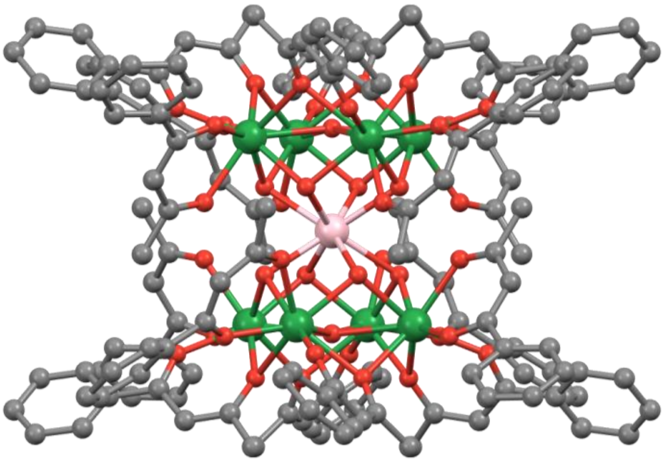

Figure 159. Crystal structure of $[Yb_8Eu(BA)_{16}(OH)_{10}]Cl$; Green (Yb), Pink (Eu), Grey (Carbon), Red (O).

Yield: 550 mg (60%)

Preparation of $[Y_8Yb(BA)_{16}(OH)_{10}]Cl$: ($Y_8Yb$-BA)

A solution was prepared by dissolving 1-phenylbutane-1,3-dione (4 mmol, 648 mg) and Piperidine (4 mmol, 0.398 mL) in 60 mL of ethanol. The mixture was then heated to 72°C until everything dissolved, followed by the slow dropwise addition of $YbCl_3\cdot 6H_2O$ (0.11 mmol, 42.62 mg) and YCl_3 (0.89 mmol, 173.78 mg) aqueous solution (10 mL). A cloudy precipitate appears and disappears on stirring as the addition of YCl_3 and $YbCl_3\cdot 6H_2O$ solution increases. The mixture was allowed to stir for 3 h at a refluxing temperature while the ethanol was being refluxed. Once the solution became clear, it was cooled slowly to room temperature and filtered into vials. The filtered solution was left undisturbed to obtain crystals of $[Y_8Yb(BA)_{16}(OH)_{10}]Cl$.

Yield: 520 mg

XRD:

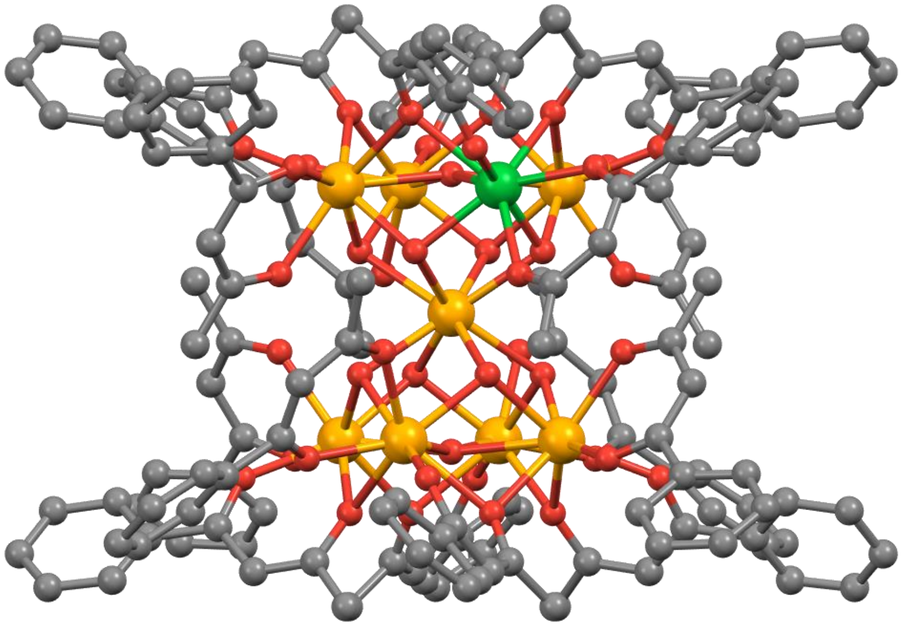

Figure 160. Crystal structure of $[Y_8Yb(BA)_{16}(OH)_{10}]Cl$. Orange (Y), Green (Yb), Grey (C), Red (O).

Table 21. Crystal data of $[Y_8Yb(BA)_{16}(OH)_{10}]Cl$.

CHEMICAL FORMULA	$C_{160}H_{154}ClO_{42}Y_8Yb$
SPACE GROUP	$P\,n\,\bar{3}\,n$ (222)

CRYSTAL SYSTEM	Cubic
CELL LENGHTS(Å)	**a** 33.3775(4) **b** 33.3775(4) **c** 33.3775(4)
CELL ANGLES(°)	**$\alpha = \beta = \gamma = 90$**
CELL VOLUME(Å^3)	37184.5
Z, Z'	**Z**: 6 **Z'**: 0
R-FACTOR(%)	5.55
TEMPERATURE (K)	150

Preparation of [$Y_8Dy(BA)_{16}(OH)_{10}$]Cl: (Y_8Dy-BA)

A solution was prepared by dissolving 1-phenylbutane-1,3-dione (4 mmol, 648 mg) and Piperidine (4 mmol, 0.398 mL) in 60 mL of ethanol. The mixture was then heated to 72°C until everything dissolved, followed by the slow dropwise addition of $DyCl_3{\cdot}6H_2O$ (0.11 mmol, 41.46 mg) and YCl_3 (0.89 mmol, 173.78 mg) aqueous solution (10 mL). A cloudy precipitate appears and disappears on stirring as the addition of YCl_3 and $DyCl_3{\cdot}6H_2O$ solution increases. The mixture was allowed to stir for 3 h at a refluxing temperature. Once the solution became clear, it was cooled slowly to room temperature and filtered into vials. The filtered solution was left undisturbed to obtain crystals of [Y_8Dy $(BA)_{16}(OH)_{10}$]Cl.

Yield: 540 mg (60%)

XRD:

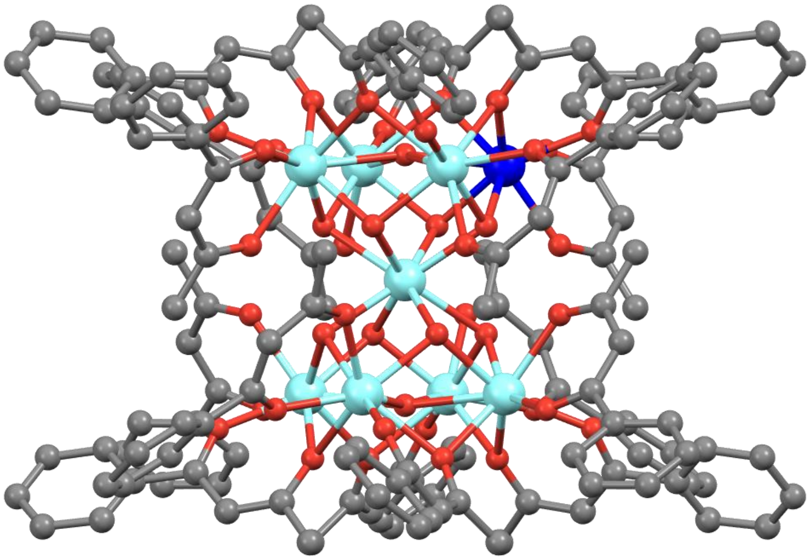

Figure 161. Crystal structure for [$Y_8Dy(BA)_{16}(OH)_{10}$]Cl. Dark blue (Dy), Light blue (Y), Grey (C), Red (O).

Table 22. Crystal data of [$Y_8Dy(BA)_{16}(OH)_{10}$]Cl.

CHEMICAL FORMULA	$C_{160}H_{154}ClO_{42}Y_8Dy$

SPACE GROUP	$P\,n\,\bar{3}\,n$ (222)
CRYSTAL SYSTEM	Cubic
CELL LENGHTS(Å)	**a** 33.5883(7) **b** 33.5883(7) **c** 33.5883(7)
CELL ANGLES(°)	**$\alpha = \beta = \gamma = 90$**
CELL VOLUME(Å^3)	37893.4
Z, Z’	**Z**: 6 **Z’**: 0.11
R-FACTOR(%)	6.25
TEMPERATURE (K)	150

Preparation of [Ho_9(BA)$_{16}$(OH)$_{10}$]Cl: (Ho_9-BA)

A solution was prepared by dissolving 1-phenylbutane-1,3-dione (4 mmol, 648 mg) and Piperidine (4 mmol, 0.398 mL) in 60 mL of ethanol. The mixture was then heated to 72°C until everything dissolved, followed by the slow dropwise addition of $HoCl_3$ (1 mmol, 271.28 mg) aqueous solution (10 mL). A cloudy precipitate appears and disappears on stirring as the addition of $HoCl_3$ solution increases. The mixture was allowed to stir for 3 h at a refluxing temperature. Once the solution became clear, it was cooled slowly to room temperature and filtered into vials. The filtered solution was left undisturbed to obtain crystals of [Ho_9(BA)$_{16}$(OH)$_{10}$]Cl.

Yield: 650 mg (63%)

ESI-TOF-MS: [Ho_9(BA)$_{16}$(OH)$_{10}$]$^+$ Calc: 4233.28 Exp: 4233.26.

XRD:

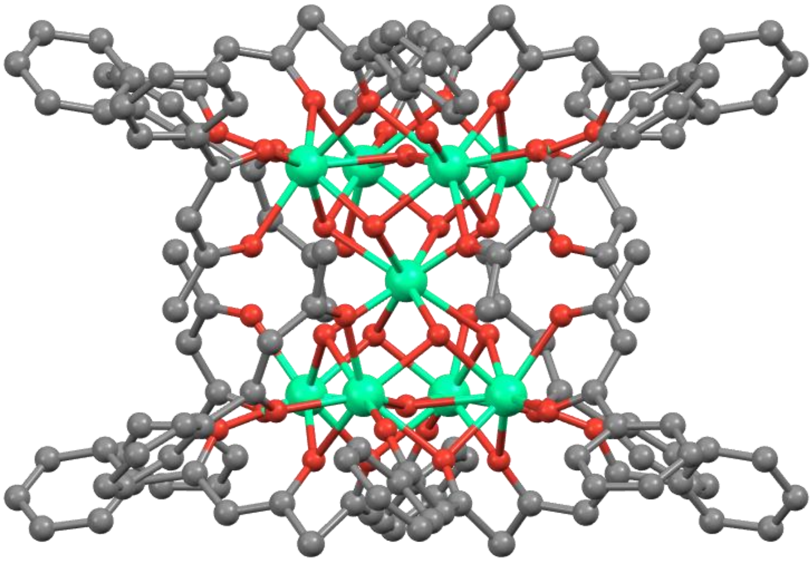

Figure 162. Crystal structure for [Ho_9(BA)$_{16}$(OH)$_{10}$]Cl. Green (Ho), Red (O), Grey (C).

Table 23. Crystal data of $[Ho_9(BA)_{16}(OH)_{10}]Cl$.

CHEMICAL FORMULA	$C_{160}H_{154}ClO_{42}Ho_9$
SPACE GROUP	$P\ n\ \bar{3}\ n$ (<u>222</u>)
CRYSTAL SYSTEM	Cubic
CELL LENGHTS(Å)	**a** 33.5865(4) **b** 33.5865(4) **c** 33.5865(4)
CELL ANGLES(°)	**α = β = γ = 90**
CELL VOLUME(Å^3)	37887.4
Z, Z’	**Z**: 6 **Z’**: 0.11
R-FACTOR(%)	4.19
TEMPERATURE (K)	150

Preparation of $[Yb(PA)_3(CH_3OH)(H_2O)]$: (Yb-PA)

A solution was prepared by dissolving 1-pyrenelbutane-1,3-dione (2 mmol, 572 mg) and Piperidine (3 mmol, 0.298 mL) in 30 mL of ethanol. The mixture was then heated to 72°C until everything dissolved, followed by the slow dropwise addition of $YbCl_3{\cdot}6H_2O$ (0.5 mmol, 193.5 mg) aqueous solution (5 mL). A cloudy precipitate appears and disappears on stirring as the addition of $YbCl_3{\cdot}6H_2O$ solution increases. The mixture was allowed to stir for 3 h at a refluxing temperature. Once the solution became clear, it was cooled slowly to room temperature and filtered into vials. The filtered solution was left undisturbed to obtain crystals of $[Yb_9(PA)_{16}(OH)_{10}]Cl$.

Yield: 250 mg (20%)

CHN analysis: $[Yb(PA)_3(CH_3OH)(H_2O)]$ Calc C: 67.9 H: 4.20; Exp: C:68.33 H:4.22

Preparation of $[Gd_9(PLN)_{16}(OH)_{10}]Cl$: ($Gd_9$-PLN)

0.15 g (0.76 mmol, 1.79 eq) of 9-hydroxyphenalen-1-one (HPLN) ligand and 0.113 g (0.427 mmol, 1 eq) of $Gd(H_2O)_6Cl_3$ were added to a round bottom flask containing 45 mL of methanol. The contents of the flask were gently heated until everything was dissolved. Following that, 0.5 mL of freshly distilled triethylamine was added dropwise to the clear stirred solution. With each drop of base added, a precipitate appeared and then disappeared due to solvent mixing. Later on, a yellow powder precipitated and remained in suspension. The suspension was stirred at room temperature for 24 hours. The solvent was then removed via rotary evaporation and the compound was dried under vacuum. It was then recrystallized from CH_2Cl_2. The resulting precipitating solid was used for ESI-TOF-MS studies after resolubilization in CH_2Cl_2 and electrospraying.

Yield: 122 mg (20%)

CHN analysis: Cal for [$Gd_9(PLN)_{16}(OH)_{10}Cl$] with a total formula of $C_{208}H_{134}ClGd_9O_{42}$, 4972.99 g/mol: C, 52.57; H, 2.59. Exp: C, 52.54 H, 2.58.

ESI-TOF-MS: $[Gd_9(PLN)_{16}(OH)_{10}]^+$ m/z: Calc: 4716.53 Exp: 4716.0704.

Preparation of [$TbY_8(BA)_{16}(OH)_{10}$]Cl: (TbY_8-BA)

A solution was prepared by dissolving 1-phenylbutane-1,3-dione (4 mmol, 648 mg) and Piperidine (4 mmol, 398 µl) in 60 ml of ethanol. The mixture was then heated to 72°C until everything dissolved, followed by the slow dropwise addition of $TbCl_3.6H_2O$ (0.11 mmol, 41.07 mg) and YCl_3 (0.89 mmol, 173.78 mg) aqueous solution (10 ml). A cloudy precipitate appears and disappears on stirring as the addition of YCl_3 & $TbCl_3.6H_2O$ solution increases. The mixture was allowed to stir for 3 h at a refluxing temperature while the ethanol was being refluxed. Once the solution became clear, it was cooled slowly to room temperature and filtered into vials. The filtered solution was left undisturbed to obtain crystals of [Y_8Tb $(BA)_{16}(OH)_{10}$]Cl.

Yield: 540 mg (55%)

CHN analysis: Cal for [$Y_8Tb(BA)_{16}(OH)_{10}$]Cl with a total formula of $C_{160}H_{154}ClTbY_8O_{42}$, 3654.53 g/mol: C, 52.58; H, 4.25. Exp: C, 52.54 H, 4.28.

Preparation of [$Y_{8.5}Dy_{0.5}(PLN)_{16}(OH)_{10}$]Cl: ($Y_{8.5}Dy_{0.5}$-PLN)

0.15 g (0.76 mmol, 1.79 eq) of 9-hydroxyphenalen-1-one (HPLN) ligand and 0.173 g (0.41 mmol, 0.95 eq) of YCl_3 and 0.19 g (0.02 mmol, 0.05 eq) of $Dy(H_2O)_6Cl_3$ were added to a round bottom flask containing 45 mL of methanol. The contents of the flask were gently heated until everything was dissolved. Following that, 0.5 mL of freshly distilled triethylamine was added dropwise to the clear stirred solution. With each drop of base added, a precipitate appeared and then disappeared due to solvent mixing. Later on, a yellow powder precipitated and remained in suspension. The suspension was stirred at room temperature for 24 hours. The solvent was then removed via rotary evaporation and the compound was dried under vacuum. It was then recrystallized from CH_2Cl_2. The resulting precipitating solid was used for ESI-TOF-MS studies after resolubilization in CH_2Cl_2 and electrospraying.

Yield: 115 mg (20%)

CHN analysis: Cal for $[Y_{8.5}Dy_{0.5}(PLN)_{16}(OH)_{10}]Cl$ with a total formula of $C_{208}H_{134}Cl Y_{8.5}Dy_{0.5}O_{42}$, 4177.67 g/mol: C, 59.75; H, 3.21. Exp: C, 59.74 H, 3.19.

Preparation of $[Y_{8.5}Dy_{0.5}(BA)_{16}(OH)_{10}]Cl$: ($Y_{8.5}Dy_{0.5}$-BA)

A solution was prepared by dissolving 1-phenylbutane-1,3-dione (4 mmol, 648 mg) and Piperidine (4 mmol, 398 µL) in 60 mL of ethanol. The mixture was then heated to 72°C until everything dissolved, followed by the slow dropwise addition of $DyCl_3.6H_2O$ (0.05 mmol, 18.85 mg) and YCl_3 (0.95 mmol, 185.50 mg) aqueous solution (10 mL). A cloudy precipitate appears and disappears on stirring as the addition of YCl_3 & $DyCl_3.6H_2O$ solution increases. The mixture was allowed to stir for 3 h at a refluxing temperature while the ethanol was being refluxed. Once the solution became clear, it was cooled slowly to room temperature and filtered into vials. The filtered solution was left undisturbed to obtain crystals of $[Y_{8.5}Dy_{0.5}(BA)_{16}(OH)_{10}]Cl$.

Yield: 135 mg (20%)

CHN analysis: Cal for $[Y_{8.5}Dy_{0.5}(BA)_{16}(OH)_{10}]Cl$ with a total formula of $C_{160}H_{154}Cl Y_{8.5}Dy_{0.5}O_{42}$, 3621.32 g/mol: C, 53.02; H, 4.25. Exp: C, 53.14 H, 4.19.

ESI-MASS-TOF: $[Y_{8.5}Dy_{0.5}(BA)_{16}(OH)_{10}]^+$ Calc 3585.87 Exp 3585.94.

Preparation of $[Y_{8.5}Tb_{0.5}(BA)_{16}(OH)_{10}]Cl$: ($Y_{8.5}Tb_{0.5}$-BA)

A solution was prepared by dissolving 1-phenylbutane-1,3-dione (4 mmol, 648 mg) and Piperidine (4 mmol, 398 µL) in 60 mL of ethanol. The mixture was then heated to 72°C until everything dissolved, followed by the slow dropwise addition of $TbCl_3.6H_2O$ (0.05 mmol, 18.67 mg) and YCl_3 (0.95 mmol, 185.50 mg) aqueous solution (10 mL). A cloudy precipitate appears and disappears on stirring as the addition of YCl_3 & $TbCl_3.6H_2O$ solution increases. The mixture was allowed to stir for 3 h at a refluxing temperature while the ethanol was being refluxed. Once the solution became clear, it was cooled slowly to room temperature and filtered into vials. The filtered solution was left undisturbed to obtain crystals of $[Y_{8.5}Tb_{0.5}(BA)_{16}(OH)_{10}]Cl$.

Yield: 135 mg (20%)

CHN analysis: Cal for $[Y_{8.5}Tb_{0.5}(BA)_{16}(OH)_{10}]Cl$ with a total formula of $C_{160}H_{154}Cl Y_{8.5}Tb_{0.5}O_{42}$, 3619.53 g/mol: C, 53.05; H, 4.25. Exp: C, 53.04 H, 4.27.

ESI-MASS-TOF: $[Y_{8.5}Tb_{0.5}(BA)_{16}(OH)_{10}]^+$ Calc 3584.08 Exp 3583.96.

Preparation of $[Y_{8.5}Ho_{0.5}(BA)_{16}(OH)_{10}]Cl$: ($Y_{8.5}Ho_{0.5}$-BA)

A solution was prepared by dissolving 1-phenylbutane-1,3-dione (4 mmol, 648 mg) and Piperidine (4 mmol, 398 µL) in 60 mL of ethanol. The mixture was then heated to 72°C until everything dissolved, followed by the slow dropwise addition of $HoCl_3$ (0.05 mmol, 13.56 mg) and YCl_3 (0.95 mmol, 185.50 mg) aqueous solution (10 mL). A cloudy precipitate appears and disappears on stirring as the addition of YCl_3 & $HoCl_3$ solution increases. The mixture was allowed to stir for 3 h at a refluxing temperature while the ethanol was being refluxed. Once the solution became clear, it was cooled slowly to room temperature and filtered into vials. The filtered solution was left undisturbed to obtain crystals of $[Y_{8.5}Ho_{0.5}(BA)_{16}(OH)_{10}]Cl$.

Yield: 140 mg (30%)

CHN analysis: Cal for $[Y_{8.5}Ho_{0.5}(BA)_{16}(OH)_{10}]Cl$ with a total formula of $C_{160}H_{154}ClY_{8.5}Ho_{0.5}O_{42}$, 3622.53 g/mol: C, 53.05; H, 4.25. Exp: C, 53.04 H, 4.29.

ESI-MASS-TOF: $[Y_{8.5}Ho_{0.5}(BA)_{16}(OH)_{10}]^+$ Calc 3587.08 Exp 3587.04.

Preparation of $[Y_{8.5}Er_{0.5}(BA)_{16}(OH)_{10}]Cl$: ($Y_{8.5}Er_{0.5}$-BA)

A solution was prepared by dissolving 1-phenylbutane-1,3-dione (4 mmol, 648 mg) and Piperidine (4 mmol, 398 µL) in 60 mL of ethanol. The mixture was then heated to 72°C until everything dissolved, followed by the slow dropwise addition of $ErCl_3$ (0.05 mmol, 13.68 mg) and YCl_3 (0.95 mmol, 185.50 mg) aqueous solution (10 mL). A cloudy precipitate appears and disappears on stirring as the addition of YCl_3 & $ErCl_3$ solution increases. The mixture was allowed to stir for 3 h at a refluxing temperature while the ethanol was being refluxed. Once the solution became clear, it was cooled slowly to room temperature and filtered into vials. The filtered solution was left undisturbed to obtain crystals of $[Y_{8.5}Er_{0.5}(BA)_{16}(OH)_{10}]Cl$.

Yield: 125 mg (30%)

CHN analysis: Cal for $[Y_{8.5}Er_{0.5}(BA)_{16}(OH)_{10}]Cl$ with a total formula of $C_{160}H_{154}ClY_{8.5}Er_{0.5}O_{42}$, 3623.70 g/mol: C, 53.03; H, 4.29. Exp: C, 53.19 H, 4.27.

ESI-MASS-TOF: $[Y_{8.5}Er_{0.5}(BA)_{16}(OH)_{10}]^+$ Calc 3588.24 Exp 3588.34.

Preparation of $[Y_{8.5}Tm_{0.5}(BA)_{16}(OH)_{10}]Cl$: ($Y_{8.5}Tm_{0.5}$-BA)

A solution was prepared by dissolving 1-phenylbutane-1,3-dione (4 mmol, 648 mg) and Piperidine (4 mmol, 398 µL) in 60 mL of ethanol. The mixture was then heated to 72°C until everything dissolved, followed by the slow dropwise addition of $TmCl_3.6H_2O$ (0.05 mmol, 19.17 mg) and YCl_3 (0.95 mmol, 185.50 mg) aqueous solution (10 mL). A cloudy precipitate appears and disappears on stirring as the addition of YCl_3 & $TmCl_3.6H_2O$ solution increases. The mixture was allowed to stir for 3 h at a refluxing temperature while the ethanol was being refluxed. Once the solution became clear, it was cooled slowly to room temperature and filtered into vials. The filtered solution was left undisturbed to obtain crystals of $[Y_{8.5}Tm_{0.5}(BA)_{16}(OH)_{10}]Cl$.

Yield: 135 mg (30%)

CHN analysis: Cal for $[Y_{8.5}Tm_{0.5}(BA)_{16}(OH)_{10}]Cl$ with a total formula of $C_{160}H_{154}ClY_{8.5}Tm_{0.5}O_{42}$, 3624.54 g/mol: C, 53.02; H, 4.29. Exp: C, 53.12 H, 4.30.

ESI-MASS-TOF: $[Y_{8.5}Tm_{0.5}(BA)_{16}(OH)_{10}]^+$ Calc 3589.08 Exp 3589.14.

Preparation of $[Y_{8.5}Yb_{0.5}(BA)_{16}(OH)_{10}]Cl$: ($Y_{8.5}Yb_{0.5}$-BA)

A solution was prepared by dissolving 1-phenylbutane-1,3-dione (4 mmol, 648 mg) and Piperidine (4 mmol, 398 µL) in 60 mL of ethanol. The mixture was then heated to 72°C until everything dissolved, followed by the slow dropwise addition of $YbCl_3.6H_2O$ (0.05 mmol, 19.37 mg) and YCl_3 (0.95 mmol, 185.50 mg) aqueous solution (10 mL). A cloudy precipitate appears and disappears on stirring as the addition of YCl_3 & $YbCl_3.6H_2O$ solution increases. The mixture was allowed to stir for 3 h at a refluxing temperature while the ethanol was being refluxed. Once the solution became clear, it was cooled slowly to room temperature and filtered into vials. The filtered solution was left undisturbed to obtain crystals of $[Y_{8.5}Yb_{0.5}(BA)_{16}(OH)_{10}]Cl$.

Yield: 110 mg (25%)

CHN analysis: Cal for $[Y_{8.5}Yb_{0.5}(BA)_{16}(OH)_{10}]Cl$ with a total formula of $C_{160}H_{154}ClY_{8.5}Yb_{0.5}O_{42}$, 3626.60 g/mol: C, 52.99; H, 4.288. Exp: C, 53.02 H, 4.30.

ESI-MASS-TOF: $[Y_{8.5}Yb_{0.5}(BA)_{16}(OH)_{10}]^+$ Calc 3531.14 Exp 3531.06.

Preparation of $[Y_{8.5}Tb_{0.5}(PLN)_{16}(OH)_{10}]Cl$: ($Y_{8.5}Tb_{0.5}$-PLN)

0.15 g (0.76 mmol, 1.79 eq) of 9-hydroxyphenalen-1-one (HPLN) ligand and 0.173 g (0.95 mmol, 0.95 eq) of YCl_3 and 0.187 g (0.05 mmol, 0.05 eq) of $Tb(H_2O)_6Cl_3$ were added to a round bottom flask containing 45 mL of methanol. The contents of the flask were gently heated until everything was dissolved. Following that, 0.5 mL of freshly distilled triethylamine was added dropwise to the clear stirred solution. With each drop of base added, a precipitate appeared and then disappeared due to solvent mixing. Later on, a yellow powder precipitated and remained in suspension. The suspension was stirred at room temperature for 24 hours. The solvent was then removed via rotary evaporation and the compound was dried under vacuum. It was then recrystallized from CH_2Cl_2. The resulting precipitating solid was used for ESI-TOF-MS studies after resolubilization in CH_2Cl_2 and electrospraying.

Yield: 115 mg (15%)

CHN analysis: Cal for $[Y_{8.5}Tb_{0.5}(PLN)_{16}(OH)_{10}]Cl$ with a total formula of $C_{208}H_{134}Cl\,Y_{8.5}Tb_{0.5}O_{42}$, 4163.79 g/mol: C, 59.99; H, 2.96. Exp: C, 59.88 H, 2.99.

Preparation of $[Y_{8.5}Yb_{0.5}(PLN)_{16}(OH)_{10}]Cl$: ($Y_{8.5}Yb_{0.5}$-PLN)

0.15 g (0.76 mmol, 1.79 eq) of 9-hydroxyphenalen-1-one (HPLN) ligand and 0.185 g (0.95 mmol, 0.95 eq) of YCl_3 and 0.1937 g (0.05 mmol, 0.05 eq) of $Yb(H_2O)_6Cl_3$ were added to a round bottom flask containing 45 mL of methanol. The contents of the flask were gently heated until everything was dissolved. Following that, 0.5 mL of freshly distilled triethylamine was added dropwise to the clear stirred solution. With each drop of base added, a precipitate appeared and then disappeared due to solvent mixing. Later on, a yellow powder precipitated and remained in suspension. The suspension was stirred at room temperature for 24 hours. The solvent was then removed via rotary evaporation and the compound was dried under vacuum. It was then recrystallized from CH_2Cl_2. The resulting precipitating solid was used for ESI-TOF-MS studies after resolubilization in CH_2Cl_2 and electrospraying.

Yield: 122 mg (20%)

CHN analysis: Cal for $[Y_{8.5}Yb_{0.5}(PLN)_{16}(OH)_{10}]Cl$ with a total formula of $C_{208}H_{134}Cl\,Y_{8.5}Yb_{0.5}O_{42}$, 4170.86 g/mol: C, 59.89; H, 2.95. Exp: C, 59.88 H, 2.99.

Concluding Remarks

Incorporating an acetylacetonate moiety with diverse aromatic scaffolds around it for the complexation of trivalent rare earth ions has led to the formation of alluring lanthanide-based nonanuclear complexes spanning the lanthanide series. A total of 29 complexes have been meticulously characterized employing single-crystal X-ray diffraction techniques and high-resolution ESI-TOF mass techniques. The cubic crystals of the complexes have been obtained through slow evaporation of ethanol/water mother-liquor. All the nonanuclear complexes with Benzoyl acetone (BA) share a common solid-state structure that can be perceived as two pentanuclear square pyramids sharing the apical Ln atom, with a torsion angle of approximately 45° between the two pyramids, resulting in square antiprismatic geometry at the central Ln. The utilization of acetylacetonates as ligands has proven to be efficacious in amalgamating various paramagnetic ions into a single entity, even when employing a combination of lanthanides and dilution with Y. These intricate complexes have demonstrated multifarious functionality, both in the realm of magnetism and luminescence. Within this thesis, we have delved into the synergistic combination of these functionalities, specifically in the areas of upconversion, magnetic coolants, and single molecule magnets.

Due to the distinctions in the coordination sphere, the nonanuclear complex exhibits two disparate coordination sites- the central site and the peripheral site. The central site is solely encompassed by the μ_3-hydroxy ligands, while the peripheral site comprises three BA ligands and two hydroxy ligands (μ_3, μ_4) in its first coordination sphere. Prior research has established that such distinct coordination environments are instrumental in promoting site selectivity for heteronuclear lanthanide clusters, with a tendency for the largest ion to occupy the central position. To verify if site selectivity was also present in the BA clusters, a set of eight homo- and heterometallic nonanuclear clusters was synthesized and crystallized. Continuous shape measures (CShMs) were conducted on X-ray crystallographic data within the series, revealing that the $\mathrm{Ln_{central}}$ site exhibits a nearly perfect square antiprismatic geometry with D_{4d} symmetry, whereas the $\mathrm{Ln_{peripheral}}$ site is a biaugmented trigonal prism with C_{2v} symmetry. Additionally, the "coordination site cavity" (also known as "pocket size") for the two distinct environments was determined by averaging the Ln-O bond lengths for each site. As shown in **Table 7**, the study demonstrated that the central pocket size is the largest. While not entirely accurate in our case, the central site being the largest favors the larger lanthanide ion in the central site and the smaller one to the periphery.

The heterometallic clusters we have investigated exhibit a statistical distribution in their composition, a phenomenon that has been extensively studied and understood through the use of high-resolution mass spectrometry. In the case of Eu_8Yb, for example, the composition of the cluster in solution was analyzed by means of electrospray ionization mass spectrometry (ESI-MS). The resulting spectrum revealed primary peaks at m/z 4116, 4137, and 4158, corresponding to the monocharged Eu_9, Eu_8Yb, and Eu_7Yb_2 complexes, respectively. The other peaks on the higher m/z side, with an intensity of less than 10% of the most abundant Eu_9 peak, are due to complexes with higher Yb content replacing Eu in the metal core (such as Eu_6Yb_3 and Eu_5Yb_4).

The relative integrals of the isotopic patterns have been employed to calculate the proportion ($\mathbf{P_i}$) of the Ln_1 and Ln_2 species at a mole fraction $\boldsymbol{x}$ of Ln_1. The experimental values demonstrate an overall good agreement with the perfect statistical distribution obtained by the distribution function under the assumption that all coordination sites in the clusters are chemically equivalent and all Ln(III) clusters have similar ionization abilities. Complexes with a higher molar fraction of Yb (>4) have a probability lower than 1%. This analysis also reveals that for a stoichiometric ratio of Yb:Eu equal to 1:8, complexes containing at least two Yb atoms represent more than 22% of all possible nonanuclear complexes formed, which is favorable to the observation of molecular upconversion with a CS mechanism.

Through the doping of Yb ions into Europium nonanuclear complexes, a first-ever multifunctional heteronuclear $[Eu_8Yb(BA)_{16}(OH)_{10}]Cl$ complex has been successfully synthesized. This complex displays a highly efficient cooperative UC luminescence in solution based on the Yb/Eu donor/acceptor pair, and a rare single molecule magnet (SMM) behavior that is characterized by a slow relaxation of magnetization. This marks a rare instance of direct cooperative sensitization (CS) upconversion within a molecular cluster that incorporates both Eu and Yb. The UC process is among the most efficient molecular or supramolecular UC probes to date, and can be observed in solution at concentrations as low as 100 nM.

The utilization of readily accessible ß-diketonate ligands, along with a diverse range of Ln donor-acceptor dyads and structures, provides a promising avenue towards achieving even more efficient upconversion (UC) systems. In addition to the attractivity of UC systems for bio-analytical applications, the development of UC luminescent Ln-SMMs is a promising field of research with many corners still left unexplored. The incorporation of multiple functionalities into a single molecule can potentially enhance our understanding of SMM behavior, especially considering that SMMs are intended for implementation in next-generation nanocircuits for quantum computation.

The combination of luminescence and magnetic properties has also garnered interest, due to the possible correlation between the electronic structure of complexes extracted from optical properties and the effective energy barriers determined by dynamic magnetic measurements. Furthermore, beyond just understanding the SMM behavior, light can be used as a non-invasive trigger to manipulate the spin state of a system, while optical measurements can act as probes to study the environment of discrete molecules.

The synthesis and characterization of homometallic 4f cages have also been achieved through a series of meticulously designed and meticulously executed experiments. The approach involved the utilization of acetylacetonate-based ligands as scaffolds for Gd-based nonanuclear complexes, which were synthesized under carefully calibrated reflux conditions. The use of acetylacetonates as ligands was found to be highly efficacious in bringing several paramagnetic ions together in a single, highly coordinated entity.

The resulting complex exhibited two distinct Gd ions in the crystal structure, with only two different Gd···Gd distances between the nine Gd ions. The shortest distances were shown in green (3.670(3) Å) while the longest was shown in orange (3.765(3) Å) (**Figure 89**). The complex had an active metal percentage of 33.7% and the density of the material to be 1.346 g cm^{-3}. The magnetic properties of both families were studied in great detail, with a special focus on their potential applications in areas such as magnetocalorics.

Simulation of the isotropic systems revealed antiferromagnetic interactions operating within each system, leading to a diminished magnetic entropy change compared to that of the non-interacting ions. The antiferromagnetic exchange interactions play a crucial role in determining whether or not these compounds are of interest for magnetic cooling.

Summarizing the findings, it was observed that signs of geometric spin frustration were evident in magnetization experiments of a molecular nanomagnet. The *M(H)* did not exhibit any saturation until 14 T, which could be a sign of some frustrated systems. More puzzling was the fact that the *M(H)* traces at 1.8 K and 2.0 K showed a plateau between 3 and 4 T. In the present investigation, adiabatic demagnetization experiments are still required through which T_{ad} could be achieved, and which in turn, would decide if this molecule is of any interest as a magnetic coolant.

In general, dipolar interactions limit the temperatures that can be reached in such experiments. These results highlight the fundamental importance of the relative magnitudes of the interaction parameters in molecular clusters in terms of their use for the magnetocaloric effect (MCE). The antiferromagnetic interactions are indispensable for spin frustration, which gives rise to large entropy changes. However, if the interactions are too large, then the full magnetic entropy will not be available on (de)magnetization. If, on the other hand, the interactions are too weak, then the MCE will be limited by dipolar interactions. Most studies of the MCE in molecular systems have simply relied on the indirect determination of MCE parameters and are blind to these crucial effects.

It has been observed that within the series of benzoylacetone complexes, only the ions with prolate electron density, such as Ytterbium (Yb) and Erbium (Er), exhibit slow magnetic relaxation behavior when subjected to an external DC field. This behavior is attributed to the equatorial coordination of the BA ligands, which is considered ideal for prolate ions. Conversely, Thulium (Tm), which also possesses prolate electron density, does not display any slow relaxation behavior, with or without the application of an external DC field. This is due to the fact that Tm is a non-Kramers ion, unlike Er and Yb.

In the Phenalenone series, it has been observed that the oblate ions such as Dysprosium (Dy) and Terbium (Tb) exhibit competent slow magnetic relaxation behavior, while the prolate Ytterbium (Yb) complex does not. This phenomenon is attributed to the axial crystal type coordination of the phenalenone ligands, as evident in their crystal packing. Axial coordination helps to stabilize the bistability of the ground state of oblate ions, which in turn exhibits slow magnetic relaxation behavior.

Moreover, the Yb-Pyreneacac complex was magnetically characterized in this study. Although the nonanuclear complexes could not be isolated due to the steric bulkiness of the ligands, a monomeric Yb complex was successfully isolated. This complex exhibited slow relaxation magnetic behavior when subjected to an external DC field of 2200 Oe.

In summary, this study demonstrates that the SMM (Single Molecule Magnet) property can be adjusted by modifying the coordination environment resulting from changes in the substituents of *ß*-diketonate ligands. The BA ligands stabilize the prolate anisotropy, whereas the PLN ligands work better for the oblate anisotropy. These complexes are expected to provide a good reference for the SMM properties of Ln-based nonanuclear analogues.

This present work expounds upon the potential of nonanuclear complexes as highly versatile materials that hold great promise for molecular upconversion and as plausible magnetic coolants. Despite the existence of numerous molecules, there remains a vast reservoir of untapped potential in the field of polynuclear lanthanide cluster research, which presents exciting opportunities for further advances. Although the realization of lanthanide-based molecular light-matter interfaces for quantum computing may still be remote, the intrinsic properties of molecular *ß*-diketonate ligand compounds offer a promising avenue of pursuit. The findings of this thesis contribute to a comprehensive understanding of cooperative sensitization, along side the slow relaxation magnetic behavior observed between Eu and Yb in solution-state molecules, which has not been evidenced hitherto. Furthermore, our study highlights the superiority of polynuclear lanthanide complexes and both their anisotropy and isotropy in the fields of magnetism and magnetocalorics.

Bibliography

1. Tannous, C.; Comstock, R. L., Magnetic information-storage materials. *Springer Handbook of Electronic and Photonic Materials* **2017**, 1-1.

2. Moore, G. E., Cramming more components onto integrated circuits, Reprinted from Electronics, volume 38, number 8, April 19, 1965, pp. 114 ff. *IEEE solid-state circuits society newsletter* **2006,** *11* (3), 33-35.

3. Fondo, M.; Escuer, A.; Herrera, J. M., Molecular Magnets. Frontiers Media SA: 2019; Vol. 7, p 229.

4. Hu, K., ChatGPT sets record for fastest-growing user base-analyst note. *Reuters* **2023,** *12*, 2023.

5. Shor, P. W. In *Algorithms for quantum computation: discrete logarithms and factoring*, Proceedings 35th annual symposium on foundations of computer science, Ieee: 1994; pp 124-134.

6. Arute, F.; Arya, K.; Babbush, R.; Bacon, D.; Bardin, J. C.; Barends, R.; Biswas, R.; Boixo, S.; Brandao, F. G.; Buell, D. A., Quantum supremacy using a programmable superconducting processor. *Nature* **2019,** *574* (7779), 505-510.

7. Grover, L. K., Quantum mechanics helps in searching for a needle in a haystack. *Physical review letters* **1997,** *79* (2), 325.

8. Moreno-Pineda, E.; Godfrin, C.; Balestro, F.; Wernsdorfer, W.; Ruben, M., Molecular spin qudits for quantum algorithms. *Chemical Society Reviews* **2018,** *47* (2), 501-513.

9. Wernsdorfer, W.; Ruben, M., Synthetic Hilbert space engineering of molecular qudits: Isotopologue chemistry. *Advanced Materials* **2019,** *31* (26), 1806687.

10. Martin-Ramos, P.; Ramos-Silva, M., *Lanthanide-based multifunctional materials: from OLEDs to SIMs*. Elsevier: 2018.

11. Eliseeva, S. V.; Bünzli, J.-C. G., Lanthanide luminescence for functional materials and bio-sciences. *Chemical Society Reviews* **2010,** *39* (1), 189-227.

12. Layfield, R. A.; Murugesu, M., *Lanthanides and actinides in molecular magnetism*. John Wiley & Sons: 2015.

13. Aguilà, D.; Roubeau, O.; Aromí, G., Designed polynuclear lanthanide complexes for quantum information processing. *Dalton Transactions* **2021,** *50* (35), 12045-12057.

14. Cotton, S., *Lanthanide and actinide chemistry*. John Wiley & Sons: 2024.

15. Housecroft, C. E.; Sharpe, A. G., *Inorganic chemistry*. Pearson Education: 2008; Vol. 1.

16. Marin, R.; Brunet, G.; Murugesu, M., Shining New Light on Multifunctional Lanthanide Single-Molecule Magnets. *Angewandte Chemie International Edition* **2021,** *60* (4), 1728-1746.

17. Dejneka, M. J.; Streltsov, A.; Pal, S.; Frutos, A. G.; Powell, C. L.; Yost, K.; Yuen, P. K.; Müller, U.; Lahiri, J., Rare earth-doped glass microbarcodes. *Proceedings of the National Academy of Sciences* **2003,** *100* (2), 389-393.

18. Manchanda, V. K.; Mohapatra, P. K., Complexation of a tris-bipyridine cryptand with americium(III). *Polyhedron* **1993,** *12* (9), 1115-1117.

19. Ma, P.; Mumper, R. J., Anthracycline nano-delivery systems to overcome multiple drug resistance: A comprehensive review. *Nano Today* **2013,** *8* (3), 313-331.

20. Lasák, P.; Motyka, K.; Kryštof, V.; Stýskala, J., Synthesis, Bacteriostatic and Anticancer Activity of Novel Phenanthridines Structurally Similar to Benzo[c]phenanthridine Alkaloids. *Molecules* **2018,** *23* (9), 2155.

21. Abbati, G. L.; Cornia, A.; Fabretti, A. C.; Caneschi, A.; Gatteschi, D., Structure and magnetic properties of a mixed-valence heptanuclear manganese cluster. *Inorganic chemistry* **1998,** *37* (15), 3759-3766.

22. Tamang, S. R.; Singh, A.; Bedi, D.; Bazkiaei, A. R.; Warner, A. A.; Glogau, K.; McDonald, C.; Unruh, D. K.; Findlater, M., Polynuclear lanthanide–diketonato clusters for the catalytic hydroboration of carboxamides and esters. *Nature Catalysis* **2020,** *3* (2), 154-162.

23. Bhula, R.; Weatherburn, D. C., Oxidative Cleavage of Triethylenetetramine (trien) to Yield Diethylenetriamine (dien): Structure of the MnII/MnIII Heptanuclear Complex [Mn7 (trien) 2 (dien) 2O4 (OAc) 8](PF6) 4· 2H2O. *Angewandte Chemie International Edition in English* **1991,** *30* (6), 688-689.

24. Parker, D.; Williams, J. A. G., Getting excited about lanthanide complexation chemistry. *Journal of the Chemical Society, Dalton Transactions* **1996,** (18), 3613-3628.

25. De Sa, G.; Malta, O.; de Mello Donegá, C.; Simas, A.; Longo, R.; Santa-Cruz, P., Jr. da Silva. *Coord. Chem. Rev* **2000,** *196*, 165.

26. Caravan, P.; Ellison, J. J.; McMurry, T. J.; Lauffer, R. B., Gadolinium (III) chelates as MRI contrast agents: structure, dynamics, and applications. *Chemical reviews* **1999,** *99* (9), 2293-2352.

27. Li, W.-h.; Fraser, S. E.; Meade, T. J., A calcium-sensitive magnetic resonance imaging contrast agent. *Journal of the American Chemical Society* **1999,** *121* (6), 1413-1414.

28. Stokes, G. G., XXX. On the change of refrangibility of light. *Philosophical Transactions of the Royal Society of London* **1852,** *142*, 463-562.

29. Auzel, F., Upconversion and Anti-Stokes Processes with f and d Ions in Solids. *Chemical Reviews* **2004,** *104* (1), 139-174.

30. Göppert-Mayer, M., Über Elementarakte mit zwei Quantensprüngen. *Annalen der Physik* **1931,** *401* (3), 273-294.

31. Franken, e. P.; Hill, A. E.; Peters, C.; Weinreich, G., Generation of optical harmonics. *Physical review letters* **1961,** *7* (4), 118.

32. Kaiser, W.; Garrett, C., Two-photon excitation in Ca F 2: Eu 2+. *Physical review letters* **1961,** *7* (6), 229.

33. Maiman, T. H., Stimulated optical radiation in ruby. **1960**.

34. Bloembergen, N., Solid State Infrared Quantum Counters. *Physical Review Letters* **1959,** *2* (3), 84-85.

35. Porter Jr, J. F., Fluorescence excitation by the absorption of two consecutive photons. *Physical Review Letters* **1961,** *7* (11), 414.

36. Auzel, F., Compteur quantique par transfert d'energie entre deux ions de terres rares dans un tungstate mixte et dans un verre. *C. R. Acad. Sci. Paris* **1966,** *262*, 1016-1019.

37. Auzel, F., Compteur quantique par transfert denergie de Yb3+ a Tm3+ dans un tungstate mixte et dans un verre germanate. *Comptes rendus hebdomadaires des seances de l academie des sciences serie b* **1966,** *263* (14), 819-&.

38. Salley, G. M.; Valiente, R.; Guedel, H. U., Luminescence upconversion mechanisms in Yb3+–Tb3+ systems. *Journal of Luminescence* **2001,** *94-95*, 305-309.

39. Livanova, L.; Saitkulov, I.; Stolov, A., Summation processes for quanta in CaF2 and SrF2 single crystals activated with Tb3+ and Yb3+ ions. *Sov. Phys. Solid State* **1969,** *11*, 750-754.

40. Souri, N.; Tian, P.; Platas-Iglesias, C.; Wong, K.-L.; Nonat, A.; Charbonnière, L. J., Upconverted photosensitization of Tb visible emission by NIR Yb excitation in discrete supramolecular heteropolynuclear complexes. *Journal of the American Chemical Society* **2017,** *139* (4), 1456-1459.

41. Nonat, A.; Bahamyirou, S.; Lecointre, A.; Przybilla, F.; Mely, Y.; Platas-Iglesias, C.; Camerel, F.; Jeannin, O.; Charbonnière, L. J., Molecular upconversion in water in heteropolynuclear supramolecular Tb/Yb assemblies. *Journal of the American Chemical Society* **2019,** *141* (4), 1568-1576.

42. Knighton, R. C.; Soro, L. K.; Lecointre, A.; Pilet, G.; Fateeva, A.; Pontille, L.; Francés-Soriano, L.; Hildebrandt, N.; Charbonniere, L. J., Upconversion in molecular hetero-nonanuclear lanthanide complexes in solution. *Chemical Communications* **2021,** *57* (1), 53-56.

43. Gao, C.; Zheng, P.; Liu, Q.; Han, S.; Li, D.; Luo, S.; Temple, H.; Xing, C.; Wang, J.; Wei, Y., Recent advances of upconversion nanomaterials in the biological field. *Nanomaterials* **2021,** *11* (10), 2474.

44. Magne, S.; Ouerdane, Y.; Druetta, M.; Goure, J.-P.; Ferdinand, P.; Monnom, G., Cooperative luminescence in an ytterbium-doped silica fibre. *Optics communications* **1994,** *111* (3-4), 310-316.

45. Chen, X.; Li, S.; Song, Z.; Du, W.; Wen, O.; Sawanobori, N., Study on strong cooperative upconversion luminescence of ytterbium-ytterbium clusters in oxyfluoride glass. *JOSA B* **2006,** *23* (12), 2581-2587.

46. Knighton, R. C.; Soro, L. K.; Francés-Soriano, L.; Rodríguez-Rodríguez, A.; Pilet, G.; Lenertz, M.; Platas-Iglesias, C.; Hildebrandt, N.; Charbonnière, L. J., Cooperative luminescence and cooperative sensitisation upconversion of lanthanide complexes in solution. *Angewandte Chemie International Edition* **2022,** *61* (4), e202113114.

47. Gálico, D. A.; Calado, C. M. S.; Murugesu, M., Lanthanide molecular cluster-aggregates as the next generation of optical materials. *Chemical Science* **2023,** *14* (22), 5827-5841.

48. Soro, L. K.; Knighton, R. C.; Avecilla, F.; Thor, W.; Przybilla, F.; Jeannin, O.; Esteban-Gomez, D.; Platas-Iglesias, C.; Charbonnière, L. J., Solution-State Cooperative Luminescence Upconversion in Molecular Ytterbium Dimers. *Advanced Optical Materials* **2023,** *11* (11), 2202307.

49. Kushida, T., Energy transfer and cooperative optical transitions in rare-earth doped inorganic materials. I. Transition probability calculation. *Journal of the physical society of Japan* **1973,** *34* (5), 1318-1326.

50. Kore, B. P.; Kumar, A.; Pandey, A.; Kroon, R. E.; Terblans, J. J.; Dhoble, S. J.; Swart, H. C., Spectroscopic investigation of up-conversion properties in green emitting BaMgF4: Yb3+, Tb3+ phosphor. *Inorganic Chemistry* **2017,** *56* (9), 4996-5005.

51. Bünzli, J.-C. G., Lanthanide luminescence for biomedical analyses and imaging. *Chemical reviews* **2010,** *110* (5), 2729-2755.

52. Heer, S.; Kömpe, K.; Güdel, H. U.; Haase, M., Highly efficient multicolour upconversion emission in transparent colloids of lanthanide-doped NaYF4 nanocrystals. *Advanced Materials* **2004,** *16* (23-24), 2102-2105.

53. Haase, M.; Schäfer, H., Upconverting nanoparticles. *Angewandte Chemie International Edition* **2011,** *50* (26), 5808-5829.

54. Park, Y. I.; Lee, K. T.; Suh, Y. D.; Hyeon, T., Upconverting nanoparticles: a versatile platform for wide-field two-photon microscopy and multi-modal in vivo imaging. *Chemical Society Reviews* **2015,** *44* (6), 1302-1317.

55. Gnach, A.; Lipinski, T.; Bednarkiewicz, A.; Rybka, J.; Capobianco, J. A., Upconverting nanoparticles: assessing the toxicity. *Chemical Society Reviews* **2015,** *44* (6), 1561-1584.

56. Suffren, Y.; Golesorkhi, B.; Zare, D.; Guénée, L.; Nozary, H.; Eliseeva, S. V.; Petoud, S.; Hauser, A.; Piguet, C., Taming lanthanide-centered upconversion at the molecular level. *Inorganic Chemistry* **2016,** *55* (20), 9964-9972.

57. Charbonnière, L. J., Bringing upconversion down to the molecular scale. *Dalton Transactions* **2018,** *47* (26), 8566-8570.

58. Englman, R.; Jortner, J., The energy gap law for radiationless transitions in large molecules. *Molecular Physics* **1970,** *18* (2), 145-164.

59. Diamente, P. R.; Raudsepp, M.; Van Veggel, F. C., Dispersible Tm3+-doped nanoparticles that exhibit strong 1.47 μm photoluminescence. *Advanced Functional Materials* **2007,** *17* (3), 363-368.

60. Pinheiro, A.; Freitas, A.; Silva, G.; Bell, M.; Anjos, V.; Carmo, A.; Dantas, N., Laser performance parameters of Yb3+ doped UV-transparent phosphate glasses. *Chemical Physics Letters* **2014,** *592*, 164-169.

61. Ning, Y.; Tang, J.; Liu, Y.-W.; Jing, J.; Sun, Y.; Zhang, J.-L., Highly luminescent, biocompatible ytterbium (III) complexes as near-infrared fluorophores for living cell imaging. *Chemical Science* **2018,** *9* (15), 3742-3753.

62. Bui, A. T.; Beyler, M.; Grichine, A.; Duperray, A.; Mulatier, J.-C.; Guyot, Y.; Andraud, C.; Tripier, R.; Brasselet, S.; Maury, O., Near infrared two photon imaging using a bright cationic Yb(iii) bioprobe spontaneously internalized into live cells. *Chemical Communications* **2017,** *53* (44), 6005-6008.

63. Mato-Iglesias, M.; Rodríguez-Blas, T.; Platas-Iglesias, C.; Starck, M.; Kadjane, P.; Ziessel, R.; Charbonnière, L., Solution structure and dynamics, stability, and NIR emission properties of lanthanide complexes with a carboxylated bispyrazolylpyridyl ligand. *Inorganic chemistry* **2009,** *48* (4), 1507-1518.

64. Bischof, C.; Wahsner, J.; Scholten, J.; Trosien, S.; Seitz, M., Quantification of C− H quenching in near-IR luminescent ytterbium and neodymium cryptates. *Journal of the American Chemical Society* **2010,** *132* (41), 14334-14335.

65. Hu, J.-Y.; Ning, Y.; Meng, Y.-S.; Zhang, J.; Wu, Z.-Y.; Gao, S.; Zhang, J.-L., Highly near-IR emissive ytterbium (III) complexes with unprecedented quantum yields. *Chemical science* **2017,** *8* (4), 2702-2709.

66. Ye, H.; Bogdanov, V.; Liu, S.; Vajandar, S.; Osipowicz, T.; Hernandez, I.; Xiong, Q., Bright photon upconversion on composite organic lanthanide molecules through localized thermal radiation. *The Journal of Physical Chemistry Letters* **2017,** *8* (23), 5695-5699.

67. Zhang, T.; Zhu, X.; Cheng, C. C.; Kwok, W.-M.; Tam, H.-L.; Hao, J.; Kwong, D. W.; Wong, W.-K.; Wong, K.-L., Water-soluble mitochondria-specific ytterbium complex with impressive NIR emission. *Journal of the American Chemical Society* **2011,** *133* (50), 20120-20122.

68. Shavaleev, N. M.; Scopelliti, R.; Gumy, F.; Bünzli, J.-C. G., Surprisingly bright near-infrared luminescence and short radiative lifetimes of ytterbium in hetero-binuclear Yb− Na chelates. *Inorganic chemistry* **2009,** *48* (16), 7937-7946.

69. Doffek, C.; Seitz, M., The Radiative Lifetime in Near-IR-Luminescent Ytterbium Cryptates: The Key to Extremely High Quantum Yields. *Angewandte Chemie International Edition* **2015,** *54* (33), 9719-9721.

70. Gamelin, D. R.; Güdel, H. U., Design of luminescent inorganic materials: new photophysical processes studied by optical spectroscopy. *Accounts of chemical research* **2000,** *33* (4), 235-242.

71. Golesorkhi, B.; Nozary, H.; Guénée, L.; Fürstenberg, A.; Piguet, C., Room-Temperature Linear Light Upconversion in a Mononuclear Erbium Molecular Complex. *Angewandte Chemie* **2018,** *130* (46), 15392-15396.

72. Nonat, A.; Chan, C. F.; Liu, T.; Platas-Iglesias, C.; Liu, Z.; Wong, W.-T.; Wong, W.-K.; Wong, K.-L.; Charbonnière, L. J., Room temperature molecular up conversion in solution. *Nature Communications* **2016,** *7* (1), 11978.

73. Xiao, X.; Haushalter, J. P.; Faris, G. W., Upconversion from aqueous phase lanthanide chelates. *Optics letters* **2005,** *30* (13), 1674-1676.

74. Yin, H. J.; Feng, Y. S.; Liang, N.; Liu, X. M.; Liu, J. X.; Wang, K. Z.; Yao, C. J., Boosting Photo Upconversion in Electropolymerised Thin Film with Yb/Er Complexes. *Advanced Optical Materials* **2023,** *11* (6), 2202550.

75. Wang, J.; Jiang, Y.; Liu, J. Y.; Xu, H. B.; Zhang, Y. X.; Peng, X.; Kurmoo, M.; Ng, S. W.; Zeng, M. H., Discrete heteropolynuclear Yb/Er assemblies: switching on molecular upconversion under mild conditions. *Angewandte Chemie* **2021,** *133* (41), 22542-22549.

76. Aboshyan-Sorgho, L.; Besnard, C.; Pattison, P.; Kittilstved, K. R.; Aebischer, A.; Bünzli, J. C. G.; Hauser, A.; Piguet, C., Near-Infrared→ Visible Light Upconversion in a Molecular Trinuclear d–f–d Complex. *Angewandte Chemie International Edition* **2011,** *50* (18), 4108-4112.
77. Golesorkhi, B.; Taarit, I.; Bolvin, H.; Nozary, H.; Jiménez, J.-R.; Besnard, C.; Guénée, L.; Fürstenberg, A.; Piguet, C., Molecular light-upconversion: we have had a problem! When excited state absorption (ESA) overcomes energy transfer upconversion (ETU) in Cr (III)/Er (III) complexes. *Dalton Transactions* **2021,** *50* (23), 7955-7968.
78. Auzel, F.; Meichenin, D.; Pelle, F.; Goldner, P., Cooperative luminescence as a defining process for RE-ions clustering in glasses and crystals. *Optical Materials* **1994,** *4* (1), 35-41.
79. Golesorkhi, B.; Fürstenberg, A.; Nozary, H.; Piguet, C., Deciphering and quantifying linear light upconversion in molecular erbium complexes. *Chemical science* **2019,** *10* (28), 6876-6885.
80. Caneschi, A.; Gatteschi, D.; Sessoli, R.; Barra, A. L.; Brunel, L. C.; Guillot, M., Alternating current susceptibility, high field magnetization, and millimeter band EPR evidence for a ground S = 10 state in [Mn12O12(Ch3COO)16(H2O)4].2CH3COOH.4H2O. *Journal of the American Chemical Society* **1991,** *113* (15), 5873-5874.
81. Benelli, C.; Gatteschi, D., *Introduction to molecular magnetism: From transition metals to lanthanides*. John Wiley & Sons: 2015.
82. Wernsdorfer, W.; Aliaga-Alcalde, N.; Hendrickson, D. N.; Christou, G., Exchange-biased quantu tunnelling in a supramolecula dimer of single-molecule magnets. *Nature* **2002,** *416* (6879), 406-409.
83. Leuenberger, M. N.; Loss, D., Quantum computing in molecular magnets. *Nature* **2001,** *410* (6830), 789-793.
84. Luis, F.; Repollés, A.; Martínez-Pérez, M. J.; Aguilà, D.; Roubeau, O.; Zueco, D.; Alonso, P. J.; Evangelisti, M.; Camón, A.; Sesé, J.; Barrios, L. A.; Aromí, G., Molecular Prototypes for Spin-Based CNOT and SWAP Quantum Gates. *Physical Review Letters* **2011,** *107* (11), 117203.
85. Martínez-Pérez, M. J.; Cardona-Serra, S.; Schlegel, C.; Moro, F.; Alonso, P. J.; Prima-García, H.; Clemente-Juan, J. M.; Evangelisti, M.; Gaita-Ariño, A.; Sesé, J.; van Slageren, J.; Coronado, E.; Luis, F., Gd-Based Single-Ion Magnets with Tunable Magnetic Anisotropy: Molecular Design of Spin Qubits. *Physical Review Letters* **2012,** *108* (24), 247213.
86. Bogani, L.; Wernsdorfer, W., Molecular spintronics using single-molecule magnets. *Nature Materials* **2008,** *7* (3), 179-186.
87. Jeon, I.-R.; Clérac, R., Controlled association of single-molecule magnets (SMMs) into coordination networks: towards a new generation of magnetic materials. *Dalton Transactions* **2012,** *41* (32), 9569-9586.
88. Tancini, E.; Rodriguez-Douton, M. J.; Sorace, L.; Barra, A.-L.; Sessoli, R.; Cornia, A., Slow Magnetic Relaxation from Hard-Axis Metal Ions in Tetranuclear Single-Molecule Magnets. *Chemistry – A European Journal* **2010,** *16* (34), 10482-10493.
89. Ishikawa, N.; Sugita, M.; Okubo, T.; Tanaka, N.; Iino, T.; Kaizu, Y., Determination of ligand-field parameters and f-electronic structures of double-decker bis(phthalocyaninato)lanthanide complexes. *Inorganic Chemistry* **2003,** *42* (7), 2440-2446.
90. Ishikawa, N.; Sugita, M.; Ishikawa, T.; Koshihara, S. Y.; Kaizu, Y., Lanthanide double-decker complexes functioning as magnets at the single-molecular level. *Journal of the American Chemical Society* **2003,** *125* (29), 8694-8695.
91. Pugh, T.; Chilton, N. F.; Layfield, R. A., A Low-Symmetry Dysprosium Metallocene Single-Molecule Magnet with a High Anisotropy Barrier. *Angewandte Chemie International Edition* **2016,** *55* (37), 11082-11085.
92. Gregson, M.; Chilton, N. F.; Ariciu, A.-M.; Tuna, F.; Crowe, I. F.; Lewis, W.; Blake, A. J.; Collison, D.; McInnes, E. J.; Winpenny, R. E., A monometallic lanthanide bis (methanediide) single

molecule magnet with a large energy barrier and complex spin relaxation behaviour. *Chemical Science* **2016,** *7* (1), 155-165.

93. Zadrozny, J. M.; Xiao, D. J.; Atanasov, M.; Long, G. J.; Grandjean, F.; Neese, F.; Long, J. R., Magnetic blocking in a linear iron(I) complex. *Nature Chemistry* **2013,** *5* (7), 577-581.

94. Blagg, R. J.; Ungur, L.; Tuna, F.; Speak, J.; Comar, P.; Collison, D.; Wernsdorfer, W.; McInnes, E. J. L.; Chibotaru, L. F.; Winpenny, R. E. P., Magnetic relaxation pathways in lanthanide single-molecule magnets. *Nature Chemistry* **2013,** *5* (8), 673-678.

95. Shiddiq, M.; Komijani, D.; Duan, Y.; Gaita-Ariño, A.; Coronado, E.; Hill, S., Enhancing coherence in molecular spin qubits via atomic clock transitions. *Nature* **2016,** *531* (7594), 348-351.

96. Moreno-Pineda, E.; Nodaraki, L. E.; Tuna, F., Chapter 1 - Molecular Nanomagnets Based on f-Elements. In *Novel Magnetic Nanostructures*, Domracheva, N.; Caporali, M.; Rentschler, E., Eds. Elsevier: 2018; pp 1-50.

97. Moreno-Pineda, E.; Nodaraki, L.; Tuna, F., Molecular Nanomagnets Based on f-Elements. 2018; pp 1-50.

98. Rinehart, J. D.; Long, J. R., Exploiting single-ion anisotropy in the design of f-element single-molecule magnets. *Chemical Science* **2011,** *2* (11), 2078-2085.

99. Stevens, K. W. H., Matrix elements and operator equivalents connected with the magnetic properties of rare earth ions. *Proceedings of the Physical Society. Section A* **1952,** *65* (3), 209-215.

100. Sorace, L.; Benelli, C.; Gatteschi, D., Lanthanides in molecular magnetism: old tools in a new field. *Chemical Society Reviews* **2011,** *40* (6), 3092-3104.

101. Thiele, S.; Vincent, R.; Holzmann, M.; Klyatskaya, S.; Ruben, M.; Balestro, F.; Wernsdorfer, W., Electrical Readout of Individual Nuclear Spin Trajectories in a Single-Molecule Magnet Spin Transistor. *Physical Review Letters* **2013,** *111* (3), 037203.

102. Gatteschi, D.; Sessoli, R., Quantum tunneling of magnetization and related phenomena in molecular materials. *Angewandte Chemie - International Edition* **2003,** *42* (3), 268-297.

103. Zadrozny, J. M.; Atanasov, M.; Bryan, A. M.; Lin, C. Y.; Rekken, B. D.; Power, P. P.; Neese, F.; Long, J. R., Slow magnetization dynamics in a series of two-coordinate iron(ii) complexes. *Chemical Science* **2013,** *4* (1), 125-138.

104. Kahn, O., Molecular Magnetism, VCH Publ. *Inc.: New York, NY, USA* **1993**, 393.

105. Jiang, S.-D.; Wang, B.-W.; Sun, H.-L.; Wang, Z.-M.; Gao, S., An organometallic single-ion magnet. *Journal of the American Chemical Society* **2011,** *133* (13), 4730-4733.

106. Han, S.-D.; Miao, X.-H.; Liu, S.-J.; Bu, X.-H., Magnetocaloric effect and slow magnetic relaxation in two dense (3, 12)-connected lanthanide complexes. *Inorganic Chemistry Frontiers* **2014,** *1* (7), 549-552.

107. Weinstein, G., The 1905 Relativity Paper and the "Light Quantum". **2013**.

108. Brisson, J., Cold-cycle dilution refrigeration. *Journal of low temperature physics* **1998,** *111*, 181-199.

109. Martin, F.; Vermeulen, G.; Camus, P.; Benoit, A., A closed cycle 3He–4He dilution refrigerator insensitive to gravity. *Cryogenics* **2010,** *50* (9), 623-627.

110. Sharples, J. W.; Collison, D., Lanthanides and the Magnetocaloric Effect. In *Lanthanides and Actinides in Molecular Magnetism*, 2015; pp 293-314.

111. Evangelisti, M.; Roubeau, O.; Palacios, E.; Camón, A.; Hooper, T. N.; Brechin, E. K.; Alonso, J. J., Cryogenic magnetocaloric effect in a ferromagnetic molecular dimer. *Angewandte Chemie International Edition* **2011,** *50* (29), 6606-6609.

112. Evangelisti, M.; Brechin, E. K., Recipes for enhanced molecular cooling. *Dalton Transactions* **2010,** *39* (20), 4672-4676.

113. McMichael, R. D.; Ritter, J.; Shull, R., Enhanced magnetocaloric effect in Gd3Ga5− x Fe x O12. *Journal of Applied Physics* **1993,** *73* (10), 6946-6948.

114. Hamilton, A. S.; Lampronti, G.; Rowley, S.; Dutton, S., Enhancement of the magnetocaloric effect driven by changes in the crystal structure of Al-doped GGG, Gd3Ga5− xAlxO12 (0≤ x≤ 5). *Journal of Physics: Condensed Matter* **2014,** *26* (11), 116001.

115. Kahn, O.; Cador, O.; Larionova, J.; Mathoniere, C.; Sutter, J. P.; Ouahab, L., Molecular magnetism: A multidisciplinary field of research. *Molecular Crystals and Liquid Crystals Science and Technology. Section A. Molecular Crystals and Liquid Crystals* **1997,** *305* (1), 1-16.

116. Lorusso, G.; Sharples, J. W.; Palacios, E.; Roubeau, O.; Brechin, E. K.; Sessoli, R.; Rossin, A.; Tuna, F.; McInnes, E. J.; Collison, D., A dense metal–organic framework for enhanced magnetic refrigeration. *Advanced materials* **2013,** *25* (33), 4653-4656.

117. Wei, W.; Xie, R.-K.; Du, S.-W.; Tian, C.-B.; Chai, G.-L., Synthesis, structure, magnetocaloric effect and DFT calculations of a MnII cluster-based inorganic coordination polymer. *Journal of Alloys and Compounds* **2021,** *878*, 160353.

118. Blagg, R. J.; Tuna, F.; McInnes, E. J.; EP, R., Lanthanoid Alkoxide & Thiolate Clusters: Synthesis, Structure & Magnetism. *Angew. Chem. Int. Ed* **2011,** *50*, 6530-6533.

119. Sharples, J. W.; Zheng, Y.-Z.; Tuna, F.; McInnes, E. J.; Collison, D., Lanthanide discs chill well and relax slowly. *Chemical Communications* **2011,** *47* (27), 7650-7652.

120. Chilton, N. F.; Anderson, R. P.; Turner, L. D.; Soncini, A.; Murray, K. S., PHI: A powerful new program for the analysis of anisotropic monomeric and exchange-coupled polynuclear d-and f-block complexes. *Journal of Computational Chemistry* **2013,** *34* (13), 1164-1175.

121. Sharples, J. W., Cooling Rapidly and Relaxing Slowly with 4f Ions. **2013**.

122. Martínez-Pérez, M. J.; Montero, O.; Evangelisti, M.; Luis, F.; Sesé, J.; Cardona-Serra, S.; Coronado, E., Fragmenting Gadolinium: Mononuclear Polyoxometalate-Based Magnetic Coolers for Ultra-Low Temperatures. *Advanced Materials* **2012,** *24* (31), 4301-4305.

123. Guo, F.-S.; Leng, J.-D.; Liu, J.-L.; Meng, Z.-S.; Tong, M.-L., Polynuclear and polymeric gadolinium acetate derivatives with large magnetocaloric effect. *Inorganic Chemistry* **2012,** *51* (1), 405-413.

124. Liu, S. J.; Xie, C. C.; Jia, J. M.; Zhao, J. P.; Han, S. D.; Cui, Y.; Li, Y.; Bu, X. H., Low-Dimensional Carboxylate-Bridged GdIII Complexes for Magnetic Refrigeration. *Chemistry–An Asian Journal* **2014,** *9* (4), 1116-1122.

125. Lorusso, G.; Palacios, M. A.; Nichol, G. S.; Brechin, E. K.; Roubeau, O.; Evangelisti, M., Increasing the dimensionality of cryogenic molecular coolers: Gd-based polymers and metal–organic frameworks. *Chemical Communications* **2012,** *48* (61), 7592-7594.

126. Guo, F. S.; Chen, Y. C.; Mao, L. L.; Lin, W. Q.; Leng, J. D.; Tarasenko, R.; Orendáč, M.; Prokleška, J.; Sechovský, V.; Tong, M. L., Anion-templated assembly and magnetocaloric properties of a nanoscale {Gd38} cage versus a {Gd48} barrel. *Chemistry–A European Journal* **2013,** *19* (44), 14876-14885.

127. Luzon, J.; Sessoli, R., Lanthanides in molecular magnetism: so fascinating, so challenging. *Dalton Transactions* **2012,** *41* (44), 13556-13567.

128. Zheng, Y.-Z.; Evangelisti, M.; Tuna, F.; Winpenny, R. E., Co–Ln mixed-metal phosphonate grids and cages as molecular magnetic refrigerants. *Journal of the American Chemical Society* **2012,** *134* (2), 1057-1065.

129. Lorusso, G.; Roubeau, O.; Evangelisti, M., Rotating Magnetocaloric Effect in an Anisotropic Molecular Dimer. *Angewandte Chemie International Edition* **2016,** *55* (10), 3360-3363.

130. Panguluri, S. P. K.; Jourdain, E.; Chakraborty, P.; Klyatskaya, S.; Kappes, M. M.; Nonat, A. M.; Charbonnière, L. J.; Ruben, M., Yb-to-Eu Cooperative Sensitization Upconversion in a Multifunctional Molecular Nonanuclear Lanthanide Cluster in Solution. *Journal of the American Chemical Society* **2024,** *146* (19), 13083-13092.

131. Zhou, B.; Yan, L.; Huang, J.; Liu, X.; Tao, L.; Zhang, Q., NIR II-responsive photon upconversion through energy migration in an ytterbium sublattice. *Nature Photonics* **2020,** *14* (12), 760-766.

132. Lee, C.; Xu, E. Z.; Liu, Y.; Teitelboim, A.; Yao, K.; Fernandez-Bravo, A.; Kotulska, A. M.; Nam, S. H.; Suh, Y. D.; Bednarkiewicz, A., Giant nonlinear optical responses from photon-avalanching nanoparticles. *Nature* **2021,** *589* (7841), 230-235.

133. Bobo, D.; Robinson, K. J.; Islam, J.; Thurecht, K. J.; Corrie, S. R., Nanoparticle-based medicines: a review of FDA-approved materials and clinical trials to date. *Pharmaceutical research* **2016,** *33*, 2373-2387.

134. Beeby, A.; Clarkson, I. M.; Dickins, R. S.; Faulkner, S.; Parker, D.; Royle, L.; De Sousa, A. S.; Williams, J. G.; Woods, M., Non-radiative deactivation of the excited states of europium, terbium and ytterbium complexes by proximate energy-matched OH, NH and CH oscillators: an improved luminescence method for establishing solution hydration states. *Journal of the Chemical Society, Perkin Transactions 2* **1999,** (3), 493-504.

135. Nonat, A. M.; Charbonnière, L. J., Upconversion of light with molecular and supramolecular lanthanide complexes. *Coordination Chemistry Reviews* **2020,** *409*, 213192.

136. Guettas, D.; Balogh, C. M.; Sonneville, C.; Malicet, Y.; Lepoivre, F.; Onal, E.; Fateeva, A.; Reber, C.; Luneau, D.; Maury, O., Nano-Nonanuclear Mixed-Lanthanide Clusters [Eu9–xTbx] Featuring Tunable Dual Luminescence Properties. *European Journal of Inorganic Chemistry* **2016,** *2016* (24), 3932-3938.

137. Xu, G.; Wang, Z.-M.; He, Z.; Lü, Z.; Liao, C.-S.; Yan, C.-H., Synthesis and structural characterization of nonanuclear lanthanide complexes. *Inorganic chemistry* **2002,** *41* (25), 6802-6807.

138. Zare, D.; Suffren, Y.; Guénée, L.; Eliseeva, S. V.; Nozary, H.; Aboshyan-Sorgho, L.; Petoud, S.; Hauser, A.; Piguet, C., Smaller than a nanoparticle with the design of discrete polynuclear molecular complexes displaying near-infrared to visible upconversion. *Dalton Transactions* **2015,** *44* (6), 2529-2540.

139. Govorov, A.; Martínez, P. L. H.; Demir, H. V., *Understanding and Modeling Förster-type Resonance Energy Transfer (FRET): Introduction to FRET, Vol. 1*. Springer: 2016.

140. Cantuel, M.; Gumy, F.; Bünzli, J.-C. G.; Piguet, C., Encapsulation of labile trivalent lanthanides into a homobimetallic chromium (III)-containing triple-stranded helicate. Synthesis, characterization, and divergent intramolecular energy transfers. *Dalton Transactions* **2006,** (22), 2647-2660.

141. Tripier, R.; Platas-Iglesias, C.; Boos, A.; Morfin, J. F.; Charbonnière, L., Towards fluoride sensing with positively charged lanthanide complexes. Wiley Online Library: 2010.

142. Lima, L. s. M.; Lecointre, A.; Morfin, J.-F. o.; de Blas, A.; Visvikis, D.; Charbonnière, L. c. J.; Platas-Iglesias, C.; Tripier, R. l., Positively charged lanthanide complexes with cyclen-based ligands: synthesis, solid-state and solution structure, and fluoride interaction. *Inorganic chemistry* **2011,** *50* (24), 12508-12521.

143. Nonat, A.; Liu, T.; Jeannin, O.; Camerel, F.; Charbonnière, L. J., Energy transfer in supramolecular heteronuclear lanthanide dimers and application to fluoride sensing in water. *Chemistry–A European Journal* **2018,** *24* (15), 3784-3792.

144. Duan, X.-F.; Zhou, L.-P.; Li, H.-R.; Hu, S.-J.; Zheng, W.; Xu, X.; Zhang, R.; Chen, X.; Guo, X.-Q.; Sun, Q.-F., Excited-Multimer Mediated Supramolecular Upconversion on Multicomponent Lanthanide-Organic Assemblies. *Journal of the American Chemical Society* **2023,** *145* (42), 23121-23130.

145. Baril-Robert, F.; Petit, S.; Pilet, G.; Chastanet, G.; Reber, C.; Luneau, D., Site-selective lanthanide doping in a nonanuclear yttrium (III) cluster revealed by crystal structures and luminescence spectra. *Inorganic chemistry* **2010,** *49* (23), 10970-10976.

146. Werts, M. H.; Jukes, R. T.; Verhoeven, J. W., The emission spectrum and the radiative lifetime of Eu 3+ in luminescent lanthanide complexes. *Physical Chemistry Chemical Physics* **2002,** *4* (9), 1542-1548.

147. Kadjane, P.; Charbonnière, L.; Camerel, F.; Lainé, P. P.; Ziessel, R., Improving visible light sensitization of luminescent europium complexes. *Journal of fluorescence* **2008,** *18*, 119-129.

148. Chen, G.; Qiu, H.; Prasad, P. N.; Chen, X., Upconversion nanoparticles: design, nanochemistry, and applications in theranostics. *Chemical reviews* **2014,** *114* (10), 5161-5214.

149. Sun, L.; Wei, R.; Feng, J.; Zhang, H., Tailored lanthanide-doped upconversion nanoparticles and their promising bioapplication prospects. *Coordination Chemistry Reviews* **2018,** *364*, 10-32.

150. Sharples, J. W.; Collison, D.; McInnes, E. J.; Schnack, J.; Palacios, E.; Evangelisti, M., Quantum signatures of a molecular nanomagnet in direct magnetocaloric measurements. *Nature communications* **2014,** *5* (1), 5321.

151. Zhitomirsky, M.; Honecker, A., Magnetocaloric effect in one-dimensional antiferromagnets. *Journal of Statistical Mechanics: Theory and Experiment* **2004,** *2004* (07), P07012.

152. Krivnov, V. Y.; Dmitriev, D.; Nishimoto, S.; Drechsler, S.-L.; Richter, J., Delta chain with ferromagnetic and antiferromagnetic interactions at the critical point. *Physical Review B* **2014,** *90* (1), 014441.

153. Honecker, A.; Wessel, S., Magnetocaloric effect in two-dimensional spin-1/2 antiferromagnets. *Physica B: Condensed Matter* **2006,** *378*, 1098-1099.

154. Wolf, B.; Tsui, Y.; Jaiswal-Nagar, D.; Tutsch, U.; Honecker, A.; Remović-Langer, K.; Hofmann, G.; Prokofiev, A.; Assmus, W.; Donath, G., Magnetocaloric effect and magnetic cooling near a field-induced quantum-critical point. *Proceedings of the National Academy of Sciences* **2011,** *108* (17), 6862-6866.

155. Khalil, G. E.; Thompson, E. K.; Gouterman, M.; Callis, J. B.; Dalton, L. R.; Turro, N. J.; Jockusch, S., NIR luminescence of gadolinium porphyrin complexes. *Chemical Physics Letters* **2007,** *435* (1), 45-49.

156. Tobita, S.; Arakawa, M.; Tanaka, I., The paramagnetic metal effect on the ligand localized S1 .apprx. .fwdarw. T1 intersystem crossing in the rare-earth-metal complexes with methyl salicylate. *The Journal of Physical Chemistry* **1985,** *89* (26), 5649-5654.

157. Tobita, S.; Arakawa, M.; Tanaka, I., Electronic relaxation processes of rare earth chelates of benzoyltrifluoroacetone. *The Journal of Physical Chemistry* **1984,** *88* (13), 2697-2702.

158. Telfer, S. G.; McLean, T. M.; Waterland, M. R., Exciton coupling in coordination compounds. *Dalton Transactions* **2011,** *40* (13), 3097-3108.

159. Renger, T.; May, V.; Kühn, O., Ultrafast excitation energy transfer dynamics in photosynthetic pigment–protein complexes. *Physics Reports* **2001,** *343* (3), 137-254.

160. Kasha, M.; Rawls, H. R.; Ashraf El-Bayoumi, M., The exciton model in molecular spectroscopy. **1965,** *11* (3-4), 371-392.

161. Pineda, E. M.; Lorusso, G.; Zangana, K. H.; Palacios, E.; Schnack, J.; Evangelisti, M.; Winpenny, R. E.; McInnes, E. J., Observation of the influence of dipolar and spin frustration effects on the magnetocaloric properties of a trigonal prismatic {Gd 7} molecular nanomagnet. *Chemical science* **2016,** *7* (8), 4891-4895.

162. Moessner, R.; Ramirez, A. P., Geometrical frustration. *Physics Today* **2006,** *59* (2), 24-29.

163. Schnack, J.; Schmidt, R.; Richter, J., Enhanced magnetocaloric effect in frustrated magnetic molecules with icosahedral symmetry. *Physical Review B* **2007,** *76* (5), 054413.

164. Wernsdorfer, W., From micro-to nano-SQUIDs: applications to nanomagnetism. *Superconductor Science and Technology* **2009,** *22* (6), 064013.

165. Alexandropoulos, D. I.; Mukherjee, S.; Papatriantafyllopoulou, C.; Raptopoulou, C. P.; Psycharis, V.; Bekiari, V.; Christou, G.; Stamatatos, T. C., A new family of nonanuclear lanthanide clusters displaying magnetic and optical properties. *Inorganic Chemistry* **2011,** *50* (22), 11276-11278.

166. Eliseeva, S. V.; Bünzli, J.-C. G., Rare earths: jewels for functional materials of the future. *New Journal of Chemistry* **2011,** *35* (6), 1165-1176.

167. Barra, A.-L.; Caneschi, A.; Cornia, A.; Gatteschi, D.; Gorini, L.; Heiniger, L.-P.; Sessoli, R.; Sorace, L., The origin of transverse anisotropy in axially symmetric single molecule magnets. *Journal of the American Chemical Society* **2007,** *129* (35), 10754-10762.

168. Bünzli, J.-C. G.; Piguet, C., Taking advantage of luminescent lanthanide ions. *Chemical Society Reviews* **2005,** *34* (12), 1048-1077.

169. Coronado, E.; Dunbar, K. R., Preface for the forum on molecular magnetism: the role of inorganic chemistry. *Inorganic chemistry* **2009,** *48* (8), 3293-3295.

170. Pombeiro, A.; Kukushkin, V. Y.; McCleverty, J.; Thomas, J., Comprehensive Coordination Chemistry II. *JA McCleverty and TJ Meyer, Eds* **2004**.

171. Brunet, G. Molecular Engineering of Metal-Organic Assemblies: Advances Toward Next Generation Porous and Magnetic Materials. Université d'Ottawa/University of Ottawa, 2020.

172. Guégan, F.; Jung, J.; Le Guennic, B.; Riobé, F.; Maury, O.; Gillon, B.; Jacquot, J.-F.; Guyot, Y.; Morell, C.; Luneau, D., Evidencing under-barrier phenomena in a Yb (III) SMM: a joint luminescence/neutron diffraction/SQUID study. *Inorganic Chemistry Frontiers* **2019,** *6* (11), 3152-3157.

173. Pointillart, F.; Cador, O.; Le Guennic, B.; Ouahab, L., Uncommon lanthanide ions in purely 4f Single Molecule Magnets. *Coordination Chemistry Reviews* **2017,** *346*, 150-175.

174. Brunet, G.; Marin, R.; Monk, M.-J.; Resch-Genger, U.; Gálico, D. A.; Sigoli, F. A.; Suturina, E. A.; Hemmer, E.; Murugesu, M., Exploring the dual functionality of an ytterbium complex for luminescence thermometry and slow magnetic relaxation. *Chemical science* **2019,** *10* (28), 6799-6808.

175. Kishi, Y.; Cornet, L.; Pointillart, F.; Riobé, F.; Lefeuvre, B.; Cador, O.; Le Guennic, B.; Maury, O.; Fujiwara, H.; Ouahab, L., Luminescence and Single-Molecule-Magnet Behaviour in Lanthanide Coordination Complexes Involving Benzothiazole-Based Tetrathiafulvalene Ligands. *European Journal of Inorganic Chemistry* **2018,** *2018* (3-4), 458-468.

176. Ruiz-Bilbao, E.; Pardo-Almanza, M.; Oyarzabal, I.; Artetxe, B. a.; Felices, L. S.; García, J. A.; Seco, J. M.; Colacio, E.; Lezama, L.; Gutiérrez-Zorrilla, J. M., Slow Magnetic Relaxation and Luminescent Properties of Mononuclear Lanthanide-Substituted Keggin-Type Polyoxotungstates with Compartmental Organic Ligands. *Inorganic Chemistry* **2022,** *61* (5), 2428-2443.

177. Ishikawa, N.; Sugita, M.; Ishikawa, T.; Koshihara, S.-y.; Kaizu, Y., Lanthanide double-decker complexes functioning as magnets at the single-molecular level. *Journal of the American Chemical Society* **2003,** *125* (29), 8694-8695.

178. Barhoumi, R.; Amokrane, A.; Klyatskaya, S.; Boero, M.; Ruben, M.; Bucher, J.-P., Screening the 4f-electron spin of TbPc 2 single-molecule magnets on metal substrates by ligand channeling. *Nanoscale* **2019,** *11* (44), 21167-21179.

179. Pederson, R.; Wysocki, A. L.; Mayhall, N.; Park, K., Multireference ab initio studies of magnetic properties of terbium-based single-molecule magnets. *The Journal of Physical Chemistry A* **2019,** *123* (32), 6996-7006.

180. Goodwin, C. A.; Ortu, F.; Reta, D.; Chilton, N. F.; Mills, D. P., Molecular magnetic hysteresis at 60 kelvin in dysprosocenium. *Nature* **2017,** *548* (7668), 439-442.

181. Gould, C. A.; McClain, K. R.; Reta, D.; Kragskow, J. G.; Marchiori, D. A.; Lachman, E.; Choi, E.-S.; Analytis, J. G.; Britt, R. D.; Chilton, N. F., Ultrahard magnetism from mixed-valence dilanthanide complexes with metal-metal bonding. *Science* **2022,** *375* (6577), 198-202.

182. Guo, F.-S.; Day, B. M.; Chen, Y.-C.; Tong, M.-L.; Mansikkamäki, A.; Layfield, R. A., Magnetic hysteresis up to 80 kelvin in a dysprosium metallocene single-molecule magnet. *Science* **2018,** *362* (6421), 1400-1403.

183. Borah, A.; Murugavel, R., Magnetic relaxation in single-ion magnets formed by less-studied lanthanide ions Ce (III), Nd (III), Gd (III), Ho (III), Tm (II/III) and Yb (III). *Coordination Chemistry Reviews* **2022,** *453*, 214288.

184. Wu, S.-G.; Ruan, Z.-Y.; Huang, G.-Z.; Zheng, J.-Y.; Vieru, V.; Taran, G.; Wang, J.; Chen, Y.-C.; Liu, J.-L.; Chibotaru, L. F., Field-induced oscillation of magnetization blocking barrier in a holmium metallacrown single-molecule magnet. *Chem* **2021,** *7* (4), 982-992.

185. Hilgar, J.; Bernbeck, M.; Flores, B.; Rinehart, J., Metal–ligand pair anisotropy in a series of mononuclear Er–COT complexes. *Chemical science* **2018,** *9* (36), 7204-7209.

186. Le Roy, J. J.; Ungur, L.; Korobkov, I.; Chibotaru, L. F.; Murugesu, M., Coupling strategies to enhance single-molecule magnet properties of erbium–cyclooctatetraenyl complexes. *Journal of the American Chemical Society* **2014,** *136* (22), 8003-8010.

187. Dei, A.; Gatteschi, D., Molecular (nano) magnets as test grounds of quantum mechanics. *Angewandte Chemie International Edition* **2011,** *50* (50), 11852-11858.

188. Scherthan, L.; Schmidt, S. F.; Auerbach, H.; Hochdörffer, T.; Wolny, J. A.; Bi, W.; Zhao, J.; Hu, M. Y.; Toellner, T.; Alp, E. E., Back Cover: 161Dy Time-Domain Synchrotron Mössbauer Spectroscopy for Investigating Single-Molecule Magnets Incorporating Dy Ions (Angew. Chem. Int. Ed. 11/2019). *Angewandte Chemie International Edition* **2019,** *58* (11), 3652-3652.

189. Benelli, C.; Gatteschi, D., Magnetism of lanthanides in molecular materials with transition-metal ions and organic radicals. *Chemical Reviews* **2002,** *102* (6), 2369-2388.

190. Koroteev, P. S.; Dobrokhotova, Z. V.; Ilyukhin, A. B.; Belova, E. V.; Yapryntsev, A. D.; Rouzières, M.; Clérac, R.; Efimov, N. N., Tetranuclear Cr–Ln ferrocenecarboxylate complexes with a defect-dicubane structure: synthesis, magnetism, and thermolysis. *Dalton Transactions* **2021,** *50* (46), 16990-16999.

191. Efimov, N.; Koroteev, P., Magnetochemistry 2016, 2, 38; f) SP Petrosyants, Zh. V. Dobrokhotova, AB Ilyukhin, NN Efimov, AV Gavrikov, PN Vasilyev, VM Novotortsev. *Eur. J. Inorg. Chem* **2017**, 3561-3569.

192. Zhang, S.; Ke, H.; Sun, L.; Li, X.; Shi, Q.; Xie, G.; Wei, Q.; Yang, D.; Wang, W.; Chen, S., Magnetization dynamics changes of dysprosium (III) single-ion magnets associated with guest molecules. *Inorganic Chemistry* **2016,** *55* (8), 3865-3871.

193. Pointillart, F.; Jung, J.; Berraud-Pache, R.; Le Guennic, B.; Dorcet, V.; Golhen, S.; Cador, O.; Maury, O.; Guyot, Y.; Decurtins, S., Luminescence and single-molecule magnet behavior in lanthanide complexes involving a tetrathiafulvalene-fused dipyridophenazine ligand. *Inorganic chemistry* **2015,** *54* (11), 5384-5397.

194. Pointillart, F.; Le Guennic, B.; Golhen, S.; Cador, O.; Maury, O.; Ouahab, L., A redox-active luminescent ytterbium based single molecule magnet. *Chemical Communications* **2013,** *49* (6), 615-617.

195. Tang, M.; Huang, Y.; Wang, Y.; Fu, L., An ytterbium complex with unique luminescence properties: detecting the temperature based on a luminescence spectrum without the interference of oxygen. *Dalton Transactions* **2015,** *44* (16), 7449-7457.

196. Ning, Y.; Liu, Y.-W.; Meng, Y.-S.; Zhang, J.-L., Design of near-infrared luminescent lanthanide complexes sensitive to environmental stimulus through rationally tuning the secondary coordination sphere. *Inorganic Chemistry* **2018,** *57* (3), 1332-1341.

197. Langley, S. K.; Wielechowski, D. P.; Vieru, V.; Chilton, N. F.; Moubaraki, B.; Chibotaru, L. F.; Murray, K. S., Modulation of slow magnetic relaxation by tuning magnetic exchange in {Cr 2 Dy 2} single molecule magnets. *Chemical Science* **2014,** *5* (8), 3246-3256.

198. Demir, S.; Jeon, I.-R.; Long, J. R.; Harris, T. D., Radical ligand-containing single-molecule magnets. *Coordination Chemistry Reviews* **2015,** *289*, 149-176.

199. Wasielewski, M. R.; Forbes, M. D.; Frank, N. L.; Kowalski, K.; Scholes, G. D.; Yuen-Zhou, J.; Baldo, M. A.; Freedman, D. E.; Goldsmith, R. H.; Goodson III, T., Exploiting chemistry and molecular systems for quantum information science. *Nature Reviews Chemistry* **2020,** *4* (9), 490-504.

200. Ardavan, A.; Rival, O.; Morton, J. J.; Blundell, S. J.; Tyryshkin, A. M.; Timco, G. A.; Winpenny, R. E., Will spin-relaxation times in molecular magnets permit quantum information processing? *Physical review letters* **2007,** *98* (5), 057201.

201. Bayliss, S.; Laorenza, D.; Mintun, P.; Kovos, B.; Freedman, D.; Awschalom, D., Optically addressable molecular spins for quantum information processing. *Science* **2020,** *370* (6522), 1309-1312.

202. Atzori, M.; Benci, S.; Morra, E.; Tesi, L.; Chiesa, M.; Torre, R.; Sorace, L.; Sessoli, R., Structural effects on the spin dynamics of potential molecular qubits. *Inorganic chemistry* **2018,** *57* (2), 731-740.

203. Atzori, M.; Morra, E.; Tesi, L.; Albino, A.; Chiesa, M.; Sorace, L.; Sessoli, R., Quantum coherence times enhancement in vanadium (IV)-based potential molecular qubits: the key role of the vanadyl moiety. *Journal of the American Chemical Society* **2016,** *138* (35), 11234-11244.

204. Gimeno, I.; Urtizberea, A.; Román-Roche, J.; Zueco, D.; Camón, A.; Alonso, P. J.; Roubeau, O.; Luis, F., Broad-band spectroscopy of a vanadyl porphyrin: a model electronuclear spin qudit. *Chemical science* **2021,** *12* (15), 5621-5630.

205. Kotrle, K.; Nemec, I.; Moncol, J.; Čižmár, E.; Herchel, R., 3d–4f magnetic exchange interactions and anisotropy in a series of heterobimetallic vanadium (IV)–lanthanide (III) Schiff base complexes. *Dalton Transactions* **2021,** *50* (39), 13883-13893.

206. Costes, J. P.; Dahan, F.; Donnadieu, B.; Garcia-Tojal, J.; Laurent, J. P., Versatility of the Nature of the Magnetic Gadolinium (III)− Vanadium (IV) Interaction− Structure and Magnetic Properties of Two Heterobinuclear [Gd, V (O)] Complexes. *European Journal of Inorganic Chemistry* **2001,** *2001* (2), 363-365.

207. Liu, R.; Liu, L.; Fang, D.; Xu, J.; Zhao, S.; Xu, W., Synthesis, Structure, and Magnetic Properties of Two Novel Dinuclear Complexes involving Lanthanide-phenoxo Anion Radical. *Zeitschrift für anorganische und allgemeine Chemie* **2015,** *641* (3-4), 728-731.

208. Wang, F.; Liu, L.-Z.; Gao, L.; Dong, W.-K., Unusual constructions of two salamo-based copper (II) complexes. *Spectrochimica Acta Part A: Molecular and Biomolecular Spectroscopy* **2018,** *203*, 56-64.

209. Valeur, B.; Berberan-Santos, M. N., *Molecular fluorescence: principles and applications*. John Wiley & Sons: 2012.

210. Olmsted, J., Calorimetric determinations of absolute fluorescence quantum yields. *Journal of Physical Chemistry* **1979,** *83* (20), 2581-2584.

211. Inagaki, S.; Saito, K.; Suto, S.; Aihara, H.; Sugawara, A.; Tamura, S.; Kawano, T., Synthesis of 5-aryl-3 (2 H)-furanones using intramolecular cyclization of sulfonium salts. *The Journal of Organic Chemistry* **2018,** *83* (22), 13834-13846.

Appendix

A.a. List of Figures

A.b. List of Tables

A.c. List of Publications

1. Shagor Chowdhury, Saibal Jana, **Sai P. K. Panguluri**, Wolfgang Wenzel, Svetlana Klayatskaya, Mario Ruben (2024): Ferrocene Appended Porphyrin-Based Bipolar Electrode Material for High-Performance Energy Storage. *ChemSusChem* 2024, e202301903, https://doi.org/10.1002/cssc.202301903
2. **Sai P. K. Panguluri**, Elsa Jourdain, Papri Chakraborty, Svetlana Klyatskaya, Manfred M. Kappes, Aline Nonat,* Loïc J. Charbonnière,* Mario Ruben* (2024): Yb-to-Eu Cooperative Sensitization Upconversion in a Multifunctional Molecular Nonanuclear Lanthanide Cluster in Solution. *J. Am. Chem. Soc.* **2024**, *146*, 19, 13083–13092. https://doi.org/10.1021/jacs.3c14527
3. **Sai P. K. Panguluri**, Eufemio Moreno Pineda,* Papri Chakraborty, Svetlana Klyatskaya, Manfred M. Kappes, Jürgen Schnack,* Marco Affronte,* Mario Ruben*: Investigating the various properties and effects in a highly symmetric Gd_9 cluster. (Manuscript in preparation).

A.d. Summer School & Conference Presentations

1. Isotopologues and The Effects on Magnetic Properties of SMMs (Poster), QUSTEC second summer school, 2022, Freiburg, Germany.

2. Upconversion & downshifting of light in a novel multifunctional Eu/Yb-nonanuclear lanthanide complex in solution (Poster), QUSTEC third summer school 2023, Durbach, Germany.

3. Upconversion & downshifting of light in a novel multifunctional Eu/Yb-nonanuclear lanthanide complex in solution (Poster), "Optically Addressable Molecular Lanthanide Qubits for Quantum Devices" 2023, Baden-Baden, Germany

4. European School of Magnetism summer school 2021, Cluj-Napoca, Romania.